

## ABSTRACT

Title of Document: Development of In-Mold Assembly Methods for  
Producing Mesoscale Revolute Joints

Arvind Ananthanarayanan,

Doctor of Philosophy, 2009

Directed By: Professor Satyandra K.Gupta  
Department of Mechanical Engineering

In-mold assembly is a promising process for producing articulated joints. It utilizes injection molding to automate assembly operations, which may otherwise require high labor times for production. Since injection molding is a high throughput process, in-mold assembly holds considerable promise in bulk production of assembled parts. However, current in-mold assembly methods cannot be used for manufacturing in-mold assembled products at the mesoscale. This is because the process changes considerably when the sizes of the molded parts are reduced. The premolded component in a mesoscale joint consists of miniature features. Hence, when a high temperature, high pressure polymer melt is injected on top of it, it is susceptible to plastic deformation. Due to presence of a mesoscale premolded component which is susceptible to deformation, traditional shrinkage models alone can not be used to characterize and control the clearances. This dissertation identifies and addresses

issues pertaining to in-mold assembly of revolute joints at the mesoscale. First, this dissertation identifies defect modes which are unique to in-mold assembly at the mesoscale. Then it develops mold design templates which can be used for manufacturing in-mold assembled mesoscale revolute joints. Further, issues related to the deformation of the mesoscale premolded component are identified. Two novel mold design solutions to realize mesoscale in-mold assembled revolute joints are presented. The first involves use of mold inserts to constrain the premolded component to inhibit its deformation. The second involves use of a bi-directional flow of the polymer melt over the premolded component to balance the deforming forces experienced by it. Finally, methods to predict and control clearances that would be obtained in mesoscale in-mold assembled revolute joints are presented. To demonstrate the utility of the tools built as part of this research effort, a case study of a miniature robotic application built using mesoscale in-mold assembly methods is presented. This dissertation provides a new approach for manufacturing mesoscale assemblies which can lead to reduction in product cost and create several new product possibilities.

Development of In-Mold Assembly Methods for Producing Mesoscale Revolute  
Joints

By

Arvind Ananthanarayanan

Dissertation submitted to the Faculty of the Graduate School of the  
University of Maryland, College Park, in partial fulfillment  
of the requirements for the degree of  
Doctor of Philosophy  
2009

Advisory Committee:

Professor Satyandra K. Gupta, Chairman/Advisor

Associate Professor Hugh A. Bruck

Professor Abhijit Dasgupta

Associate Professor Srinivasa Raghavan

Dr. Chandrasekhar Thamire

© Copyright by  
Arvind Ananthanarayanan  
2009



## Acknowledgements

First and foremost I would like to thank my parents for their constant support and inspiration. Without this every step of graduate school would have been impossible. I would also like to thank my grandparents for their love and affection.

Professor Satyandra K. Gupta, my advisor and mentor has been a constant source of inspiration during my stay in graduate school. It would have been impossible to carry out this research effort if not for his motivation and patient mentoring. I would also like to thank Professor Hugh Bruck for giving me extremely valuable feedback about my research along every step of the way. He taught me to think critically and attack a problem with an unbiased approach. I would also like to thank my committee members Professor Abhijit Dasgupta, Professor Srinivasa Raghavan and Dr. Chandrasekhar Thamire for providing me with valuable insight on my research.

This work was supported by the Army Research Office through MAV MURI Program (Grant No. ARMY W911NF0410176). I am thankful to the University of Maryland, the Mechanical Engineering Department for the opportunity and support.

I would also like to thank my colleagues and friends in the Advanced Manufacturing lab – Alan, Arvind, Arun, Dan, Dominik, John and Wojciech who provided a very friendly and motivating work environment. Anita, Guru, Leicester, Patrick and Sergej helped me with the several experiments I had to conduct.

My roommates, Anand and Ashis, provided for a friendly and peaceful environment at home throughout my stay in graduate school. I would also like to thank Aftab, Gaurav and Rishi who fueled some interesting research ideas during some of our passionate discussions at evening dinner parties. Special thanks must go out to Vivek,

Chrisy and Prabha for providing me with company and making sure I never felt lonely away from home. Finally I would like to thank my cousins Archana and Aiswarya for their constant love and affection. They have never failed to motivate me during the many troubled times I have had during my stay at graduate school.

# Table of Contents

Acknowledgements .....	ii
Table of Contents .....	iv
Index of Figures .....	ix
1 Introduction.....	1
1.1 Background .....	1
1.2 Motivation and Challenges .....	7
1.3 Dissertation Goals and Scope .....	10
2 Literature Review.....	15
2.1 Advances in In-Mold Assembly .....	17
2.2 Prediction of Shrinkage in Injection Molding .....	23
2.3 Mold Deformation during Injection Molding .....	31
2.4 Fluid Structure Interaction for Non-Newtonian Flows .....	36
2.5 Real-time Measurement of Injection Molding Process .....	42
2.6 Weld-lines in Injection Molded parts .....	49
2.7 Summary .....	60
3 Issues in In-Mold Assembly at the Mesoscale.....	63
3.1 Motivation.....	63
3.2 Defects Modes at the Mesoscale.....	63
3.2.1 Cavity Shape Change Methods .....	63
3.2.2 Molding Sequence for Mesoscale In-Mold Assembly.....	65
3.2.3 Summary .....	71
3.3 Experimental Methods for Understanding Size Effects.....	73

3.4	Generalized Framework for Modeling Interaction between Melt Flow and Premolded Component.....	78
3.4.1	Definition of Deformation Problem for Premolded Components.....	78
3.4.2	Mechanics-based Modeling of Plastic Deformation in Premolded Components .....	79
3.5	Modeling Premolded Component Deformation.....	83
3.5.1	Force on Premolded Component .....	83
3.5.2	Non-linear Deformation of Premolded Component .....	86
3.6	Results and Discussion .....	87
3.7	Summary .....	94
4	Characterization and Control of Plastic Deformation in Mesoscale Premolded Components Using Single Gated Mold Design .....	96
4.1	Motivation.....	96
4.2	Development of a Novel Mold for Realizing Mesoscale Revolute Joints...	98
4.3	Experimental Implementation of the Mechanics-Based Model for Controlling Plastic Deformation in Premolded Components .....	102
4.3.1	Experimental Configuration.....	102
4.3.2	Development of a Predictive Model for Estimating Premolded Component Deformation .....	104
4.3.3	Comparison of Modeling Results with Experimental Data .....	106
4.4	Results and Discussion .....	108
4.5	Summary .....	112

5	Characterization and Control of Plastic Deformation in Mesoscale Premolded Components Using Multi Gated Mold Design .....	114
5.1	Motivation.....	114
5.2	Bi-directional Filling for In-mold Assembly .....	115
5.3	Analysis of Weld-lines in In-Mold Assembled Mesoscale Revolute Joints 118	
5.4	Experimental Setup.....	121
5.5	Mechanics-based Model for Predicting the Plastic Deformation as a Function of Flow Front Progression .....	124
5.5.1	Overview of Approach.....	124
5.5.2	Force Modeling on Premolded Component.....	127
5.5.3	Computing Premolded Component Deformations.....	128
5.5.4	Total Flow Front Progression .....	129
5.5.5	Iterative Computational Modeling for Obtaining Net Plastic Deformation .....	130
5.6	Results and Discussion .....	132
5.7	Summary .....	141
6	Characterization and Control of Pin Diameter.....	143
6.1	Motivation.....	143
6.2	Clearances at the Mesoscale .....	144
6.3	Experimental Setup.....	151
6.4	Results and Discussion .....	156
6.5	Summary .....	166

7	Design and Development of In-mold Assembled Miniature Robot .....	168
7.1	Motivation.....	168
7.2	Challenges in Manufacturing Miniature Robots.....	168
7.3	Robot Redesign for In-Mold Assembly.....	170
7.4	Design of In-Mold Assembly Methods.....	172
7.4.1	Selecting the Molding Sequence.....	173
7.4.2	Selection of the Mold Filling Strategy.....	175
7.4.3	Selection of Design Parameters .....	175
7.4.4	Mold Design.....	178
7.5	Results and Discussion .....	180
7.6	Summary .....	186
8	Conclusions.....	188
8.1	Intellectual Contributions.....	188
8.1.1	Identification of Defect Modes Specific to Mesoscale In-Mold Assembly.....	188
8.1.2	Development of Mold Design Solutions for Realizing In-Mold Assembly of Mesoscale Revolute Joints.....	189
8.1.3	Characterization of Pin Diameter in In-Mold Assembled Mesoscale Revolute Joints.....	191
8.2	Anticipated Benefits.....	191
8.3	Future Directions .....	192
8.3.1	Development of Mold Design Templates to Manufacture Other Classes of Mesoscale Articulating Joints.....	193

8.3.2	Experimental Methods for Real-time Force Measurement inside the Mold.....	193
8.3.3	Ejection of In-Mold Assembled Mesoscale Revolute Joints .....	195
8.3.4	In-Mold Assembly at the Mesoscale Using Filled Polymers.....	197
References.....		199

## Index of Figures

Figure 1.1 Babyplast injection molding machine .....	1
Figure 1.2 Injection molding process (a) Simplified diagram and (b) schematic flow diagram illustrating the injection molding process. [1] .....	2
Figure 1.3 Representative applications of in-mold assembly .....	3
Figure 1.4 Piezoelectric sensor made using miniature molding methods [7] .....	4
Figure 1.5 Steps for in-mold assembly of a macroscale revolute joint.....	5
Figure 1.6 Examples of different ways to change cavity shape during second stage [8] .....	5
Figure 1.7 Example defective component due to inaccurate cavity movement .....	8
Figure 1.8 Example defective component due to plastic deformation of premolded component.....	9
Figure 1.9 Example mesoscale revolute joint rendered ineffective due to excessive flash.....	9
Figure 2.1 Force-displacement curves for the three bonded cases and the two debonded cases[19].....	19
Figure 2.2 Examples of multi-material objects studied by Kumar and Gupta [23]....	20
Figure 2.3 1-Degree of freedom combination interface [17].....	21
Figure 2.4 Mold design template for in-mold assembly of a prismatic joint [8] .....	22
Figure 2.5 Different aspects of micro assembly injection molding [26] .....	23
Figure 2.6 Influence of packing pressure on shrinkage of HDPE [49].....	25
Figure 2.7 Influence of the holding pressure and core surface temperature on the ejection force for Polycarbonate (PC) [46].....	26



Figure 2.8 Working principle of the sensor used for in situ monitoring of shrinkage in PS [51] .....	27
Figure 2.9 Experimental and predicted values for shrinkage with varying packing pressure [42].....	30
Figure 2.10 Mold material influence on volumetric shrinkage (I. – Soft tooling; II. – Hard tooling; III. – Conventional molds) [41].....	31
Figure 2.11 Comparison between measured pressures and simulated pressures versus time [34].....	33
Figure 2.12 (a) Calculated mold deflection versus residual cavity pressure (b) Mold reinforcement effect on cavity pressure [34] .....	35
Figure 2.13 Effect of machine compliance [53] .....	36
Figure 2.14 Flow rate versus distance for constant injection pressure isothermal filling [59].....	37
Figure 2.15 Half melt velocity profile at various z-locations for constant injection pressure isothermal filling [59] .....	38
Figure 2.16 Distribution of pressure and tangential and normal stress on the cylinder surface as a function of angle.....	40
Figure 2.17 Schematic representation of a channel confined Poiseuille flow over a circular cylinder .....	40
Figure 2.18 Distribution of pressure coefficient ( $C_p$ ) over the surface of the cylinder for the Reynolds number ( $Re$ ) of 1 and a range of the power-law index ( $n$ ) at $\beta = 1.6$ .....	41

Figure 2.19 (a) Cabled cavity pressure sensor and (b) Wireless cavity pressure sensor .....	42
Figure 2.20 Interface design of the virtual sensor [81] .....	43
Figure 2.21 Model prediction results for virtual sensing of nozzle pressure (a) Best Case (b) Worst Case [81] .....	44
Figure 2.22 The cavity pressure measure and analysis system. 1) spiral channel mold, 2) pressure sensor, 3) amplifier, 4) data acquisition system, and 5) personal computer .....	45
Figure 2.23 Illustration of melt flow during filling stage [84] .....	46
Figure 2.24 A typical plot of capacitive transducer output in an injection cycle for the hot-runner mold [1] .....	47
Figure 2.25 Setup for measuring temperatures inside the mold cavity [85] .....	48
Figure 2.26 Cold and Hot weld-lines [65] .....	50
Figure 2.27 Weld-lines formed due to presence of an obstacle [62] .....	51
Figure 2.28 Effect of obstacle size on the weld-line strengths of injection molded polystyrene [62] .....	51
Figure 2.29 Evolution of the tensile strength when the weld-line notch is eliminated (PS) [71] .....	53
Figure 2.30 Comparison between the model predictions (-) and the experimental data (•) of the weld-line strength of polycarbonate [69] .....	54
Figure 2.31 Microhardness, $H$ , measured at the surface of the molding along the injection direction, $z$ , for PC with melt temperature of 270°C [72] .....	56

Figure 2.32 Relationship between tensile strength of injection molded PS parts and depth of cut under different process conditions [63] .....	56
Figure 2.33 V-notch depth along the flow direction [68] .....	57
Figure 2.34 Fracture toughness v/s position: (a) nonweld, (b) square pin, (c) circular pin, and (d) rhombus pin [74] .....	58
Figure 2.35 Variations of degree of bonding with melt temperature under different plate thickness [75] .....	59
Figure 2.36 Variation of the degree of bonding with melt temperatures [75] .....	60
Figure 3.1 Mesoscale Premolded Component .....	64
Figure 3.2 Design of in-mold assembled revolute joint.....	66
Figure 3.3 Schematic representation of inaccurate alignment of SAMI.....	67
Figure 3.4 Deformation of side action mold core due to injection pressure.....	68
Figure 3.5 Inaccurate side action resulting in shearing of mesoscale core.....	69
Figure 3.6 Deformation of mesoscale core due to second stage injection.....	70
Figure 3.7 Side action mold insert (SAMI) used for accurate movement of mold pieces.....	72
Figure 3.8 Premolded component for experiments.....	74
Figure 3.9 Second stage injection .....	74
Figure 3.10 Online monitoring system for measuring transverse force on premolded component.....	75
Figure 3.11 Block diagram of experimental setup for force measurement.....	76
Figure 3.12 Surrogate strain sensor made of a metallic cantilever beam .....	76

Figure 3.13 ABS beam loaded in flexure for determination of non-linear material properties.....	77
Figure 3.14 Finite element mesh for flow simulation to determine effective pressure on mesoscale core .....	84
Figure 3.15 Force modeling on the premolded component. ....	86
Figure 3.16 Flow front progression .....	87
Figure 3.17 Strain on premolded component as flow front progresses .....	88
Figure 3.18 Sample result of FE simulation to compute strain on sensor .....	88
Figure 3.19. Load versus deformation for the ABS beam .....	91
Figure 3.20 Measurement of plastic deformation of premolded component.....	92
Figure 3.21 Plastic deformation of pin with varying diameter of the pin.....	93
Figure 3.22 Distinction between macroscale and mesoscale from the in-mold assembly perspective .....	94
Figure 4.1 Mold assembly for Stage 1.....	98
Figure 4.2 Bending of pin due to unsupported second stage injection .....	99
Figure 4.3 Mold design iterations for second stage injection .....	100
Figure 4.4 Mold assembly for stage 2.....	101
Figure 4.5 Premolded component for experiments.....	103
Figure 4.6 Experimental setup for correlation of support length with deformation of core.....	104
Figure 4.7 Force modeling on the premolded component. ....	106
Figure 4.8 Measurement of maximum deformation $d_m$ .....	106
Figure 4.9 Deformed sample with radial support length of 6.66%.....	107

Figure 4.10 Sample results for ANSYS analysis for 6.66% Radial support length..	107
Figure 4.11 Injection molded first stage component. ....	108
Figure 4.12 Effective pressure on mesoscale core obtained from flow simulation ..	109
Figure 4.13. Finite element analysis for deformation versus radial support length for a flow rate of 12 cc/s.....	110
Figure 4.14. Two configurations of the in mold assembled mesoscale revolute joint demonstrating rotation of the joint.....	111
Figure 5.1 Schematic of the two stage mold design using multi gate bi-directional filling strategy .....	116
Figure 5.2 Spatial and temporal gate misalignment.....	117
Figure 5.3 Types of weld-lines .....	119
Figure 5.4 Weld-lines formed in uni-directional and bi-directional filling in second stage .....	119
Figure 5.5 Premolded component for experiments.....	122
Figure 5.6 Modular second stage mold design .....	122
Figure 5.7 Dogbone specimen to analyze strength of cold weld-lines .....	123
Figure 5.8 Deformation of premolded component with flow front progression.....	125
Figure 5.9 Force applied on premolded component to predict deformation.....	128
Figure 5.10 Weld-line location for temporally misaligned gates .....	129
Figure 5.11 Modeling framework for predicting pin deformation during mesoscale in- mold assembly process using iterative coupling.....	132
Figure 5.12 In-mold assembled mesoscale revolute half joint .....	133
Figure 5.13 Dogbone specimen tested for weld-line strength of Nylon-12.....	134

Figure 5.14 Force on Premolded Component as a Function of Flow Front Progression .....	135
Figure 5.15 Deformation as a Function of Applied Force .....	136
Figure 5.16 Sample ANSYS 11.0 simulation result for force on 1.2 N .....	137
Figure 5.17 Determination of Total Flow Front Progression .....	137
Figure 5.18 Sample simulation result in Moldflow for gate misalignment of 1.25 mm .....	138
Figure 5.19 Plastic deformation of mesoscale premolded component relating to the gate misalignment .....	140
Figure 6.1 clearances in in-mold assembled Macroscale revolute joints.....	144
Figure 6.2 Mold design strategy for creating mesoscale in-mold assembled revolute joints.....	145
Figure 6.3 Asymmetric deformation during second stage injection and packing.....	149
Figure 6.4 Boundary conditions for finite element solver .....	151
Figure 6.5 Experimental setup for macroscale experiments .....	152
Figure 6.6 Premolded component for experiments.....	153
Figure 6.7 Second stage mold design .....	154
Figure 6.8 Measuring change in pin diameter .....	155
Figure 6.9 macroscale premolded component before and after second stage injection .....	157
Figure 6.10 Percentage change in diameter of pin v/s original pin diameter .....	158
Figure 6.11 Sample ANSYS analysis for a pin diameter of 1.2 mm .....	158
Figure 6.12 Shearing of pin due to excessive drag resistance .....	159

Figure 6.13 Measurement of diameter and length variation of premolded mesoscale pin .....	161
Figure 6.14 Experimentally recorded diameter variation v/s change in length .....	162
Figure 6.15 Sample results from finite element analysis .....	163
Figure 6.16 Designed support cavity lengths for desired value of diameter variation .....	165
Figure 7.1 MINIR: A 6-DOF robot with the various components [96].....	170
Figure 7.2 Design of Robot for In-mold Assembly .....	172
Figure 7.3 Molding sequence for in-mold assembly of 6 DOF robot.....	174
Figure 7.4 Mesh used for flow simulations for filling of second stage polymer melt .....	176
Figure 7.5 Mold assembly for first stage part .....	178
Figure 7.6 Mold assembly for second stage.....	179
Figure 7.7 Force estimate on premolded component v/s Flow front progression ....	180
Figure 7.8 Sample flow simulations in FLUENT for flow front progression = 0.2 mm .....	181
Figure 7.9 Sample ANSYS results for two different radial support lengths .....	182
Figure 7.10 Plastic deformation of premolded component as a function of the radial support length.....	183
Figure 7.11 Two different orientations of prototype of 6 DOF robot manufactured using in-mold assembly .....	184
Figure 7.12 Distinction between 6 DOF robot and finger inspired robot.....	185
Figure 7.13 Design change for fabricating Hand Robot.....	186

Figure 7.14 Hand robot consisting of 5 finger inspired robots ..... 186

Figure 8.1: Measurement of displacement to estimate compressive force ..... 194

Figure 8.2: Surface based ejection system..... 196



# 1 Introduction

## 1.1 Background

Manufacturing mesoscale 3D articulated devices with moving parts remains a challenge for the manufacturing community. Manufacturing technologies exist for large scale production of piece parts which are made of a single component. However, assembling them into articulating joints is a challenging problem. Manual assembly is not an option at the size scales involved. Current technology of using complex micro-assembly systems are highly inefficient and can not be used for production in high volumes due to the production time and cost involved. They also pose design constraints which rule out several product possibilities. Hence scalable and cost effective automated assembly methods suitable to high volume production have to be explored.



Figure 1.1 Babyplast injection molding machine

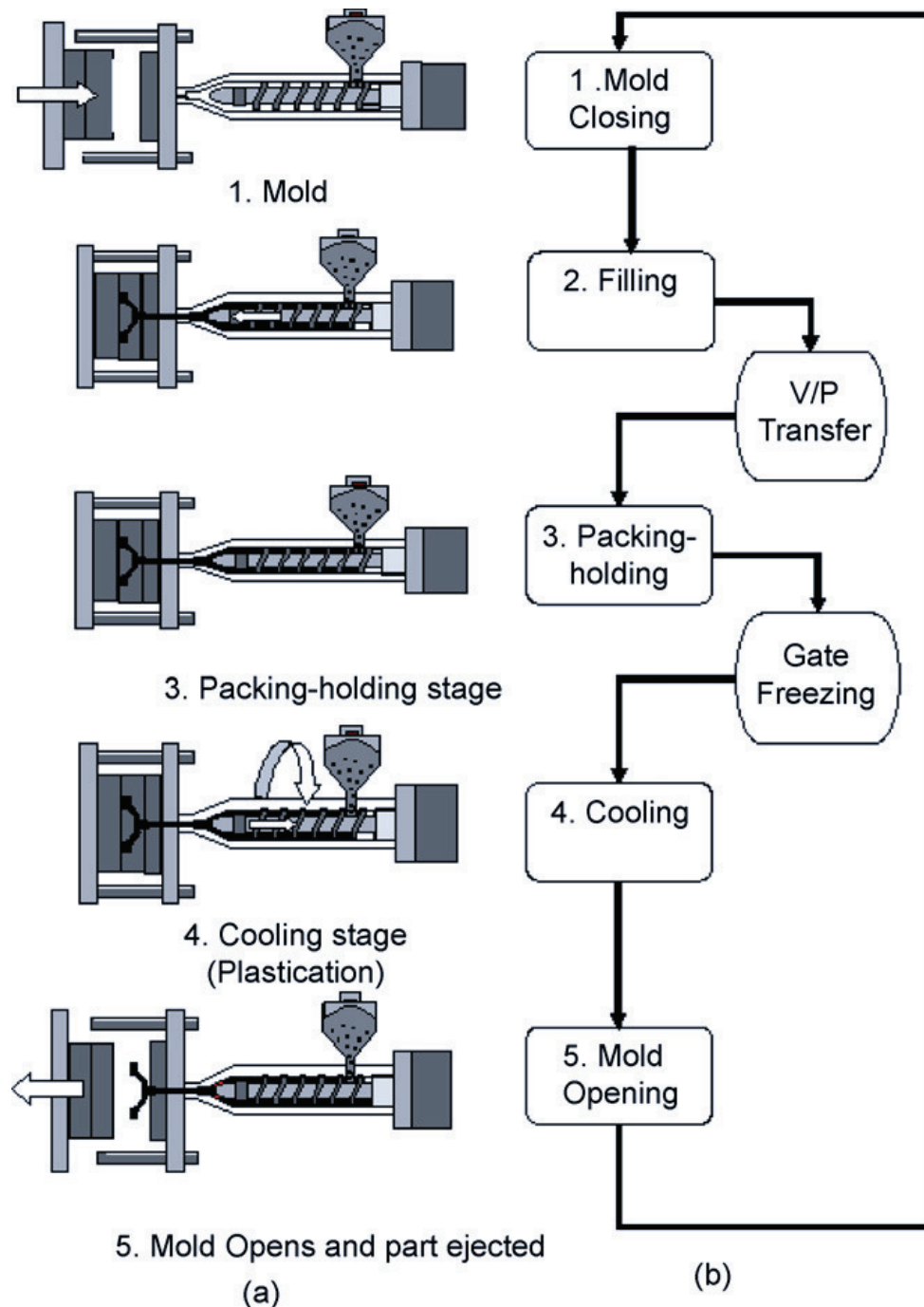


Figure 1.2 Injection molding process (a) Simplified diagram and (b) schematic flow diagram illustrating the injection molding process. [1]

Injection molding is a high throughput method for polymer processing and is being used to produce a wide variety of products with varying shapes and sizes [2-6]. In this

process a high pressure, high temperature polymer melt is injected into a mold cavity. This melt solidifies to take the shape of the cavity. After cooling and ejection of the part from the mold, this process is repeated in a cyclic manner. One of a typical injection molding machine which is used in the Manufacturing Automation lab at the University of Maryland is illustrated in Figure 1.1. Figure 1.2 illustrates the injection molding process.

In-mold assembly is a popular process which is used widely in the industry. Figure 1.3 shows some representative applications that have been manufactured using different in-mold assembly methods.



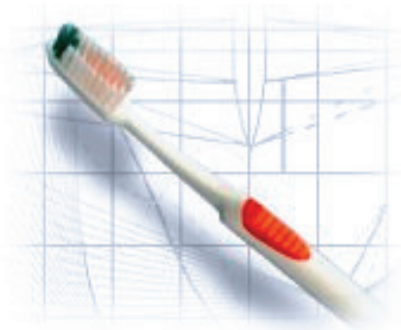
Toys



Medical Valve



Saw Housing



Compliant Tooth Brush

Figure 1.3 Representative applications of in-mold assembly

In the past few years, many advances have also been reported in the field of miniature molding. Figure 1.4 illustrates a piezoelectric sensor which was manufactured using miniature molding methods. This method can be used to accurately manufacture intricate miniature features such as that shown in Figure 1.4. Considering the low cycle time of the injection molding process, this manufacturing method is also highly cost effective.



Figure 1.4 Piezoelectric sensor made using miniature molding methods [7]

At the mesoscale, it is currently very difficult to manufacture intricate assemblies due to the difficulty to assemble them. In-mold assembly at the mesoscale or miniature sizes therefore holds tremendous promise and promise several new product possibilities. Both the fields of in-mold assembly at the macroscale and miniature molding of individual parts have seen several advances. However methods to combine the two processes do not currently exist. This dissertation aims to combine the benefits of both these processes and bring the manufacturing community a step closer to mass production of in-mold assemblies at the mesoscale.

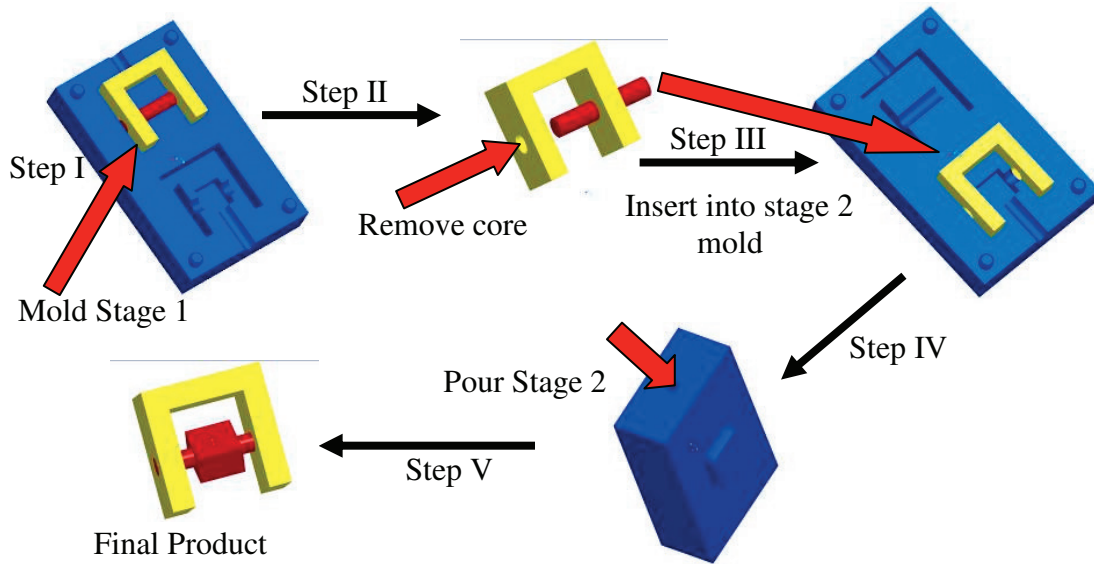


Figure 1.5 Steps for in-mold assembly of a macroscale revolute joint

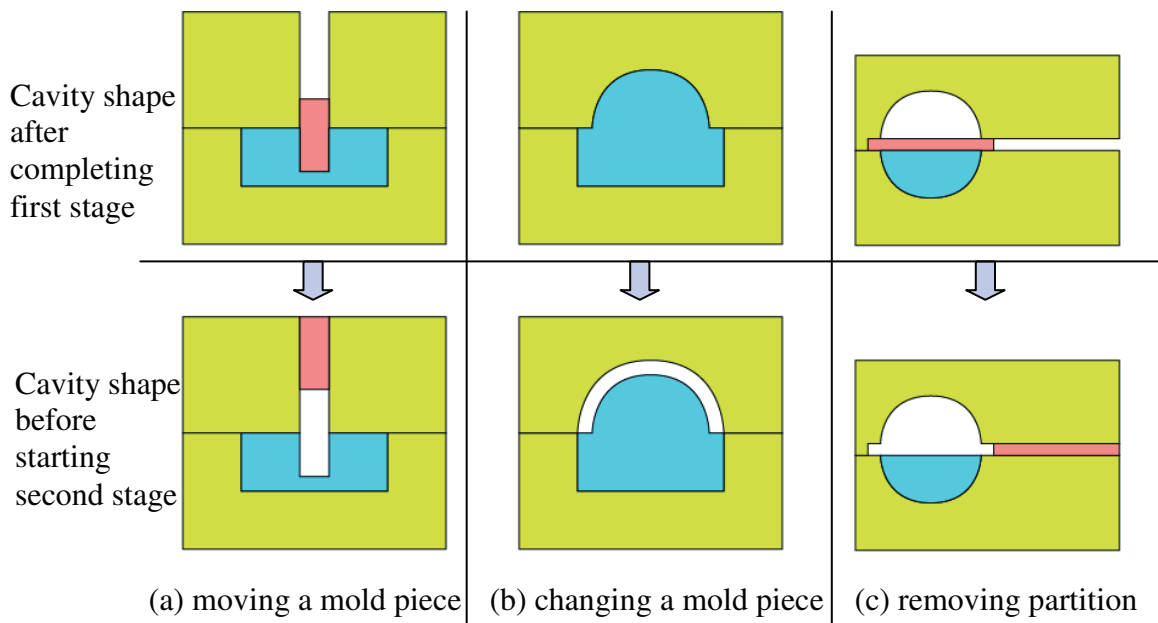


Figure 1.6 Examples of different ways to change cavity shape during second stage [8]

There are two ways to realize the in-mold assembly process for a two-material structure at the macroscale. The first method involves use of the overmolding process. A component is first molded using a regular injection mold. This component is then

either manually or automatically inserted into another mold cavity before injecting the second stage polymer. So essentially, two parts of the two-material structure are produced using traditional molds. The process steps used to manufacture in-mold assembled macroscale revolute joints is illustrated in Figure 1.5.

The second method involves use of a varying cavity shape mold and is often referred as multi-shot injection molding process. In this method, the first stage part does not leave the mold during the second stage injection. Instead, some of the mold pieces move to create room for the second stage injection. Cavity shape change can be accomplished in many different ways. Popular cavity shape change methods include:

- 1) Realignment of one or more mold pieces after injection of the first stage component to change the cavity shape;
- 2) Swapping one or more mold pieces in the initial cavity with a mold piece with a different shape; and
- 3) Adding partitions or shut off surfaces in the initial cavity and removing them during subsequent stages.

Figure 1.6 illustrates these methods. While the cavity shape is being altered, the premolded component should stay in place and should not move. Moreover, the method should satisfy the assembly and disassembly constraints imposed on the mold pieces. The first stage part is usually referred to as the premoloded component during the second stage molding.

Micro- and meso-molding of polymers is a promising process that has gained popularity during the last few years [9, 10]. Parts with features sizes as small as 10

microns are being molded [11]. New methods have been developed for mold flow simulations, thermal management and time dependent flow during filling for miniature parts [12-14]. In-mold assembly has also been successfully demonstrated at the macroscale [8, 15-17]. This has proven to be an effective manufacturing process to develop articulated parts with reduced production times and lead times. Considering the success of micro and mesomolding and in-mold assembly at macro scale, it is envisaged that mesomolding and in-mold assembly can be potentially combined to develop a manufacturing process for making mesoscale articulated parts.

## ***1.2 Motivation and Challenges***

In-mold assembly methods for macro-scale rigid body joints have been successfully developed and demonstrated in the past [8, 15-17]. But direct scaling down of macroscale processes to the mesoscale is not expected to be successful. In order to develop a scalable manufacturing process, it is therefore imperative to realize the limitations of the process at smaller size scales. Development of a molding process that combines the benefits of mesoscale molding and in-mold assembly requires us to address several challenges. These challenges include: (1) developing mold configurations that support molds with varying cavity shape to perform in-mold assembly, (2) developing accurate positioning methods to realize cavity shape change to avoid damage to delicate mesoscale parts created during molding, (3) developing a method to limit the adhesion at the interfaces and hence provide articulation, and (4) developing a method to successfully remove parts from molds.

Overmolding is not a viable option for making mesoscale in-mold assembled revolute joints. This is because the overmolding process involves ejection of the

mesoscale first stage part from the mold cavity and insertion into a new mold. Owing to the delicate mesoscale features that are present in the premolded component, this process may lead to irreparable damages to the first stage part. As a result, cavity morphing methods are the only feasible option for mesoscale in-mold assembly. However imprecise movement of the core pieces in the mold for cavity change operations can lead to the failure of the first stage part. An example of a failed specimen is illustrated in Figure 1.7.

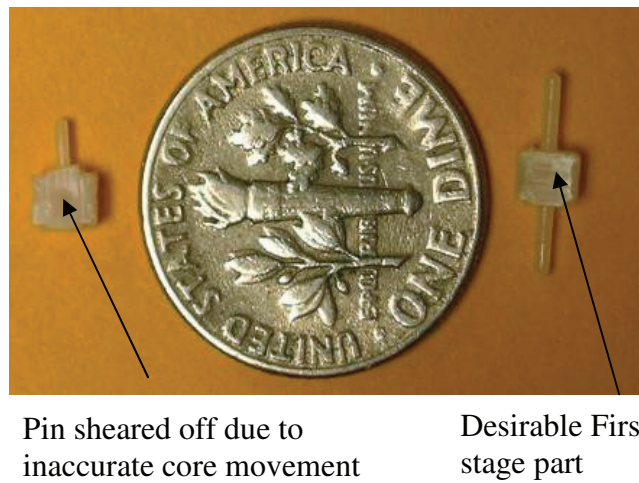


Figure 1.7 Example defective component due to inaccurate cavity movement

Another impending issue in mesoscale in-mold assembly is that of the plastic deformation of the premolded component. During the in-mold assembly process, a premolded component is placed inside a second stage molding cavity. This premolded component is subjected to thermal and mechanical loading during the injection molding process. Unlike in macroscale in-mold assembly, one can observe significant plastic deformation of the premolded component at the mesoscale if the component is not properly constrained. This problem arises due to the fact that the meso-scale parts have significantly less structural rigidity and thermal resistance compared to macro-



scale parts. However, the mechanical and thermal loading is not significantly reduced at the meso-scale. An example defective component formed due to plastic deformation of the premolded component is illustrated in Figure 1.8.

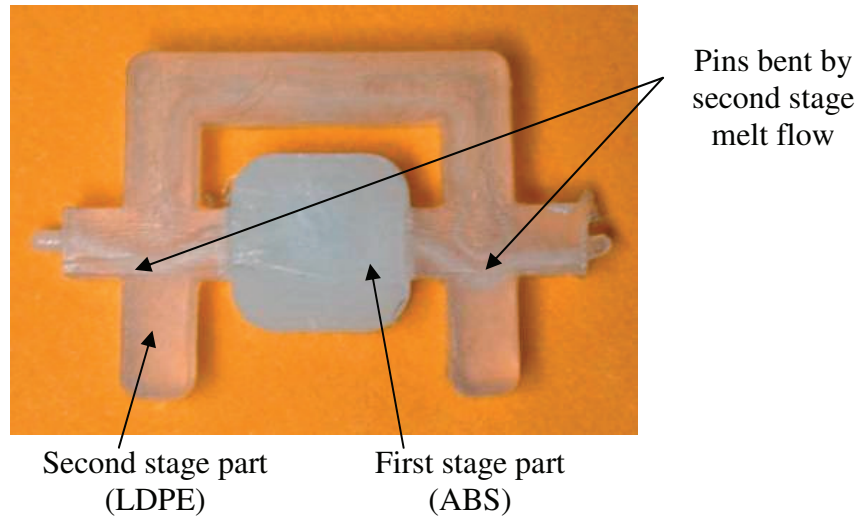


Figure 1.8 Example defective component due to plastic deformation of premolded component



Figure 1.9 Example mesoscale revolute joint rendered ineffective due to excessive flash

Flash is also another issue that is a cause of major concern in the case of mesoscale in-mold assemblies. Considering the small sizes of the parts, the machining tolerances available for manufacturing the molds are relatively low. Any inaccuracy in mold

machining/assembly causes gaps in the injection molding cavity which makes the part susceptible to flash. This flash is difficult to remove owing to the low overall size of the part. Also, flash on the revolving portion of the first stage renders the joint ineffective since the extra material tends to jam the joint. An example flashed mesoscale in-mold assembled revolute joint is shown in Figure 1.9.

Given these issues, mesoscale in-mold assembly is a challenging problem which cannot be solved by the current state of the art. This dissertation is therefore seen as a first step to overcome some of the major challenges in mesoscale in-mold assembly.

### ***1.3 Dissertation Goals and Scope***

The challenges outlined in the previous section elucidate that in-mold assembly at the mesoscale is a non trivial problem. Due to the presence of a mesoscale premolded component in the mold, the molding process is significantly different from conventional injection molding. The goals of this dissertation are (1) develop novel mold design solutions to enable in-mold assembly of mesoscale revolute joints, (2) to understand and characterize the sources of deformation in joints and methods to control it, as well as (3) to understand and characterize the clearance in joints and methods to control it. This dissertation identifies some of the impending challenges in in-mold assembly at the mesoscale. Mold design strategies have been developed to address some of these challenges. Detailed computational models have been developed to understand the in-mold assembly process at the mesoscale.

The computational models that are developed in this dissertation are aimed at addressing only the onset of the defects during mesoscale in-mold assembly. The models are not intended to capture the defects in highly defective parts. Hence the

computational models can be used simply as a tool to select the appropriate mold design parameters and processing parameters which will ensure manufacture of good quality mesoscale revolute joints.

As part of this effort, detailed understanding has been developed in distinct aspects of the in-mold assembly process. In order to develop a feasible in-mold assembly process which can be used at the mesoscale, it is imperative to identify and categorize the defects associated with in-mold assembly at the mesoscale. Mold designs subsequently developed for mesoscale in-mold assembly should overcome these defects.

In the next chapter, a detailed literature review on the contemporary issues in in-mold assembly is presented. In order to identify these defects, it is necessary to conduct experiments with different mold design configurations and record the observations. However, overcoming these defects involves development of physics based reasoning to understand and predict the defect modes. To model the defects, it was therefore necessary to develop an understanding of the loads exerted by the second stage polymer melt on the premolded component. Hence an experimental technique to measure this force real-time during the injection molding process has been developed. Chapter 3 discusses the defects associated with in-mold assembly at the mesoscale.

Two different mold design configurations have been developed for accomplishing mesoscale in-mold assembly. The first is designed to facilitate the in-mold assembly process for polymer combinations having significantly different material properties viz. melting temperatures. This requires significantly different designs compared to

molds used for manufacturing macroscale in-mold assembled revolute joints. The premolded component made of a polymer is highly susceptible to deformation due to its small size and due to the high temperature and pressure it encounters due to the flow of the second stage melt. This necessitates a mold design which constrains the premolded component to inhibit its deformation. Chapter 4 will discuss this problem and will explain a detailed mold design. Subsequently, a detailed mechanics based predictive model is described to obtain the design parameters which would be required for such a mold design.

For polymer combinations of comparable melting points, an alternate in-mold assembly strategy is required. This strategy should ensure that the premolded component does not get thermally softened due to the second stage polymer melt flow around it. This is accomplished by minimizing the time of exposure of the premolded component to the polymer melt during the filling phase. Hence a mold design involving multiple injection locations can be used. Molds can be designed in such a way that the flow of the second stage polymer melt from the multiple locations will neutralize the forces on the premolded component. However, this mold design exposes several other challenges.

One such challenge is development of an understanding of the tolerance of the mold design to temporal misalignment of gates. If the gates are not positioned equidistant from the premolded component, a temporal misalignment is induced. This causes imbalance in the force neutralization. Chapter 5 discusses a strategy which uses a multi gate mold design to prevent this.

Another challenge involves the interaction between a polymer melt and the premolded component as well as non-linear deformations of the premolded component. An iterative approach to solving this coupled problem is described. This methodology adopts the solutions to individual decoupled problems using metamodels and applies them iteratively to the physical problem which needs to be modeled.

Revolute joints require a clearance fit between the core and the cavity for desirable operation. At the macroscale, this clearance can be obtained and controlled by controlling the shrinkage of the molded components. However, at the mesoscale, due to use of a reversed molding sequence, shrinkage may result in joint jamming which is undesirable for production of revolute joints. Chapter 6 therefore presents an innovative mold design method to control the joint jamming. The design utilizes the plastic deformation of the small size premolded component as a desirable feature. This plastic deformation is controlled using appropriate design parameters to manufacture good quality revolute joints. A computational modeling method is also described which predicts the size scales at which mesoscale in-mold assembly methods are no longer feasible. A modeling effort is also described to select the design parameters necessary to control the joint quality.

Chapter 7 describes a case study of a miniature robot which was in-mold assembled using the mold design methods and computational modeling strategy described in this dissertation.

Finally, chapter 8 will present the conclusions of this work and the intellectual contributions it has made. It will also suggest some future directions that can be initiated as a follow up of this research work.

## 2 Literature Review

In-mold assembly is a multi stage process where different polymers are sequentially injected into the mold cavity to form an articulating joint. This process is very similar to sandwich molding also known as co-injection molding, multi shot molding or multi material molding [8, 16-32]. Hence it is necessary to develop an understanding of the state of the art in in-mold assembly. Section 2.1 will review the body of work in the area of in-mold assembly and allied fields.

Researchers have been studying in-mold assembly at the macroscale for several years now [8, 16-19, 23, 25]. However, the in-mold assembly process at the mesoscale is significantly different from that at the macro scale. It involves a mesoscale premolded component acting as a mold-piece. During the second stage molding, the melt enters the mold at high velocity impacts the premolded component and then flows around it. Once the mold is filled the flow stops and the melt solidifies. The flow of the melt can induce mechanical loading on the premolded component due to viscous and/or impact forces. It is worth noting that the melt is a non-Newtonian fluid and the mechanical loading occurs mainly under transient flow conditions. In addition, the premolded component also gets heated up by the melt entering the mold cavity. As a result of the heating the premolded part may soften and its strength may be reduced. As a result of the time-varying thermo-mechanical loading, the premolded component undergoes elastic and under some conditions plastic deformation.

Another important issue that needs to be addressed is that of clearances in the mesoscale revolute joint. As explained earlier, the processing steps employed to

fabricate a mesoscale in-mold assembled revolute joint, involves using the mesoscale premolded component as a mold insert for the second stage part. Hence the premolded component would be expected to undergo deformation due to injection molding pressures and temperatures. These deformations are instrumental in increasing the effective mold dimensions of the part. Subsequently the injection molded second stage part has a tendency to shrink in the presence of the premolded component. This shrinkage, if appropriately controlled, would provide the required clearances for the operation of the articulating joint.

Hence, in order to gain proper understanding of the in-mold assembly process at the mesoscale, it is important to address the problems and the corresponding state of the art in the areas of:

- 1) Shrinkage in injection molded parts [33-51]. Section 2.2 will examine the work done in this field.
- 2) Deformation of mold pieces due to injection molding [34, 48, 52-56]. This will be dealt with in section 2.3.
- 3) Interaction between the high pressure, high velocity, non-newtonian flow of the polymer and the premolded mesoscale component present as a mold piece inside the mold [57-60]. This will be covered in section 2.4.

As mentioned before, a high pressure, high velocity, non-newtonian flow of the second stage polymer melt applies a force on the premolded mesoscale component. In order to characterize this force and thereby develop models to select appropriate design parameters, it is important to develop experimental methods to measure this force. Researchers have developed various experimental methods to measure different



parameters of the injection molding process real-time. The state of the art in these measurement techniques therefore will help develop an insight into an experimental method to measure the forces applied by a polymer melt on a mold piece. This will be reviewed in Section 2.5.

To overcome the problem of deformation of the mesoscale premolded component due to second stage injection, an alternate strategy involves having multiple injection locations or gates in the mold. These gates are placed in such a way that the forces on the premolded component are balanced thus limiting its deformation. However, this approach leads to formation of a weld-line in the second stage injection molded part. The strength of a weld-line is known to be less than that of the base material [61-76]. Hence it is important to come up with strategies to attain the highest possible strength of the weld-line while ensuring a functional in-mold assembled articulating joint. For this purpose it is important to develop an understanding of the relevant body of work conducted in the area of weld-lines in injection molding. This will be examined in Section 2.6. Finally a summary of the literature review will be presented in Section 2.7.

## ***2.1 Advances in In-Mold Assembly***

Several researchers have studied sandwich molding, multi component injection molding or co-injection molding [21, 22, 27-32, 77-79]. In this process, single piece products are made out of multiple materials. The co-injection molding process utilizes the contrasting properties of the materials to make a product consisting of both materials. E.g. A tough material would form the skin of the molded structure while

the core would be formed of a lighter material. This would make the sandwich molded part tough on the outside while being light weight.

Zoetelief et al [77] in their work have described a numerical simulation of the multi component injection molding process wherein they describe the mold filling process. This helps in predicting the material distribution of the molded part.

Kadota et al [22] studied the structural gradient obtained in co-injection molded parts. They conducted their studies on immiscible polymers such as Polystyrene and Polypropylene injected simultaneously into the mold cavity. This study enabled them to establish relationships between the properties of the product thus molded and the processing parameters.

Schlatter et al [28] conducted a numerical investigation based on the transport equation to determine the location of the interface in sequentially injection molded sandwich molded parts. From their investigation they related the interface between the two materials and the injection molding processing parameters.

Similarly several other researchers [21, 24, 27, 29-32, 78, 79] have studied the properties of the skin and core obtained as part of a sandwich molding process.

Cheng et al [20] have described an approach for diagnosis of core arrival, core flow speed, part solidification, part detachment from the mold, thickness of skin and core and core length at the mold using a real time non intrusive, non destructive methodology which utilizes integrated ultrasonic sensors. Part solidification and part detachment inside the mold cavity were observed using ultrasound. They have also presented ultrasonic techniques to measure the average flow speed, core, and skin

layer thicknesses and core length. Their findings indicate that when the injected core volume percentages increased, the core length became greater.

Arzondo et al [18] studied the adhesion between sequentially injection molded parts. They conducted peel tests to evaluate the bonding strengths between ethylene octene copolymer and a low-density polymer. Wide ranges of overmolding and cooling interface temperatures and packing pressures were explored. Their findings indicate that ethylene-octene copolymer can be used for overmolding on PP homopolymer, and the bonding that can be obtained may be useful for a range of applications. Other low-density polyethylenes and ethylene copolymers may or may not be as good as the random ethylene-octene copolymer.

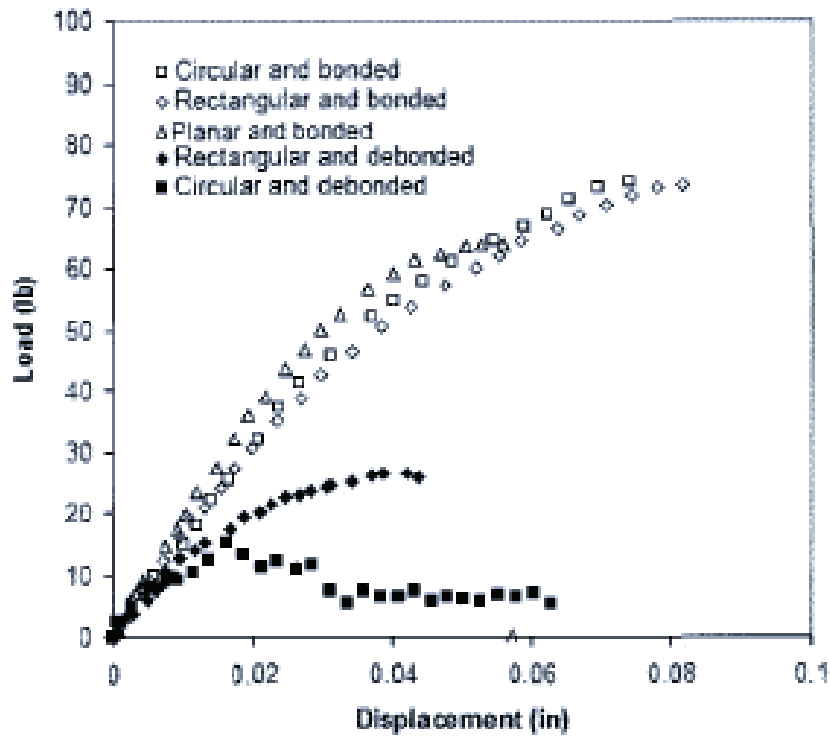


Figure 2.1 Force-displacement curves for the three bonded cases and the two debonded cases[19]

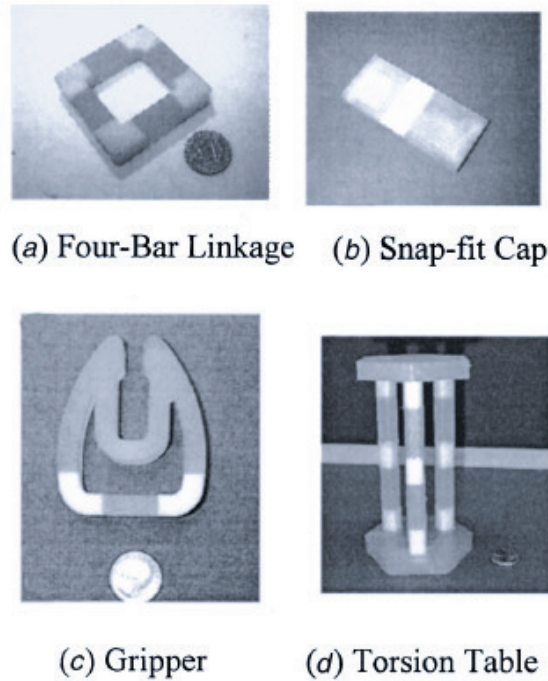


Figure 2.2 Examples of multi-material objects studied by Kumar and Gupta [23]

In a subsequent work, Bruck et al [19] used geometric complexity to enhance the strength of co-injection molded parts. They have reported results for both bonded and debonded joints which have a geometrically complex interface. Their findings indicate that increasing the geometric complexity of the interface, greatly enhances the strength of the interface. Figure 2.1 reports the interfacial strength obtained for different geometries both in bonded and debonded cases.

Kumar and Gupta [23] in their work, developed algorithms for automated design of multi stage molds. Their focus was on designing molds for multi material parts which are sequentially injected into the mold cavity. The class of parts that they have studied is illustrated in Figure 2.2.

In a subsequent work Li and Gupta [25] developed algorithms for automated design of rotary platen molds for multi stage injection molding.

Gouker et al [17] in their work demonstrated a method to manufacture multi material compliant mechanisms using multi-shot molding. In their work, they have demonstrated the use of a combination of a rigid and compliant material in making compliant mechanisms. They have noted that it is necessary to achieve high levels of bonding between the rigid and compliant material which may or may not be chemically compatible. Hence they have devised a method to enhance the strength of the bond using geometrical complexity of the interface. Their findings indicate that an interface as illustrated in Figure 2.3 can be used to obtain maximum bonding strength.

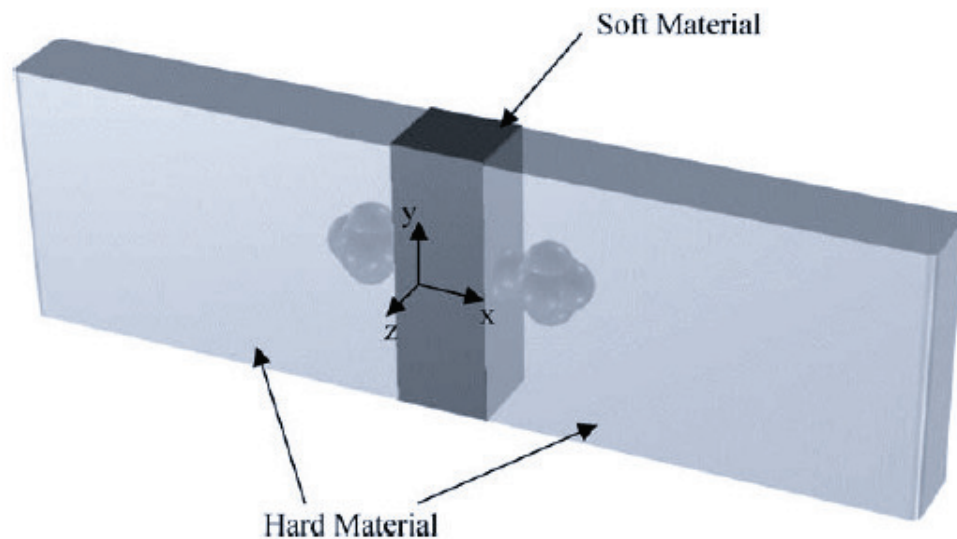


Figure 2.3 1-Degree of freedom combination interface [17]

Banerjee et al [16] suggested incorporating manufacturability considerations to redesign assemblies so they could be fabricated using in-mold assembly. As part of their work, they designed algorithms to identify design changes that were required for fabricating the part using in-mold assembly methods.

Subsequently Priyadarshi et al [8] as part of their work, developed algorithms to automatically develop mold design templates for manufacturing in-mold assembled

rigid body joints. They verified these mold designs to fabricate physical molded parts which were in-mold assembled.

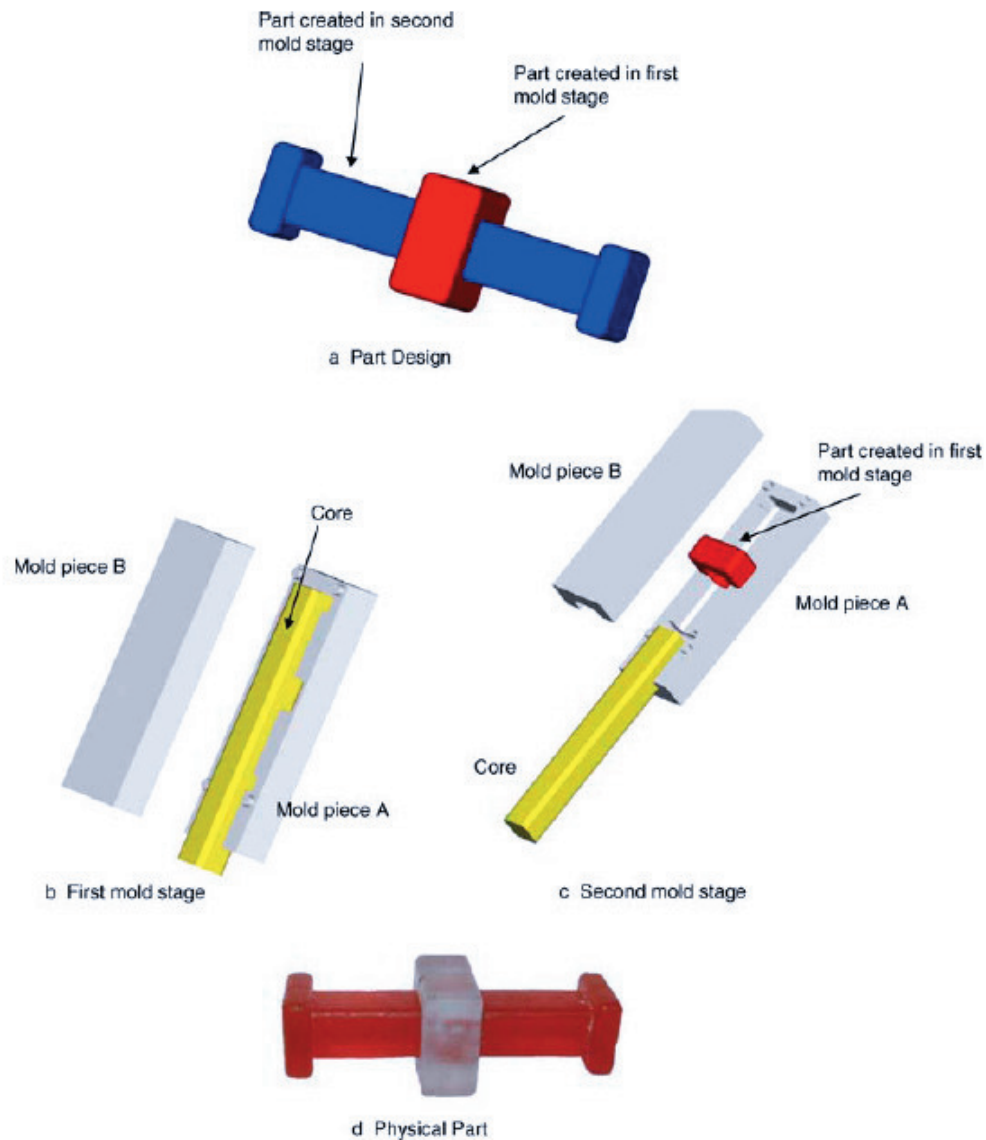


Figure 2.4 Mold design template for in-mold assembly of a prismatic joint [8]

In a representative work towards micro assembly using injection molding, Michaeli et al [26] developed a process to manufacture hybrid microsystems by molding polymer combinations sequentially using injection molding. The different classes of products that they have studied are illustrated in Figure 2.5.

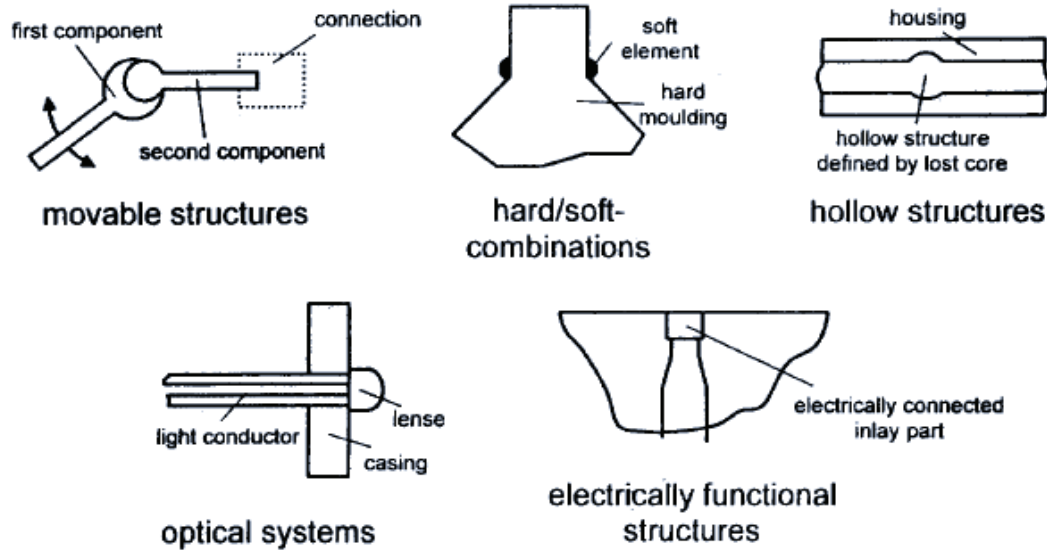


Figure 2.5 Different aspects of micro assembly injection molding [26]

## 2.2 Prediction of Shrinkage in Injection Molding

Prediction of in-mold shrinkage is a very important step in ensuring required clearances in in-mold assembled revolute joints. The problem of shrinkage continues to receive attention from the research community. Several researchers have performed computational and experimental investigations to develop models to predict shrinkage as a function of processing conditions.

Huang et al [50] studied the shrinkage in parts manufactured using micro injection molding. Their findings reveal that relative values of shrinkage in micro injection molded parts to be the same as that for macroscale parts manufactured using injection molding. Hence in order to understand shrinkages in mesoscale in-mold assembled parts, it is important to develop an understanding of shrinkage modeling in the macroscale.

Existing efforts have explored the effect of various processing parameters on the residual stresses and the shrinkage observed in the injection molded parts. Several

researchers [33, 38] have studied the effects of the mold walls on the shrinkage of the part. Models have been developed that account for the compensation of the volumetric shrinkage due to the application of packing pressure. They discuss the in-plane shrinkage and the longitudinal shrinkage separately thus bringing out the anisotropy in shrinkage of injection molded parts.

Titomanlio and Jansen [48] describe a decoupled model for the shrinkage of the injection molded component in length and thickness directions. In this model they incorporate the effect of mold wall boundaries in calculating shrinkage. They present three separate cases where:

- a) Only thickness shrinkage occurs
- b) Only length shrinkage occurs
- c) Both length and thickness shrinkage occur

Jansen et al [39] studied the shrinkage of amorphous Polystyrene when the holding times and packing pressures were varied. They report that the packing pressure has a significant effect on the shrinkage. The shrinkage was observed to change from 0.6% to 0.1% by varying packing pressure. They also noted that the shrinkage tended to increase along the flow length. Holding time was not noted to be a major component unless it was less than the gate freeze off time. Several other researchers [38-40, 48, 49] have performed similar studies to correlate the shrinkage with processing parameters. They report the packing pressure as one of the main influencing parameters for shrinkage. Chen et al [49] report that a high packing pressure also leads to negative shrinkage. Negative shrinkage can be attributed to high residual stresses in the part due to overpacking as well as mold deformation. Figure 2.6



illustrates the relationship between packing pressure and shrinkage for high density Polyethylene (HDPE).

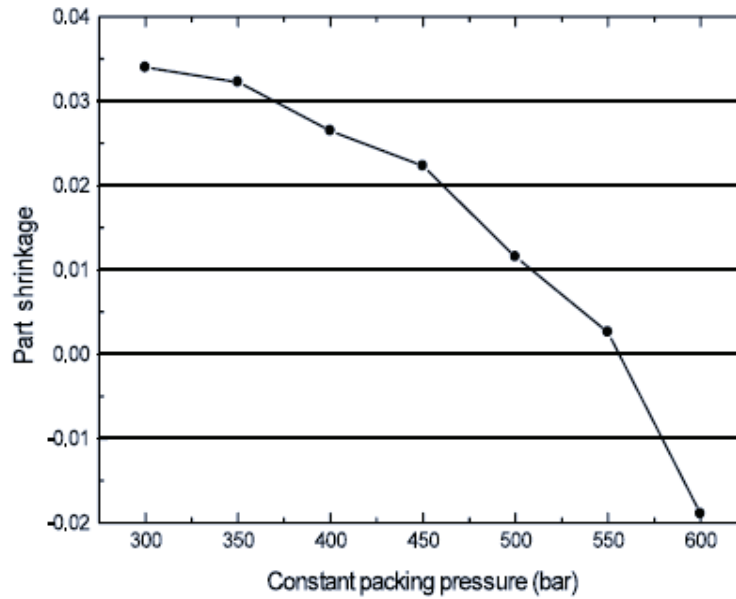


Figure 2.6 Influence of packing pressure on shrinkage of HDPE [49]

Recent investigations have explored how the mold deformation affects the shrinkage [34]. It has been realized that higher packing pressure leads to mold deflections which significantly lower the observed values of shrinkage. This will be covered in more depth in the next section.

Pontes and Pouzada [46] have investigated the effect of shrinkage in tubular fittings on the force required for ejection of the part from the mold. To develop an understanding of the ejection forces, they have conducted a study to correlate the ejection force with the processing parameters. They have reported that the two main parameters influencing the ejection forces are the holding pressure and the surface temperature of the core. Increasing either of them leads to a decrease in ejection forces. This is illustrated in Figure 2.7. The ejection forces are directly correlated with the shrinkage of the tubular fittings. They note that tubular fittings shrink onto the

core requiring higher ejection forces with higher shrinkage. Hence, lower shrinkage results in lower ejection forces.

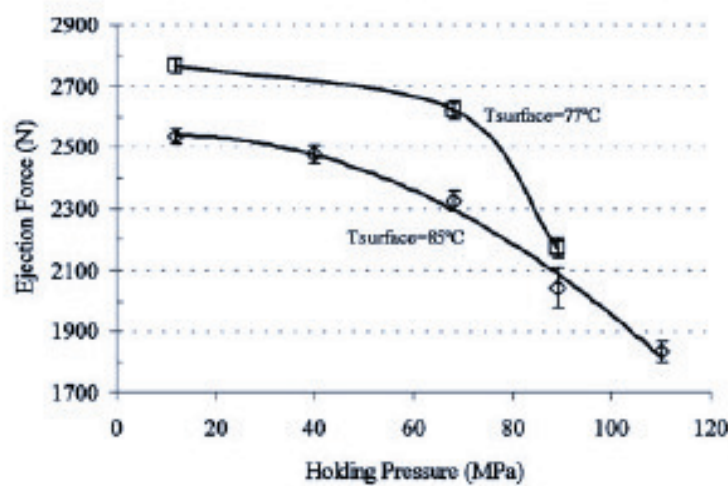


Figure 2.7 Influence of the holding pressure and core surface temperature on the ejection force for Polycarbonate (PC) [46]

Products with different geometries exhibit different shrinkage characteristics due to different constraints imposed by the mold pieces on the shrinking parts. Investigations have been conducted to explore how certain classes of highly specialized geometric shapes shrink during the injection molding cycle [45].

Some studies have also been conducted to experimentally observe the shrinkage of the product in-mold [35, 51]. Thomas and Bur [51] use Helium light as a sensor to monitor the shrinkage of Polystyrene while it is still inside the mold. During the molding cycle, the sensor performs four functions:

1. Detects the instant of mold filling at the sensor site
2. Monitors crystallization of crystallizable resins
3. Detects the separation of resin from the mold wall upon shrinkage
4. Monitors resin shrinkage and rate of shrinkage

This is illustrated in Figure 2.8.

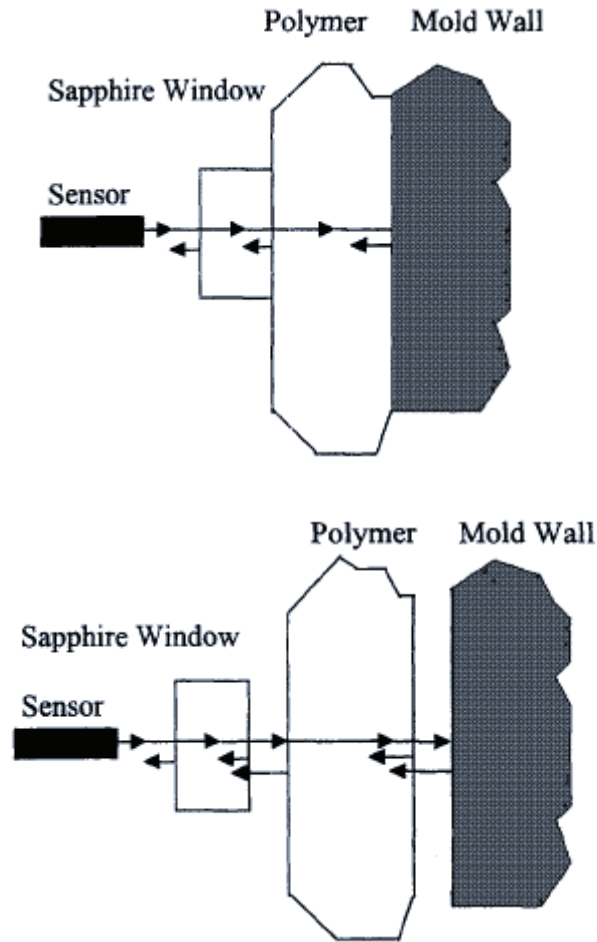


Figure 2.8 Working principle of the sensor used for in situ monitoring of shrinkage in PS [51]

Fathi and Behraves [35] conducted similar experiments to visualize shrinkage of Acrylonitrile Butadiene Styrene (ABS) using a high speed camera. They also introduced an obstacle pin in the mold to observe the shrinkage of the polymer around the obstacle pin.

Hieber, in his work [37], describes a model for predicting the time dependent shrinkage based on the experiments conducted by Thomas and Bur [51].

Shrinkage prediction of crystalline polymers is a challenging task. This is because of the complications of the crystallization process and associated material property changes. This task is simplified for slowly crystallizing polymers because the effective crystallinity of the polymer remains low after solidification of the polymer owing to the short solidification times in injection molding. Han and Wang [36] described an approach to predict the shrinkage for such slowly crystallizing polymers. They conduct their studies on PET (polyethylene terephthalate). They obtain the crystallinity of the final solidified polymer from equation 2.1.

$$\chi = \frac{Q - Q_a}{Q_c - Q_a} \quad 2.1$$

Here  $\chi$  is the crystallinity of the final polymer.  $Q$ ,  $Q_a$  and  $Q_c$  denote the density of the injection molded sample of the amorphous phase and of the crystalline phase respectively. Finally they use a modified Hele-Shaw approximation (equation 2.2) equation for simulation of the heat transfer. This equation takes into account the heat generated due to crystallization of the polymer.

$$QC_p \left( \frac{\partial T}{\partial t} + u \frac{\partial T}{\partial x} + v \frac{\partial T}{\partial y} \right) = \frac{\partial}{\partial z} \left( k \frac{\partial T}{\partial z} \right) + \eta \dot{\gamma}^2 + \frac{d\chi_r}{dt} H_m \quad 2.2$$

Here  $u$ ,  $v$  and  $w$  are the velocity components in the  $x$ ,  $y$  and  $z$  directions respectively (with  $z$  corresponding to the gap thickness direction.)  $Q$  is the density,  $C_p$  is the heat capacity,  $k$  is the thermal conductivity,  $\eta$  is the viscosity,  $\dot{\gamma}$  is the shear rate and  $H_m$  is the total heat generation due to crystallization.

Kwon et al [42-44] developed a model to predict the shrinkage of different kinds of polymers. Their model takes into account the orientation of the polymer chains in the

part leading to determination of the crystallinity, the effect of packing pressure and the effect of anisotropy of the polymer on the shrinkage. In their approach, they calculate the volumetric shrinkage of the polymer from equation 2.3.

$$S_v = \frac{\bar{V}_i - V_f}{\bar{V}_i} \quad 2.3$$

Here  $S_v$  is the volumetric shrinkage.  $\bar{V}_i$  is the initial specific volume of the melt and  $V_f$  is the final specific volume at room temperature. The initial specific volume is calculated from the pressure and temperature conditions experienced by the polymer inside the mold. The final specific volume is dependent on the PvT relationship of the polymer which is calculated from the heat transfer equation. Subsequently, the orientation functions of the polymer chains are calculated by measuring the birefringence of the polymer. These orientation functions give rise to the final crystallinity of the polymer which is then used to calculate the shrinkage in the length and the width directions. Equations 2.4 and 2.5 show the length and the width shrinkages respectively.

$$S_x = (1 - \chi)\alpha_x^a(T_g - T_\infty) - \chi\alpha_x^c(T_m - T_\infty) - \beta_x \bar{P}_s + S_{\gamma_\infty} \quad 2.4$$

$$S_y = (1 - \chi)\alpha_y^a(T_s - T_\infty) - \chi\alpha_y^c(T_m - T_\infty) - \beta_y \bar{P}_s - S_{\gamma_\infty} \quad 2.5$$

Here  $\chi$  is the final crystallinity of the polymer.  $\alpha_x^a$ ,  $\alpha_y^a$ ,  $\alpha_x^c$ ,  $\alpha_y^c$ ,  $\beta_x$  and  $\beta_y$  are the orientation functions of the polymer after solidification. The explanation of each orientation function can be seen in Kwon et al [42-44].  $T_g$  is the glass transition

temperature,  $T_{\infty}$  is the room temperature and  $T_m$  is the melting temperature of the polymer.  $S_{\gamma_{\infty}}$  is the elastic recovery due to crystallization.

Finally, the thickness shrinkage is calculated using equation 2.6.

$$S_z \cong S_v - (S_x + S_y) \quad 2.6$$

They verified these simulation results for amorphous [42] and semicrystalline [44] polymers and polyesters [43]. Their results suggest that the thickness shrinkage is most dependent on processing parameters like packing pressure etc. Figure 2.9 illustrates a sample result for amorphous polystyrene.

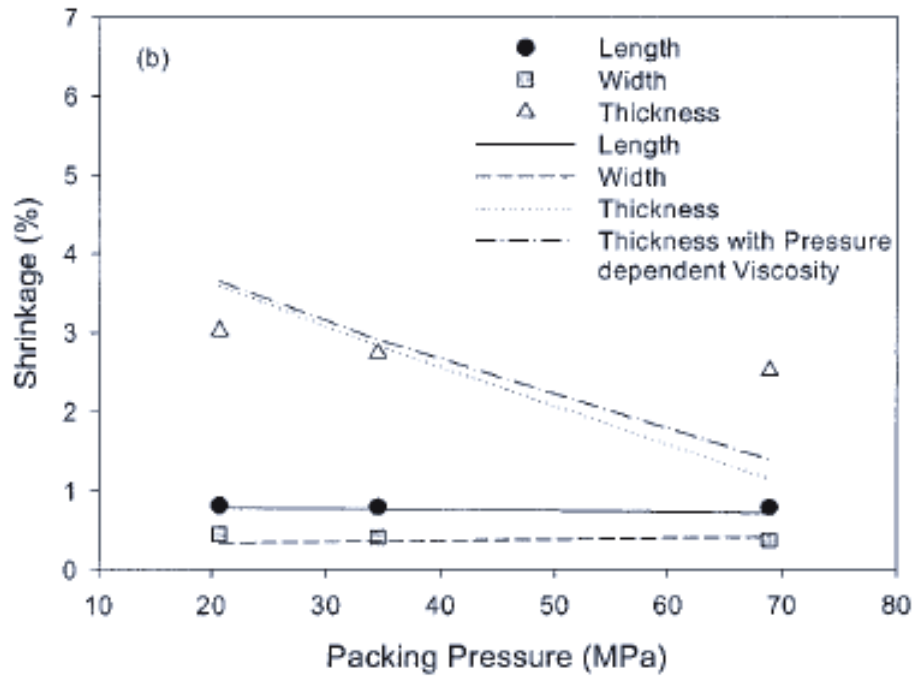


Figure 2.9 Experimental and predicted values for shrinkage with varying packing pressure [42]

Sridhar et al [47] argued that in the post filling stage, there is a gap between the mold wall and the polymer. This gap has a different thermal resistance than the mold

material and the polymer. Hence this needs to be taken into account while solving the heat transfer equation for shrinkage modeling.

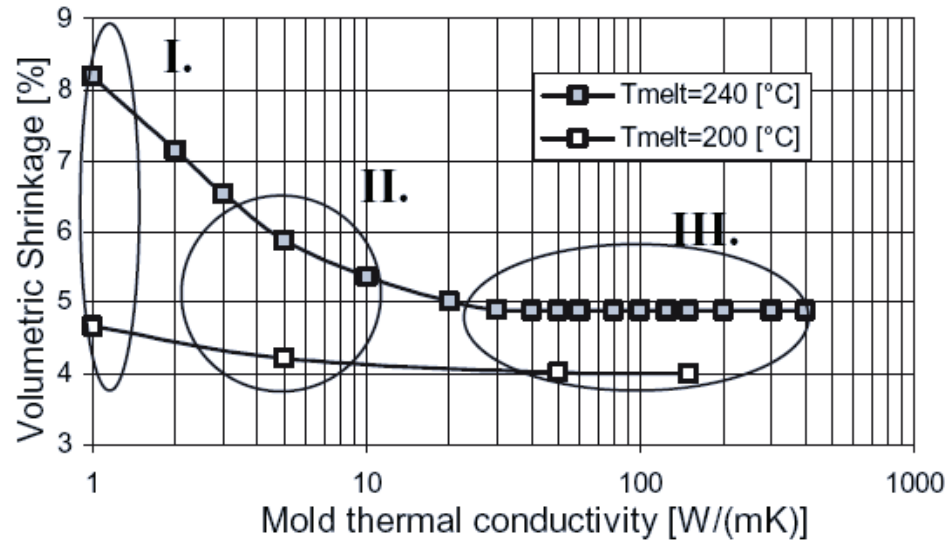


Figure 2.10 Mold material influence on volumetric shrinkage (I. – Soft tooling; II. – Hard tooling; III. – Conventional molds) [41]

In a recent work, Kovacs [41] has conducted a comparative study on the shrinkage in soft mold and hard mold components. He considers three different types of mold materials; these being, soft tooling (Epoxy), hard tooling (direct metal inserts) and conventional molds (High Speed Steel). He argues that the thermal conductivity of the hard mold and soft mold pieces are significantly different. This has a considerable effect on the shrinkage of the parts. He has observed that shrinkage decreases with increasing thermal conductivity of the mold. This is illustrated in Figure 2.10.

### **2.3 Mold Deformation during Injection Molding**

Multi-stage molding involves the use of previously molded components inside the mold. These pieces act as mold inserts. When the plastic piece present inside the mold

experiences the injection pressure, it undergoes deformation. This deformation is orders of magnitude greater than the deformation experienced by tool steel mold pieces. Such deformation changes shrinkage characteristics significantly. Existing shrinkage prediction models do not account for presence of plastically deformable mold pieces. There is, however, considerable work in elastic deformation of the mold due to overpacking.

Boitout et al [52] presented for the first time, a methodology to calculate the residual stresses in the injection molded part after incorporating the effect of mold deformations. For this purpose they present a simplified model to predict the deformation of the mold due to the normal stresses on the walls of the mold induced by the injection molding pressure.

Leo et. al [54] provided one of the first thorough investigations of thickness prediction, taking into account the deformation of the mold. They found that at nominal pressures higher than about 150 MPa, when using HSS molds, deviation due to packing pressure needs to be taken into account. They take into account simple elastic deformations of the mold due to the stresses applied. The gate size was found to be an important parameter for mold deflection. It was found that the mold deflection was proportional to the gate size of the cavity. The cavity deformation leads to overpacking or negative shrinkage which is usually unacceptable for industrial applications since it leads to problems with ejection.



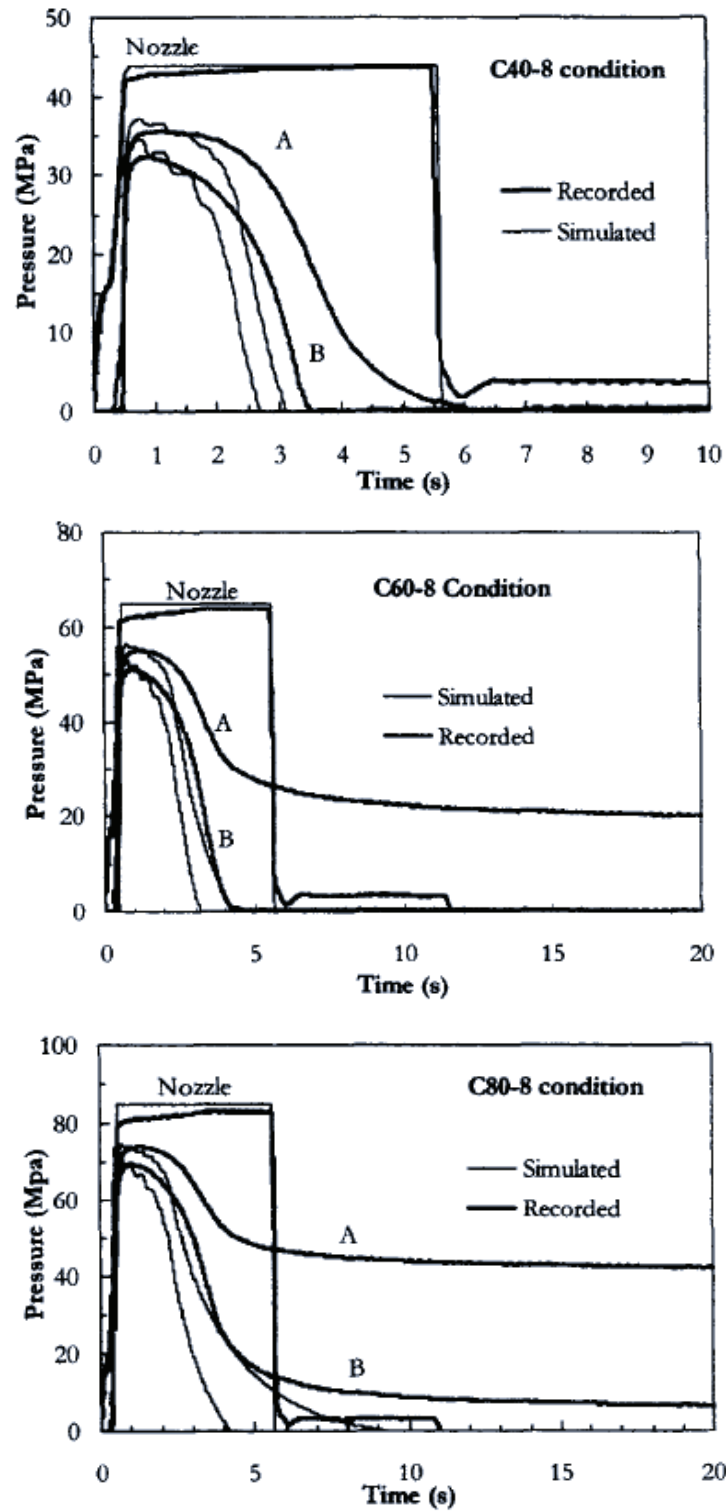


Figure 2.11 Comparison between measured pressures and simulated pressures versus time [34]

Jansen et al [48] also studied the effect of mold deflection on the shrinkage of a molded component. Although their focus was more on establishing friction as one of the major players in limiting shrinkage in the length direction under high packing pressures, this was one of the earlier works to characterize the mold deflection and its effect on shrinkage of the molded components.

Delaunay et al [34] studied the influence of mold deformation on the pressure history observed in the mold during the packing phase. They note that the difference between recorded and predicted pressure decay during the cooling phase rises dramatically as the holding pressure increases. They compared different mold materials in order to establish the effect of mold deviation on the pressure history. This is illustrated in Figure 2.11.

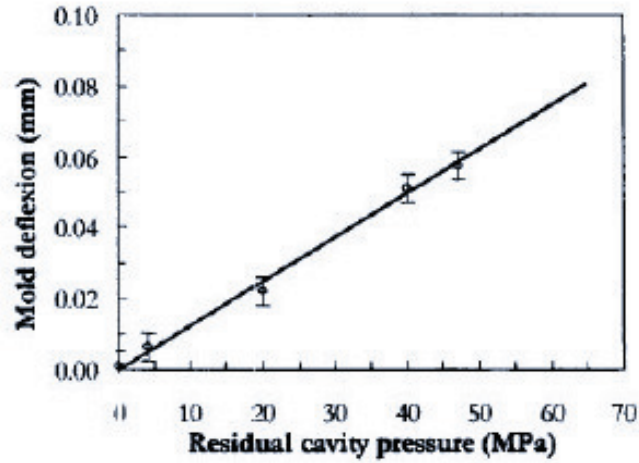
They subsequently present a detailed description of the continuum mechanics methodology used to calculate the mold deflection. As part of their experiments and simulations, they find that in-plane shrinkage does not depend on mold deflection. The model developed for strains due to mold deflection in the thickness direction is described by equations 2.7 and 2.8.

$$\epsilon_z = -\frac{\nu}{1-\nu}(S_p + S_n) + \frac{1+\nu}{1-\nu}\left(\alpha(T_m - T_a) - \frac{p}{E}(1-\nu)\right) \quad 2.7$$

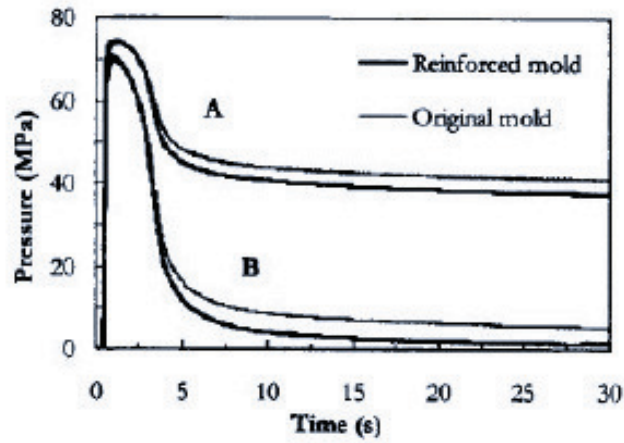
$$\epsilon_z = \frac{(t_c + d) - t_a}{t_a} \quad 2.8$$

Where  $\nu$  is defined as the Poisson ratio,  $E$  is the Young's modulus,  $\alpha$  is the linear expansion coefficient.  $S_p$  is the local in-plane shrinkage measured in the filling flow direction.  $S_n$  is the local in-plane shrinkage, which is perpendicular to the flow

direction.  $T_m$  is the mold temperature,  $T_a$  is the ambient temperature.  $t_c$  is the empty cavity thickness,  $t_a$  is the thickness after ejection and  $d$  is the deflection of the mold.



(a)



(b)

Figure 2.12 (a) Calculated mold deflection versus residual cavity pressure (b) Mold reinforcement effect on cavity pressure [34]

Pantani et al [55] in a subsequent work used amorphous polystyrene in order to understand the effects of mold deflection by eliminating the factor of crystallinity of the polymer.

Carpenter et al [53] worked on establishing the relationship between the compliance of the injection molding machine and the deformation of the mold. They argue that since the one of the mold halves is movable, some deflection in the mold may occur due to machine compliance caused by clamping pressure and injection molding pressure. This is aptly represented by Figure 2.13.

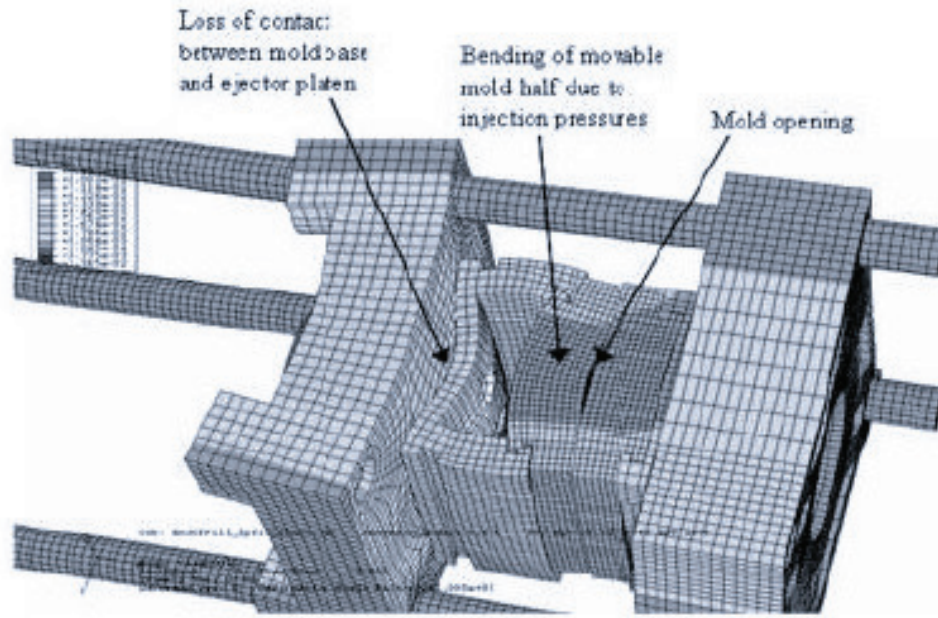


Figure 2.13 Effect of machine compliance [53]

Some researchers [56] have also studied the effect of mold deflection on the prediction of the final dimensions of the injection molded components.

## ***2.4 Fluid Structure Interaction for Non-Newtonian Flows***

The interaction between a fluid and an obstacle in its flow is a problem that has been studied by several researchers over the past several decades. This problem is particularly of interest in in-mold assembly since it is necessary to understand the interaction between the premolded component and the second stage polymer melt

flow. Several researchers have assumed the flow to be a Newtonian flow and have conducted simulations of fluid structure interaction for such flows. However, the flow of a polymer in a mold cavity is known to be non-Newtonian since the viscosity of the polymer melt is related to the shear rate of the flow [59]. Hence it is necessary to treat the fluid structure interaction problem in this domain.

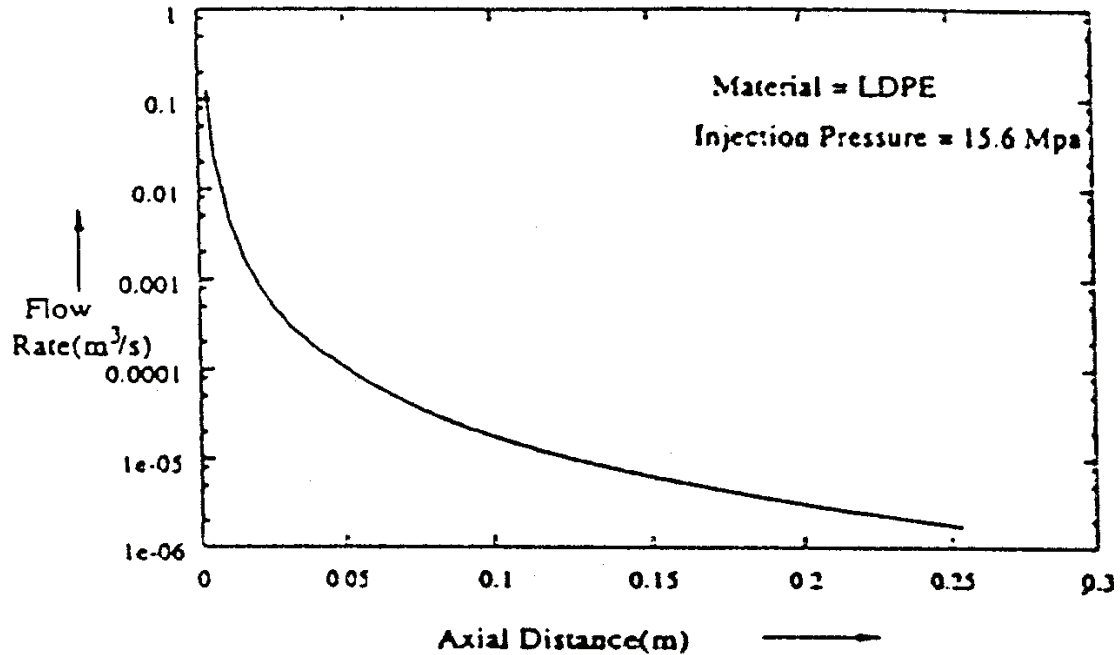


Figure 2.14 Flow rate versus distance for constant injection pressure isothermal filling [59]

Several researchers have conducted studies on simulation of polymer filling into mold cavities. A representative work was conducted by Kumar and Ghoshdastidar [59]. They studied the filling of a cylindrical cavity with a polymer. They have considered three distinct cases.

- 1) Isothermal filling at constant injection pressure
- 2) Isothermal filling at constant flow rate and

3) Nonisothermal filling at constant flow rate. For this case, the viscosity of LDPE is also a function of temperature.

For each of these cases, they have considered the filling of a thin mold cavity. From this simulation, they have plotted the velocity profiles and pressure profiles as a function of the time until the filling is completed. These profiles are illustrated in Figure 2.13 and Figure 2.14 respectively

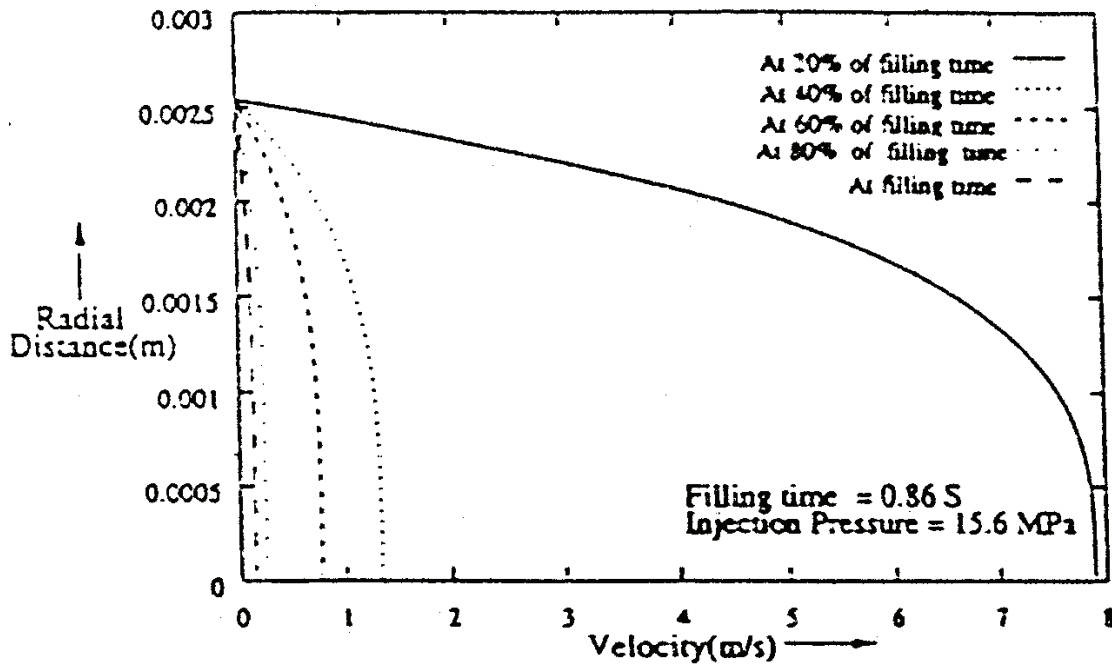


Figure 2.15 Half melt velocity profile at various z-locations for constant injection pressure isothermal filling [59]

In a subsequent study, De Besses et al. [57] studied the flow of a viscoplastic fluid around a cylinder in an infinite medium. They assume the viscoplastic properties of the polymer to follow the Herschel-Bulkley model. This model is described in equation 2.9.

$$\tau_{ij} = 2 \left( K \dot{\gamma}^{n-1} + \frac{\tau_0}{\dot{\gamma}} \right) D_{ij} \quad \text{if} \quad \tau_{II} > \tau_0 \quad 2.9$$

$$D_{ij} = 0 \quad \text{if} \quad \tau_{II} \leq \tau_0$$

Where  $D_{ij}$  is the strain rate tensor defined by:

$$D_{ij} = \frac{1}{2} \left( \frac{\partial u_i}{\partial x_j} + \frac{\partial u_j}{\partial x_i} \right) \quad 2.10$$

and the second invariant of the strain rate tensor is given by

$$\dot{\gamma} = \sqrt{2 D_{ij} D_{ij}} \quad 2.11$$

and the second invariant of the stress tensor is given by

$$\tau_{II} = \sqrt{\frac{1}{2} \tau_{ij} \tau_{ij}} \quad 2.12$$

$K$  is the consistency coefficient,  $n$  is the shear thinning index and  $\tau_0$  is the yield stress below which flow is no longer deformed.

In their formulation, they calculate the force on an infinitely long cylinder which is an obstacle in an infinite flow between two walls which are separated by a distance  $d$ . The force distribution on the cylinder that was thus calculated is illustrated in Figure 2.16.

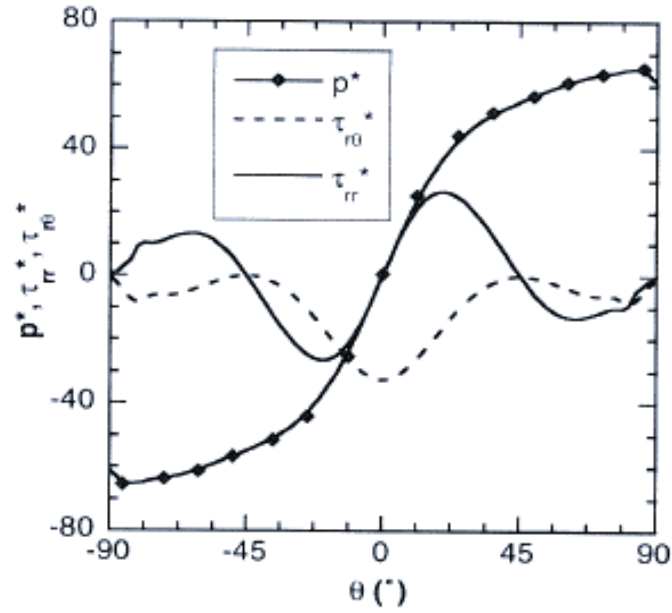


Figure 2.16 Distribution of pressure and tangential and normal stress on the cylinder surface as a function of angle

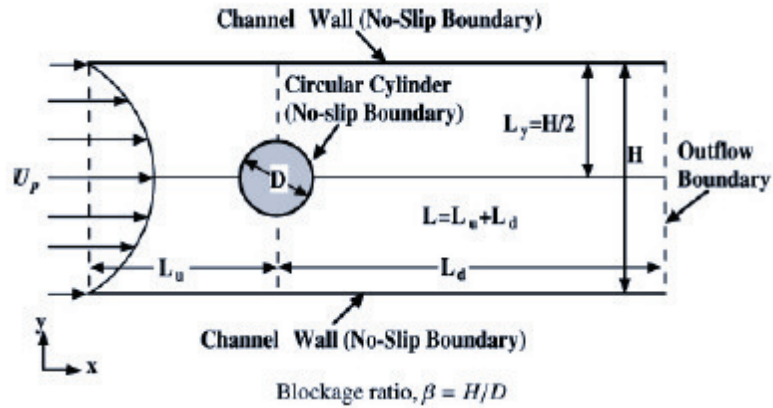


Figure 2.17 Schematic representation of a channel confined Poiseuille flow over a circular cylinder

Subsequently Mitsoulis [60] conducted the same simulations for a Bingham plastic. A Bingham plastic is a viscoplastic material that behaves as a rigid body at low



stresses but flows as a viscous fluid at high stress. The simulations that they have conducted are also for an infinite cylinder in an infinite flow.

Esirgemez et al [58] studied the flow physics of a free round air jet prior to impinging on a convex cylindrical surface. They plotted the forces on the cylinder due to such a flow.

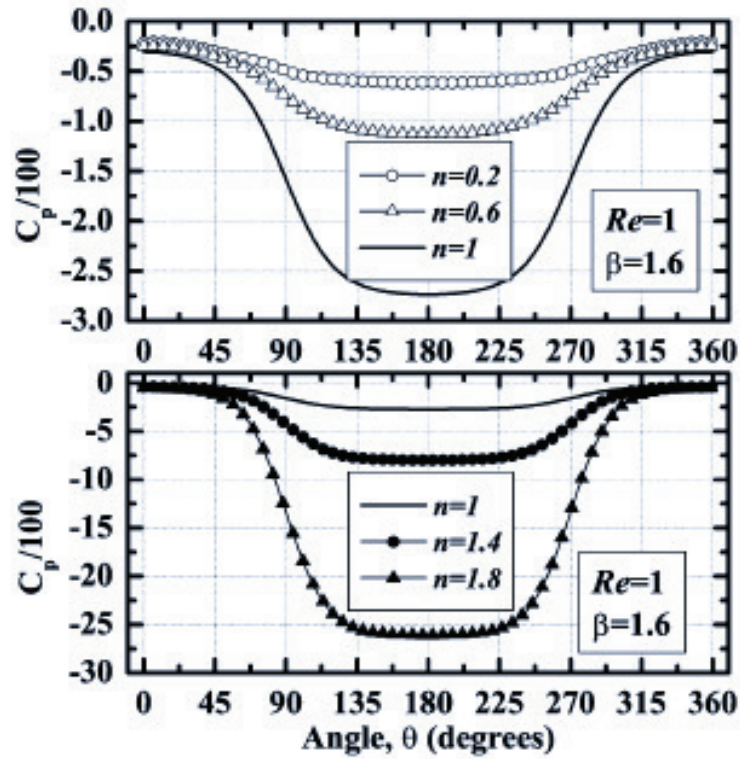


Figure 2.18 Distribution of pressure coefficient ( $C_p$ ) over the surface of the cylinder for the Reynolds number ( $Re$ ) of 1 and a range of the power-law index ( $n$ ) at  $\beta = 1.6$

Bharti et al [80] studied the non-Newtonian Poiseuille flow around an infinite cylinder in an infinite medium. The non-Newtonian properties of the fluid were described as a power law which is described in equation 2.13. In this equation  $\eta$  is the viscosity of the flowing polymer,  $n$  is the power law index,  $K$  is the flow consistency index and  $\dot{\gamma}$  is the shear rate of the flow.

$$\eta = K \dot{\gamma}^{n-1} \quad 2.13$$

The flow medium was described as infinite in one direction and finite in the other. This is illustrated in Figure 2.17. Their results indicate that the drag force on a cylinder in Newtonian flow with low Reynolds number is up to 8 times higher than the drag force on a cylinder in non-Newtonian flow. This is valid when the blockage ratio  $\beta$ , as illustrated in Figure 2.17, is less than 1.5. A representative result of pressure coefficient on the cylinder for low Reynolds number flow is illustrated in Figure 2.18.

## 2.5 Real-time Measurement of Injection Molding Process

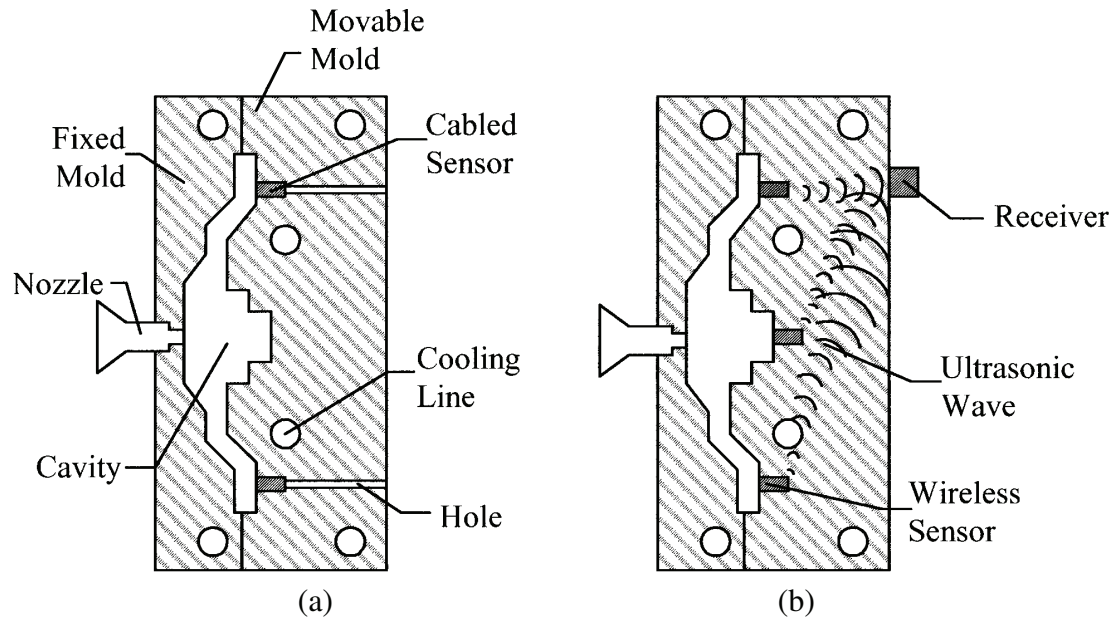


Figure 2.19 (a) Cabled cavity pressure sensor and (b) Wireless cavity pressure sensor

For the past few years, researchers have developed different experimental techniques to measure various parameters during the injection molding process real-

time. Some of these include cavity pressure [56, 81, 82], melt flow length [1, 81-84], temperature [85] etc. This section will summarize some of these techniques.

Theurer et al. [82] have developed a wireless sensory technique to measure the cavity pressure. Their setup is illustrated in Figure 2.19. Their underlying concept is to extract energy from the injection molding process itself and using this energy to discretize the pressure information into a series of ultrasonic pulse signals to enable a mechanical wireless data transmission out of the injection mold. This process is designed such that it does not suffer from the shielding effect on electromagnetic waves cause by the sealed metallic environment of the molds.

Cheng et al. [81] described a virtual sensing approach for on-line monitoring and regulating process variables of the injection molding process. Their technique exploits easily obtainable quantities such as injection pressure and screw position to estimate the Nozzle pressure (Figure 2.20). They use a model based approach by exploiting the dynamic interaction between the process and machine variables using the nonlinear observer theory. To validate their approach they have also measured the actual nozzle pressure using a Kistler 4085A nozzle pressure sensor and a data acquisition board. The results of their findings can be seen in Figure 2.21.

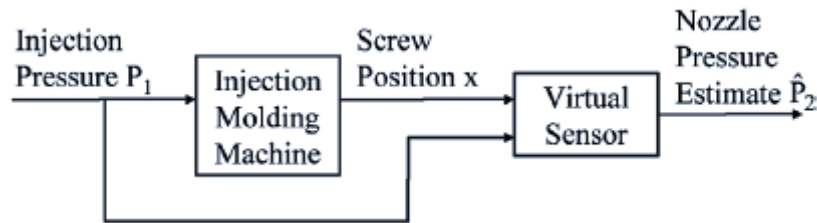
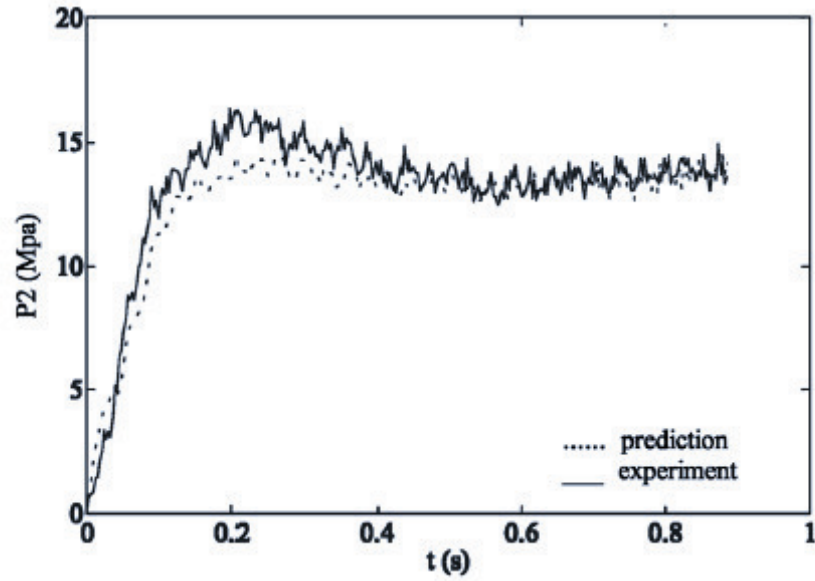
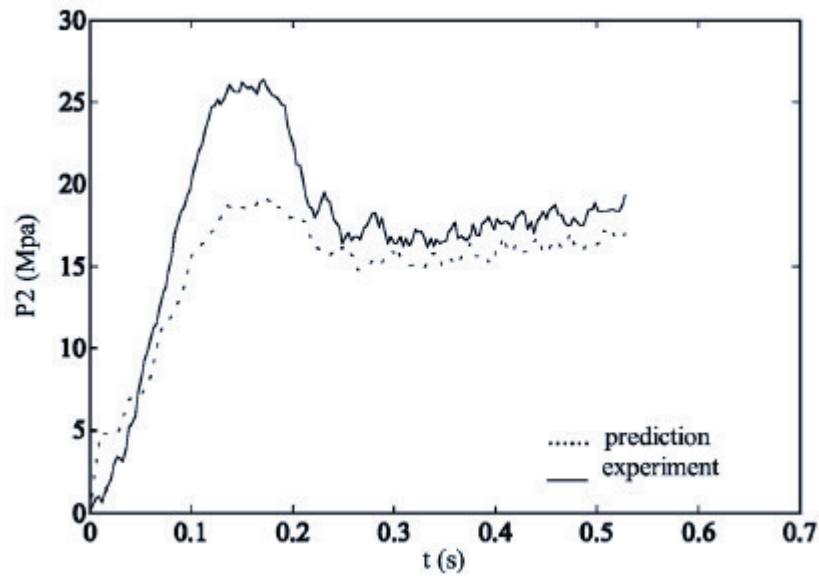


Figure 2.20 Interface design of the virtual sensor [81]



(a)



(b)

Figure 2.21 Model prediction results for virtual sensing of nozzle pressure (a) Best Case (b) Worst Case [81]

Wu et al [83] developed a sensory technique to measure the cavity pressure and the melt flow length inside a mold cavity. They used the classic Archimedes spiral channel mold to conduct their experiments. Their setup is illustrated in Figure 2.22. They use these measurement techniques to understand the effects of various injection

molding parameters such as injection pressure, injection velocity and mold temperature on the melt flow length and cavity pressure in the mold. Their results indicate that as the injection pressure ascends, cavity pressure and flow length increases synchronously. The mold temperature has little or no effect on the cavity pressure. However the melt flow length increases as a result of using a heated mold.

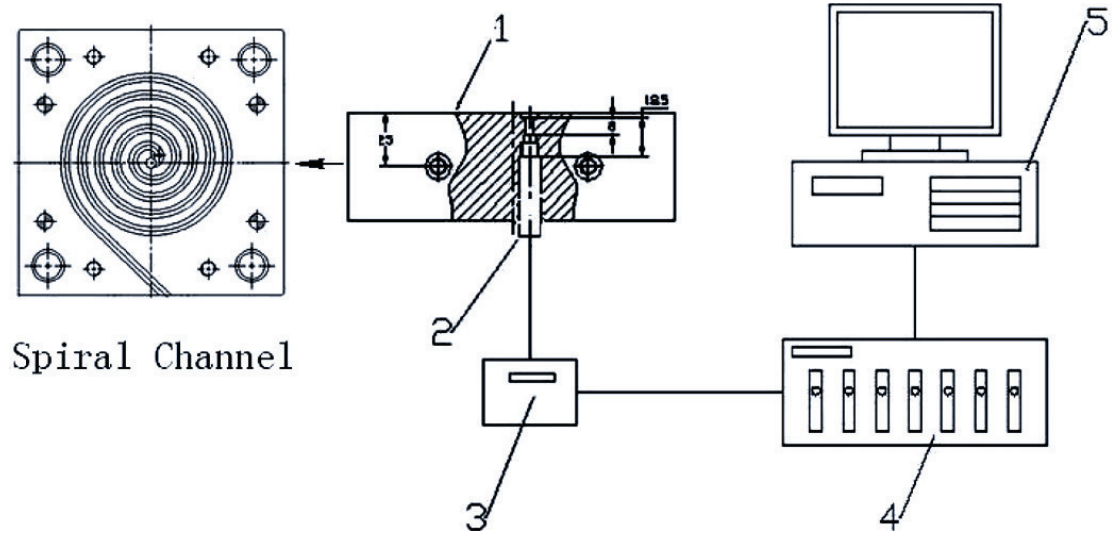


Figure 2.22 The cavity pressure measure and analysis system. 1) spiral channel mold, 2) pressure sensor, 3) amplifier, 4) data acquisition system, and 5) personal computer

Chen et al. [84] have developed a capacitive transducer based measurement technique to measure the melt flow length in real-time. They have used the dielectric properties of the polymer melt to determine the flow front progression in real-time. This is illustrated in Figure 2.23. The average melt flow length is calculated using the equation 2.14.

$$afl/L = (C/C_0 - 1)/(k-1) \quad 2.14$$

Here afl is the average melt flow length, L is the overall length of the cavity, C is the measured capacitance of the cavity,  $C_0$  is the capacitance of the cavity in the beginning of the fill and k is the dielectric constant of the polymer.

In a subsequent work Chen et al. [82] developed a virtual sensing method utilizing the quantifiable injection molding parameters such as injection pressure and injection velocity as inputs to determine the melt flow length. They used different mold geometries to train the neural network they used to model the melt flow length. Using this neural network they have developed a technique to predict the melt flow length using easily measurable parameters such as injection pressure and injection velocity.

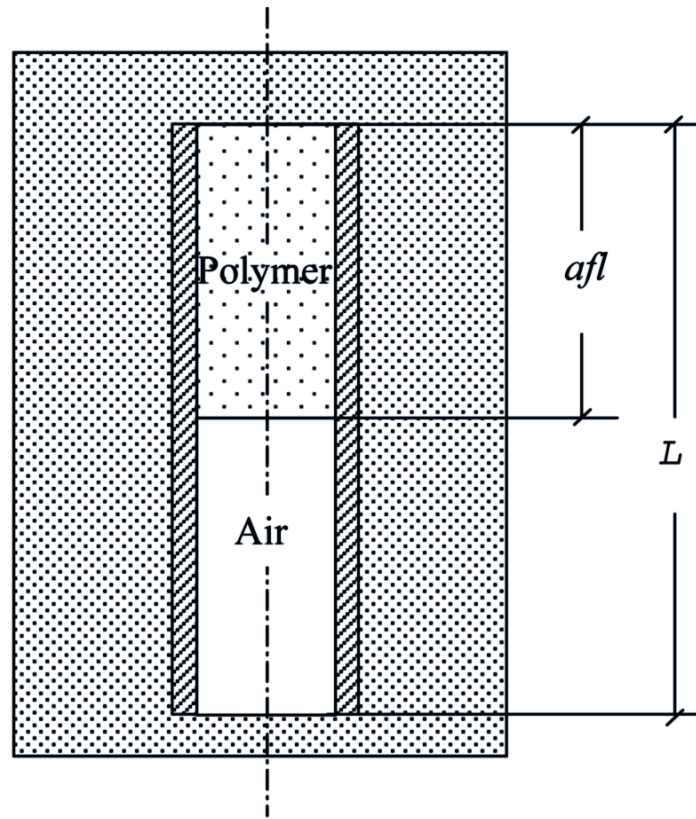


Figure 2.23 Illustration of melt flow during filling stage [84]

In a later work Wong et al. [1] extend the capacitive transducer based measurement technique developed by Chen et al. [84] to predict the start and end of the mold filling accurately. Their system predicts the beginning and end of different phases of the injection molding cycle. This is illustrated in Figure 2.24.

Lin et al [86] have also developed virtual sensors for observing the melt filling using injection pressure, injection velocity and nozzle pressure.

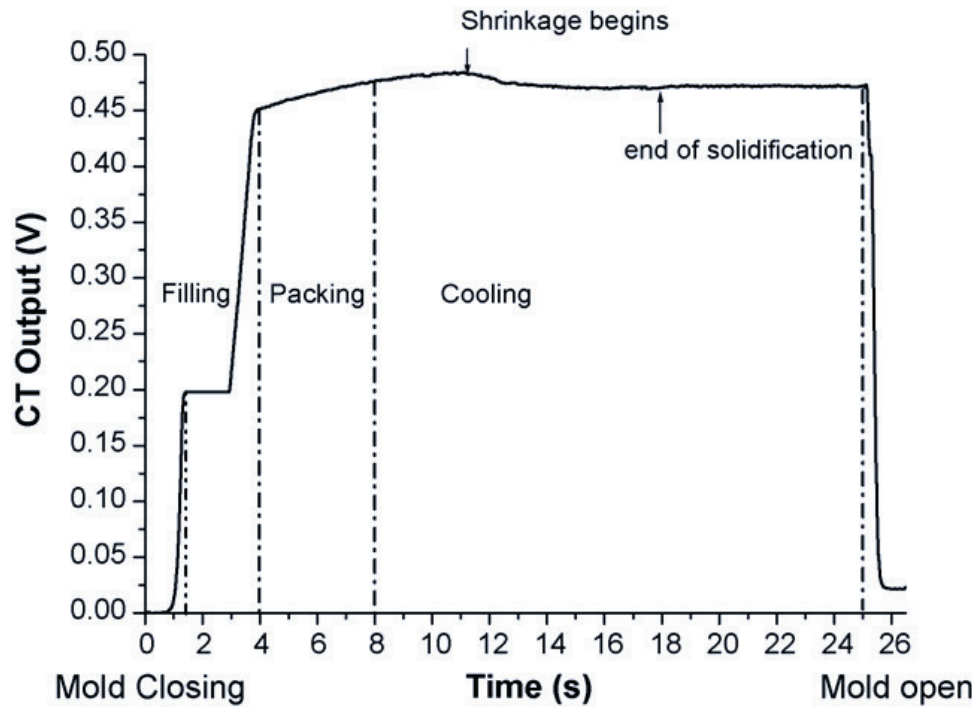


Figure 2.24 A typical plot of capacitive transducer output in an injection cycle for the hot-runner mold [1]

Farouq et al. [85] have developed an experimental setup to accurately measure the temperature of the polymer melt inside the injection mold cavity real-time during the injection molding process. They use a rigid temperature probe to ensure that it doesn't deviate from its position during the mold filling. This setup is illustrated in Figure 2.25. The labels in the figure represent the following components:

- (a) Mold cavity
- (b) Temperature probe housing cavity
- (c) Feed orifice
- (d) Needle

(e) Thermoplastic elastomer block housing

(f) Runner

(g) Temperature probe

(h) Transducer

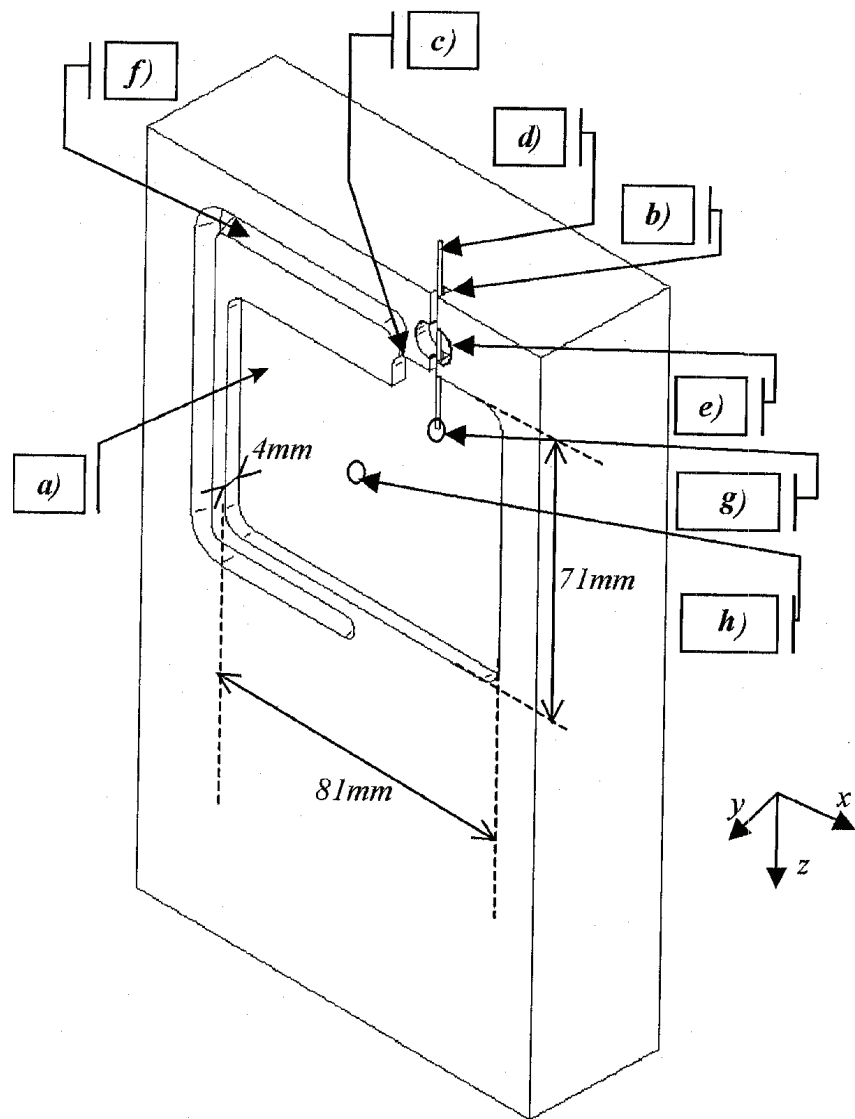


Figure 2.25 Setup for measuring temperatures inside the mold cavity [85]



## ***2.6 Weld-lines in Injection Molded parts***

Several researchers have been studying the effect of weld-lines on the structural properties of the injection molded part. Weld-lines are a cause for low mechanical strength of the part. Researchers have identified the cause for the low strength to be [65]:

1. Unfavorable molecular orientation (parallel to the weld-line instead of being parallel to the surface of the part)
2. Insufficient bonding (due to insufficient entanglements)
3. Formation of a V-notch.

Several researchers [62, 65, 68, 70, 74] have indicated that the strength of hot weld-lines, meld lines or adjacent flow weld-lines is significantly more than that of cold weld-lines or butt weld-lines. Hot weld-lines are those where the flow of the polymers continues even after they meet. i.e. the two flows are parallel to each other when they meet. On the other hand, in cold weld-lines, the flows meet head on i.e. at an angle of  $180^\circ$  to each other. The two types of weld-lines are illustrated in Figure 2.26.

Selden [65] studied the strength of both hot and cold weld-lines for 5 different thermoplastics. He conducted impact, tensile and flexural tests on the polymer specimen with and without weld-lines. Weld-line properties are often defined in the form of a weld-line factor defined in equation 2.15. The strength indicated in the equation is the ultimate tensile strength of the material.

His findings indicate that cold weld-lines produced lower weld-line factors than hot weld-lines for the class of polymers that he studied. Also, he indicates that

changing the injection molding parameters did not have a significant effect on the weld-line factor. Also, the weld-line factors are observed to be lower in filled polymers than in unfilled polymers. This is because there is little intermingling of the fillers in the two meeting flows in the filled polymers. Unfilled polymers on the other hand have a higher degree of mixing. He finds that the weld-line factors for cold weld-lines in unfilled Acrylonitrile Butadiene Styrene (ABS) and PPO (Noryl 110) was 0.92 and 0.9 respectively.

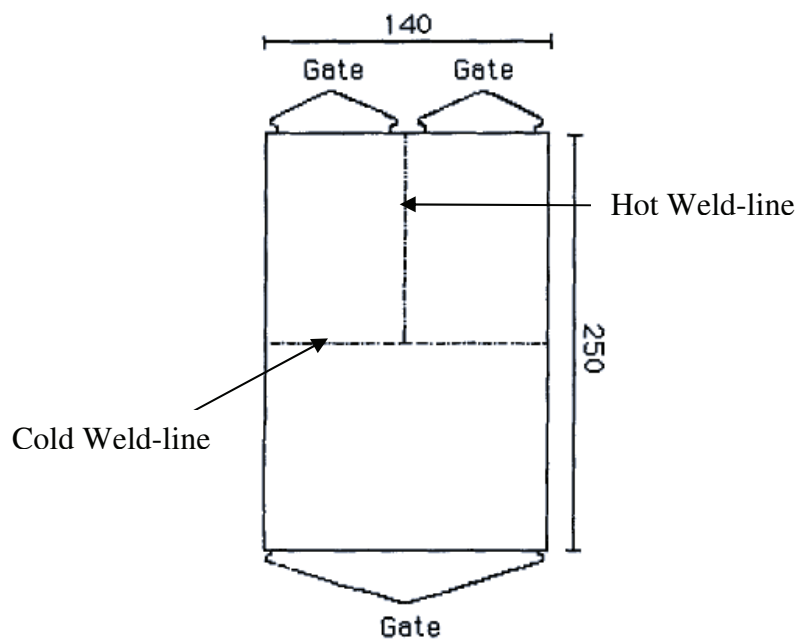


Figure 2.26 Cold and Hot weld-lines [65]

$$\text{WL-factor} = \frac{\text{Strength with weld line}}{\text{Strength without weld line}} \quad 2.15$$

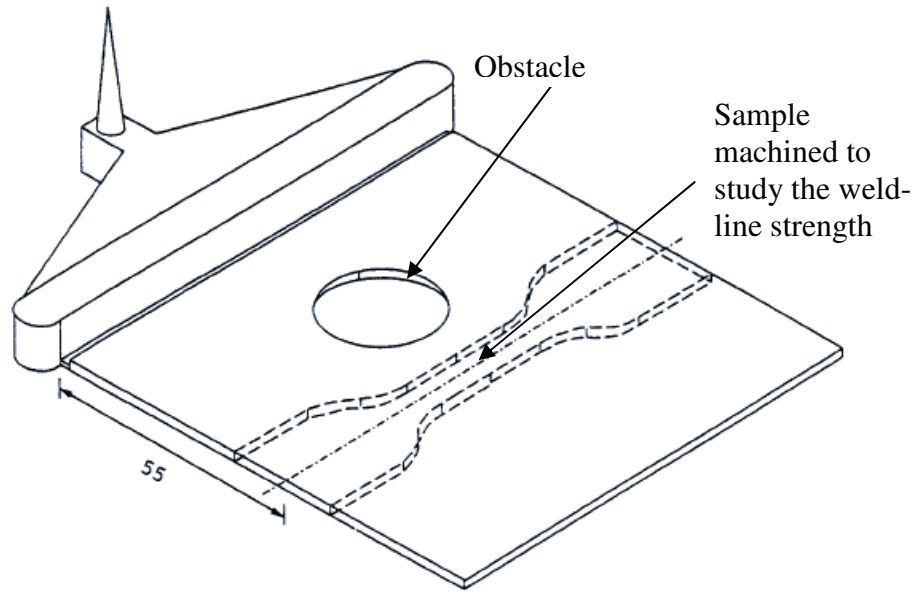


Figure 2.27 Weld-lines formed due to presence of an obstacle [62]

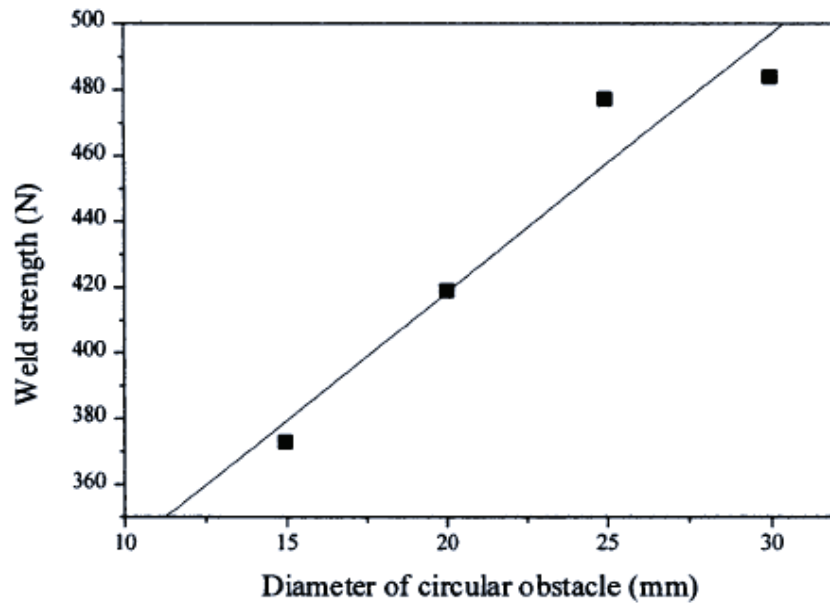


Figure 2.28 Effect of obstacle size on the weld-line strengths of injection molded polystyrene [62]

Liu et al [62] conducted weld-line strength studies on hot weld-lines formed due to the presence of an obstacle in the flow as illustrated in Figure 2.27. They studied the

strength of the weld-lines in injection molded polystyrene for different sizes and geometries of the obstacle. Their findings indicate that the strength of weld-lines increase with the size of the obstacles. This effect is illustrated in Figure 2.28 for a circular obstacle. They also indicate that the strength of the weld-line increases with increasing melt temperature and mold temperature. Melt injection pressure, on the other hand, has very little effect on the weld-line strength.

Nguyen-Chung [64] in his work studied the formation of cold weld-lines in polystyrene. As part of this study, he has also conducted simulations to understand the sources of weld-line weakness. He correlates the weld-line weakness to the flow history of the polymer in the mold cavity. From simulations he has shown the orientation of the polymer chains at the weld-line interface.

Debondue et al [71] studied the effect of weld-lines in two different polymers. These being Polystyrene (PS) and Polycarbonate (PC). They report that the weld-line sensitivity is significantly higher for PS compared with that of PC. As part of their work, they have reported the effect of the weld-line notch on the strength of the specimen. To illustrate this, they have conducted tests on the molded weld-line specimen after eliminating the notch by polishing the surface using a sand paper. They also report that the weld-line strength increases with melt temperature. These are illustrated in Figure 2.29.

Mekhilef et al [69] have described a model for predicting the weld-line strength in injection molded Polycarbonate (PC) and its blend with high density polyethylene (PE). They describe their model based on the model described by Kim and Suh [76].

This model is described considering isothermal conditions and takes into account the diffusion coefficient of the polymer. This model is described in equation 2.16.

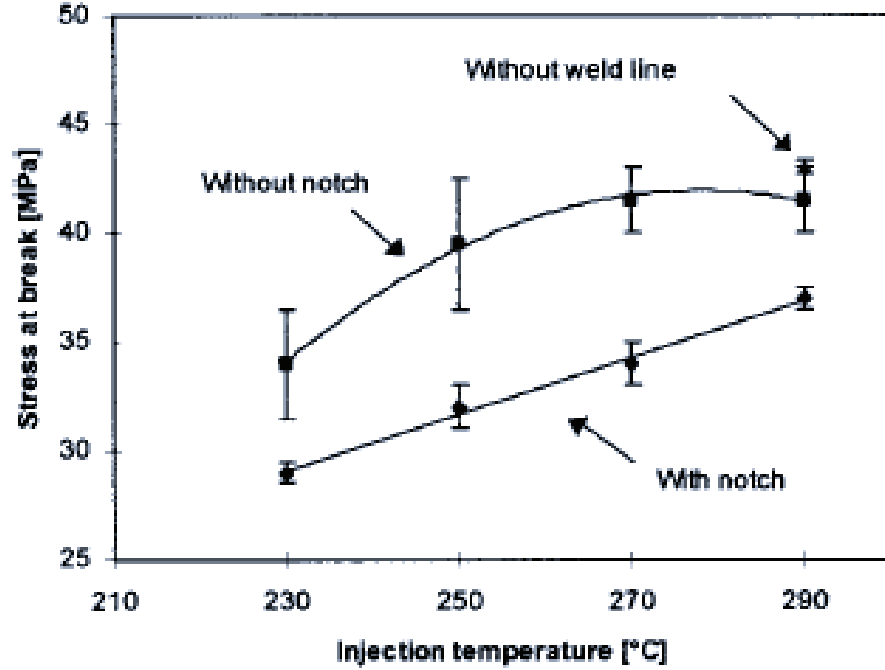


Figure 2.29 Evolution of the tensile strength when the weld-line notch is eliminated  
(PS) [71]

$$\frac{\sigma_w}{\sigma_b} = 1 - \exp\left(\frac{CD}{kT}[-2\gamma + kT\delta x_0\delta n_0 \ln(1/2)]t\right) \quad 2.16$$

Here  $\sigma_w$  and  $\sigma_b$  are the tensile strengths of the polymer with and without the weld-line respectively, C is the rate of diffusion at the glass transition temperature of the polymer, D is the diffusion coefficient, k is the Boltzmann constant, T is the temperature of the melt,  $\gamma$  is the surface tension,  $\delta x_0$  is the diffusion thickness and  $\delta n_0$  is the number of lattices per unit volume and t is the time. To calculate the diffusion coefficient they use the model described in equation 2.17.

$$D = \frac{G_0}{135} \left( \rho \frac{RT}{G_0} \right)^2 \left( \frac{R_e^2}{M_w} \right) \left( \frac{M_{cr}}{M_w^2} \eta_{0,cr} \right) \quad 2.17$$

Here  $G_0$  is the plateau modulus,  $\rho$  is the density,  $R$  is the universal gas constant,  $R_e^2 / M_w$  is the ratio of the mean square end to end distance of the molecules to average molecular weight,  $\eta_{0,cr}$  is the zero shear viscosity at the critical molecular weight for entanglements and  $M_{cr}$  is the critical molecular weight.

Their model suggests that the weld-line strength increases substantially with melt temperature. They describe the weld-line strength of the material as the degree of bonding. Their results for PC are illustrated in Figure 2.30.

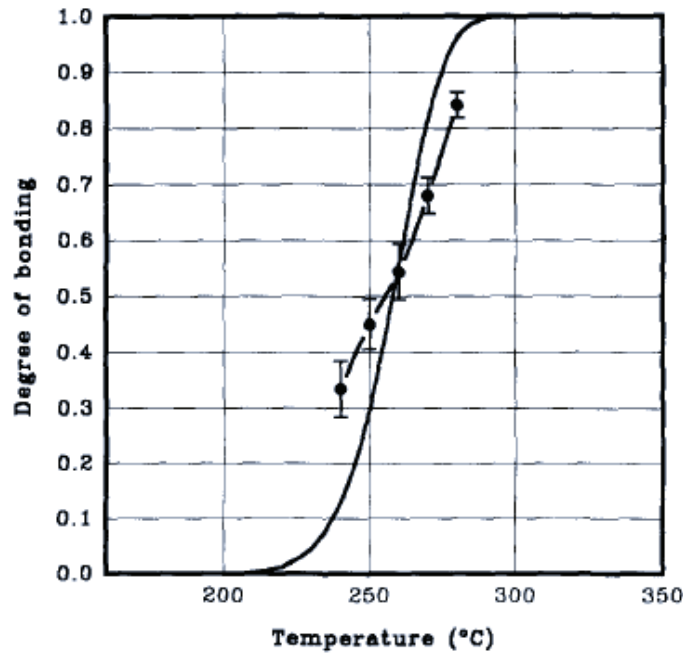


Figure 2.30 Comparison between the model predictions (-) and the experimental data (•) of the weld-line strength of polycarbonate [69]

Kim et al [70] conducted tests of mechanical properties for weld-lines in injection molded poly(butylene terephthalate) (PBT). They report that the strength of pure PBT

is not influenced by the presence of a weld-line whereas the weld-line strength of glass filled PBT is almost half that of the specimen without a weld-line. They have also conducted simulations to find the molecular orientation of the fillers in the specimen and found them to agree with the experimental results.

Boyanova et al [72] studied the quality of the weld-line by conducting a microhardness test at the weld-line of injection molded PC and PS. They used a two component injection molding machine to conduct their tests so that two different colors of the same material can be introduced into the cavity. This helped them in identifying the weld-line accurately. Subsequently, they conduct microhardness tests on the samples to accurately identify the position of the weld-line in the part. As seen in Figure 2.31 there is a clearly distinguishable drop in the hardness at the weld-line interface of the injection molded polymer.  $Z = 0$  is the location of the weld-line in the samples.

Lu et al [63, 73] used an innovative method to improve the strength of the weld-lines. They have evaluated the effect of ultrasonic vibrations on the strength of the weld-line. They report that due to the ultrasonic vibrations, the molecular diffusion is better leading to a higher strength of the weld-line. To study the strength of the weld-line, they remove the surface of the weld-line by milling. Both the top and the bottom surfaces, which included the weld-line, were cut in various depths by a mill. They prepared the samples for two modes of ultrasonic vibrations and studied the strength of the weld-lines for both modes. The results for neat PS are reported in Figure 2.32.

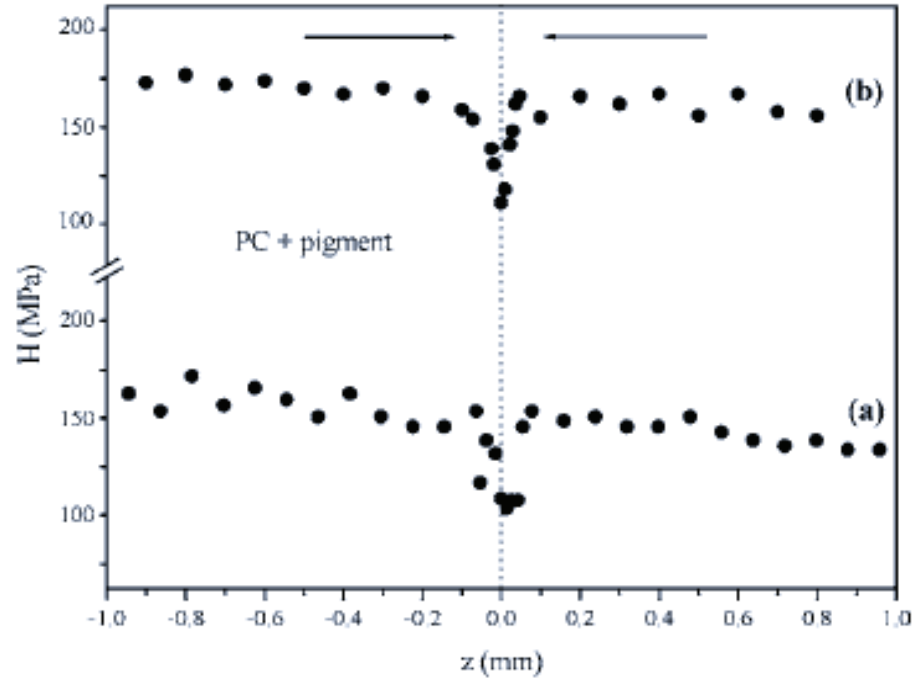


Figure 2.31 Microhardness,  $H$ , measured at the surface of the molding along the injection direction,  $z$ , for PC with melt temperature of 270°C [72]

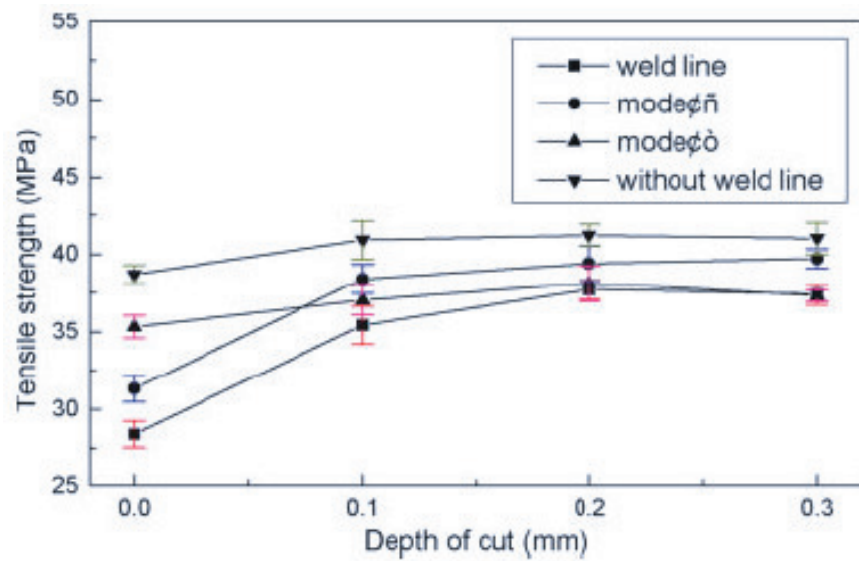


Figure 2.32 Relationship between tensile strength of injection molded PS parts and depth of cut under different process conditions [63]



Yamada et al. [68] studied the strength of adjacent flow weld-lines as part of their work. They introduced an obstacle in the flow to create an adjacent flow weld-line downstream of the obstacle. Subsequently, they studied the strength of the weld-line and the depth of the v-notch with increasing distance from the obstacle. They report that the depth of the v-notch decreases with increasing distance. This in turn leads to increased weld-line strength with distance. This is illustrated in Figure 2.33. They also studied the effect of milling the weld-line surface on the strength of the specimen. They argue that the main cause of lower strength of the weld-lines is the surface defects. This is supported by their findings which reveal that removing material from the surface of the weld-line specimen leads to increase in weld-line strength.

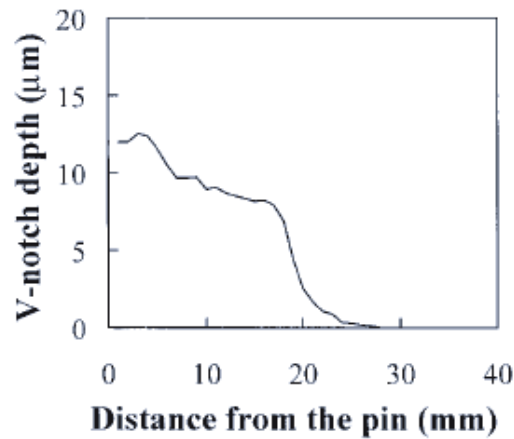


Figure 2.33 V-notch depth along the flow direction [68]

As part of another work [74], they have reported the fracture toughness in injection molded parts with adjacent flow weld-lines. They have conducted tests on injection molded PS specimen with different obstacle geometries (circle, rhombus and square) to support their claims. They report that Fracture toughness decreases steeply beyond the meeting point. This tendency was due to flow-induced molecular orientation at

the sub skin layer of the weld-line interface. In contrast, relatively higher toughness was shown in the vicinity of the meeting point than the bulk area. This was attributed to the fact that the stagnation promoted the intermolecular entanglement across the weld-line interface. This phenomenon is illustrated for various geometries in Figure 2.34.

Wu and Liang [67] as part of their work studied the effect of geometry and injection molding parameters on the weld-line strength. They modeled 5 different dimensions of a rectangular cross section to study the effect of geometry on the weld-line strength. Their findings reveal that mesoscale geometry of 0.3 X 0.3 mm cross section had the maximum weld-line strength. The effect of processing parameters on the other hand, was not found to be as predominant. They also reported that the effect of mold and melt temperature is the most pronounced in weld-line strength.

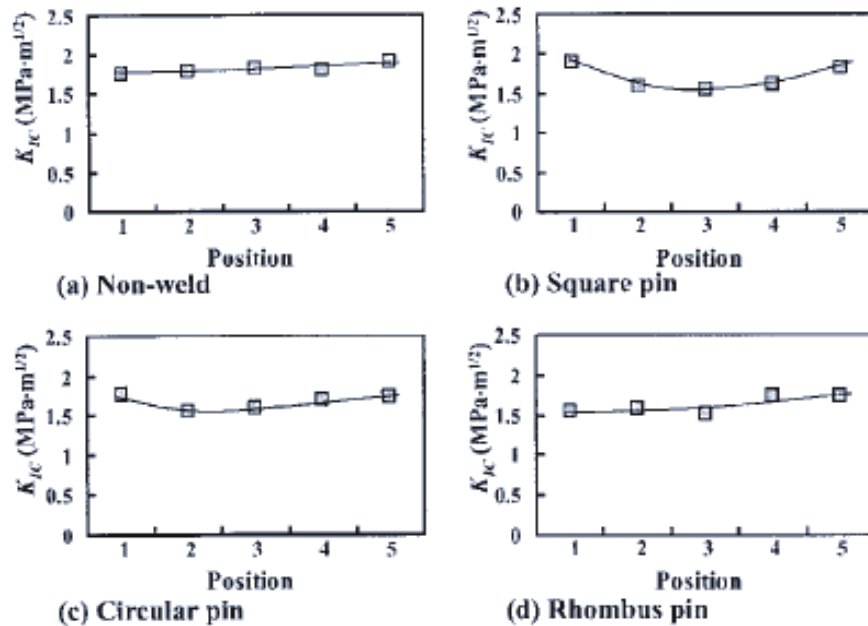


Figure 2.34 Fracture toughness v/s position: (a) nonweld, (b) square pin, (c) circular pin, and (d) rhombus pin [74]

Chen et al [75] investigated the weld-line strength of thin-wall injection molded parts. Their findings also indicate that the strength of the weld-lines increases with decreasing thickness of the wall. This is illustrated in Figure 2.35. They also verify the experimental findings with the help of an analytical model similar to that described by Mekhilef et al [69]. The results of the modeling are illustrated in Figure 2.36.

Feteceau and Stan [61] as part of their recent work, conducted simulations to predict the weld-line defects in injection molding. They also present mold design suggestions to overcome the weld-line defects in the injection molded parts.

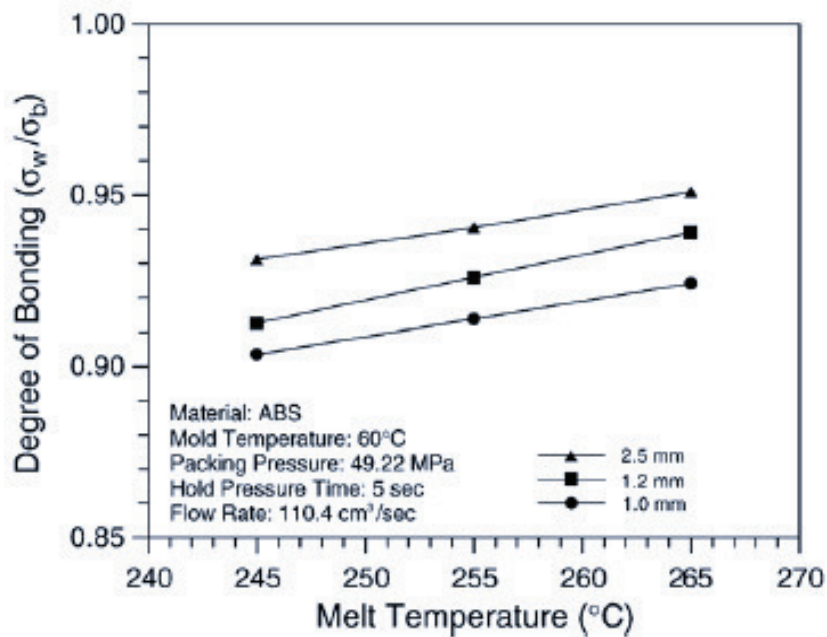


Figure 2.35 Variations of degree of bonding with melt temperature under different plate thickness [75]

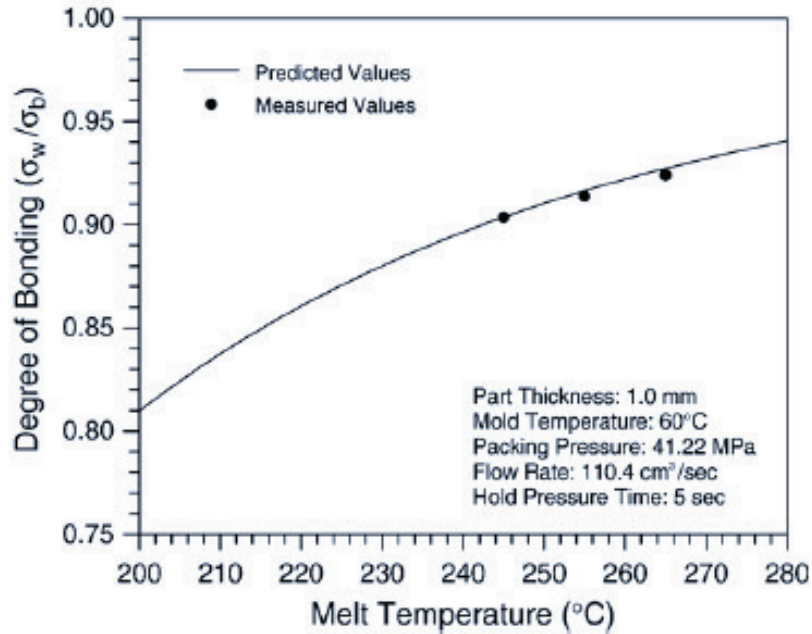


Figure 2.36 Variation of the degree of bonding with melt temperatures [75]

## 2.7 Summary

This chapter summarizes the body of work conducted in the field of

- 1) In-mold assembly
- 2) Prediction of shrinkage in injection molding
- 3) Mold deformation during injection molding
- 4) Fluid structure interaction for non-newtonian polymer flow
- 5) Real-time measurement of injection molding process
- 6) Weld-lines in injection molded part

Several people have reported advances in in-mold assembly. However, most in-mold assembly methods that have been studied, apply to the macroscale. There is no work which addresses the issues that arise in in-mold assembly at the mesoscale.

Prediction of shrinkage is also a problem that has been studied by researchers for several decades now. Recent work has taken into account the effect of mold

deformation on shrinkage of injection molded parts. However, the results reported for shrinkage are predominantly for molds that are made of tool steel. These molds have a significantly higher resistance to deformations when compared to soft mold inserts which are prominent in the in-mold assembly case.

Fluid structure interaction is also a problem which has been studied by researchers for several years now. The focus of the research in this area had been on Newtonian flows. Recent work has extended these to non-Newtonian fluids as well. However, the body of the work deals with infinitely long obstacles in the flow. Hence edge effects are ignored in the drag force prediction on the obstacle which results from the flow around it.

Several researchers have developed experimental methods to measure the melt flow length and the cavity pressure developed inside the mold real-time during the injection molding process. Some researchers have also developed methods to measure the temperature inside the mold. There is also some work on mounting strain sensors on the surface of the mold to measure the effect of machine compliance on the deformation of the mold. However, there is no published work which measures the transient force experienced by the mold pieces due to the flow of the polymer melt. This force is of considerable importance especially when a soft mold piece, as is the case in in-mold assembly, is involved.

Weld-lines are prominent in multi-gated injection molded parts. There are several scenarios where multi-gated molds turn out to be unavoidable. Hence researchers have been studying the strength of weld-lines for several decades. However, there is a dearth of published work which captures the size effects of the molded parts while

predicting the strengths of weld-lines. Also, published models have limited capabilities in predicting the weld-line strengths of crystalline polymers such as LDPE.

## **3 Issues in In-Mold Assembly at the Mesoscale**

### ***3.1 Motivation***

In-mold assembly methods for macro scale rigid body joints have been successfully developed and demonstrated in the past [8, 15-17]. But direct scaling down of macroscale processes to the mesoscale is not expected to be successful. To develop a scalable manufacturing process, it is therefore imperative to realize the limitations of the process at smaller size scales. Hence, to come up with a feasible approach to manufacture functional in-mold assembled mesoscale revolute joints, considerable effort was devoted to identify the unique defect modes associated with direct scaling down of the in-mold assembly process at the macroscale to the mesoscale. This chapter will describe the different challenges associated with in-mold assembly at the mesoscale and discuss the physics behind some of the observed phenomenon.

### ***3.2 Defects Modes at the Mesoscale***

#### **3.2.1 Cavity Shape Change Methods**

In order to carry out in-mold assembly, the cavity shape needs to change after every molding stage. The first stage of the molding process starts with a first stage material being injected into an empty cavity. The material fills the cavity completely and solidifies. Before starting the second stage molding, the cavity shape needs to be altered to create room for injecting the second stage material. The two primary methods for changing cavity shapes are overmolding and morphing cavity method. These methods are described in detail in Chapter 1.

Use of the overmolding strategy requires the first stage components to be molded in a separate first stage mold, ejected from the first stage mold and inserted into the second stage mold consisting of a different cavity shape. At the mesoscale, the maximum dimensions of the individual components of the assembly are of the order of 3-4 mm (Figure 3.1). These components consist of intricate mesoscale features (eg. the mesoscale pin in Figure 3.1). Ejecting these components from one mold and inserting them into a second stage mold requires very delicate handling of the parts. From the manufacturing standpoint, requirement of such delicate handling increases the cycle time and the production cost considerably. Hence the overmolding strategy for in-mold assembly at the mesoscale is highly inefficient and therefore undesirable.

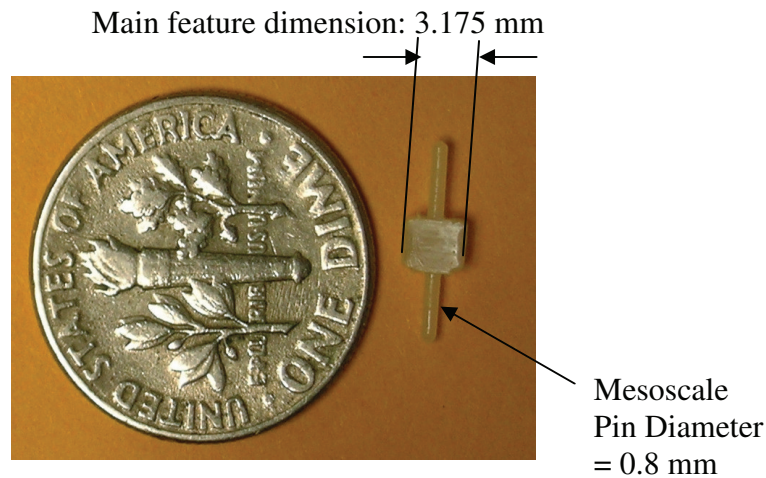


Figure 3.1 Mesoscale Premolded Component

The morphing cavity mold uses mold pieces to create shutoff surfaces in the mold in order to control the cavity shape during first stage and second stage mold filling. Some morphing cavities also use introduction of additional mold pieces to create additional partition surfaces during the first and second stage mold filling. Using only



one of these strategies for changing cavity shape is often inadequate for designing molds for mesoscale in-mold assembly. Hence a combined approach involving moving mold pieces and adding partitions to the initial cavity would produce the best results for creating mesoscale revolute joints.

### **3.2.2 Molding Sequence for Mesoscale In-Mold Assembly**

A CAD model of a revolute joint with mesoscale features which is designed for in-mold assembled can be seen in Figure 3.2. This model was designed using Pro/E Wildfire 3.0 To understand the implications of in-mold assembly at the mesoscale, exploratory experiments were conducted to determine a feasible mold design and molding sequence to manufacture in-mold assembled mesoscale revolute joints. These experiments were conducted using *Hival ABS HG6 Natural* distributed by *Ashland Chemicals Inc.* as the material for the first stage part and *LDPE 722* distributed by *Dow Plastics* as the material for the second stage part. ABS was chosen as the first stage polymer because it was more rigid compared to other available polymers. Hence it was able to withstand higher forces. LDPE was an appropriate choice for the second stage polymer since its translucent nature allowed visualization of the plastic deformation in the premolded component. Also it has a lower melting temperature compared to ABS. Hence it did not thermally soften the premolded component during second stage filling. Some of the significant defects which occurred due to direct scaling of the in-mold assembly process for manufacturing macroscale revolute joints were recorded and are described below.

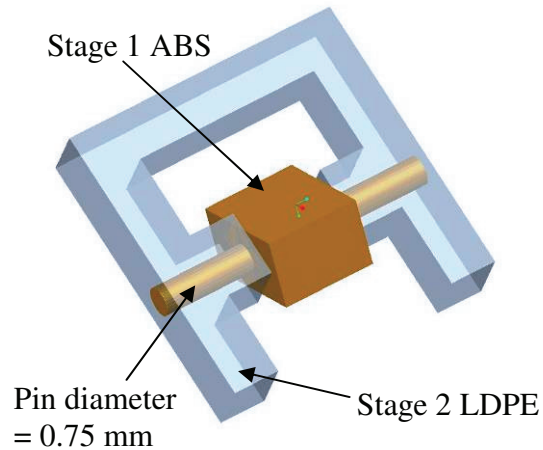


Figure 3.2 Design of in-mold assembled revolute joint.

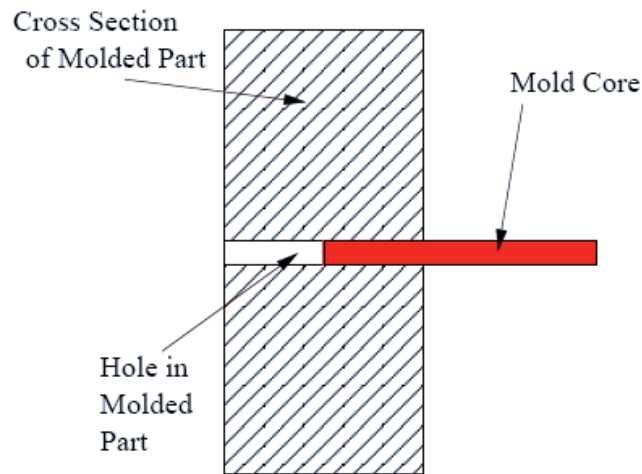
In order to have a smooth running revolute joint at the macro scale, the pin is usually molded inside the cavity such that the pin shrinks radially to provide the required clearances. The cavity in the premolded component is made by using a side action mold insert (SAMI) of the requisite diameter. The mesoscale feature on the premolded component is referred to as the pin. Cavity refers to the mesoscale cavity in the premolded component. The mold piece used for molding the mesoscale pin is referred to as the side action mold cavity (SAMC).

### 3.2.2.1 Using a SAMI with Small Diameter

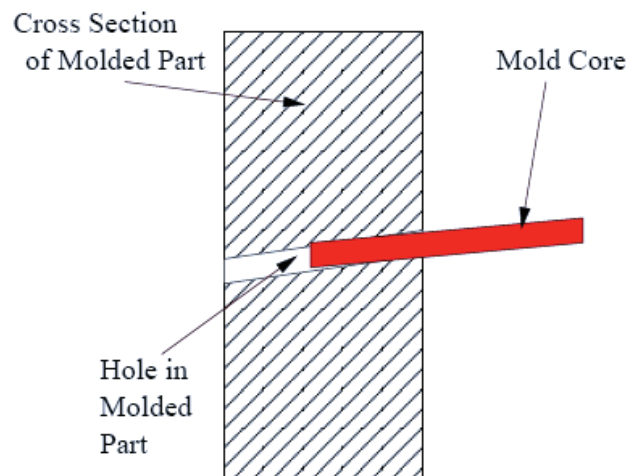
As described previously, in-mold assembly at the macroscale involves molding the cavity in the first stage and molding the pin in the second stage. In the first experiment, this macroscale process was directly scaled down to the mesoscale and the corresponding defects were noted.

Molding the cavity in the first stage requires the use of a side action mold insert (SAMI) as a mold piece. For making the mesoscale joint using this strategy the steps illustrated in Figure 1.5 were scaled down directly. After careful consideration of the

part design, it was noted that making a SAMI with small diameter would be an expensive process. Also a SAMI with a small diameter poses alignment problems and was prone to failure due to forces applied by the injection speed and pressure. Figure 3.3 illustrates the problem posed due to inaccurate alignment of the SAMI. Figure 3.4 shows a defective component manufactured due to deformation of the SAMI.

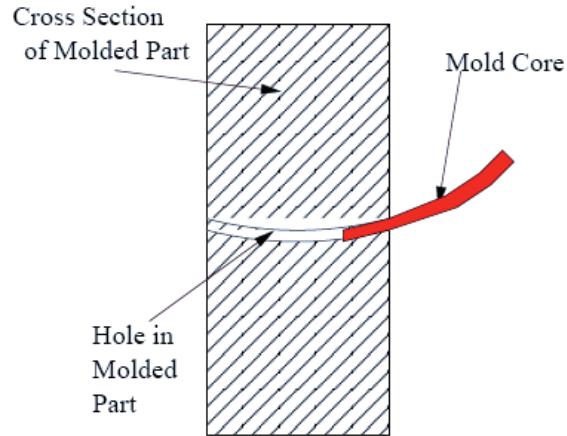


(a) Accurate SAMI positioning and movement

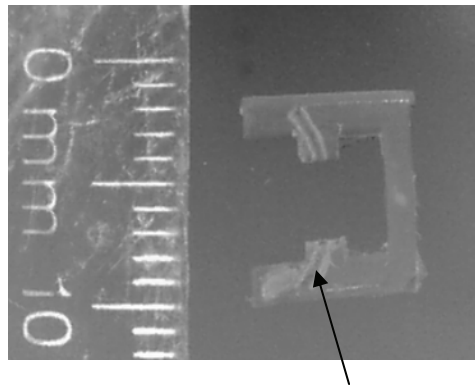


(b) Inaccurate SAMI positioning

Figure 3.3 Schematic representation of inaccurate alignment of SAMI



(a) SAMI plastically deforms due to high temperature and pressure



Defomed meso scale features

(b) Example of Defective Component

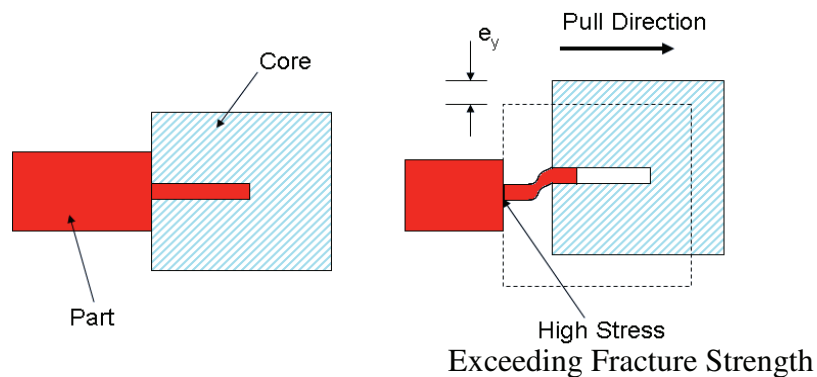
Figure 3.4 Deformation of side action mold core due to injection pressure

### 3.2.2.2 Reversing the Molding Sequence

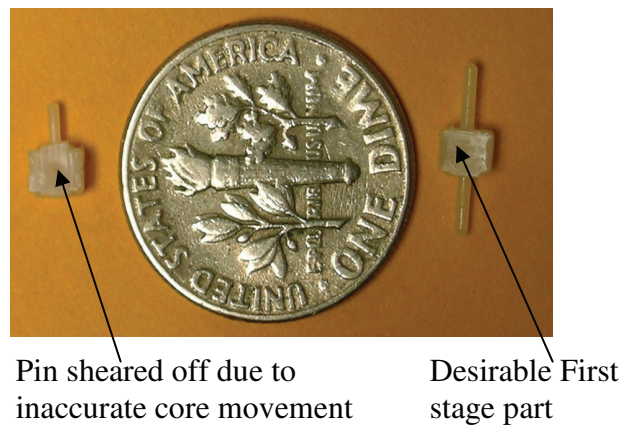
In the next experiment, the molding sequence was reversed to mold the mesoscale pin first and then mold the cavity. Making a side action mold cavity (SAMC) with a small diameter is much easier than making a side action mold core insert (SAMI) with a small diameter. Hence, this method simplifies the mold design. Also SAMC is less fragile as compared to the SAMI. Hence the mold pieces do not have to be

handled as delicately. This reduces the handling cost and therefore the overall production cost.

When using this sequence, two significant defects were observed. The first defect was due to inaccurate movement of the SAMC which resulted in shearing of the mesoscale pin which resulted in molding of defective parts. This defect is illustrated in Figure 3.5.



(a) Shearing of Meso Scale features due to inaccurate core movement



(b) Example of Defective Component

Figure 3.5 Inaccurate side action resulting in shearing of mesoscale core

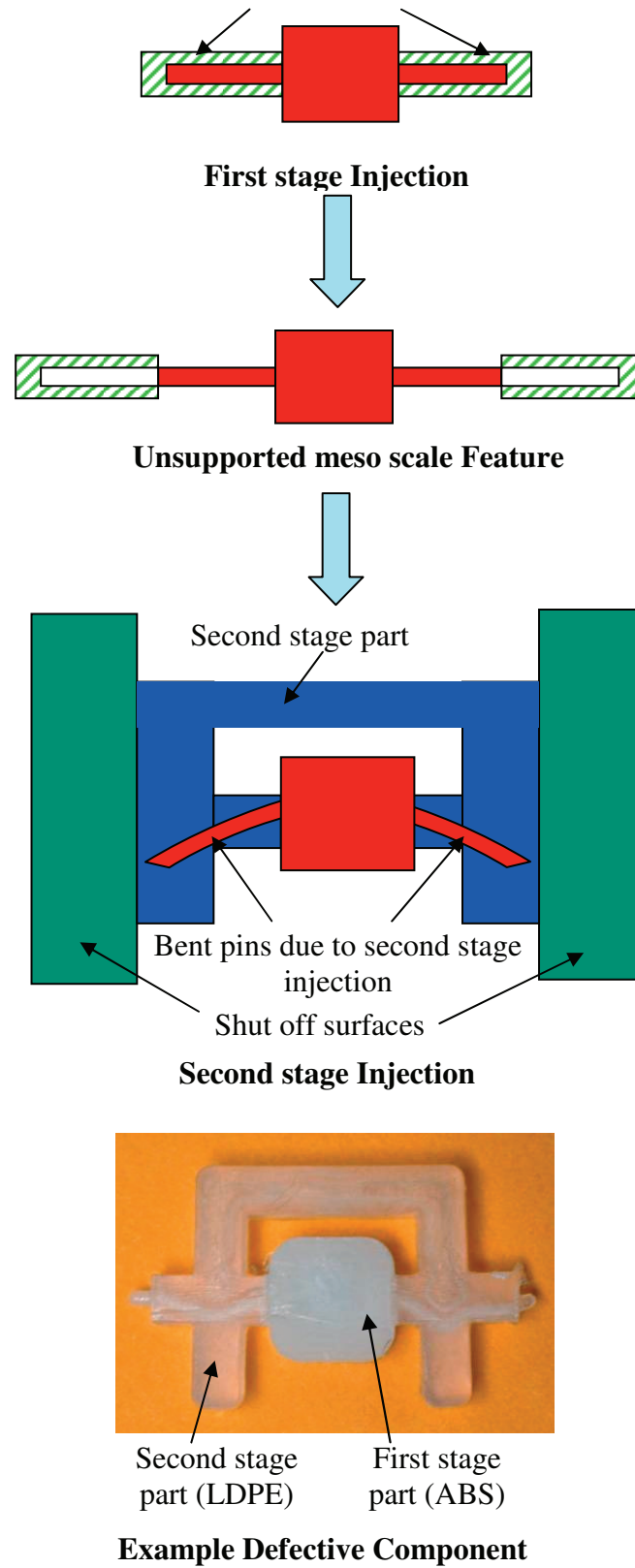


Figure 3.6 Deformation of mesoscale core due to second stage injection

Another significant defect was observed to be the plastic deformation of the premolded mesoscale core when the second stage part with the cavity was injected. During the exploratory experiments, the core was designed to be left as an overhanging structure. When the second stage polymer was injected, the flow induced forces on the mesoscale core generating bending stress that was sufficient to exceed the strength of the material and separate it from the base. Figure 3.6 shows a defective component resulting from the plastic deformation of the premolded component. To overcome the defect modes identified in this section, we developed a new mold design for mesoscale revolute joints. The new mold design requires using a different approach than the simple scaling down of the macro scale molds as discussed above.

### **3.2.3 Summary**

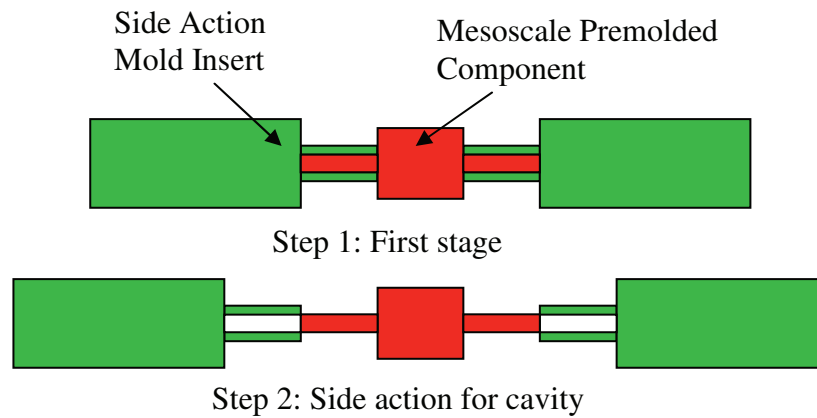
This section described the different defect modes associated with in-mold assembly at the mesoscale. From the experiments it is clear that these defects are specific to components at the mesoscale. Among the defect modes identified in the previous section, most defects can be resolved by implementing simple changes to the mold design.

In order to overcome pin shearing due to inaccurate movement of the mold pieces, a simple modification to the SAMI as illustrated in Figure 3.7 suffices. The original design of the SAMI consisted of a mold insert with a square cross section. Due to clearance between the SAMI and the mold, this design caused inaccurate movement of the SAMI when it was retracted. However when a combination of a cylindrical cross section and a square cross section of the SAMI as illustrated in Figure 3.7 (a) is

used, the clearance between the SAMI and the mold cancel out causing an accurate movement of the SAMI when it is retracted.



(a) Side Action Mold Insert (SAMI)



(b) Process sequence for molding mesoscale premolded components

Figure 3.7 Side action mold insert (SAMI) used for accurate movement of mold pieces

However, one of the most important defect modes noted by the experiments was the plastic deformation of the premolded component. We understand that macroscale in-mold assembly processes can not be directly scaled down to manufacture mesoscale in-mold assembled revolute joints. However, in order to select the right in-mold assembly process, it is important to establish the size scales at which the defects start occurring. This information will help researchers and manufacturers choose the right in-mold assembly process for the application. The following sections will describe the



experimental results and computational models that were developed to establish the effect of the size of the premolded component on the defects associated with using macroscale in-mold assembly processes.

### **3.3 Experimental Methods for Understanding Size Effects**

In order to develop an understanding of the relationship between the size of the mesoscale pin on the premolded component and its plastic deformation during second stage injection, experiments were conducted by varying the size of the pin while keeping the geometry of the flow constant. The deformation of the mesoscale pin was then measured and plotted. Due to the inherent symmetry in the premolded component, a geometry consisting of only one mesoscale pin was used for the experiment. This geometry is illustrated in Figure 3.8. These components were molded using *Hival ABS HG6* distributed by *Ashland Chemicals*.

The second stage polymer was injected in the cavity as illustrated in Figure 3.9. *LDPE 722* distributed by *Dow Plastics* was used as the material for the second stage part. The experiments were repeated for different pin diameter  $d$ . The pin diameters were fixed at 0.79 mm, 0.99 mm, 1.19 mm, 1.39 mm and 1.59 mm. 5 samples were created for each pin diameter. At the end of the filling for each experiment, the assembly was ejected from the mold and the final plastic deformation of the pin in the premolded component was measured and recorded.

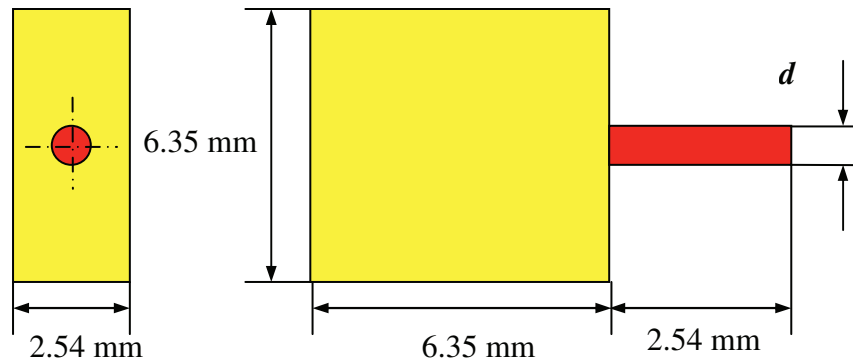


Figure 3.8 Premolded component for experiments

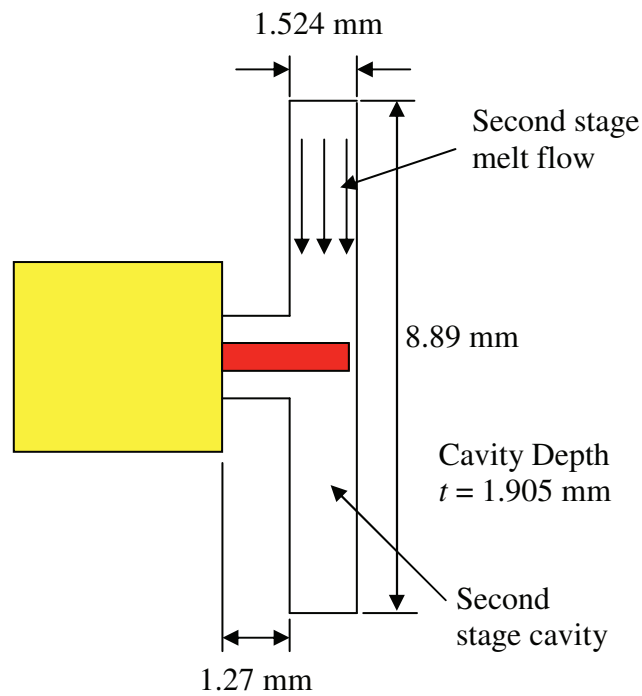


Figure 3.9 Second stage injection

During the second stage mold filling, the polymer melt flow applies a uni-directional force on the premolded component which results in the plastic deformation of the premolded component. In order to determine the whether the premolded component would deform plastically due to the second stage melt flow, it is imperative to develop an understanding of the force applied by the second stage

polymer melt flow on the premolded component. To measure this force experimentally, a surrogate strain sensor based on a cantilever beam made of Aluminum was developed.

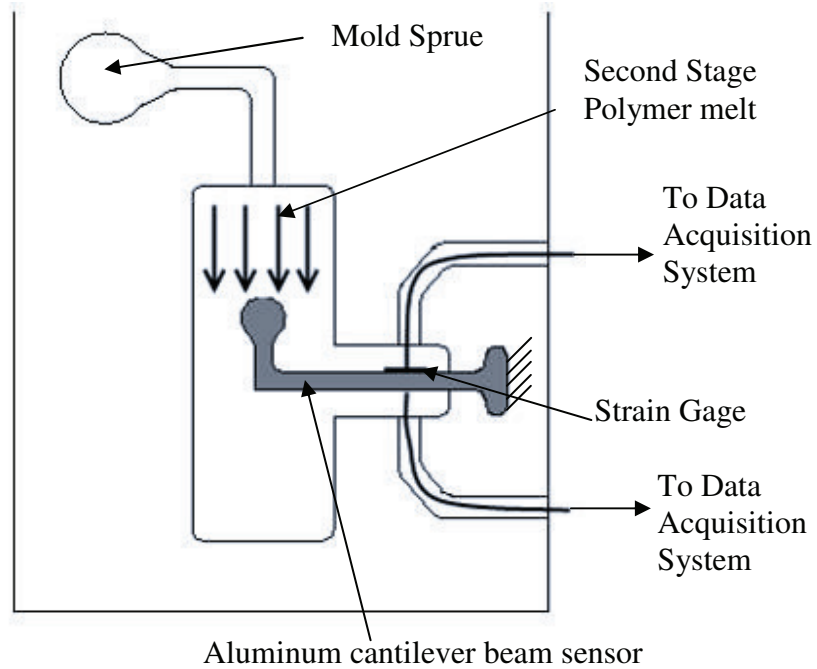


Figure 3.10 Online monitoring system for measuring transverse force on premolded component

This setup is illustrated in Figure 3.10. A block diagram of the experimental setup and its connection to the data acquisition system is illustrated in Figure 3.11. The Aluminum cantilever beam sensor with the strain gage mounted is illustrated in Figure 3.12. *031CF* strain gages procured from *Vishay Micro-Measurements* were used for the experiment. The gage factor of the strain gage was *2.05* and the grid resistance was *350 Ohms*. The force is applied on the cylinder in the melt flow field as illustrated in the figure. The force applied on the cylinder by the second stage polymer melt flow causes the aluminum cantilever beam sensor to deform resulting in an effective strain reading seen by the strain gage.

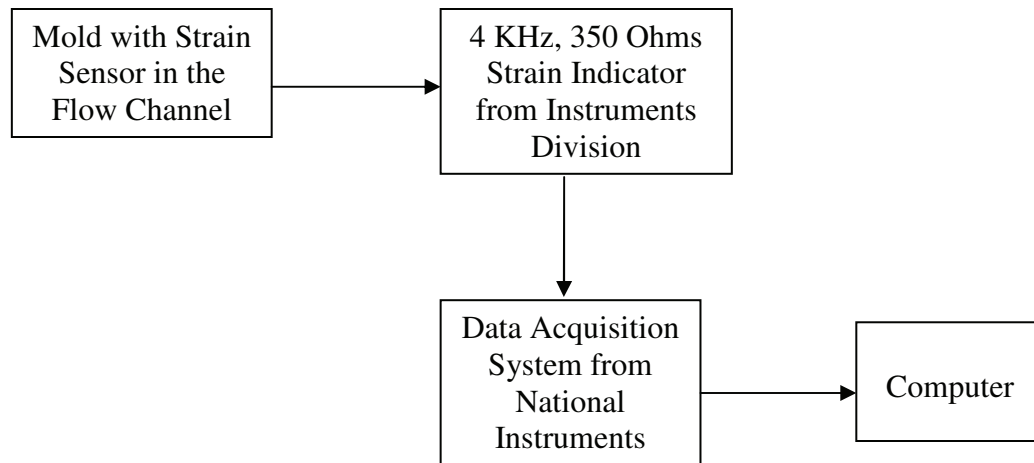


Figure 3.11 Block diagram of experimental setup for force measurement

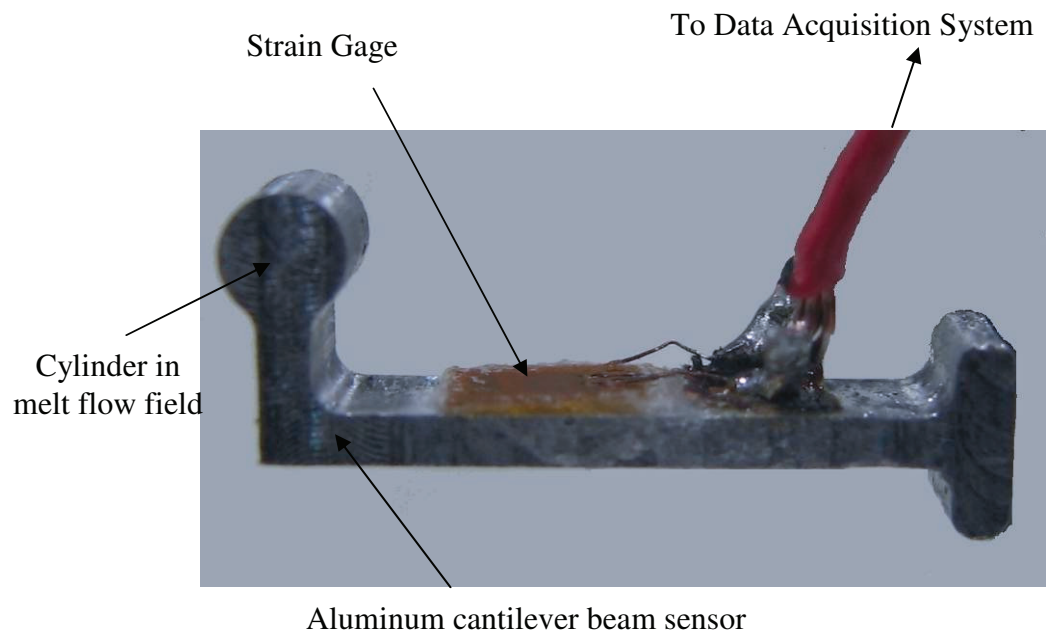


Figure 3.12 Surrogate strain sensor made of a metallic cantilever beam

This strain is recorded by a data acquisition system at a frequency of 4 KHz. Hence the force on the strain sensor is recorded as a function of time. The experimental setup used for force measurement becomes intrusive from the in-mold assembly

perspective as soon as the second stage melt flow front comes in contact with the cantilever beam portion of the Aluminum sensor. Hence the strain measurements after this point were not considered for force measurement purposes.

The deformation of the mesoscale pin in the premolded component was noted to be nonlinear since there was very little elastic recovery after disassembly of the premolded component and second stage part. Hence for developing a predictive model for the plastic deformation it was necessary to establish the nonlinear structural material properties of the premolded component in flexure. Since the injection temperature of the second stage melt is greater than 120°C, it was important to consider the change in material properties of the premolded component, ABS, with temperature.

To accomplish this, ABS beam with a square cross section was injection molded. The geometry of the beam used is illustrated in Figure 3.13. This beam was then loaded in flexure to obtain the force versus deformation curve for multiple specimens. Force versus deformation data were recorded for four different temperature profiles.

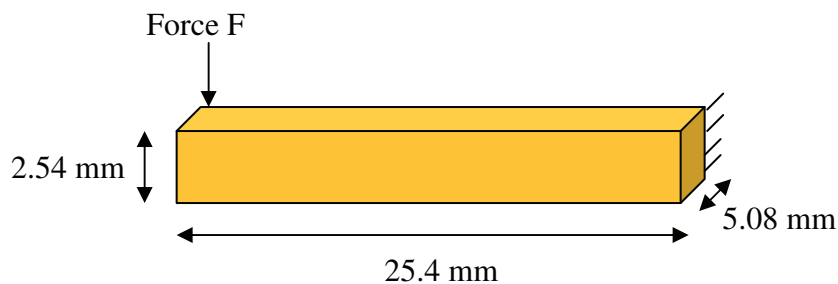


Figure 3.13 ABS beam loaded in flexure for determination of non-linear material properties

Finally to obtain the stress-strain behavior of ABS, we calibrated the experimental data for the force versus deformation with a finite element analysis in ANSYS 11.0 for the same geometry.

### ***3.4 Generalized Framework for Modeling Interaction between Melt Flow and Premolded Component***

This section discusses a generalized modeling framework that will be adapted to the specific class of in-mold assembled mesoscale revolute joints developed as part of this work.

#### **3.4.1 Definition of Deformation Problem for Premolded Components**

During the second stage molding, the melt enters the mold at high velocity impacting the premolded component and then flows around it. Once the mold is filled the flow stops and the melt solidifies. The flow of the melt can induce mechanical loading on the premolded component due to viscous and/or impact forces. It is worth noting that the melt is a non-Newtonian fluid and the mechanical loading occurs mainly under transient flow conditions. In addition, the premolded component also gets heated up by the melt entering the mold cavity. As a result of the heating the premolded part may soften and its strength may reduce. As a result of the time-varying thermo-mechanical loading, the premolded component undergoes elastic and under some conditions plastic deformation. In summary, this problem involves time-varying non-Newtonian flow, heat transfer, and elastic-plastic deformation. Solving

this problem in full generality is almost intractable and may not be necessary from the manufacturing point of view.

From the manufacturing point of view, we are interested in achieving reasonable accuracy in estimating the plastic deformation for the parts that are considered acceptable or border-line defective. These parts should have very low levels of plastic deformation of the premolded components. Defective parts on the other hand have relatively large levels of plastic deformation of the premolded components. From the manufacturing point of view, there is not much to be gained in accurately predicting the deformation for highly defective parts. Usually, it is good enough to know that the part will deform significantly and hence be defective. Moreover, in order to ensure reasonably good manufacturing quality control, an appropriate factor of safety will need to be used to limit the influence of deformation. So an approach that overestimates the deformation for small deformation cases will be considered an acceptable modeling approach from the manufacturing point of view. We will now try to develop a simplified modeling approach to meet the needs of the manufacturing community.

### **3.4.2 Mechanics-based Modeling of Plastic Deformation in Premolded Components**

There are two important issues for developing a mechanics-based model of the plastic deformation of premolded components: (1) appropriate material properties for the premolded component, and (2) the boundary conditions that are experienced by the premolded component during the melt flow. First consider the material properties. There are two effects that can complicate the modeling approach due to material

properties: (1) time-dependent deformations (i.e., viscoelasticity), and (2) thermal softening. For either of these effects, it is necessary to have sufficient time for the component to heat up and soften and for the deformations to accumulate. In polymers, both of these effects are diffusion-controlled, therefore the time scales are similar. At the mesoscale, the time scale associated with the melt completely filling the mold is relatively short. In most cases, volumetric flow rates of  $12,000 \text{ mm}^3/\text{sec}$  and mold cavity volumes on the order of  $15 \text{ mm}^3$  result in mold cavities being completely filled in one second or less. The premolded part will experience peak loading shortly after encountering the melt, since the loading will begin to approach hydrostatic equilibrium as the cavity is filled. So the actual time in which the premolded component deforms can be substantially less than the mold filling time. In this dissertation, polymers that have low thermal conductivity are of primary interest, so only slight changes in thermal softening and negligible time-dependent behavior is expected. Therefore, it is reasonable to expect that incorporating a detailed model of the thermal history and associated change in time-dependent deformations of the premolded component during melt flow is not necessary, and a simpler approach only considering the thermal softening effects can suffice.

#### **3.4.2.1 Material Properties of Premolded Component**

One approach to approximating thermal softening on material properties is to only consider material properties at the maximum temperature rise the premolded component will experience. These material properties can be determined by estimating the temperature of the first stage part towards the end of the mold filling and then experimentally determining the stress-strain curves at the estimated



temperature using an appropriate specimen. This approach will be necessary only for those materials that exhibit significant thermal softening at the estimated temperature towards the end of mold filling. An alternative approach to approximate thermal softening effects is to assume the stress-strain curve is the same as it is at room temperature, but the effective load on the premolded component is increased to account for the higher plastic deformation levels due to thermal softening. This can be accomplished by molding a specimen of suitable geometry, measuring deformation, and then estimating the effective loads that lead to the observed plastic deformations. Each of these approaches is valid for different conditions. The validity of the approach would depend on the choice of polymers, the injection temperatures and the geometry of the mold. Hence the approach that would be most applicable to the respective problem should be determined based on these conditions. This approach is discussed in further detail in Section 3.5 for mesoscale revolute joints.

#### **3.4.2.2 Boundary Conditions on Premolded Component**

The boundary conditions on a premolded component result from the interaction of the component with the melt flow. As the melt impacts the premolded component and starts flowing around it, the premolded component starts experiencing loading in the direction of flow. This load builds up from zero to a high level and then drops as the pressure equilibrates around the component upon the mold filling. Rather than modeling the time dependent load, it is possible to just use the highest load that the component experiences during the melt flow. Usually, the dynamic pressure heads associated with melt flow are quite low at the meso-scale. For a flow rate of 12 cc/s inside the mold cavity, the dynamic pressure head due to the flow of the second stage

melt flow is about 0.65 bar. So, the effect of impact can be ignored and only transient flow modeling is needed to determine the highest drag force on the component and use it to generate the pressure distribution. In case of simple geometries, the overall drag force can be estimated on the component and distributed uniformly on the surface of the component facing the flow to estimate deformation. Whether the uniform pressure distribution would be accurate or not can be determined by applying a uniform pressure distribution in the mechanics-based model and then matching the estimated plastic deformation trends with the experimentally observed deformation trends. In case of more complex geometries, it will be necessary to accurately model the non-uniform pressure distributions. A transient computational fluid dynamics (CFD) simulation around the premolded component can be used to provide the profile for the pressure distribution. This flow modeling strategy adopted for the mesoscale revolute joint is described in Section 3.5.1.

Once the pressure distribution that results from the melt flow is determined, it is possible to apply it as a boundary condition on the premolded part using appropriately measured material properties. To solve the mechanics-based boundary value problem and estimate the plastic deformation of the premolded component, Finite Element Analysis (FEA) is employed. As the premolded component deforms during the second stage injection, there is relative movement between the first stage part and the mold pieces. Hence, friction between the first stage part and the mold pieces will play some role. However, the effect of friction would be negligible for low deformations and hence it can be ignored. This approach is described in detail in Section 3.5.2.

### ***3.5 Modeling Premolded Component Deformation***

To develop a predictive model for the plastic deformation of the mesoscale core due to varying support lengths, several modeling parameters need to be determined. These are: (a) the effective force experienced by the mesoscale core in the premolded component as the second stage melt flows around it and (b) the nonlinear deformation of the premolded component due to the applied force. This section will describe the strategy used to develop a predictive model for answering these two questions. This model can be used by researchers and manufacturers to predict the expected deformation of the premolded component based on the material and geometry used for in-mold assembly.

#### **3.5.1 Force on Premolded Component**

The flow of the second stage polymer around the pin on the premolded component results in a drag force which is responsible for its plastic deformation. This drag force can be modeled by assuming a fluid flow around a cylinder. The physics of the injection molding flow problem is significantly different from a steady flow of a fluid around a cylinder. In steady state formulations, a continuous stream of fluid is assumed to be flowing at a constant flow rate for a sufficiently long time. However in the injection molding case, unlike in steady state formations, the fluid or the polymer melt encounters a mold wall downstream of the cylinder. As soon as the fluid flow reaches the mold wall, a steady back pressure develops in the flow leading to equilibration of the drag flow forces on the cylinder. Hence in order to obtain an appropriate estimate of the forces on the cylinder, it is important to model the transient flow of the polymer melt around the cylinder. Hence we only considered the

flow time before the polymer melt reaches the mold wall downstream of the cylinder. This time is usually equal or smaller than as the fill time for the polymer melt.

The pressure acting on the mesoscale core was estimated using the commercial CFD code known as FLUENT 6.3.26 [87]. A three dimensional model of the mold cavity for the second stage injection was constructed using a cylindrical cross section to represent the mesoscale core of the first stage part. The flow stream inside of the mold cavity is illustrated in Figure 3.14. The flow stream was meshed using a 7 element thick boundary layer on the flow boundaries around the mesoscale core and the mold walls. Each element layer along the boundary constituted of 30 elements along the cylinder and 160 elements along the mold walls. The remaining volume of the flow stream was meshed using a uniform triangulated mesh with 35 elements along the edges. A convergence study was conducted by comparing the solutions for different mesh sizes to determine that the meshing was numerically adequate.

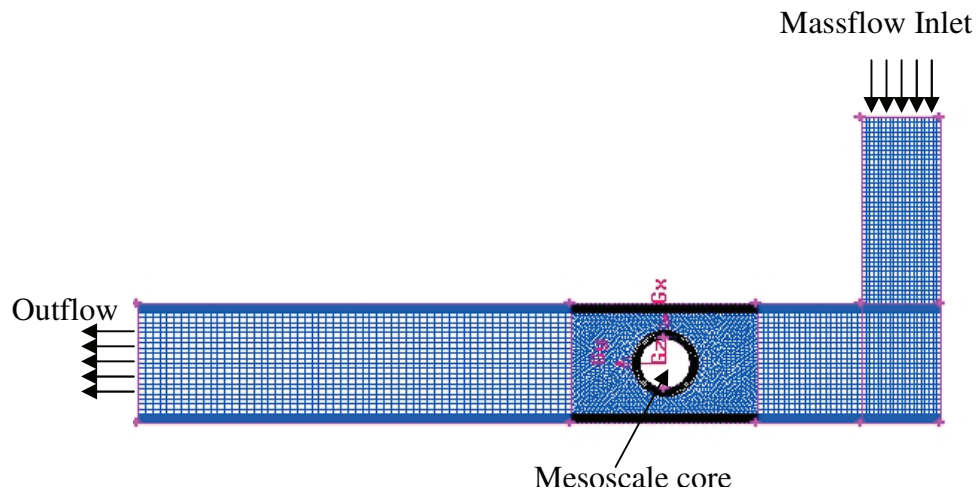


Figure 3.14 Finite element mesh for flow simulation to determine effective pressure on mesoscale core

A transient, mixture flow was used in the CFD model. The mold cavity consisted of air with a volume fraction of 1 at time  $t=0$ . An initial condition of 0.0064 kg/s was then prescribed at the inlet for the LDPE, which corresponds to the constant volumetric flow rate of 12 cc/s observed in the mold during second stage injection. The face downstream of the mesoscale core was described as a uniform outlet flow. The flow of the LDPE is described as a non-Newtonian, shear thinning flow which is described as a power law viscosity flow shown in equation 3.1 [60, 80, 88]:

$$\mu = K \dot{\gamma}^{n-1} \quad 3.1$$

The properties used for modeling the flow of LDPE are tabulated in Table 3.1

Table 3.1 Flow properties of LDPE [59]

<b>Density</b>	525 kg/m <sup>3</sup>
<b>k</b>	11220
<b>n</b>	0.41
<b>Minimum Viscosity</b>	5 Pa-s
<b>Maximum Viscosity</b>	6300 Pa-s

Each time step in the simulation corresponded to  $10^{-4}$  s in real time. We ran the simulation for 20 time steps. By the 16th time step the LDPE flow hit the mold wall downstream of the mesoscale core. In order to obtain the effective pressure on the mesoscale core as a function of time, we conducted another simulation with a finer timestep of  $10^{-5}$ s. The starting time for this simulation was 0.0012s. The solution for the coarse solution at this timestep was used as the initial condition. We ran this simulation for 50 timesteps. The force experienced by the mesoscale core is a sum of the pressure forces and the viscous forces of the flow. This force is averaged over the profile of the mesoscale core to calculate the effective pressure experienced by it. As mentioned previously, the CFD simulation is valid only till the LDPE flow reaches

the mold wall downstream of the mesoscale core. Subsequently the force on the mesoscale core equilibrates causing a drop in the effective pressure experienced by it. Hence the maximum effective pressure experienced by the mesoscale core before this time, is taken into account for calculating the plastic deformation of the mesoscale core.

### 3.5.2 Non-linear Deformation of Premolded Component

To determine the effective plastic deformation of the premolded component due to the force applied by the polymer melt flow, a finite element simulation in the commercial software ANSYS 11.0 was implemented as follows [89].

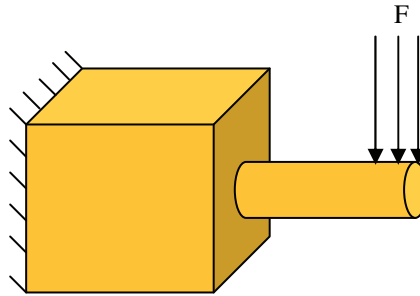


Figure 3.15 Force modeling on the premolded component.

The steps employed for the solution were as follows:

- 1) The premolded component was modeled and meshed in ANSYS 11.0. For the meshing the pin was line sized into 30 elements along its length and 12 elements along the diameter. This line sizing was used to obtain the final mesh using a tetrahedral element (SOLID92).
- 2) Displacement constraints in all directions were applied to the cuboidal portion of the premolded component.

- 3) An equivalent pressure based on the injection flow rate was applied on the top half core on 1/3<sup>rd</sup> of the overall length as shown in Figure 3.15. This equivalent pressure was determined using the flow simulation described in the previous subsection.
- 4) Non-linear material properties of the premolded component (ABS) were applied to the model. These properties were obtained from the flexural experiments that are described in the previous section.
- 5) This problem was solved using automatic timestepping with a designated number of maximum timesteps in ANSYS 11.0.
- 6) The mesh size and timestep size was varied until the solution converged to acceptable tolerances in the overall deformations.

### **3.6 Results and Discussion**

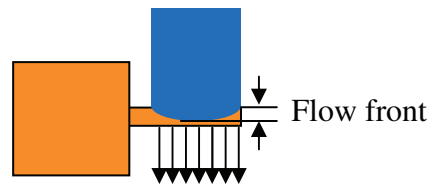


Figure 3.16 Flow front progression

In order to develop an insight into the cause for the plastic deformation of the premolded component during second stage polymer melt flow, the first part of the problem is to understand the force due to the second stage melt flow. Experiments were conducted to measure these forces realtime using the setup described in section 3.3. These forces were measured as the flow front progressed. The flow front progression is illustrated in Figure 3.16. The results of this experiment to measure the realtime strain on the Aluminum strain sensor are illustrated in Figure 3.17.

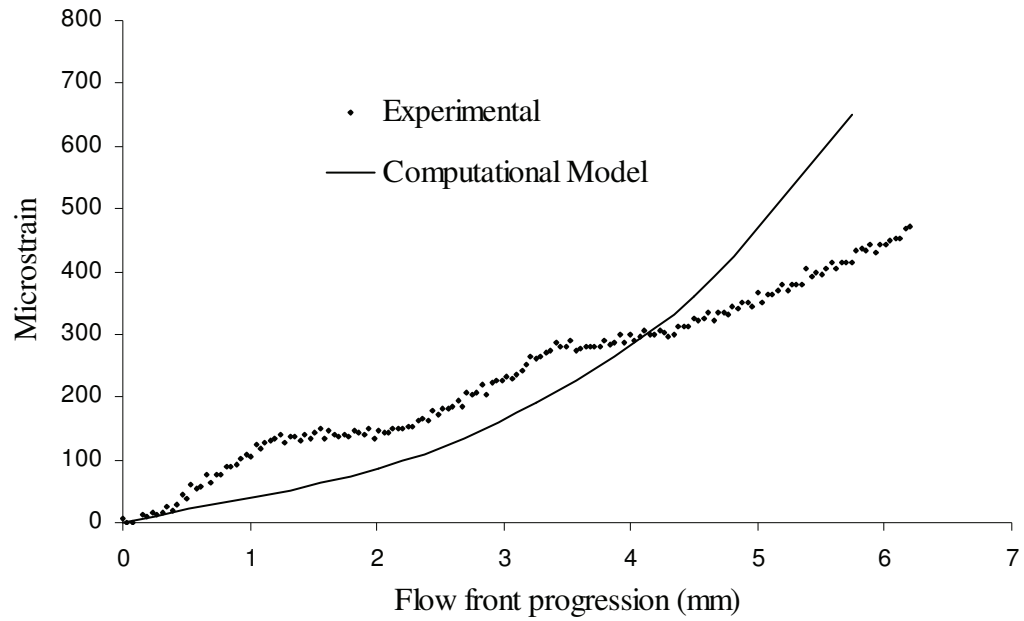


Figure 3.17 Strain on premolded component as flow front progresses

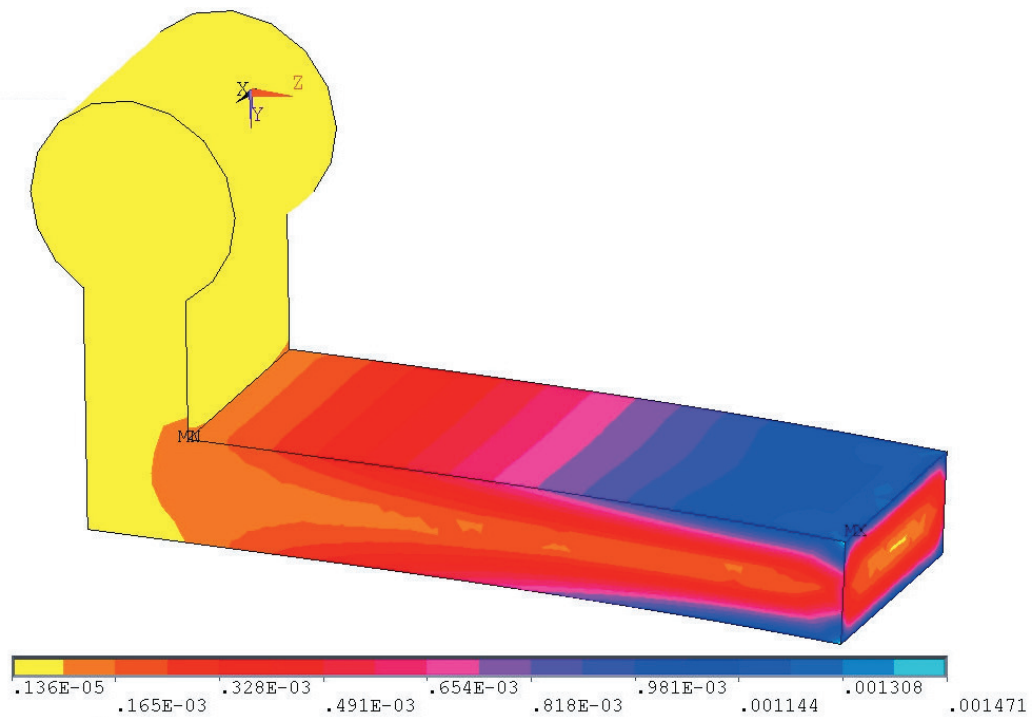


Figure 3.18 Sample result of FE simulation to compute strain on sensor



A computational model to predict the force on the Aluminum sensor due to the second stage polymer melt flow was also developed using the strategy described in Section 3.5.1. This computational model revealed that the force on the premolded component increases with increasing velocity of the second stage melt. When the volumetric flow rate of the polymer melt flow was doubled from 3 cc/s to 6 cc/s, the effective force experienced by the premolded component went up by a factor of 2.75. The figure shows a comparison between the experimental data obtained and the force prediction using the computational modeling using FLUENT 6.3.26 and ANSYS 11.0. Figure 3.18 shows a sample result of the FE simulation in ANSYS 11.0 to computationally predict the deformation of the Aluminum strain sensor due to the force predicted from the flow simulations in FLUENT 6.3.26. The model seems to be in reasonable agreement with the experiments.

As can be seen in the figure, the model predicts the force on the Aluminum strain sensor within reasonable accuracy for low values of flow front progression. However as the flow front progresses beyond the end of the cylinder, the model overpredicts the force on the Aluminum sensor. This is attributed to the specific modeling strategy adopted in the flow simulations to predict the force on the sensor. The flow simulation assumes that the sensor is rigid and does not actively deform due to the force applied. However in the real scenario, the sensor deforms due to the applied force. Hence the actual resulting force on the sensor would be expected to be less than that predicted by the flow simulations. However from the manufacturing perspective, we are not interested in predicting the force on the premolded component accurately for higher force levels. This is because high force levels produce high levels of plastic

deformation of the premolded components. These high levels of plastic deformation are of limited or no interest to the manufacturing community since the in-mold assembled joints thus produced are defective. Hence since the computational model predicts the force and deformation within reasonable accuracy for low values of deformation it can be seen as an efficient strategy for the problem under consideration.

The results of the experiment to determine the material properties of the premolded component are illustrated in Figure 3.19. It shows the material behavior for four different temperatures. As seen in the figure, there is no significant change in the linear portion of the stress-strain behavior (flexural modulus) of the material with temperature for 25°C, 33°C and 50°C. The differences in the nonlinear portion of the stress-strain curve can be attributed to some amount of thermal softening at elevated temperatures. On the other hand, the flexural modulus of the material was observed to be significantly lower at 62°C. This behavior is expected since this temperature is above the Vicat softening point for ABS (around 55°C).

From this experiment, we were able to conclude that the material properties of the first stage polymer are not affected significantly for a temperature change of 10-15°C. The rise in temperature of the first stage part is not expected to be more than 10-15°C since, (a) ABS is a poor conductor. So it has a high resistance to temperature change. (b) The effect of the temperature change needs to be considered only during filling. The time in which filling is completed is negligible when compared to the amount of time required to heat ABS to a high temperature. Considering these factors, we felt

that the change in material properties of the polymer due to thermal softening could be ignored in this case.

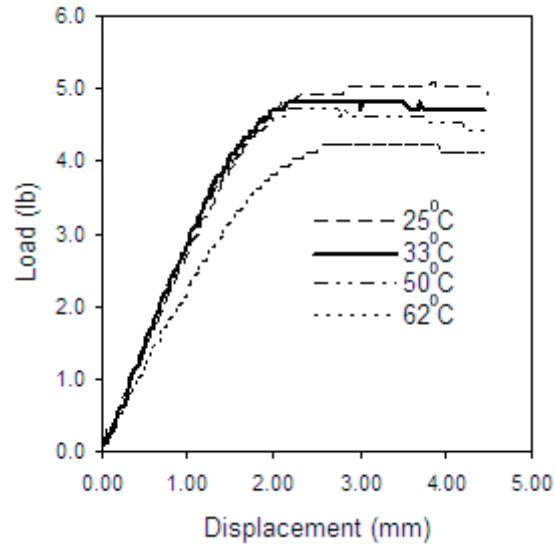


Figure 3.19. Load versus deformation for the ABS beam

Hence the results of the experiment at 25°C were used to determine the non-linear stress strain behavior of the ABS premolded component using the commercial FE solver ANSYS 11.0. A multilinear stress strain behavior was used to describe the properties of ABS. They are listed in Table 3.2.

Table 3.2 Nonlinear stress strain properties of ABS

Stress (Pa)	Strain
0	0
1.80E+07	8.00E-03
3.60E+07	1.60E-02
5.20E+07	5.00E-02
6.00E+07	1.25E-01
6.20E+07	1.53E-01
6.36E+07	1.70E-01
6.42E+07	1.88E-01
6.53E+07	2.81E-01

The experiments to measure the plastic deformation of the premolded component of different pin sizes were conducted on a Milacron Babyplast injection molding machine using the processing parameters described in Table 3.3.

Table 3.3 Injection molding parameters

	Stage 1	Stage 2
<b>Material</b>	ABS	LDPE
<b>Injection Temp.</b>	220°C	130°C
<b>Injection pressure</b>	600 bars	600 bars
<b>Cooling time</b>	15s	5s

The experimental components after injection of the second stage polymer melt flow around the premolded component were ejected from the mold. The overall plastic deformation  $\delta$  of the premolded component was then measured using the strategy illustrated in Figure 3.20. Figure 3.21 shows the experimental results of the ratio of the plastic deformation and pin diameter of the premolded component for different pin diameters. The results indicate that the deformation drops considerably for increasing pin diameters.

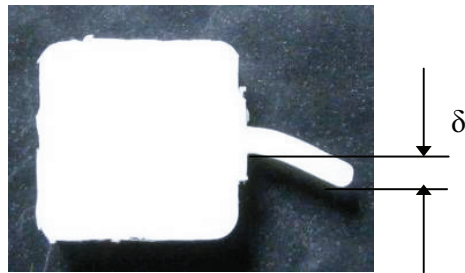


Figure 3.20 Measurement of plastic deformation of premolded component

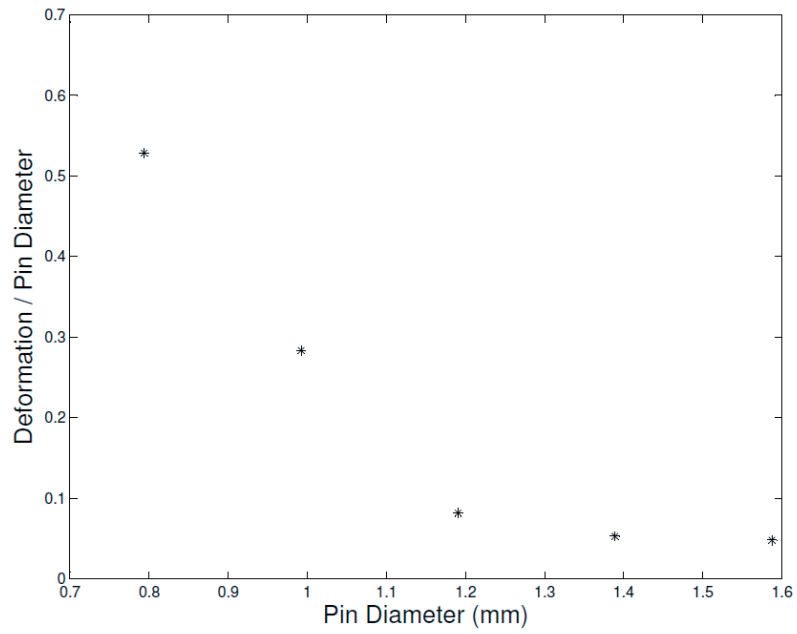


Figure 3.21 Plastic deformation of pin with varying diameter of the pin

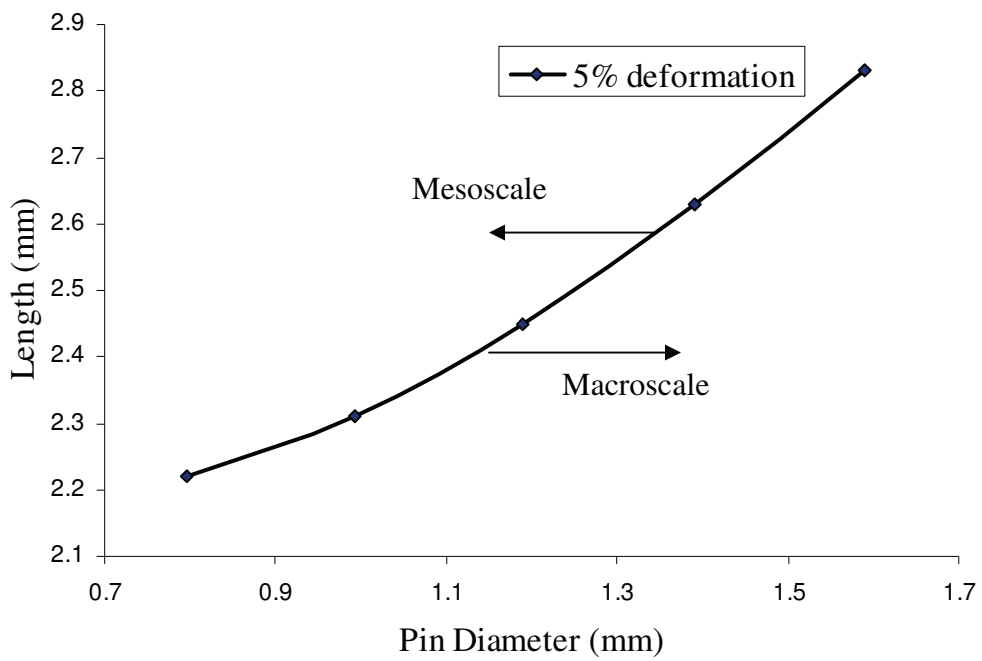


Figure 3.22 Distinction between macroscale and mesoscale from the in-mold assembly perspective

From the experimental results for plastic deformation of the pin, the force per unit length on the premolded component due to the second stage melt flow could be computed using structural simulations in ANSYS 11.0. Using this force per unit length, structural simulations were conducted by varying the length of the pin to compute a clear distinction between mesoscale and macroscale based on the pin diameter and the length of the premolded component. From the manufacturing perspective a deformation of 5% of the pin diameter is acceptable for good quality revolute joints. These results are illustrated in Figure 3.22 Hence it is clear that different in-mold assembly strategies are required for the macroscale and the mesoscale.

### **3.7 Summary**

Different defect modes occurring during direct scaling down of macroscale processes to manufacture in-mold assembled mesoscale revolute joints have been discussed in this chapter. One of the most significant defects has been identified as the plastic deformation of the mesoscale premolded component due to flow of the second stage polymer melt around it. Results have been presented which elucidate the effect of the size of the in-mold assembly on the associated defect mode. Experimental results for realtime measurement of forces on the premolded component due to flow of the second stage polymer melt around it have been reported. The results indicate that a drag force applied by the flow of the second stage polymer melt on the premolded component is responsible for its plastic deformation.

This chapter also presents methods to effectively estimate the deformation of the premolded component via computational tools. Some of the significant modeling results presented in this chapter are:

- 1) A predictive computational model to estimate the force experienced by the premolded component due to the second stage polymer melt flow.
- 2) A predictive computational model to estimate the overall plastic deformation of the premolded component for a given geometry.

The results presented in this chapter clearly indicate a need for an alternate strategy for achieving in-mold assembly at the mesoscale. The following chapters will describe different strategies for mesoscale in-mold assembly and present results which can be used as a mold design tool for manufacturing in-mold assembled mesoscale revolute joints using different materials and different geometries.

## **4 Characterization and Control of Plastic Deformation in Mesoscale Premolded Components Using Single Gated Mold Design**

### ***4.1 Motivation***

During the in-mold assembly process, a premolded component is placed inside a second stage molding cavity. This premolded component is subjected to thermal and mechanical loading due to the injection molding process. Unlike the macroscale in-mold assembly, one can observe significant plastic deformation in the premolded component at the mesoscale if the component is not properly constrained. This problem arises due to the fact that, owing to their sizes, the meso-scale parts have significantly less structural rigidity and thermal resistance compared to the macroscale parts. However, the mechanical and thermal loading is not significantly reduced at the meso-scale. To overcome this problem, the premolded component can be constrained in the mold cavity to minimize the deformation. However, such constraining limits the available design choices and also may increase the mold complexity. In order to determine the best way of constraining the premolded component, it is necessary to understand how the premolded component will deform during the injection molding process. Once this is understood through the mechanics of the deformation process, it will be possible to evaluate different ways of properly constraining the premolded part.



This chapter addresses challenges which are unique to the in-mold assembly process at the mesoscale through innovative mold design and fabrication methods. The mold design strategy reported in this chapter uses uni-directional filling of the second stage melt around the premolded component. The design and processing parameters that are used to address these differences in order to successfully realize mesoscale revolute joints are also described. A detailed modeling approach is also presented to characterize and control this deformation. The following results are reported in this chapter.

- 1) A mesoscale mold design with varying cavity shape to perform in-mold assembly of the mesoscale revolute joint.
- 2) A transient flow based modeling approach based on the strategy described in the previous chapter to determine the forces experienced by the mesoscale parts due to injection molding.
- 3) A mechanics-based model developed using experimental data and numerical CFD and FEA simulations is presented for the determination of critical mold design parameters that are necessary for repeatable fabrication of articulating mesoscale revolute joints.

Using the advances reported in this chapter a mesoscale revolute joint has been successfully molded. To the best of our knowledge, this is the first demonstration of in-mold assembly process using a morphing cavity mold design to create an articulating mesoscale revolute joint.

To the best of our knowledge a scalable in-mold assembly method for creating mesoscale revolute joint has not been demonstrated so far. This work is seen as a first

step towards realizing in-mold assembly at the mesoscale, and develops a mechanics-based model that is essential to understanding the physics of interaction between the melt flow and premolded parts in multi-shot injection molding processes.

## **4.2 Development of a Novel Mold for Realizing Mesoscale**

### ***Revolute Joints***

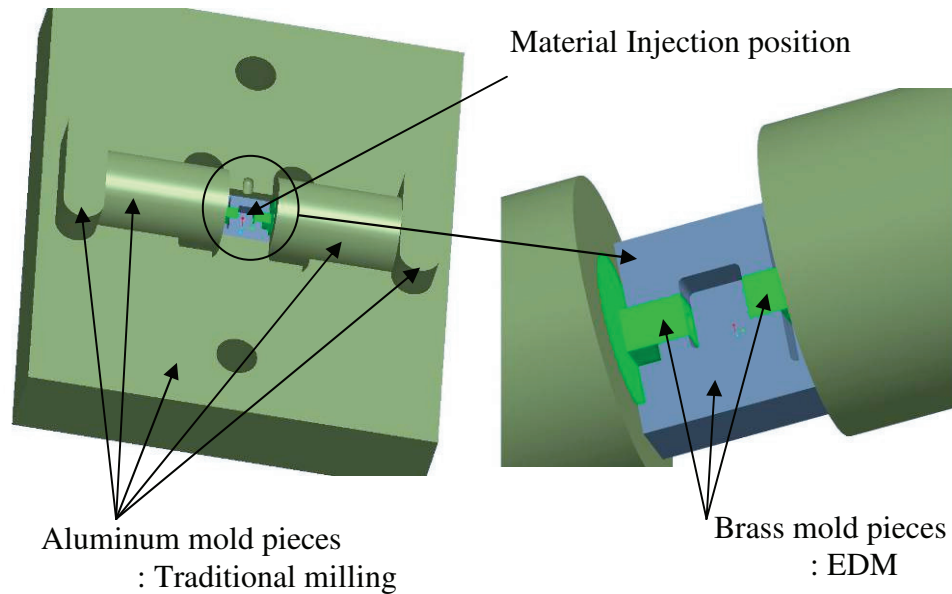
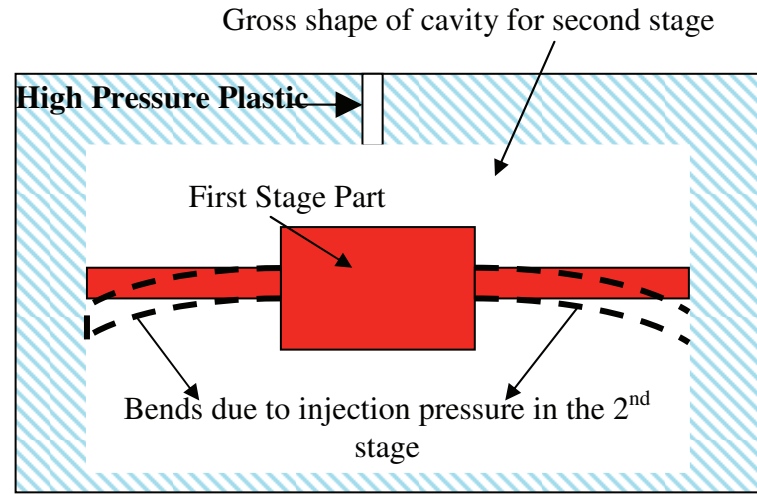


Figure 4.1 Mold assembly for Stage 1.

There are two possible molding sequences for manufacturing an in-mold assembled mesoscale revolute joint. These are reported in the previous chapter. It was therefore important to pick the molding sequence with lower susceptibility to defects in order to manufacture mesoscale in-mold assembled revolute joints. Molding the cavity as the premolded component was considered as the initial solution. To accurately position the SAMI, additional support structures had to be provided. This led to an increase in machining costs for the mold and also increased susceptibility to flash by increasing the number of parting lines in the mold cavity. On the other hand, molding

the pin first does not require any significant redesign. Hence, considering lower costs and lower susceptibility to flash, it was decided to mold the mesoscale core as the premolded component.



(a) Initial Concept

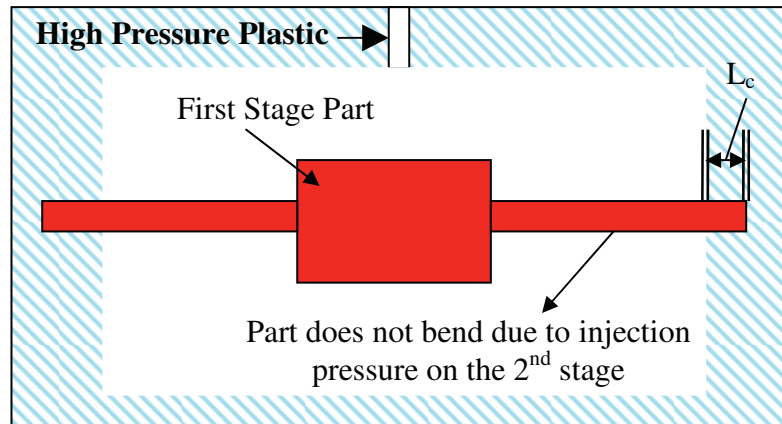


Figure 4.2 Bending of pin due to unsupported second stage injection

Significant effort was devoted to developing a mold design that eliminates the deformation of the premolded component. Figure 4.1 shows the mold assembly for the first stage of the in-mold assembly process to manufacture the revolute joint with mesoscale features where the mesoscale core is molded first. This mold design

ensures that no seam marks are present on the first stage part, and hence there are no adhesion problems in the joint. This design also ensures that mold pieces move accurately during cavity shape change and do not cause any damage to the part.

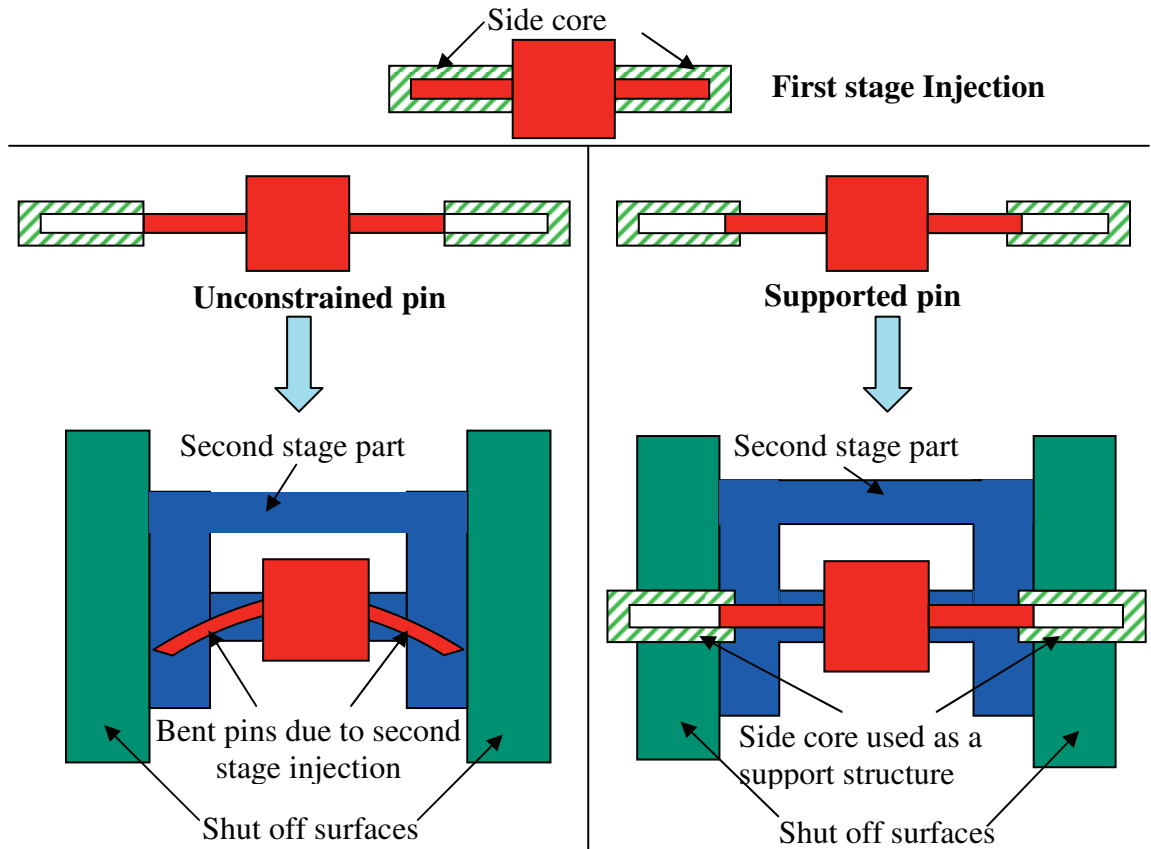


Figure 4.3 Mold design iterations for second stage injection

When the mesoscale pin is molded first, there is a concern that the melt flow during the second stage will bend or break the delicate pins. In order to overcome this problem, the bending stress needs to be minimized. Therefore, the mesoscale pin was constrained on the other end to form a simply supported structure. This was achieved by retracting the SAMI partially after the first molding stage. This limited bending deformations in the premolded component, as illustrated in Figure 4.2. The pin was

supported at each end by a distance of  $L_c$ . This adds a new parameter to the mold design that will be addressed later in the chapter.

The support length needs to be long enough such that the plastic deformation of the core is controlled, but not so large that it would significantly decrease the overall length of the mesoscale pin in the premolded component and thereby increasing molding costs. While doing this, it was ensured that the final in-mold assembled part would be fully constrained. A schematic illustration of the two design iterations for the second stage designs can be seen in Figure 4.3. Two new mold pieces were added to the mold assembly for the second stage while reusing all other mold pieces from the first stage mold assembly. These pieces were introduced to provide a shut-off surface for the second stage part. The complete mold assembly for the second stage molding process is illustrated in Figure 4.4.

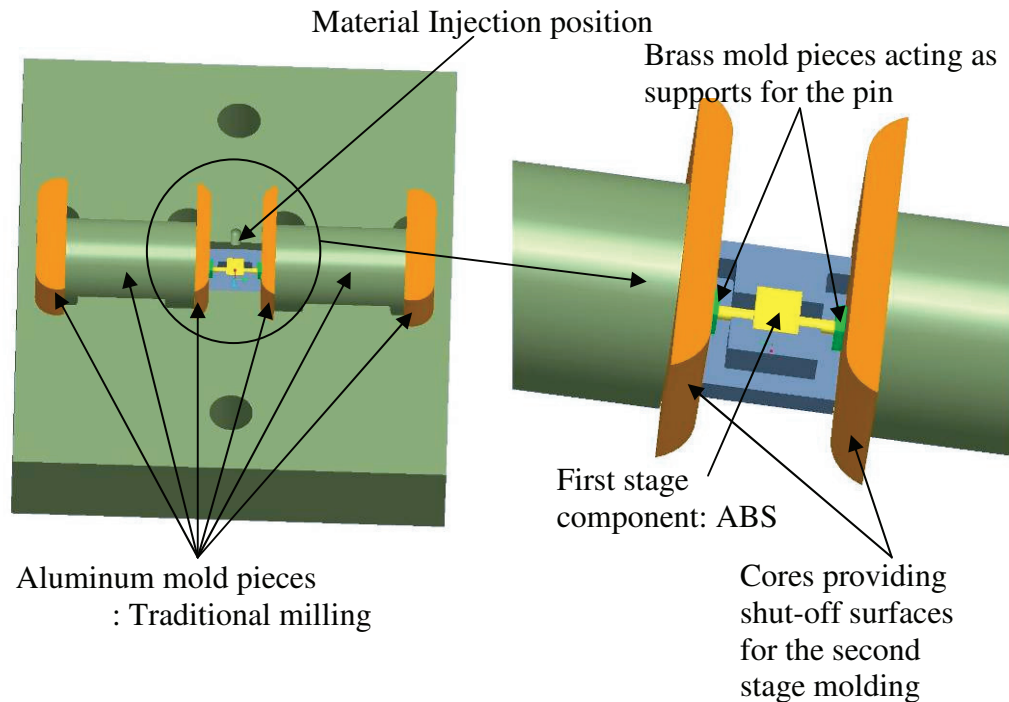


Figure 4.4 Mold assembly for stage 2

To develop a feasible manufacturing approach for in-mold assembly of mesoscale revolute joint, it is imperative to accurately predict the radial support length required for creating a functional joint. However to predict the radial support length, there is a need to have a better understanding of the physical interaction between melt flow and the core.

### ***4.3 Experimental Implementation of the Mechanics-Based Model for Controlling Plastic Deformation in Premolded Components***

The physics of the melt flow plays a significant role in the plastic deformation of the premolded component that occurs in the injection molding process during the filling phase. Experiments were conducted to obtain data to quantify the previously discussed parameters that affect the plastic deformation. These experiments enabled the mechanics-based model to be implemented for controlling the plastic deformation of the premolded component, which in this investigation was a mesoscale core whose plastic deformation is a function of the radial support length.

#### **4.3.1 Experimental Configuration**

The revolute joint example shown in Figure 3.2 features an assembly formed by two mesoscale pins. Owing to the inherent symmetry in the assembly, a design involving only one mesoscale pin will suffice for the purpose of this experimental study. This design helps in simplifying the experiment without any loss of information related to the actual mesoscale revolute joint illustrated in Figure 3.2. For this reason, we designed the first stage part to have only one mesoscale feature as

illustrated in Figure 4.5 to collect data related to the effect of temporal misalignment on the plastic deformation of the premolded component.

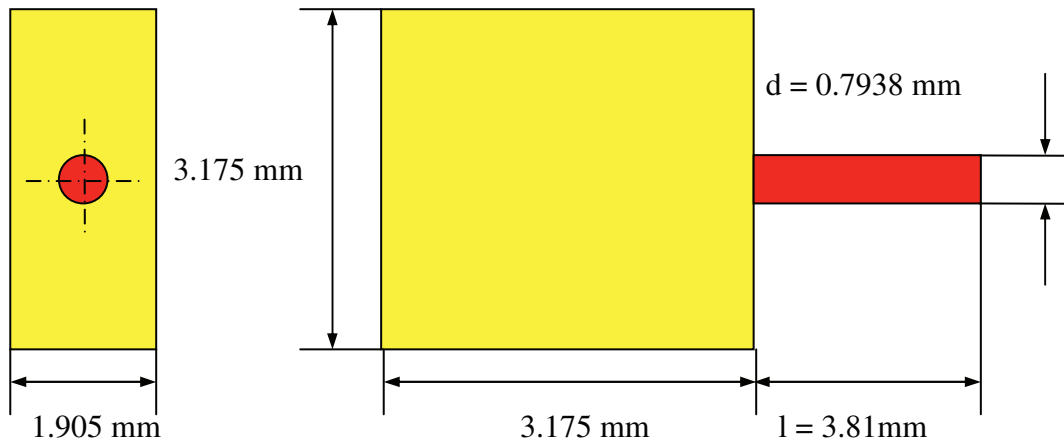


Figure 4.5 Premolded component for experiments

To understand the effect of the radial support length on the plastic deformation of the premolded mesoscale core, it was important to control this length accurately with a high resolution. To achieve this, we designed a wedge type mold for the experimental setup. This setup is illustrated in Figure 4.6. This mold was designed such that if the wedge was moved by a distance  $x$ , the support moved by a distance of  $x/10$ . Utilizing the symmetry of the mesoscale revolute joint, we designed the experimental setup to have only one mesoscale core. This simplified the experimental procedure since the geometric constraints between the first stage part and the second stage part were removed. Hence we were able to separate the first stage part and the second stage part and examine them separately. The injection molding parameters used for each stage of the experiment can be seen in Table 4.1.

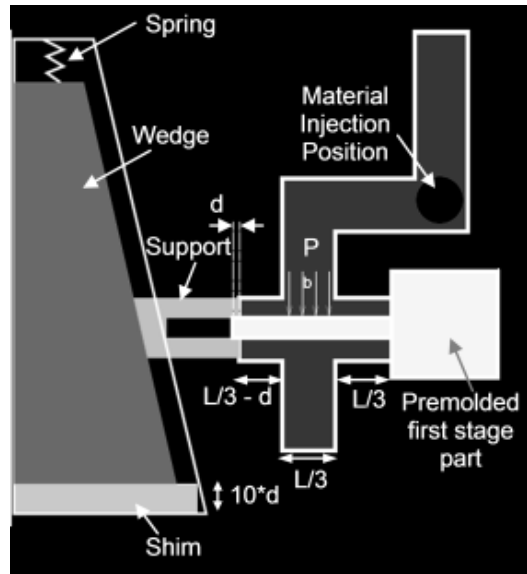


Figure 4.6 Experimental setup for correlation of support length with deformation of core

Table 4.1 Injection molding parameters

	<b>Stage 1</b>	<b>Stage 2</b>
<b>Material</b>	ABS	LDPE
<b>Injection Temp.</b>	220°C	130°C
<b>Injection pressure</b>	600 bars	600 bars
<b>Cooling time</b>	15s	5s

#### 4.3.2 Development of a Predictive Model for Estimating Premolded Component Deformation

Estimation of the deformation of the premolded component as a function of the radial support length requires development of a computational model for 1) The force applied on the premolded component by the second stage polymer melt flow and 2) The non-linear deformation of the premolded component as a function of the applied force. Computational methods to solve these two problems have been elucidated in the previous chapter under section 3.5.



The force acting on the mesoscale core was estimated by computationally simulating the non-Newtonian flow of the second stage polymer melt around the premolded component. The flow simulations for this force prediction was done using the commercial CFD code FLUENT 6.3.26 [87] using the strategy described in section 3.5.1. From these simulations, the maximum force on the pin was obtained. The maximum force was noted as the force on the pin when the second stage polymer melt flow comes in contact with the mold wall downstream of the premolded component.

Computational finite element simulations were conducted to determine the effective plastic deformation of the premolded component due to the applied force using the non-linear material properties of the premolded component (ABS) which were obtained experimentally (section 3.6). To obtain the effective plastic deformation, the effective force obtained from the flow simulation was incorporated into the FE model. Subsequently simulations were performed using ANSYS 11.0 [89] using the following strategy.

- 1) The pin is segmented into four sections as illustrated in Figure 4.7. An equivalent pressure based on the injection flow rate was applied on the top half core on section II. We determined this equivalent pressure using the LDPE flow simulation described in the previous section.
- 2) Section IV was constrained in the Y and Z direction. However it was free to move in the X direction.

- 3) We modeled material nonlinearities using piecewise linear elastic properties. We obtained these properties based for ABS experimentally as explained earlier. Table 3.2 lists the nonlinear stress-strain data that was obtained from experiments.
- 4) For meshing the model, the cylinder was line sized using 12 radial elements and 20 axial elements. The model was then meshed as a tetrahedral element (Solid92) which supports plastic deformation. The finite element problem thus formulated was solved to obtain the plastic deformations.
- 5) Finally, these solutions were tabulated for different support lengths.

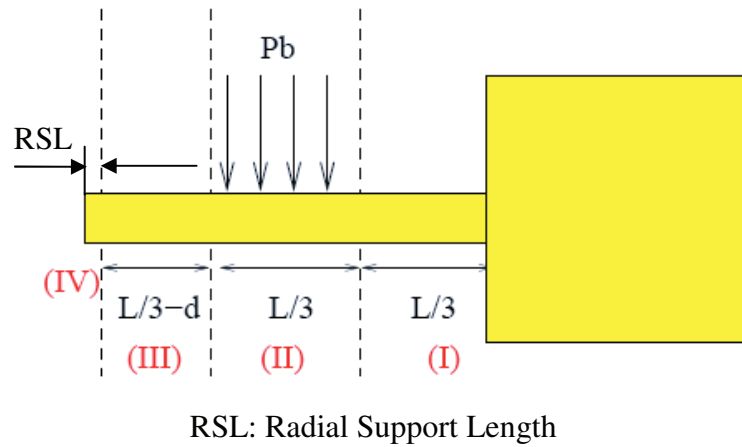


Figure 4.7 Force modeling on the premolded component.

#### 4.3.3 Comparison of Modeling Results with Experimental Data

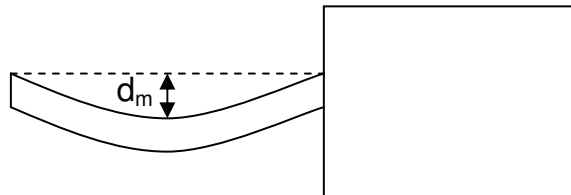


Figure 4.8 Measurement of maximum deformation  $d_m$

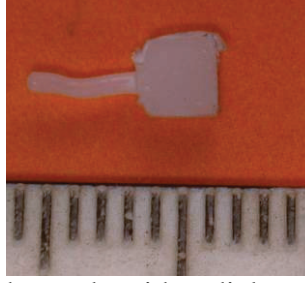


Figure 4.9 Deformed sample with radial support length of 6.66%

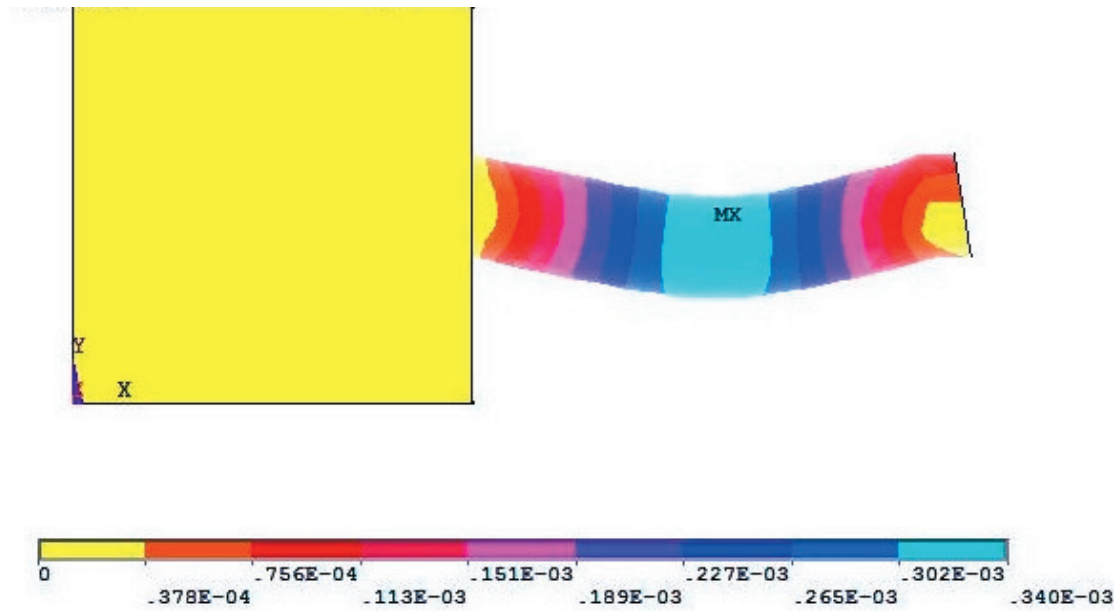


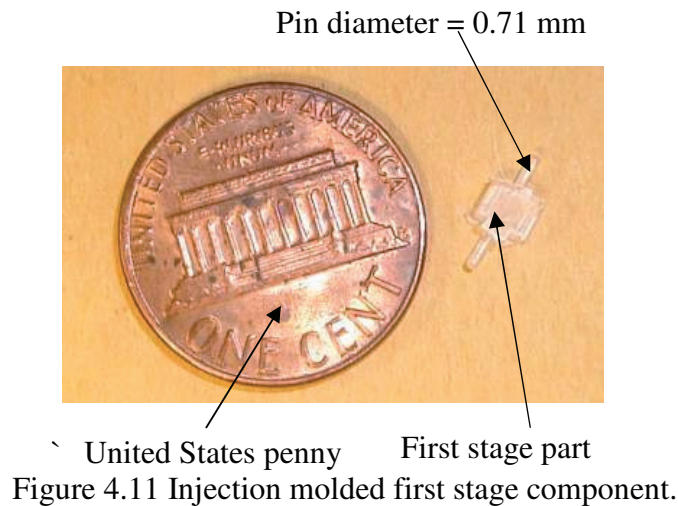
Figure 4.10 Sample results for ANSYS analysis for 6.66% Radial support length

In order to validate the previously described model, experiments were conducted where the maximum deformation,  $d_m$ , of the mesoscale core due to the second stage material flow was recorded, as illustrated in Figure 4.8. An example of a deformed sample can be seen in Figure 4.9. This sample was obtained by radially supporting the mesoscale core by 6.66% of its overall length. Results from the finite element analysis for the same radial support length can be seen in Figure 4.10. In the next

section, results obtained from the experiments and the finite element analyses are discussed in further detail.

#### **4.4 Results and Discussion**

The experiments were conducted on a Milacron Babyplast injection molding machine using the processing parameters described in Table 4.1. Figure 4.11 shows the first stage part successfully molded using the methods described in the previous sections.



This component was subsequently used to continue with the in-mold assembly process. The results of the experimental and finite element analysis described in the previous section were subsequently used to determine the adequate radial support length required to manufacture functional joints. For the first part of the analysis, we obtained plots for the maximum plastic deformation of the first stage part when the radial support length was varied. This experiment was conducted at the recommended injection pressure (635 bars) for the polymer and the mold material. A flow rate of 12 cc/s was used to calculate the effective pressure on the mesoscale core. From the flow

simulations, the relationship between the effective pressure on the mesoscale core and the flow time was obtained.

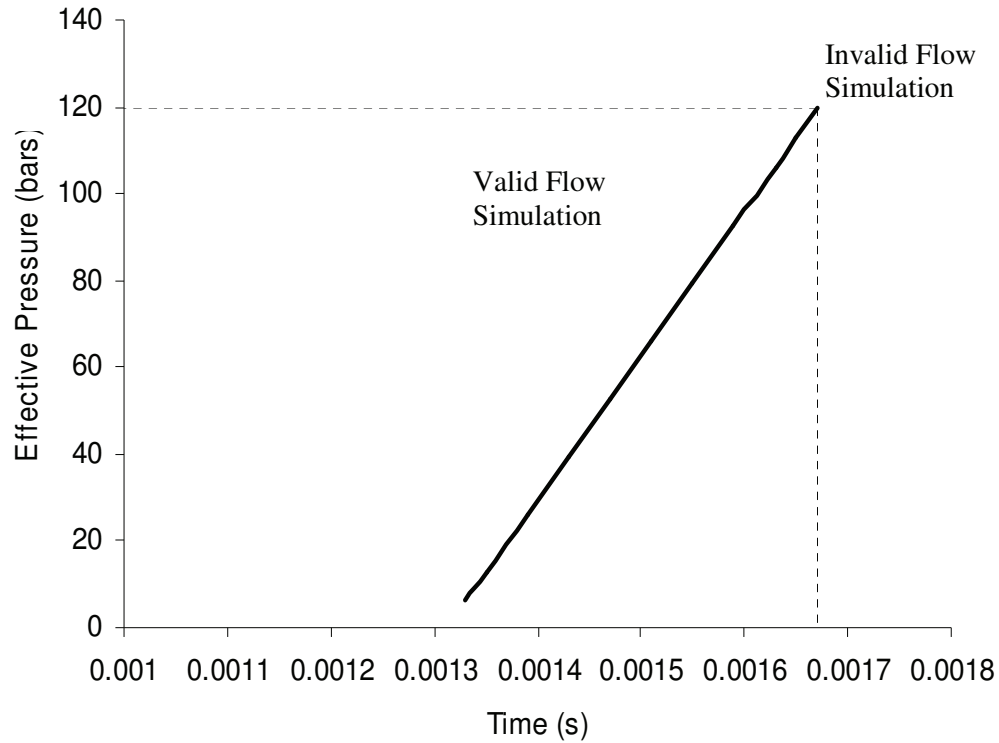


Figure 4.12 Effective pressure on mesoscale core obtained from flow simulation

As shown in Figure 4.12, the effective pressure on the mesoscale core increases linearly as a function of time. The maximum effective pressure acting on the mesoscale core determined by the point on the curve where the melt flow begins to equilibrate corresponds to 120 bars. Therefore, this pressure was used as the boundary conditions in the finite element analysis of bending deformation of the mesoscale core.

An important observation from Figure 4.12 provides counterintuitive insight into the relationship that exists between the interaction of the polymer melt and the mesoscale core as a function of the mold geometry, in this case the channel length

downstream of the mesoscale core used to determine the maximum pressure. Intuitively, it would be reasonable to assume that once the melt reaches the mesoscale core, the loading state resulting in the observed experimental deformations would have been achieved. However, there is a substantial time scale over which the loading evolves in steady state melt flow. Since the channel downstream of the mesoscale core interrupts this flow, it effectively limits the time scale over which the loads can evolve. Thus, the model suggests the mold geometry can possibly be used to limit the interaction between the mesoscale core and the melt flow by reducing the size of the channel downstream.

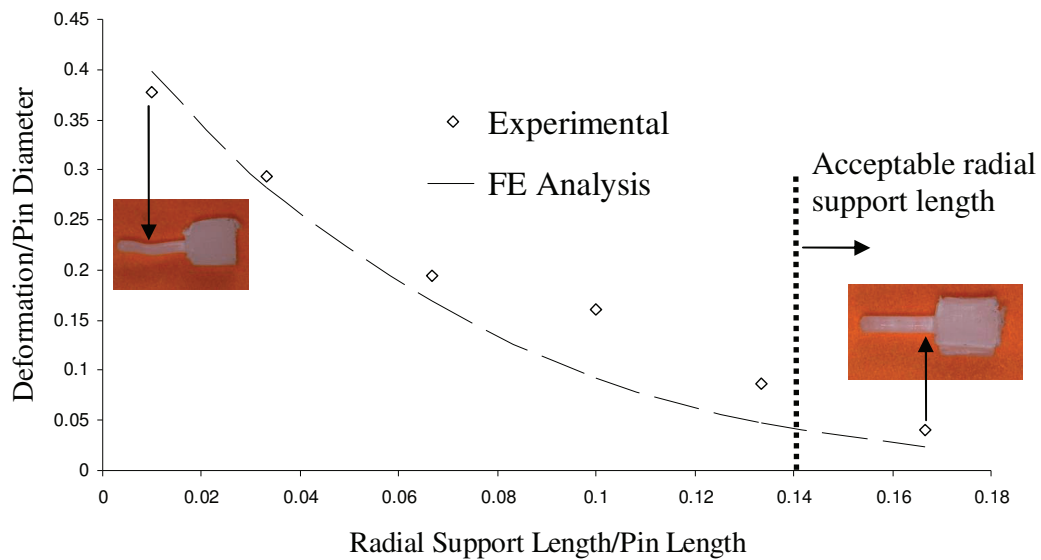


Figure 4.13. Finite element analysis for deformation versus radial support length for a flow rate of 12 cc/s

The results of the finite element analysis of the bending deformation for the mesoscale core conducted in ANSYS agree well with the experimental data recorded for the deformation versus radial support length for this pressure. These results are illustrated in Figure 4.13. The model predicts the deformation of the mesoscale core

to decrease with increasing radial support length. The plastic deformation of the mesoscale core tends to zero for radial support lengths higher than 20% of the length. However from the manufacturing perspective, deformations less than 5% of the diameter of the pin are acceptable from a quality control point of view. Hence a radial support length greater than 14% of the length of pin can be used to manufacture good quality mesoscale revolute joints. This region is illustrated in Figure 4.13.

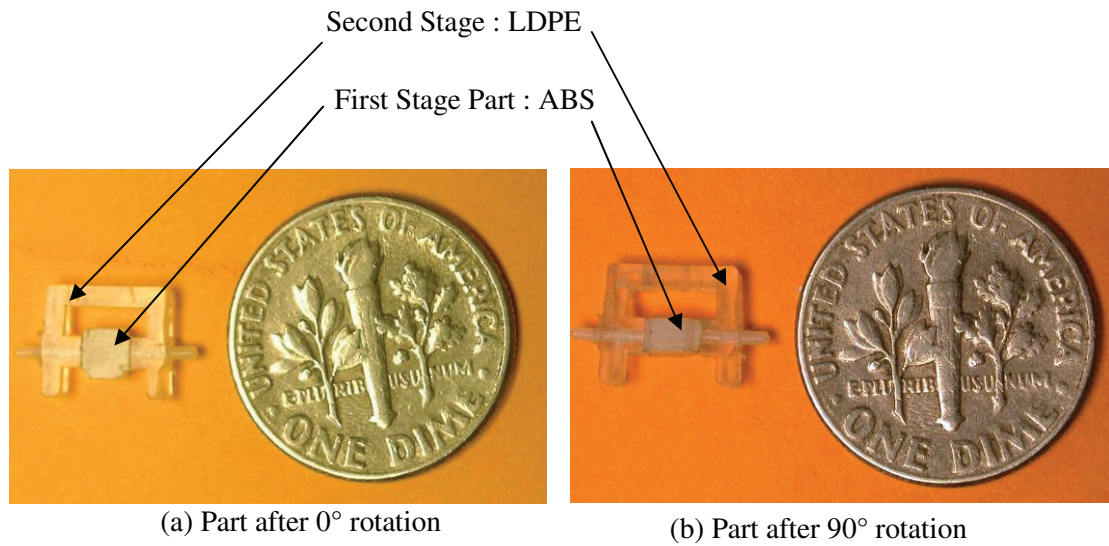


Figure 4.14. Two configurations of the in mold assembled mesoscale revolute joint demonstrating rotation of the joint

In subsequent experiments for manufacturing in-mold assembled revolute joints the mesoscale cores were supported on both sides along 30% of its length as described above. This solved the problem of the plastic deformations due to high bending moments applied by the flow of the second stage polymer. This method enabled manufacturing of fully functional in mold assembled revolute joint. This is illustrated in Figure 4.14. After determining the mold design that would result in properly functionally assemblies, 8 functioning assemblies were molded. Using the techniques

described above enabled a repeatable manufacturing process for these assemblies without any defective parts.

## **4.5 Summary**

This chapter establishes the technical feasibility of using in-mold assembly process for creating articulating mesoscale revolute joints. The following new results are reported in this chapter. First, a mold design is described with varying cavity shape to perform in-mold assembly. Second, a modeling method is described to determine the forces on the premolded component due to the second stage injection. Third a modeling method is described to determine the deformation of the premolded mesoscale component due to the second stage injection. These methods are then used to select the required radial support length for obtaining functional mesoscale revolute joints. This joint is fully functional and can be manufactured repeatably using the process described. The deformations of the mesoscale premolded component fall within the acceptable joint tolerances. To the best of our knowledge, this is the first demonstration of in-mold assembly process to create a mesoscale revolute joint.

As part of the modeling effort, a process is described to estimate the effective pressure experienced by a cylinder which falls in the flow path of an injection molding melt. A non-newtonian flow CFD model is used to estimate this pressure. The estimate provided has an error margin of up to 10%. This model is the first attempt at understanding the physics of interaction between the melt flow and free-standing structures in multi-shot molding processes, and suggests a non-intuitive



influence of the mold geometry on the loading experienced by the free-standing structure.

A nonlinear FEA model is also described for predicting the deformation of a mesoscale core when placed in the polymer flow environment. This model agrees with the experimental deformation with an error of around  $\pm 2\%$ .

The in-mold assembly method described in this chapter, works extremely well when the melt temperatures of the two polymers are significantly different. This ensures that the premolded component would not get heated beyond its glass transition temperature or softening point when it comes in contact with the second stage polymer melt.

However, there are few scenarios when this process would not be suitable for fabrication of in-mold assembled mesoscale revolute joints. This process is unsuitable for situations where the melt temperatures of the two polymers are similar. This is because the second stage injection melt would have sufficient thermal energy to elevate the temperature of the premolded component above its glass transition temperature. This would cause significant changes in the material properties of the premolded component. The premolded component would soften considerably thereby inducing higher levels of plastic deformations for the same flow properties of the second stage melt. This would require a higher radial support length for manufacturing functional mesoscale revolute joints.

In the next chapter, an alternate mold design methodology to overcome this problem will be discussed.

## **5 Characterization and Control of Plastic Deformation in Mesoscale Premolded Components Using Multi Gated Mold Design**

### ***5.1 Motivation***

The previous chapter presents an approach to inhibit the plastic deformation of the premolded component due to the second stage polymer melt flow. However, it is only suitable for polymer combinations having large differences in melting temperature. This difference ensures that the premolded component does not undergo thermal softening during its interaction with the high temperature high pressure second stage polymer melt flow. Also, mesoscale features in the premolded components need to be longer than the requirement needed by the design to provide sufficient length for the radial supports. Making such high aspect ratio mesoscale structures significantly increases the mold tooling cost.

As described previously, the plastic deformation of the premolded component is caused by the impingement of the second stage polymer melt on the premolded mesoscale component. This impingement leads to the application of an effective drag force on the premolded component. To overcome this effect, an opposing force can be introduced on the premolded component to minimize plastic deformation. Introduction of this opposing force using bi-directional filling presents an alternate strategy that is preferable to the radial support strategy when using a combination of materials with similar melting points and when tooling costs are a concern. Details of

this alternate mesoscale in-mold assembly strategy will be presented in this chapter. However, this new strategy introduces some new challenges. These challenges and methods to overcome them will be elucidated in this chapter.

## ***5.2 Bi-directional Filling for In-mold Assembly***

As described earlier, during in-mold assembly of mesoscale revolute joints, the mesoscale premolded component tends to deform plastically due to the force applied by the second stage melt flow. This deformation is caused by the uni-directional lateral force applied on the mesoscale features in the premolded component by the second stage polymer melt flow [90]. If an opposing force is applied to the mesoscale feature on the premolded component, then it is possible to neutralize the force caused by the uni-directional second stage polymer melt flow and inhibit plastic deformation. To realize this force, a bi-directional filling strategy was introduced for the second stage polymer melt. This is illustrated in Figure 5.1.

However, in order to completely neutralize the force on the mesoscale feature the gates for the two flows have to be placed exactly equidistant from the mesoscale feature. In several design scenarios it may not be possible for the gates to be aligned exactly. Any misalignment will result in an un-equilibrated force on the premolded component. This un-equilibrated force may cause plastic deformation of the mesoscale structures in the premolded component.

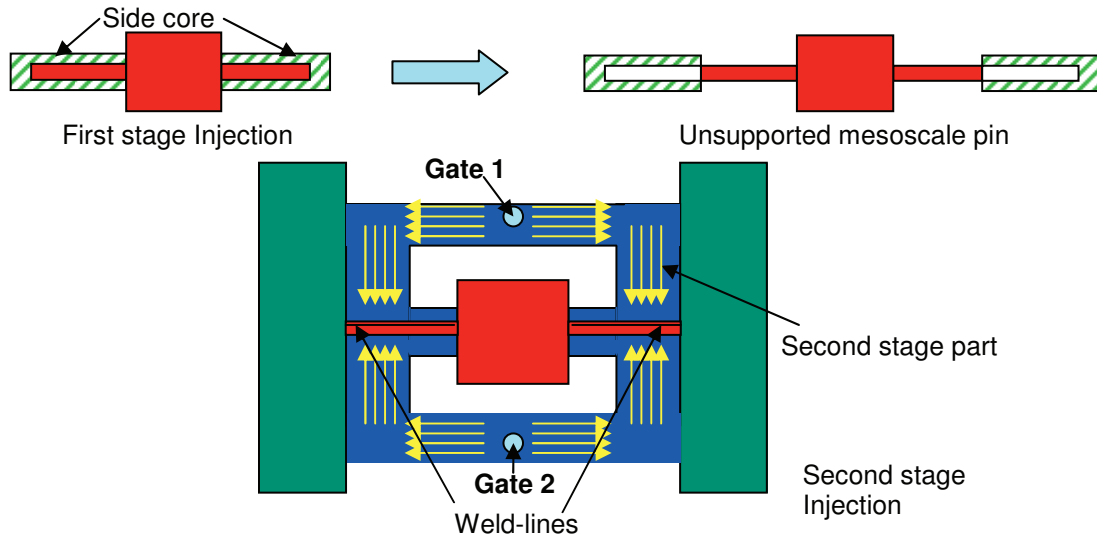


Figure 5.1 Schematic of the two stage mold design using multi gate bi-directional filling strategy

Another important consideration while using the bi-directional filling strategy is the formation of cold weld-lines at the joint interface. This is illustrated in Figure 5.1. Weld-lines are formed at the position where the flows from the two gates meet. For some polymers, weld-lines are a major source of structural weakness [67, 91-93]. Hence a weld-line at this position, if weak, may be unacceptable in several design scenarios. Introduction of misalignment in the gate positions could be a possible strategy to move the weld-lines to a structurally less demanding location.

To address some of these concerns, it is imperative to obtain an understanding of the sensitivity of the plastic deformation of the mesoscale premolded component to any misalignment in the gate locations. There are several types of gate misalignment. Two prominent types of gate misalignments are: (1) temporal misalignment, and (2) spatial misalignment. The two misalignments are illustrated in Figure 5.2 (b) and (c) respectively. Both misalignments may cause plastic deformation in the premolded

component as shown in the figure. This dissertation will only address the temporal misalignment case.

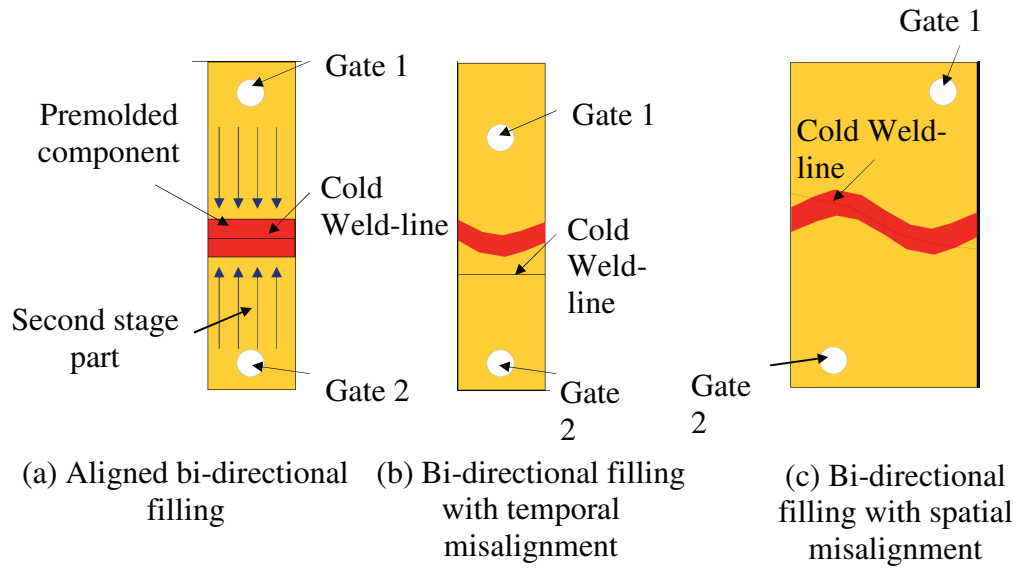


Figure 5.2 Spatial and temporal gate misalignment

Section 5.3, will describe the influence of a weld-line on the quality of an in-mold assembled mesoscale revolute joint. Section 5.4 will describe the experimental setup that was used to record the strength of the cold weld-line of the polymer combination used and the plastic deformation of the premolded component as a function of the temporal misalignment. Section 5.5 will describe the approach used to build a theoretical predictive model for relating the plastic deformation to the temporal misalignment of gates. Section 5.6 will report results of the experimental analysis as well as preliminary results of a computational model. Finally Section 5.7 will conclude this chapter with a summary.

### **5.3 Analysis of Weld-lines in In-Mold Assembled Mesoscale Revolute Joints**

There are several scenarios which necessitate the use of multiple gates for filling injection mold cavities. In complex cavities having multiple different features, using a multi gated mold cavity ensures more uniform filling. If designed appropriately, multi gated molds can be used to eliminate short shots. They also have the added advantage of limiting part warpage due to differential shrinkage [92].

In the context of in-mold assembly, use of multiple gates, when positioned appropriately overcomes the problem of deformation of the premolded component due to the flow of the second stage polymer around it as has been discussed in the previous section.

However use of multiple gates in the mold leads to the undesirable appearance of weld-lines, which are formed when the two different injection molding flows meet at a frontier. Weld-lines can be classified into two types.

- 1) Cold weld-lines: These are formed at the meeting point of two opposing flows which are aligned at an angle of  $180^\circ$  to each other. In this case, there is no further flow at the interface after the two opposing flows meet.
- 2) Meld-lines: These are formed when two flows meet each other at an angle and continue to flow after meeting.

The two types of weld-lines are illustrated in Figure 5.3.

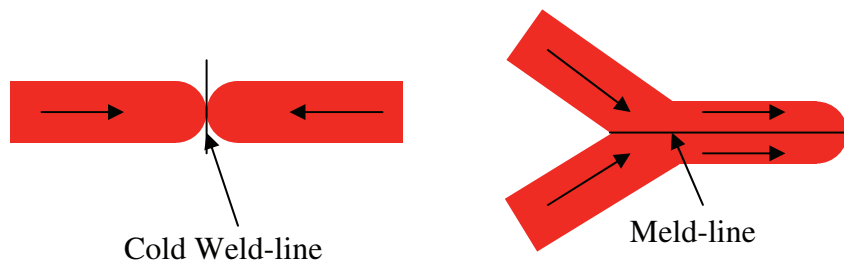


Figure 5.3 Types of weld-lines

Although weld-lines are formed when a multi gated mold is used, they could also be formed in single gated molds. This could occur due to an obstacle in the flow [62, 65, 68, 70, 74]. The polymer flow splits near the obstacle and subsequently meets downstream of the obstacle. The weld-line that is thus formed is an adjacent flow weld-line or a meld line.

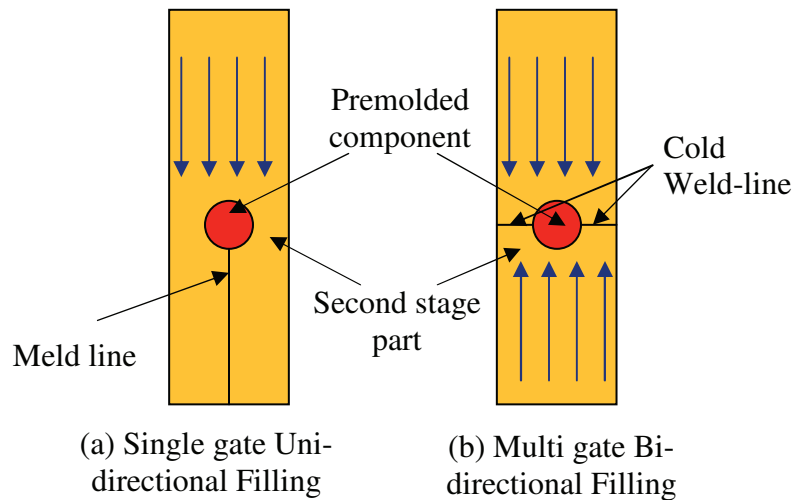


Figure 5.4 Weld-lines formed in uni-directional and bi-directional filling in second stage

Table 5.1 Comparison of uni-directional and bi-directional filling

<b><u>Single Gate Uni-directional Filling</u></b>	<b><u>Multi Gate Bi-directional Filling</u></b>
Single gate positioned at appropriate location is required	Multiple gates required which need to be positioned exactly equidistant from the mesoscale core
Deformation of mesoscale core needs to be controlled using radial supports	No deformation
Entire length of mesoscale core cannot be utilized in the joint	Entire length utilized
Adjacent flow weld-line/meld-line formed	Cold weld-line formed at the joint
Overall size of the joint cannot be restrained	Overall size of the joint can be restrained

In the case of in-mold assembly at the mesoscale, the appearance of weld-lines is highly relevant because the bi-directional filling strategy employed to manufacture in-mold assembled mesoscale revolute joints, leads to formation of cold weld-lines at the joint interface. However, if a uni-directional filling strategy, as described in the previous chapter, is employed, an adjacent flow weld-line or a meld-line is obtained. This weld-line is formed due to the presence of the premolded component in the flow path. The premolded component acts as an obstacle in the flow leading to formation of a meld line. Figure 5.4 illustrates the two different weld-lines formed due to the two strategies employed to fabricate in-mold assembled mesoscale revolute joints. Table 5.1 shows a comparison between uni-directional and bi-directional filling for fabricating in-mold assembled mesoscale revolute joints.

It is well known that due to inappropriate bonding of the polymer melts in the two flows, the strength of the weld-lines is lower than that of the base polymer in a molded component [61-76]. Literature also suggests that the strength of a cold weld-line is lower than that formed due to an obstacle in the flow [62, 65, 68, 70, 74].



However the absolute strength of the cold weld-line depends on the material and the processing conditions used to injection mold the part. Industrial standards suggest that a weld-line strength greater than 70% is acceptable for most parts.

Hence in order to employ the bi-directional filling strategy it is important to choose the right material combination for the premolded component and the second stage polymer. The most appropriate in-mold assembly is dependent not only on the capability of manufacturing functional revolute joints but also on the polymer combination that is required. This would directly map to the kind of applications that the revolute joints need to be used for since most applications directly impact the material choice.

#### ***5.4 Experimental Setup***

The revolute joint example shown in Figure 3.2 features an assembly formed by two mesoscale pins. Owing to the inherent symmetry in the assembly, a design involving only one mesoscale pin will suffice for the purpose of this experimental study. This design helps in simplifying the experiment without any loss of information related to the actual mesoscale revolute joint illustrated in Figure 3.2. For this reason, we designed the first stage part to have only one mesoscale feature as illustrated in Figure 5.5 to collect data related to the effect of temporal misalignment on the plastic deformation of the premolded component.

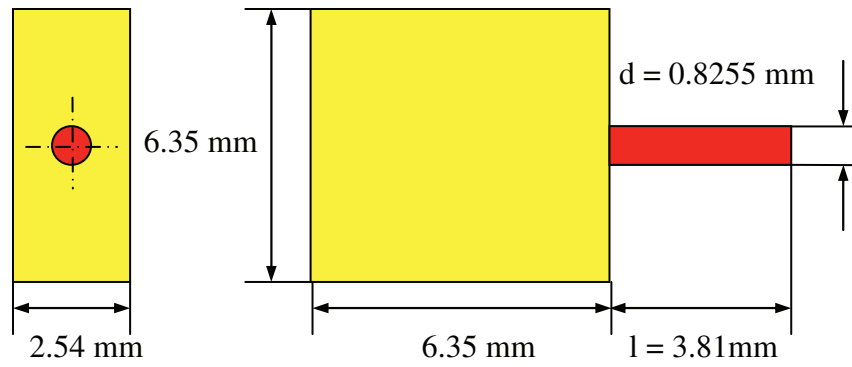


Figure 5.5 Premolded component for experiments

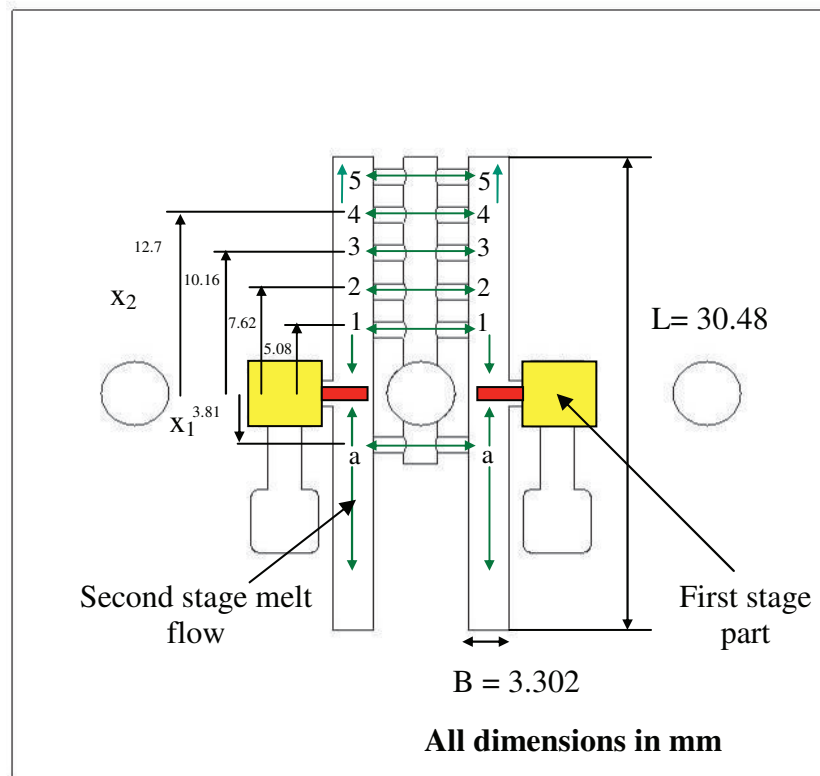
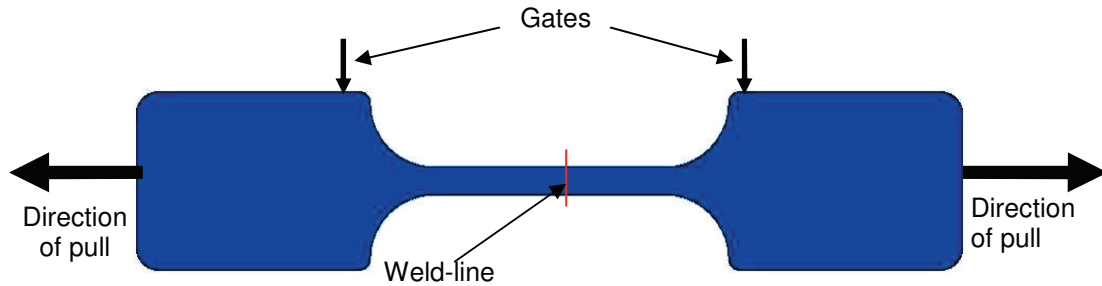


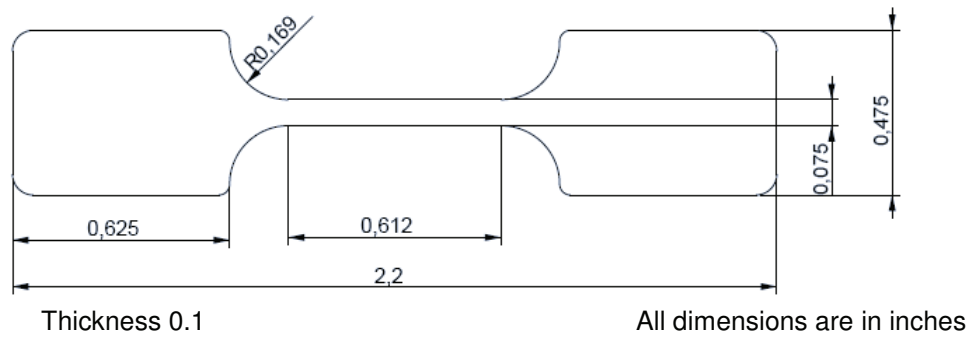
Figure 5.6 Modular second stage mold design

We designed the second stage mold to be modular in nature so as to collect data for different gate locations using the same mold. This mold is illustrated in Figure 5.6. This mold could be used to generate two samples in each shot. The mold contained a total of 6 gates. At any given time, we kept 2 gates (gate (a) and one of gates 1 to 5) open and 4 closed. By opening and closing different gate combinations for different

shots, we were able to use this mold to obtain 5 different sets of temporal misalignment of gates.



(a) Location of gates and weld-line in the molded dogbone



(b) Dimensions of the dogbone specimen

Figure 5.7 Dogbone specimen to analyze strength of cold weld-lines

While choosing the material combination for in-mold assembly we took the following into consideration: (1) the melting temperatures of the premolded component and second stage polymer should be comparable, and (2) The strength of the cold weld-line for the second stage should be at least 70% of the base material. To study the weld-line strengths, we tested dogbone specimen made of the material for the second stage polymer melt. The dogbone specimen was molded both in a multi gate mold cavity and a single gate mold cavity. The multi gate mold cavity was used to produce specimen with a weld-line in the gage length. This strategy was taken from established experimental methods outlined in the literature [65, 67, 94].

## ***5.5 Mechanics-based Model for Predicting the Plastic***

### ***Deformation as a Function of Flow Front Progression***

This section will outline the issues related to modeling in-mold assembly at the mesoscale. An approach is presented to develop an understanding of the predominant issue of temporal misalignment faced during bi-directional filling to fabricate mesoscale in-mold assembled revolute joints. In order to develop a complete understanding of the effect of the temporal misalignment on the plastic deformation of the premolded component, a framework was developed to build a simple model. The objective is to predict the plastic deformation of the premolded component for a given temporal misalignment. This framework can be applied for this class of problems across any polymer combination and any injection molding parameter.

#### **5.5.1 Overview of Approach**

Before building a modeling framework, let us review the complexity of the problem we are trying to model. During the second stage mold filling of the in-mold assembly operation, the mesoscale premolded component acts as a soft mold insert for the second stage polymer melt flow. The premolded component is made of a viscoelastic material. The deformation of this material therefore follows a highly non-linear stress-strain curve. The second stage polymer melt flow on the other hand, is a non-Newtonian fluid flow, i.e., the viscosity of the flow is dependent on the shear rate of the flow. Also, there are two independent flows in the mold cavity owing to the presence of two gates. Due to the two independent flows in the mold cavity, the force on the premolded component is dependent on the transient fluid flow effects. The

mixing of the two polymer flows in the vicinity of the premolded component also influences the force on the premolded component. In summary, this problem involves time-varying non-Newtonian flow and elastic-plastic deformation. However, solving this problem in full generality is almost intractable and may not be necessary from the manufacturing point of view.

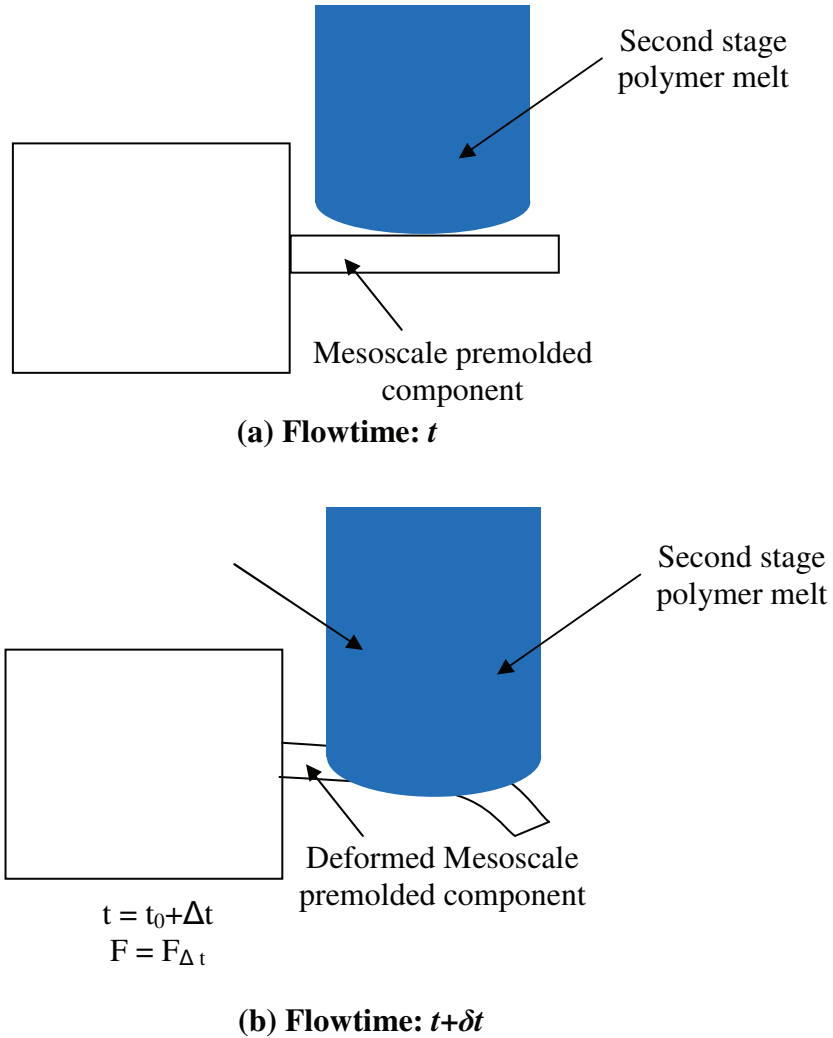


Figure 5.8 Deformation of premolded component with flow front progression

The plastic deformation problem described above can be explained as an effect of transient loading caused by the flow of the second stage polymer melt. The drag force applied by the second stage polymer melt on the mesoscale premolded component

monotonically increases with the progress of the flow front [3]. However as the force builds up, an elastic-plastic deformation progressively builds up on the premolded component as well. This is illustrated in Figure 5.8. Hence, as the flow front progresses further, the force is being applied on a premolded component whose shape is changing.

This force continues to increase monotonically, inducing elastic-plastic deformations on the premolded component until it encounters the opposing flow. Once the flow is stopped by the opposing flow, the drag force on the premolded component stops building up further. Hence, the full blown process modeling problem in its complete generality involves solving an initial value problem with varying force due to flow front progression and elastic-plastic deformation of the premolded component at each time step. In this problem there is direct coupling between the force experienced by the premolded component due to flow front progression and its deformation. Hence solving the full blown modeling problem is highly intractable and not essential from the manufacturing perspective.

From the manufacturing perspective, we are only interested in estimating the plastic deformation of the parts to determine whether the in-mold assembly process is a repeatable process capable of fabricating functional mesoscale revolute joints. Hence, it was attempted to decouple the problem from its full generality to estimate the plastic deformation within acceptable factor of safety limits to meet the needs of manufacturing.

In the first step, the modeling parameters that needed to be considered were identified. These include: (1) the *Geometric parameters*, i.e., the dimensions of the

premolded component and the second stage component, (2) the *Mold design parameters*, i.e., the temporal misalignment, and other mold dimensions such as sprue and runner dimensions, (3) the *Material properties*, i.e., the structural properties of the premolded component and the flow properties of the second stage polymer melt, and (4) the *Molding parameters* which are used during the in-mold assembly operation.

After identification of the modeling parameters, the next step involves decoupling the physics of the process and breaking them down into tractable problems. As explained previously the physics of the process involves coupling between:

- 1) Force on a mesoscale premolded component as a result of non-newtonian polymer flow around it;
- 2) The deformation response of the mesoscale premolded component as a result of the applied force; and
- 3) Location of the meeting point of two flows.

These processes are well understood phenomenon which can be solved using conventional analytical and computational techniques. The following sections will explain the strategy used to obtain these individual solutions and finally combine them to obtain the effective plastic deformation of the premolded component.

### **5.5.2 Force Modeling on Premolded Component**

In the first step, the force applied on the premolded component due to the second stage melt flow was obtained. As the flow progresses, a drag force builds up on the premolded component. This drag force is responsible for causing elastic plastic deformation of the premolded component. For predicting the force on the premolded

component applied by the second stage polymer melt flow a non-Newtonian fluid flow around a cylinder having the same dimensions as the mesoscale premolded component was solved computationally. This strategy involved modeling the second stage polymer melt flow as a multiphase, transient, VOF problem in FLUENT 6.3.26. The second stage mold cavity was modeled as the flow channel for the second stage melt which contained the mesoscale premolded component. From the time dependent solutions obtained from the simulations, the effective force on the premolded component in the flow stream was obtained computationally as a function of the flow front progression. This information was then extracted from the flow simulations to develop a metamodel for the force on the premolded component as a function of flow front progression.

### 5.5.3 Computing Premolded Component Deformations

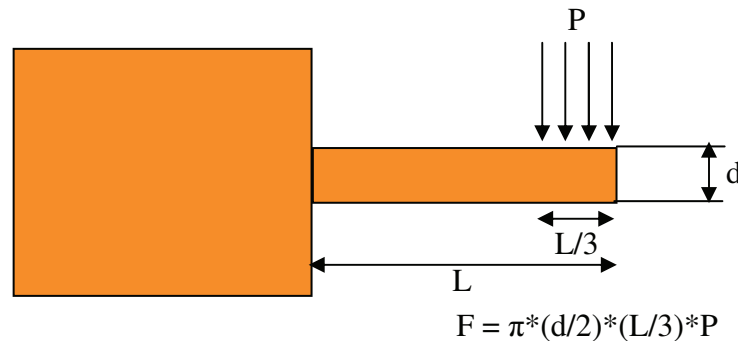


Figure 5.9 Force applied on premolded component to predict deformation

Next the elastic-plastic deformation of the premolded component was computed as a function of an applied force. A pressure was applied on the premolded component which resulted in elastic-plastic deformation of the premolded component. Figure 5.9 shows the location of the applied force on the premolded component. As illustrated in the figure, the force was applied on the premolded component as a transverse



pressure. To solve for this deformation, a finite element model was developed using ANSYS 11.0. The premolded component was modeled and meshed using a line sizing of 12 for the circular cross section of the pin and 60 along its length. The solution was then obtained for the elastic and plastic components of the deformations of the premolded components as a function of the applied force. This information was extracted into a metamodel which was used for computing the effective plastic deformation as a function of the flow front progression.

#### 5.5.4 Total Flow Front Progression

The second stage polymer melt flow applies a force on the premolded component until the flow comes to a stop. This stop can be provided either by a mold wall or an opposing flow. In the bi-directional filling case being considered, the flow is stopped by an opposing flow. Figure 5.10 illustrates the location of the weld-line ( $d$ ) for a temporal misalignment of ( $L1-L2$ ). Hence it is necessary to determine the position of this meeting point. Information about this meeting point can be used to determine the total flow front progression which can subsequently be used to determine the effective plastic deformation.

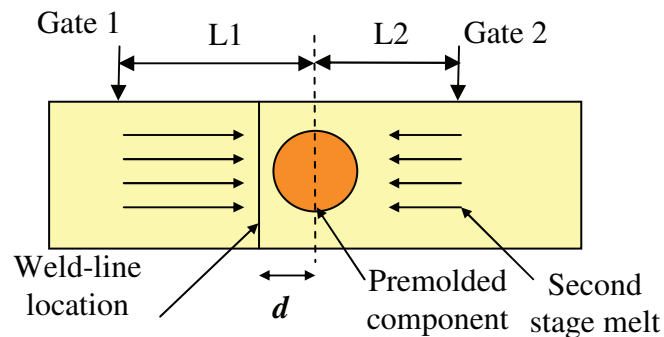


Figure 5.10 Weld-line location for temporally misaligned gates

To computationally predict the location of the weld-line in the in-mold assembled part, mold filling simulations were conducted in Moldflow Plastics Insight 7.1. A metamodel of this solution was extracted and applied it to the iterative computational strategy to compute the effective plastic deformation. This strategy is described in the next subsection.

### **5.5.5 Iterative Computational Modeling for Obtaining Net Plastic Deformation**

In the next step, the process under consideration was discretized and the metamodels from the individual phenomena discussed previously were applied. Subsequently the solutions to these individual problems were applied iteratively to develop a solution to the complete problem. The iterative process basically involves discretizing the process into finite elements, applying the metamodels of the individual solutions to each element and then marching forward with respect to time.

As explained previously, the plastic deformation of the premolded component during mesoscale in-mold assembly involves a three way coupling. Figure 5.11 illustrates the solution strategy for predicting premolded component deformations using the methodology described above. In this strategy, the mesoscale pin is discretized along its length into  $n$  elements. The force applied by the second stage polymer melt flow depends on the location of the melt with respect to the pin. Hence the force applied on each discrete element of the pin varies according to the deformed structure of the pin as illustrated in Figure 5.8. Finally the overall moment on the deformed pin is computed based on the force on the individual discrete elements. This moment is then used to compute further deformation of the pin. Subsequently the

forward time marching was discretized into  $T$  timesteps. In each timestep, the flow front progresses by the requisite amount. The force on each element of the pin during each timestep depended on its location with respect to the melt flow front. The location of each element was determined by evaluating the deformation level of the overall structure of the pin due to the force applied in the previous timestep. The numerical value of the force was calculated on each element using the metamodel of the force on the premolded component as a function of flow front progression illustrated in Figure 5.11. Finally the force on the individual elements was integrated to evaluate the net effective force on the pin. This force was used to evaluate the overall deformation of the pin using the metamodel for deformation as a function of applied force. A forward time marching based on the discretization timestep was then applied until the flow front reached the opposing flow. This position was determined using the metamodel for the weld-line location. This is because the two opposing polymer melt flows exert forces on the premolded component only while they are moving across the component. However, the flows come to a complete stop once they meet each other at the weld-line location. They then cease to apply any force on the premolded component, and there is no further deformation of the premolded component.

Once the flow comes to a stop, thereby removing transverse forces on the premolded component, the premolded component relaxes elastically. The residual deformation is purely plastic. This plastic deformation can then be used to determine whether the particular temporal misalignment can be used to manufacture acceptable in-mold assembled mesoscale revolute joints or not.

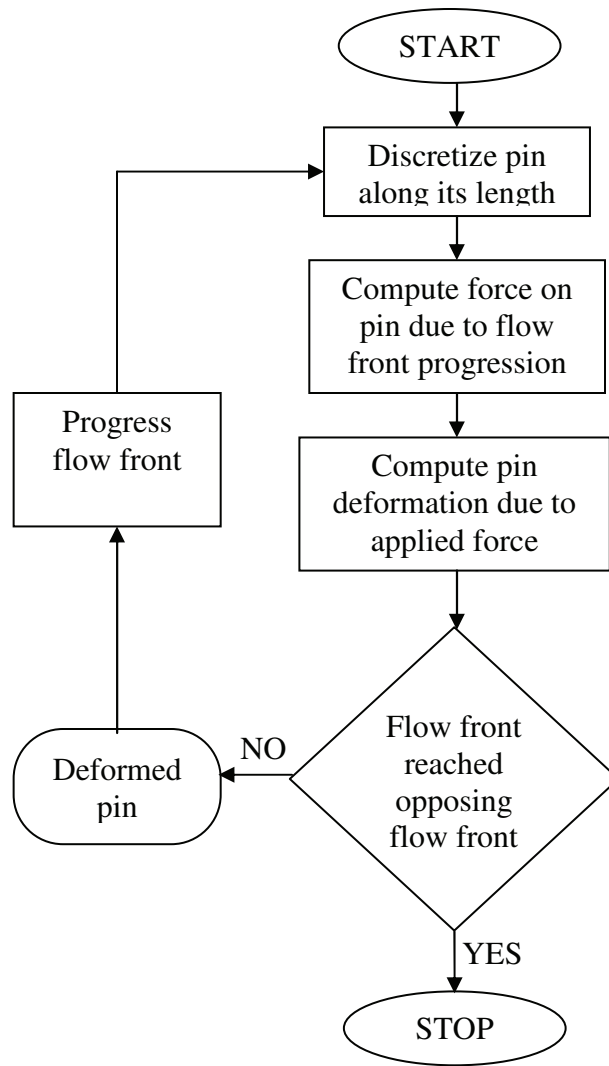


Figure 5.11 Modeling framework for predicting pin deformation during mesoscale in-mold assembly process using iterative coupling

## 5.6 Results and Discussion

Experiments were conducted on a Milacron Babyplast injection molding machine. *Acrylonitrile Butadiene Styrene* (ABS) manufactured by *Ashland Chemicals* as the material was chosen for the premolded component. For the second stage material *Grillamid-L16 LM* (Nylon 12) manufactured by *EMS Grivory* was chosen.

Table 5.2. Injection molding parameters

	Stage 1	Stage 2
<b>Material</b>	ABS	NYLON 12
<b>Injection Temp.</b>	240°C	190°C
<b>Injection Velocity</b>	12 cc/s	12 cc/s
<b>Injection pressure</b>	600 bars	600 bars
<b>Cooling time</b>	3s	3s

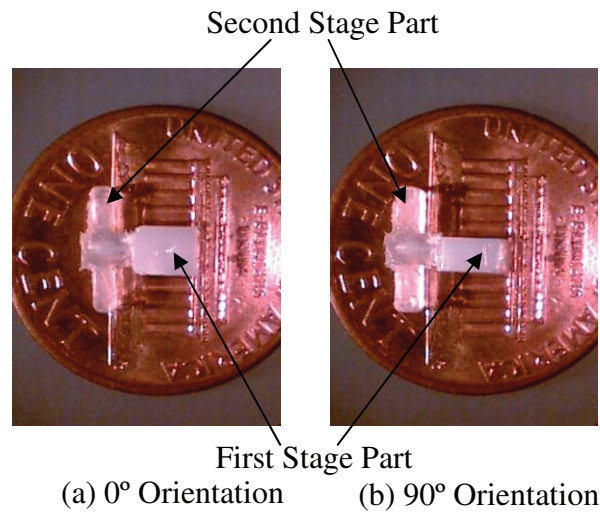


Figure 5.12 In-mold assembled mesoscale revolute half joint

Tests conducted to measure the weld-line strength of the second stage material Nylon-12 revealed that the failure strength of the cold weld-line for this material is approximately 82% that of the native material. The images of the dogbone specimen tested for weld-line strengths are illustrated in Figure 5.13. This strength is sufficiently high for making good quality injection molded parts. Also, owing to the low difference in melting temperatures of the two polymers, this material combination was appropriate.

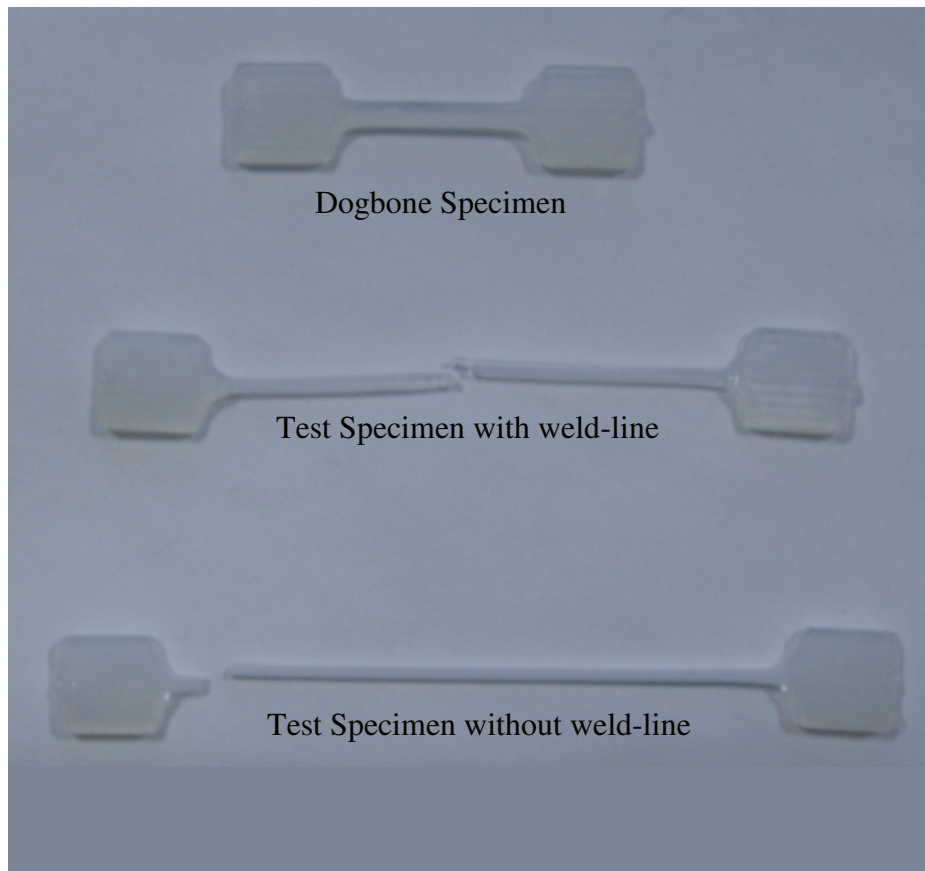


Figure 5.13 Dogbone specimen tested for weld-line strength of Nylon-12

The processing parameters that were used are described in Table 5.2. Figure 5.12 shows a successfully in-mold assembled mesoscale revolute half joint fabricated using the bi-directional filling strategy discussed in this paper. The gates were positioned exactly equidistant from the mesoscale feature on the premolded component for this particular half joint, i.e., there was no temporal misalignment. Subsequently experiments were conducted to measure the plastic deformation of the premolded component by varying the gate misalignment temporally. Deformations were measured using the same strategy as described in Figure 3.20 in chapter 3.

In order to develop a computational model of the plastic deformation of the premolded component, the methodology described in the previous section was used.

The non-Newtonian viscous properties of Nylon were modeled using a cross-WLF viscosity model. The properties of the Nylon 12 that were used are listed in Table 5.3. Subsequently CFD simulations in FLUENT 6.3.26 were conducted using the strategy described in section 3.5.1 to compute the force as a function of the flow front progression.

Table 5.3 Flow properties of NYLON-12

<b>Density</b>	870 kg/m <sup>3</sup>
<b>Tau</b>	343505
<b>n</b>	0.196
<b>D1</b>	2.24342E+11
<b>D2</b>	323.15
<b>D3</b>	0
<b>A1</b>	26.96
<b>A2</b>	51.6

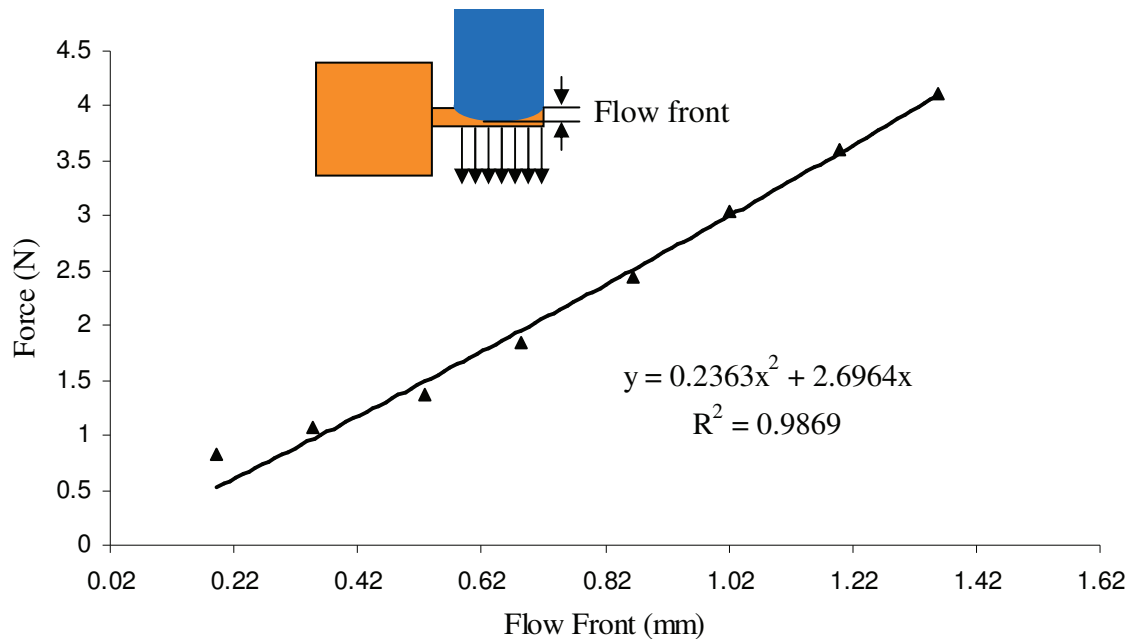


Figure 5.14 Force on Premolded Component as a Function of Flow Front Progression

CFD simulations in FLUENT 6.3.26 reveal that a drag force builds up on the premolded component as the second stage flow front progresses. This drag force

builds up monotonically on the premolded component as described in section 3.5.1. The metamodel of the force on the premolded component as a function of flow front progression is illustrated in Figure 5.14.

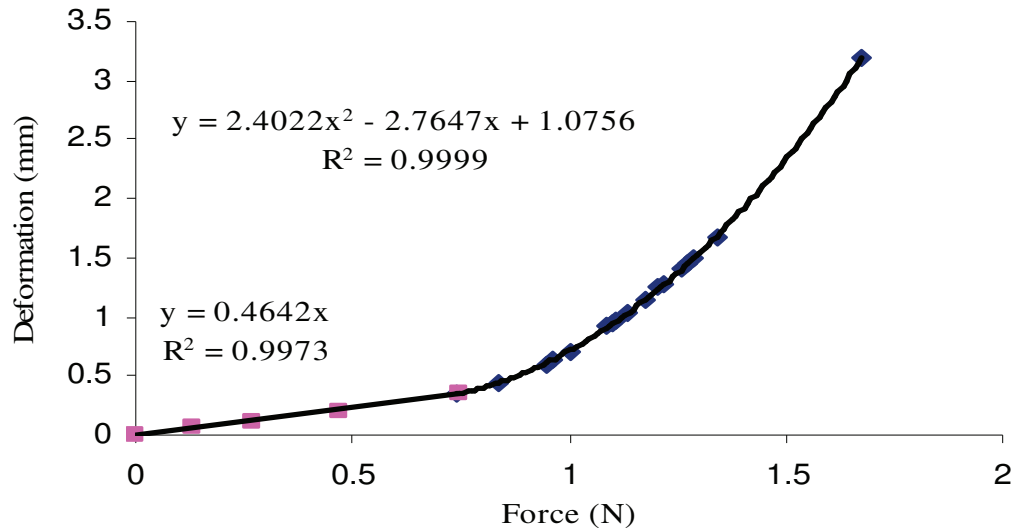


Figure 5.15 Deformation as a Function of Applied Force

Next the elastic-plastic deformation of the premolded component as a function of the applied force was computed. A pressure was applied on the premolded component which resulted in elastic-plastic deformation of the premolded component. To solve for this deformation, a finite element model was developed using ANSYS 11.0 as described in section 5.5.3. In order to develop the metamodel for the deformation using ANSYS FE simulations, the effective force was modeled as a pressure distribution using the equation described in the Figure 5.9. Table 3.2 tabulates the non-linear material properties of ABS used for the computing the elastic plastic deformation of the premolded component. The metamodel of the premolded component deformation that was thus obtained is illustrated in Figure 5.15. A sample ANSYS 11.0 simulation result for a force of 1.2 N is illustrated in Figure 5.16.



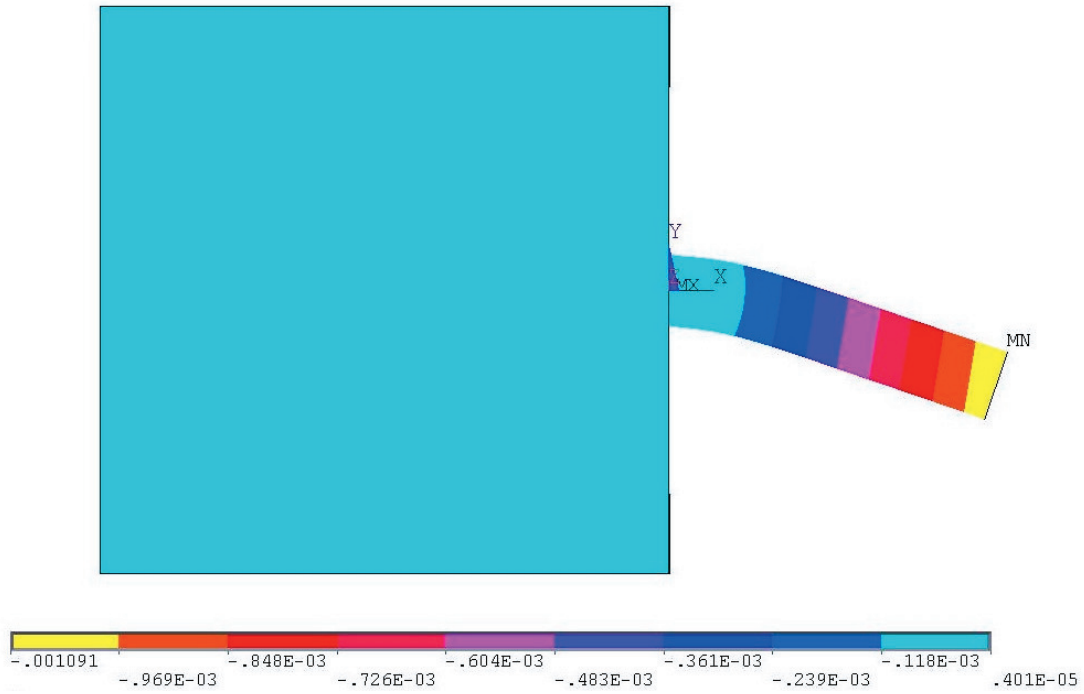


Figure 5.16 Sample ANSYS 11.0 simulation result for force on 1.2 N

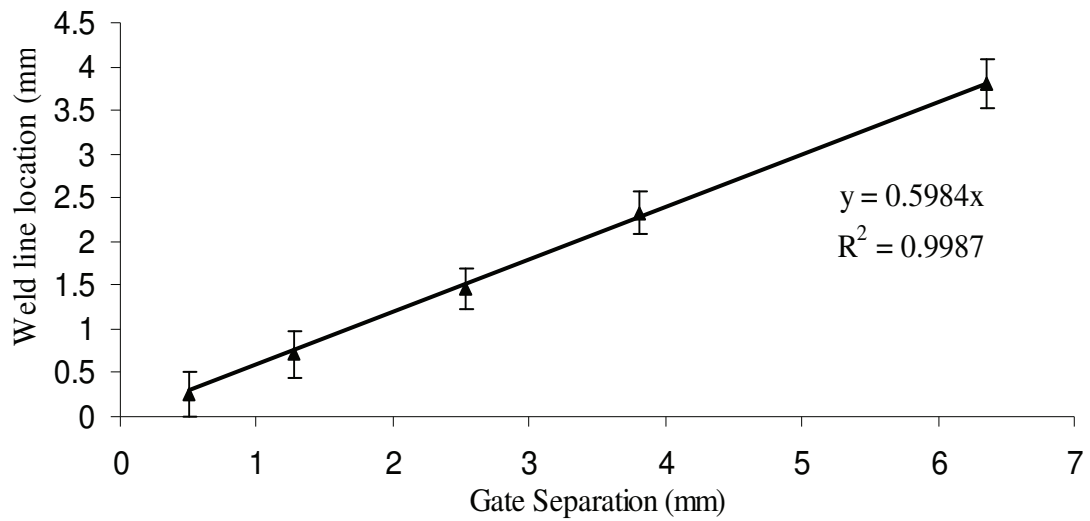


Figure 5.17 Determination of Total Flow Front Progression

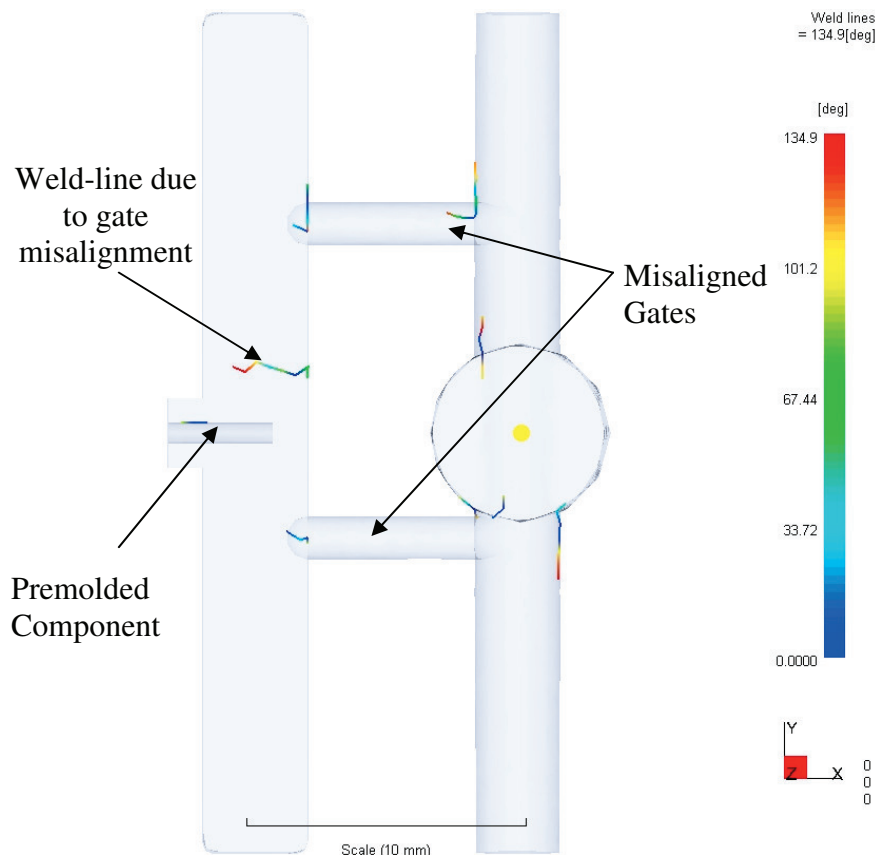


Figure 5.18 Sample simulation result in Moldflow for gate misalignment of 1.25 mm

To predict the location of the weld-line in the in-mold assembled part, we conducted mold filling simulations in Moldflow Plastics Insight 7.1. The metamodel of the weld-line location for the given gate misalignment is illustrated in Figure 5.17. A sample simulation in Moldflow for a gate misalignment of 1.25 mm is illustrated in Figure 5.18.

The iterative strategy described in section 5.5.5 was then employed to obtain the net plastic deformation of the premolded component as a function of the temporal misalignment of gates. In order to confirm the convergence of our solution, the number of discretization elements for the pin ( $n$ ) and the number of timesteps ( $T$ )

were varied until mesh independence was achieved. Mesh independence for a convergence of 0.05% final deformation was achieved at  $n = 20$  and  $T=100$ .

These individual metamodels were iteratively solved to computationally obtain the final plastic deformation of the premolded components as a function of the gate misalignment. The experimental deformations of the premolded component with varying gate misalignment and the corresponding computational model is illustrated in Figure 5.19. In order to verify the quality of our solution, discretization independence checks were performed by increasing the total number of elements used to discretize the premolded component until convergence was reached.

As can be seen in the figure, the computational model is in excellent agreement with the experimental values of plastic deformation when the temporal misalignment is kept low. However, for higher values of plastic deformation the model over predicts the plastic deformation. This phenomenon is observed because the fluid flow model used to predict the forces on the premolded component assumes the premolded component to be a rigid structure. Hence the structure in the computational model provides a higher resistive force. However, in reality, the premolded component is actively deforming due to the force applied by the second stage polymer melt. Hence the true force on the premolded component is lower compared to that predicted by the computational model. This resistive force and the disagreements between the predictive forces and real forces would be more prevalent when the deformations of the premolded component are higher. This happens at higher values of flow front progression or temporal misalignment.

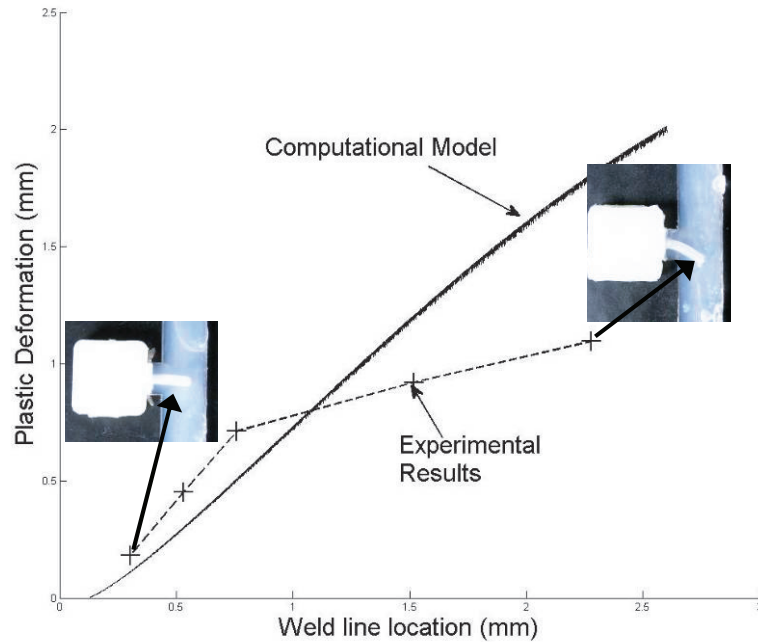


Figure 5.19 Plastic deformation of mesoscale premolded component relating to the gate misalignment

This theory is reiterated by the online strain measurements that have been performed. The experimental data and the corresponding computational model illustrated in Figure 3.10 clearly indicate that as the flow front has progressed beyond a certain point the model overpredicts the force on the premolded component. This clearly indicates that the computational model is powerful only for small values of plastic deformation or gate misalignment.

From the manufacturing perspective, high values of deformation are clearly unacceptable parts. Hence from the quality control point of view, plastic deformations which are higher than 15% of the length of the pin are definitely defective. In the case under consideration mesoscale parts with plastic deformation of premolded component greater than 0.6 mm are of no manufacturing interest. Therefore it is not of any practical interest in developing computational models for high values of plastic

deformation. At lower values of plastic deformation, the computational model is in agreement with the experimental results by upto 5%. The computational model developed therefore suffices for predicting the plastic deformation of the premolded components. This modeling strategy can be used as a design tool to select the acceptable level of gate misalignment for manufacturing in-mold assembled mesoscale revolute joints using the bi-directional filling strategy.

## **5.7 Summary**

This chapter described an alternative strategy for controlling premolded component deformations. This involves a mesoscale in-mold assembly strategy having a multi-gate mold design allowing for bi-directional filling. This strategy allows for: (1) control of deformation of premolded components without use of radial supports as described in chapter 4, and (2) use of polymers of comparable melting points for in-mold assembly. This chapter establishes the technical feasibility for using bi-directional flow of second stage polymer melt for manufacturing in-mold assembled mesoscale revolute joints to overcome challenges presented by alternative radial support strategy.

This chapter also presents the first attempt at studying the effect of temporal misalignment of gates on the plastic deformation of premolded components. The results presented indicate that mesoscale premolded components are highly sensitive to the temporal misalignment of the gates. Methods are reported to select the appropriate temporal misalignment that can be tolerated during manufacturing of functional mesoscale revolute joints using the bi-directional filling approach.

A modeling approach to solve this complex physical problem by employing metamodels of decoupled systems, and subsequently obtaining a solution using iterative techniques is reported. This approach for predicting plastic deformations of premolded components as a function of the gate misalignment has been demonstrated.

Researchers can use the advances reported by this work to predict forces on the mold inserts during injection molding. The computational model presented in this chapter eliminates the need to perform any further experiments to understand the process to manufacture injection molded parts in a mold containing mesoscale soft mold inserts. Manufacturers can therefore use the methods presented in this work as a generalized tool to select the right mold design parameters and processing parameters for manufacturing injection molded parts in a mold containing mesoscale soft mold inserts.

## 6 Characterization and Control of Pin Diameter

### 6.1 Motivation

For proper functioning of a revolute joint, a clearance fit is required between the pin and the hole. At the macroscale, this clearance is ensured by the shrinkage of the pin after cooling and ejection. This is because the pin is molded in the second stage. As the pin shrinks during the solidification process, it moves away from the cavity and provides the clearance for the joint to function. The value of clearance in the macroscale joint can be controlled by carefully selecting the process parameters and the material for the pin.

However as described in previous chapters of this dissertation, at the mesoscale the cavity is molded in the second stage. This strategy is counter intuitive based on the experiences at the macro-scale. At the macroscale, as the cavity shrinks around the pin, the joint is jammed. After cooling and ejection, the shrinkage of the hole leads to an interference fit. This may lead to a non functional joint. Figure 6.1 illustrates this concept. In the figure,  $d_h$  is the hole diameter and  $d_p$  is the pin diameter. So a fundamental question is why this counter-intuitive strategy works at the mesoscale.

However, as described in the previous chapters macro scale concepts can not be directly scaled down to the mesoscale. Hence we need to develop a better understanding of how clearances are obtained in in-mold assemblies at the mesoscale. Several scenarios also necessitate the clearances to be engineered to meet the design requirements. Hence, there is an impending need to develop manufacturing methods

to control the clearances in mesoscale in-mold assemblies so as to give the designer the freedom to choose the appropriate clearance for the functioning of the component.

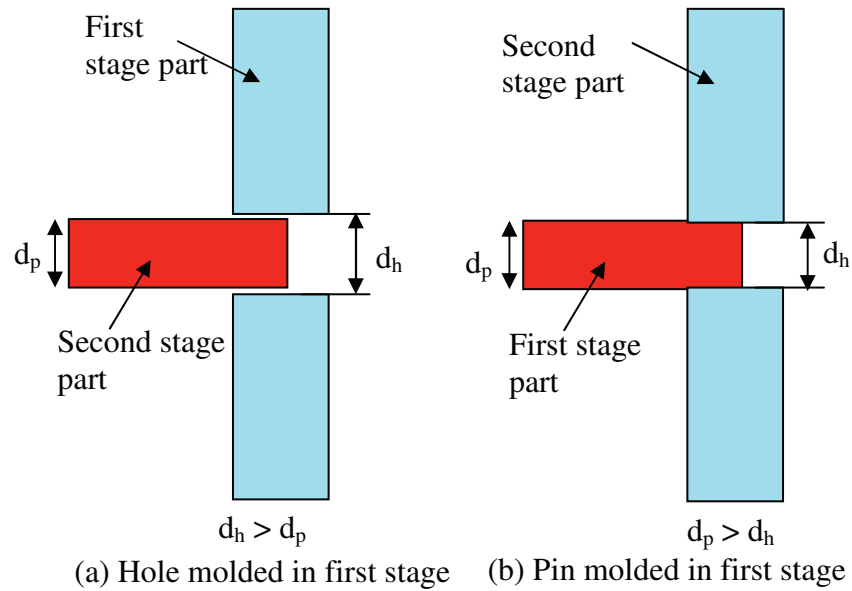


Figure 6.1 clearances in in-mold assembled Macroscale revolute joints

This chapter will show that at the mesoscale, the joint jamming is prevented because of the deformation of the pin under the compressive loading during the second stage molding. It will also describe features in the mold that can control the pin deformation and hence control the joint parameters. Experimental data and computational models to show how mesoscale revolute joints can be formed will be presented. The methods described in this chapter can be used to fabricate mesoscale in-mold assembled revolute joints with appropriate clearances.

## 6.2 Clearances at the Mesoscale

At the mesoscale, fabricating a mesoscale revolute joint involves premolding the component with the mesoscale features in the first stage then forming the second component in a second stage. However, the high pressure, high temperature polymer



injected in the mold cavity during the second stage causes the mesoscale features in the premolded component to deform plastically, as illustrated in Figure 3.6. In order to inhibit this deformation, Chapter 4 describes a novel mold design strategy which involves supporting the premolded component by 20-33% of its length. This approach is illustrated in Figure 4.3.

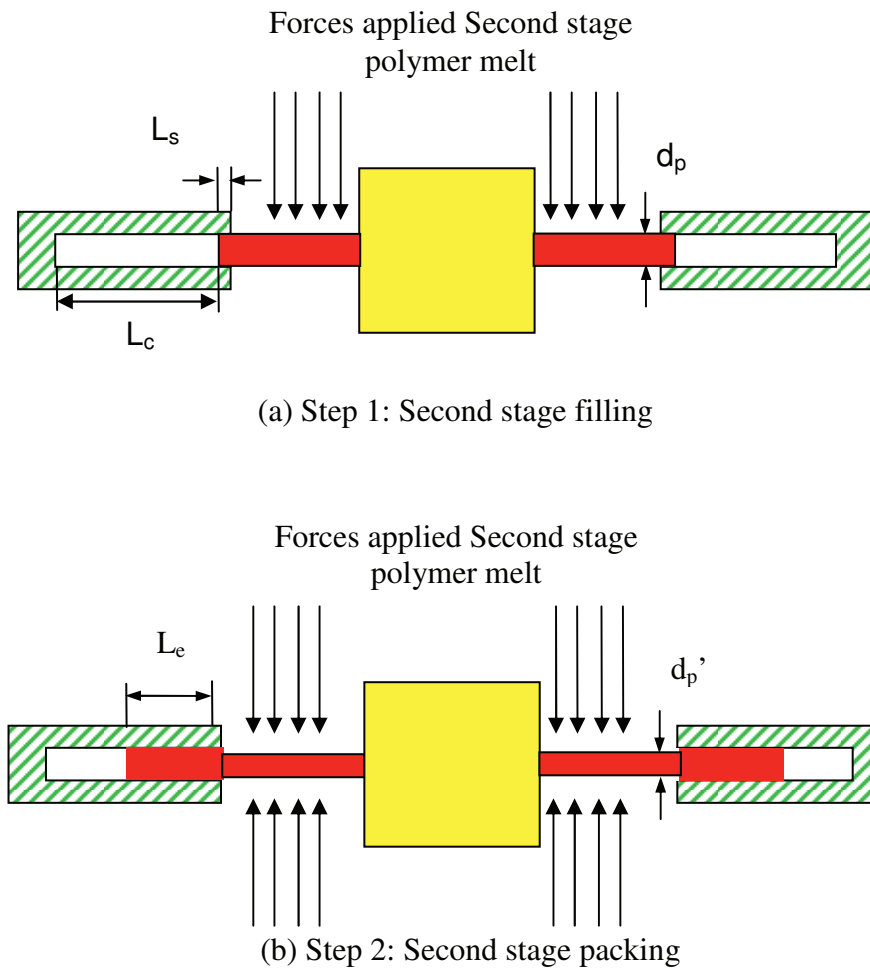


Figure 6.2 Mold design strategy for creating mesoscale in-mold assembled revolute joints

Assembly clearances in the mesoscale revolute joint can be produced by the reduction in diameter of the premolded component after second stage injection. This

reduction in diameter is caused by the aforementioned plastic deformation of the premolded component as illustrated in Figure 6.2. In the figure,  $d_p$  is the diameter of the pin and  $L_s$  is the radial support length (as described in Chapter 4) provided to the premolded mesoscale pin during the second stage injection.

$L_c$  is the support cavity length i.e. the length of the cavity in the radial supports used to constrain the mesoscale premolded component. The support cavity length  $L_c$  plays an important role in determining the final diameter  $d_p'$  and the change in overall length  $L_e$  of the mesoscale pin after second stage injection, and therefore the level of clearance in the revolute joint.

In order to understand the effect of the support cavity length, let us review the complexity of the mesoscale in-mold assembly process. In the first step, the first stage part is molded and the side core supports are retracted as illustrated in Figure 6.2. During the second stage cavity filling, the mesoscale premolded component acts as a soft mold insert for the second stage polymer melt flow. The premolded component is made of an elastoplastic material that can plastically deform due to the forces applied by the second stage melt [90, 95]. This bending can be inhibited by the presence of the radial supports. However, in the second step of the molding process, a very high compressive load is applied to the premolded mesoscale component after completion of cavity filling. This compressive load can also cause plastic deformation in the form of extrusion of the premolded component, as previously illustrated in Figure 6.2. This plastic deformation leads to change the diameter of the mesoscale premolded component from  $d_p$  to  $d_p'$ . During this plastic compression of the mesoscale pin, the portion of the pin which is supported by the radial support gets extruded into the

cavity. The final length of the pin that is supported by the radial supports is  $L_e$  as illustrated in the figure. Hence the length of the extrusion can be  $L_e - L_s$ . However this length of extrusion can not be greater than the support cavity length  $L_c$ . This gives rise to the following constraint:

$$L_e \leq L_s + L_c \quad 6.1$$

where  $L_s$  becomes the design requirement in order to prevent the plastic bending of the premolded component due to the second stage polymer melt flow. Hence by controlling  $L_c$ , we can control the length of the extrusion. This will also have an effect on the final deformed diameter of the mesoscale pin  $d_p'$ .

Another important factor that needs to be considered is development of asymmetry in the joint due to the in-mold assembly process. As described previously, the second stage polymer melt flows around the premolded component during filling. This flow applies a force on the premolded component resulting in its elastic-plastic deformation. Although use of appropriate radial supports inhibits the plastic deformation, the premolded component continues to deform elastically due to the applied force. After completion of filling, this transverse force is removed. The premolded component, which has already deformed elastically, now attempts to recover from this deformation. However at the end of filling, a radial compressive force is applied on the premolded component during the packing/holding phase (Figure 1.2). This force causes the premolded component to deform plastically as illustrated in Figure 6.2. However due to the pre-existing elastic deformation of the premolded component, the plastic deformation resulting from the radial compressive force is asymmetric. This is illustrated in Figure 6.3. This asymmetry in the

premolded component leads to a non-functional revolute joint. Hence it is important to control it.

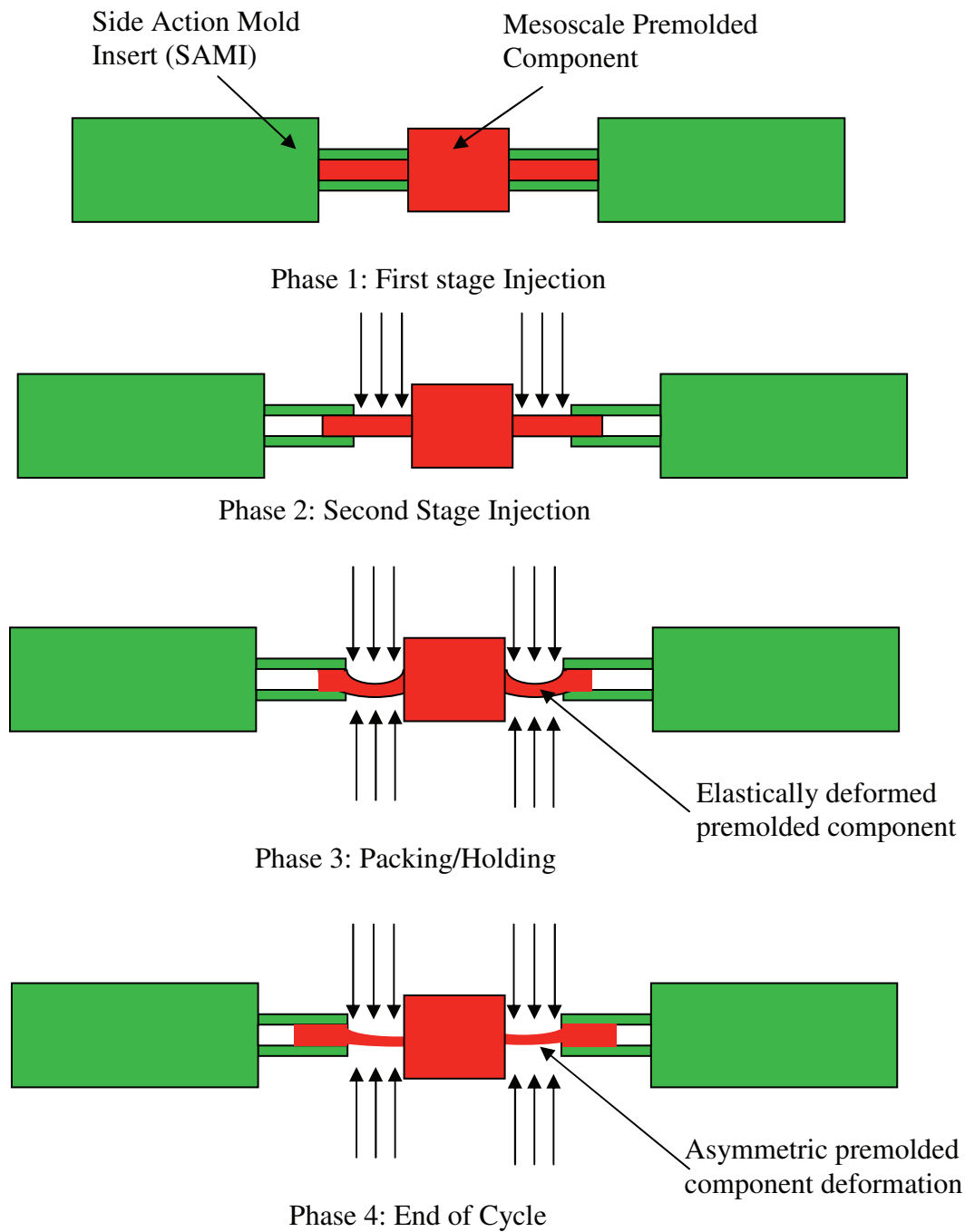


Figure 6.3 Asymmetric deformation during second stage injection and packing

From the mechanics perspective, it is important to keep the change in diameter  $d_p' - d_p$  as low as possible. This is because a large change in this diameter induces high levels of plasticity in the mesoscale component. This causes the part to be considerably weaker than the original part because of the reduced cross section area and moment of inertia. However, from the manufacturing perspective this plastic deformation is necessary to prevent jamming in the in-mold assembled mesoscale revolute joint.

Hence there is a need to characterize and control this plastic deformation which leads to change in the diameter of the premolded mesoscale component. While controlling the change in diameter it is also important to control the asymmetry in the premolded component deformation. It is therefore imperative to develop methods which will enable us to fabricate mesoscale in-mold assemblies with appropriate assembly clearances without compromising on the component strength.

In order to characterize and control the plastic deformation, one should identify the parameters that need to be considered. These include *geometric parameters* which are the dimensions of the premolded component and the second stage component, *mold design parameters* which are the length of the support cavity length  $L_c$ , the radial support length  $L_s$  and other mold dimensions such as sprue and runner dimensions, *material properties* which are the structural properties of the premolded component and the flow properties of the second stage polymer melt, and *molding conditions* which are used during the in-mold assembly operation, such as temperature and pressure of the melt.

To develop a predictive model for the plastic deformation of the mesoscale premolded component, there is a need to develop an understanding of the compressive force that will act on the component. The packing pressure parameter of injection molding can be used to determine the compressive pressure applied on the premolded component after taking into account an effective pressure drop inside the cavity. This force can then be applied to a computational finite element solver to obtain the configuration of the deformed premolded component resulting from the second stage filling. To solve the FE problem a time-stepped solution had to be obtained. In the first time-step, the pin which was radially supported was subject to a transverse force which was applied by the second stage polymer melt flow. This caused the pin to deform elastically. The next time-step began when the filling was completed. In this time step, a compressive force was applied on the pin due to the packing pressure. The final solution to predict the pin diameter therefore simulated the actual injection molding conditions during in-mold assembly. The boundary conditions used in the FE solver for the two time-steps are illustrated in Figure 6.4. In the figure,  $U_x$ ,  $U_y$  and  $U_z$  are the allowed displacements in the x, y and z directions respectively.  $L_c$  and  $L_s$  are described earlier in the section.

In order to validate the change in diameter predicted by the finite element model, it is necessary to compare the results of the FE simulations with experimental results. Then next section will outline the experimental approach used to determine the diameter of the mesoscale premolded component after the second stage injection.

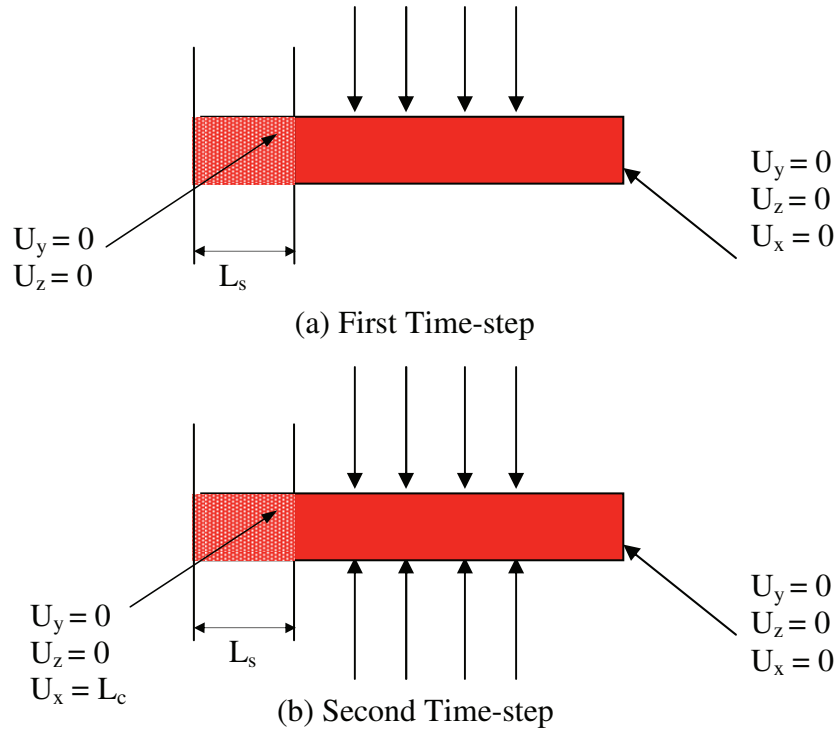


Figure 6.4 Boundary conditions for finite element solver

### 6.3 Experimental Setup

In order to establish the effect of the pin diameter on the plastic deformation of pin, experiments were conducted at the macroscale to verify the joint jamming after second stage injection. A macroscale in-mold assembled revolute half joint with pin diameter of 6.35 mm was fabricated. The first stage and second stage parts designed for this experiment are illustrated in Figure 6.5. It is worthwhile to note at this point that at the macroscale, the molding sequence involved molding the cavity in the first stage for in-mold assembly. However in this experiment this molding sequence is reversed. This involves the pin being molded in the first stage and the cavity in the second stage. Subsequently, the change in the diameter of the pin after the second stage molding was recorded to characterize the plastic deformation.

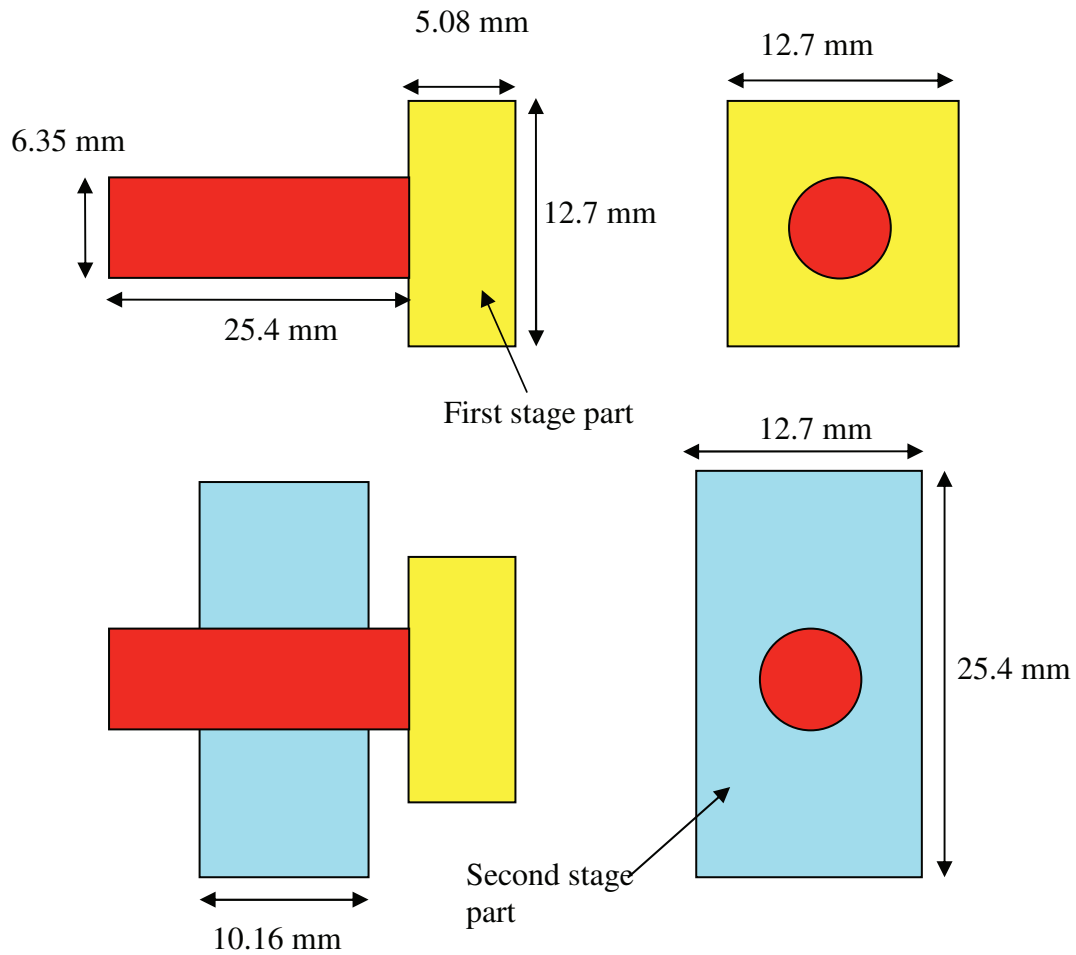


Figure 6.5 Experimental setup for macroscale experiments

Subsequently experiments were conducted at the mesoscale by varying the pin diameter  $d_p$  between 0.79 mm to 1.59 mm. This is illustrated in Figure 6.6. Experiments were conducted for five different diameters. 6 samples were molded for each data point and the average change in diameter was recorded. The base of the premolded mesoscale pin was kept macroscale with dimension 6.35 mm X 6.35 mm in order to make it easier to record the diameter variation in the pins. However, since the variation in pin diameter is dependent only on the dimensions of the mesoscale



feature, the results of these experiments would be valid for smaller base dimensions as well.

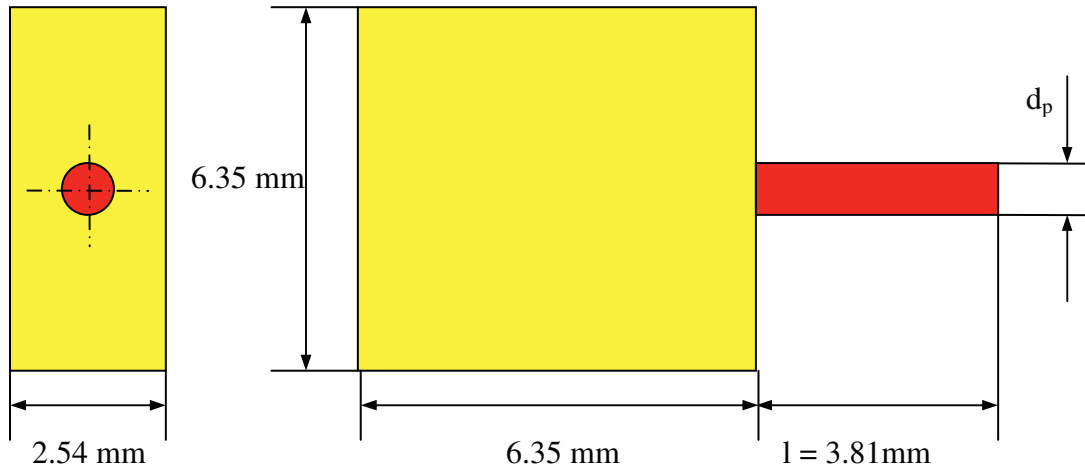


Figure 6.6 Premolded component for experiments

The second stage mold design was kept unchanged for all the different pin diameters. This ensured that the force applied by the melt flow on the premolded component was not affected by the second stage mold dimensions. The second stage mold is illustrated in Figure 6.7. For this experiment, the length of the support cavity  $L_c$  was kept constant at 1.27 mm. This experiment helped determine the cut-off pin diameter at which the mesoscale in-mold assembly methods can not be applied.

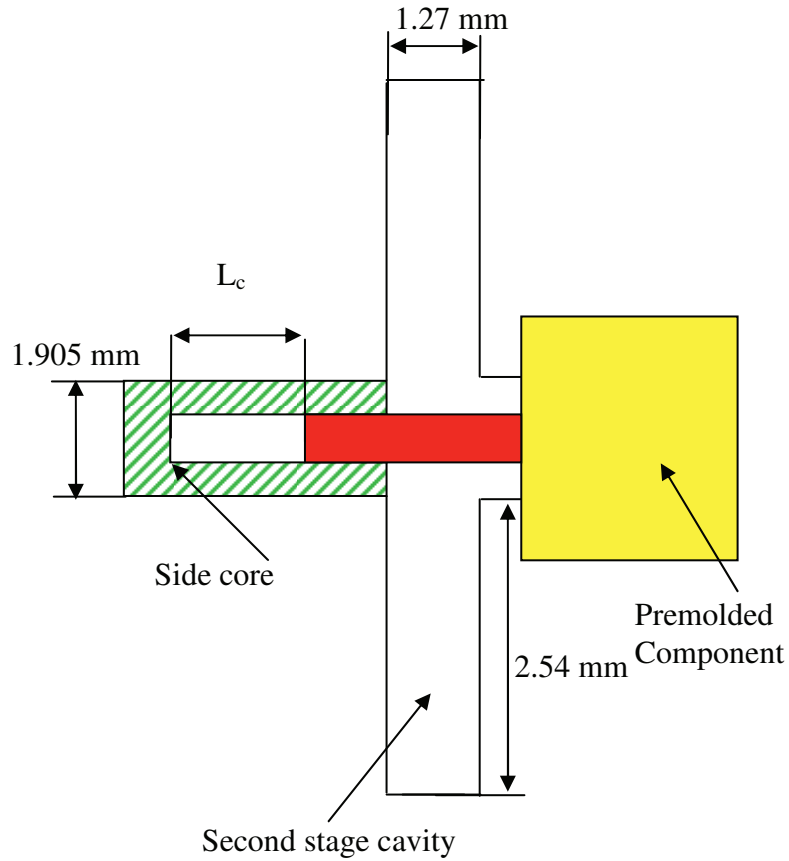
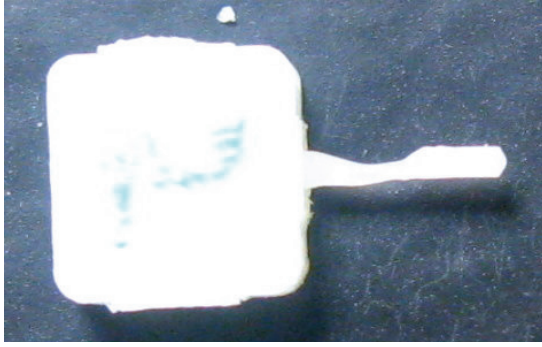
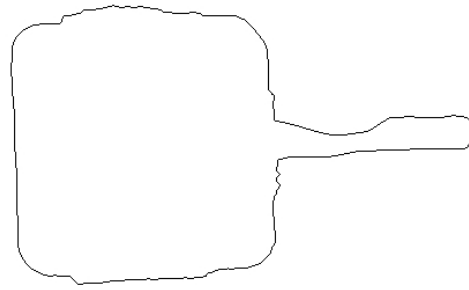


Figure 6.7 Second stage mold design

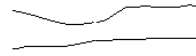
As discussed previously, when a compressive radial force is applied on the pin, the pin tends to deform plastically. However if the pin is unable to elongate when a compressive force is applied, the change in pin diameter will be inhibited. In other words, the change in pin diameter would be directly related to the amount by which it can elongate. The length of the elongation can be controlled by applying a physical stop using a mold piece to prevent the pin elongation beyond allowable limits. This can be accomplished by varying the support cavity length  $L_c$  as illustrated in Figure 6.7. Therefore to control the pin deformation the control parameter  $L_c$  can be chosen appropriately.



Step 1: Part Image



Step 2: Finding Edges



Step 3: Mapping pin diameters

Figure 6.8 Measuring change in pin diameter

To develop an understanding of the effect of the control parameter  $L_c$  experiments were conducted by fixing the pin diameter at 0.796 mm. However the support cavity length  $L_c$  was varied between 0.254 mm and 1.3 mm. This enabled data collection to understand the relationship between the change in diameter and the elongation of the pin.

To measure the change in diameter, the premolded component was separated from the second stage part and it was photographed. Subsequently, the photograph of the premolded component was processed using MATLAB to find the change in diameter relative to the original diameter of the premolded component. The steps taken to find the premolded component deformation are illustrated in Figure 6.8.

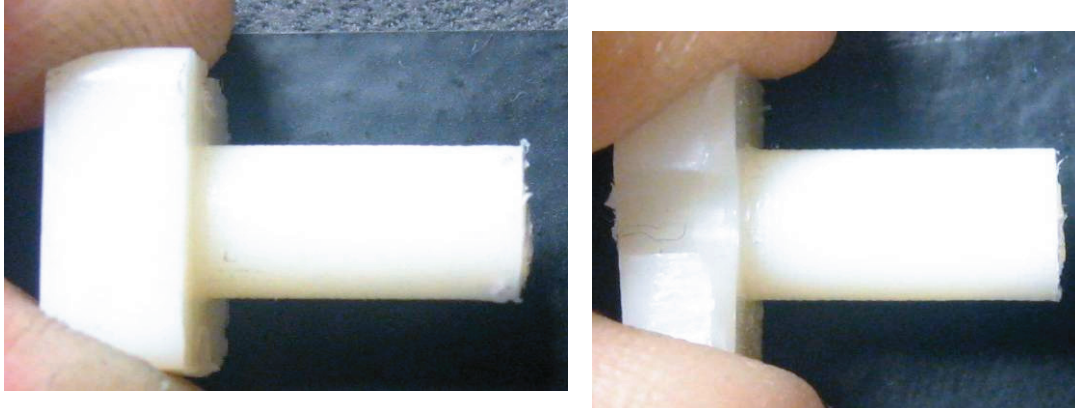
TABLE 6.1. INJECTION MOLDING CONDITIONS

	Stage 1	Stage 2
Material	ABS	LDPE
Injection Temp.	240°C	140°C
Injection Velocity	12 cc/s	12 cc/s
Injection pressure	600 bars	600 bars
Cooling time	3s	3s

A material combination has chosen to ensure the melting temperature of the second stage material is sufficiently lower than that of the first stage material. We chose *Acrylonitrile Butadiene Styrene* (ABS) manufactured by *Ashland Chemicals* as the material for the premolded component. For the second stage material, we chose *Low Density Polyethylene* (LDPE) manufactured by *Dow Chemicals*. This minimizes the thermal softening of the premolded component by the high temperature second stage melt. For the final control parameter (4) molding conditions, processing parameters described in TABLE 6.1 were used on a Milacron Babyplast injection molding machine.

#### **6.4 Results and Discussion**

The macroscale premolded pin before and after second stage injection can be seen in Figure 6.9. However, the pin was not easily removed from the second stage component, indicating that the desired clearance was not achieved. Also, there was no appreciable change in diameter of the part after second stage injection, which indicated that all of the deformation during the second molding stage was perfectly elastic. Hence macroscale in-mold assemblies can clearly not be produced using the molding sequence suitable for mesoscale in-mold assemblies.



(a) Before second stage injection

(b) After second stage injection

Figure 6.9 macroscale premolded component before and after second stage injection

The next experiment involved premolded components of different pin sizes at the mesoscale. These premolded components were inserted in the second stage molds and the polymer melt was injected. Subsequently the change in diameter of the premolded component was measured using the procedure illustrated in Figure 6.8. A finite element based computational model was developed using ANSYS 11.0 to predict the change in diameter of the premolded component as a function of the pin diameter. The material properties of ABS illustrated in Table 3.2 were used for the purpose of the FE simulations. The experimental results and the corresponding computational model is illustrated in Figure 6.10. A sample simulation in ANSYS 11.0 is illustrated in Figure 6.11. The ANSYS simulation clearly demonstrates the asymmetry in the pin diameters obtained due to the initial elastic deformation of the pin due to the transverse force applied by the second stage polymer melt.

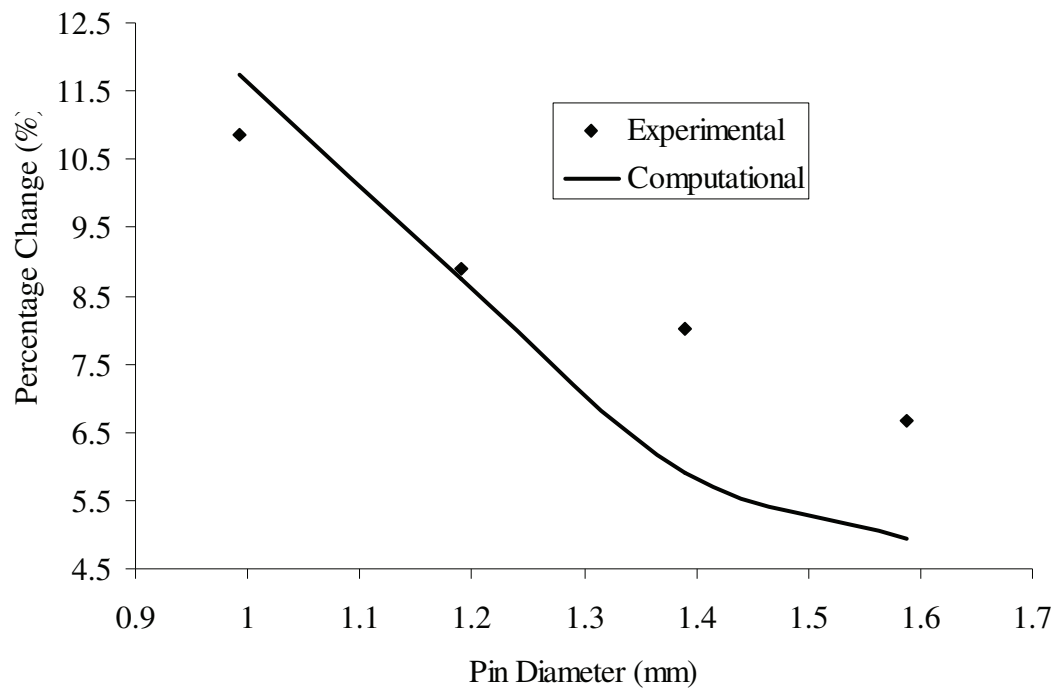


Figure 6.10 Percentage change in diameter of pin v/s original pin diameter

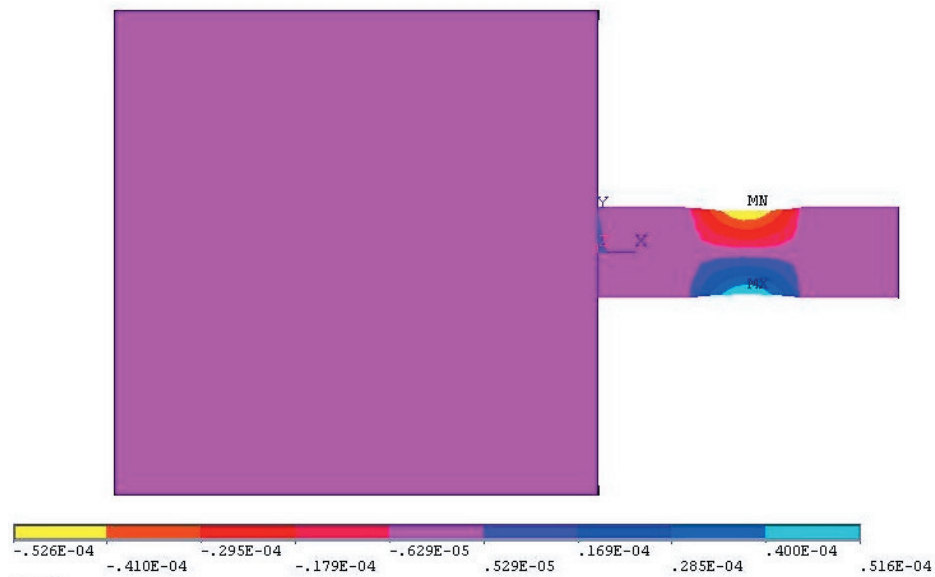


Figure 6.11 Sample ANSYS analysis for a pin diameter of 1.2 mm

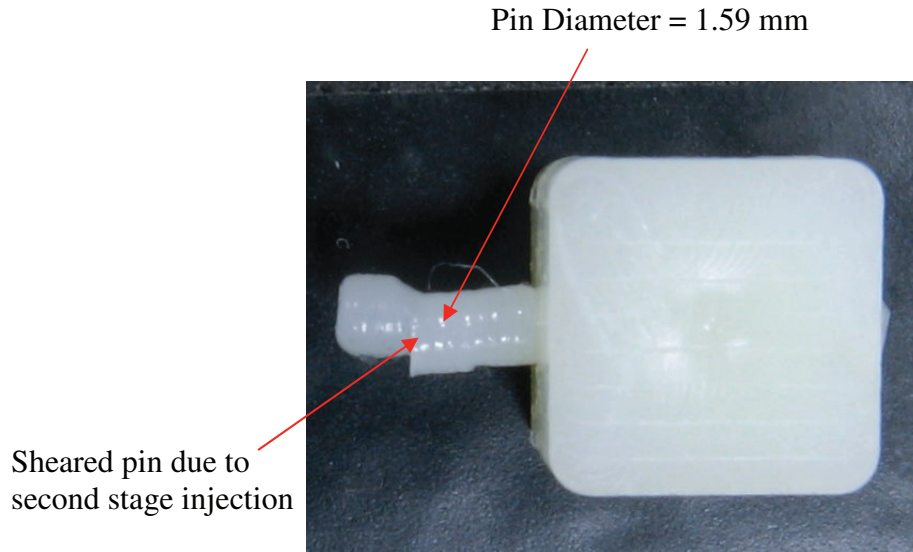


Figure 6.12 Shearing of pin due to excessive drag resistance

The plot in Figure 6.10 clearly indicates that the change in pin diameter of the premolded component due to the second stage has a decreasing trend as the pin diameter is increased. Hence the in-mold assembly process which has been developed for the mesoscale can clearly not be used for the macroscale. For a material combination of ABS and LDPE as is the case here, mesoscale in-mold assembly methods can not be used for pin diameters greater than 1.5 mm. This is observed due to two reasons.

- 1) The change in pin diameter for premolded components with pins greater than 1.5 mm is not appreciable. This may lead to jammed in-mold assembled revolute joints
- 2) The change in cross-section of the second stage melt cavity as the second stage polymer melt encounters the pin in the premolded component increases as the pin diameter increases. This change induces a change in velocity of the second stage polymer melt around the pin. This concept is illustrated in Figure 6.12. A higher

change results in a higher increase in the velocity of the polymer melt. Higher velocities of the polymer melt results in a higher drag force on the premolded component. However the pin is constrained by the radial supports. This inhibits the deformation of the pin. However the pin offers a high resistive force to the drag force. This resistive force may result in shearing of the pin as illustrated in Figure 6.12.

Manufacturers can find the delimiting diameter at which mesoscale methods can not be used by conducting a simple finite element simulation to predict the change in diameter of the premolded component as the second stage polymer melt flows around it. The procedure outlined in section 6.2 can be adopted to conduct these simulations.

Next experiments were conducted by varying the support cavity length  $L_c$  while keeping the pin diameter constant. For the mesoscale premolded pin, 5 samples were produced at 4 different values of support cavity length, and the maximum diameter variation ( $d_v$ ) of the pin was recorded as a function of the length variation ( $L_v$ ) due to extrusion ( $L_e-L_s$ ). To accurately measure the diameter, image processing techniques as illustrated in Figure 6.8 were employed on photographs of the samples. The diameter variation was then obtained from the difference in the maximum and the minimum diameter of the premolded component after the second stage injection. To record the length variation, we recorded the pin lengths of the samples before and after second stage injection. A sample premolded component after second stage injection is illustrated in Figure 6.13. The image clearly illustrates the asymmetry in the variation of pin diameter during the in-mold assembly process.



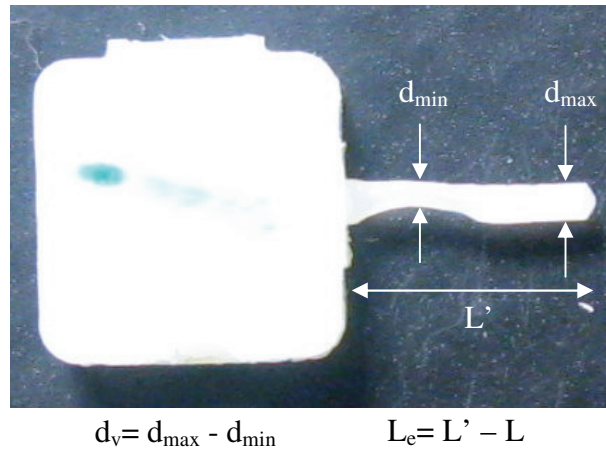


Figure 6.13 Measurement of diameter and length variation of premolded mesoscale pin

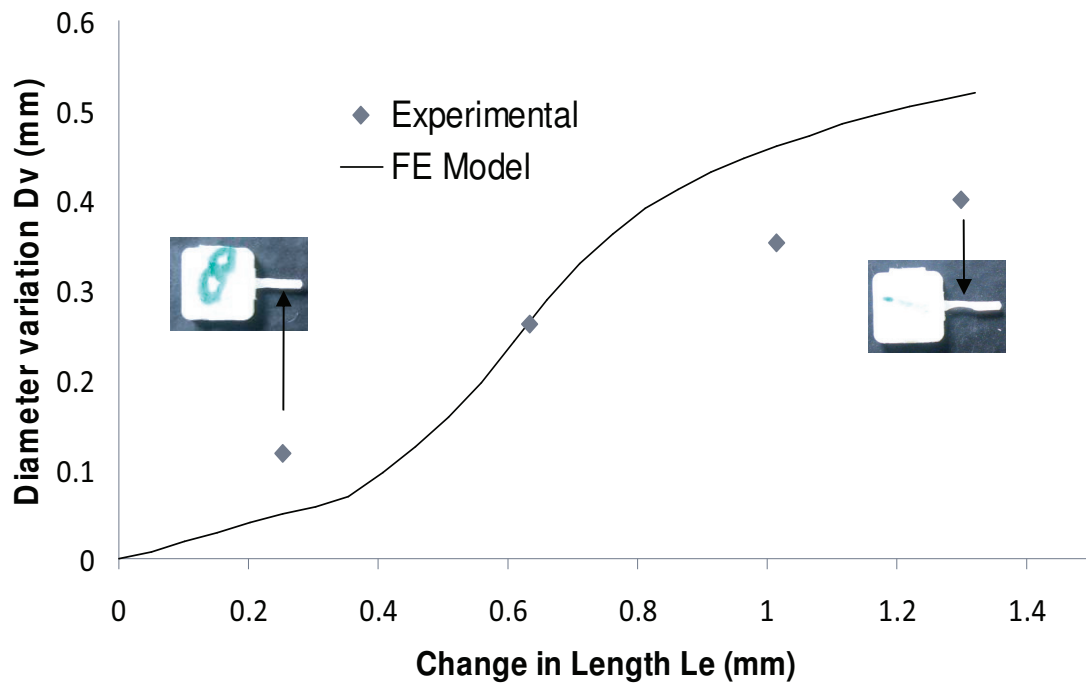


Figure 6.14 Experimentally recorded diameter variation v/s change in length

Figure 6.14 shows the experimental observations and a corresponding computation model relating the diameter variation in the premolded mesoscale components with

the length variation. The variation in length was recorded to be equal to the support cavity length  $L_c$  for the first three experimental points. i.e. the force applied by the second stage melt causes the pin to extrude till it encounters a mold wall. For the last point, the length variation recorded was 1.3 mm. However the support cavity length was 2.54 mm. This was considerably higher than the actual length variation (i.e.,  $L_e < L_s + L_c$ ).

The results clearly indicate that the diameter variation is high for increasing support cavity lengths. However the results also show a tendency of the diameter variation to stagnate for high values of  $L_c$ . This indicates that for low values of  $L_c$ , the pin extrudes such that  $L_e = L_s + L_c$  as explained in equation 1. However for larger cavity support lengths,  $L_e$  reaches a stagnation value such that  $L_e < L_s + L_c$ . After this point,  $L_e$  becomes independent of the cavity support length  $L_c$ . Hence the diameter variation reaches a stagnation value such that it becomes independent of the cavity support length. However the experimentally recorded diameter variation for the highest value of  $L_c$  is as much as 0.38 mm which is 48% of the original pin diameter. This amount of plastic deformation leads to severe weakening in the premolded component. Hence this would render the mesoscale revolute joint unusable. Therefore, it is necessary to develop an understanding of the optimum support cavity length leading to manufacture of functional mesoscale revolute joints.

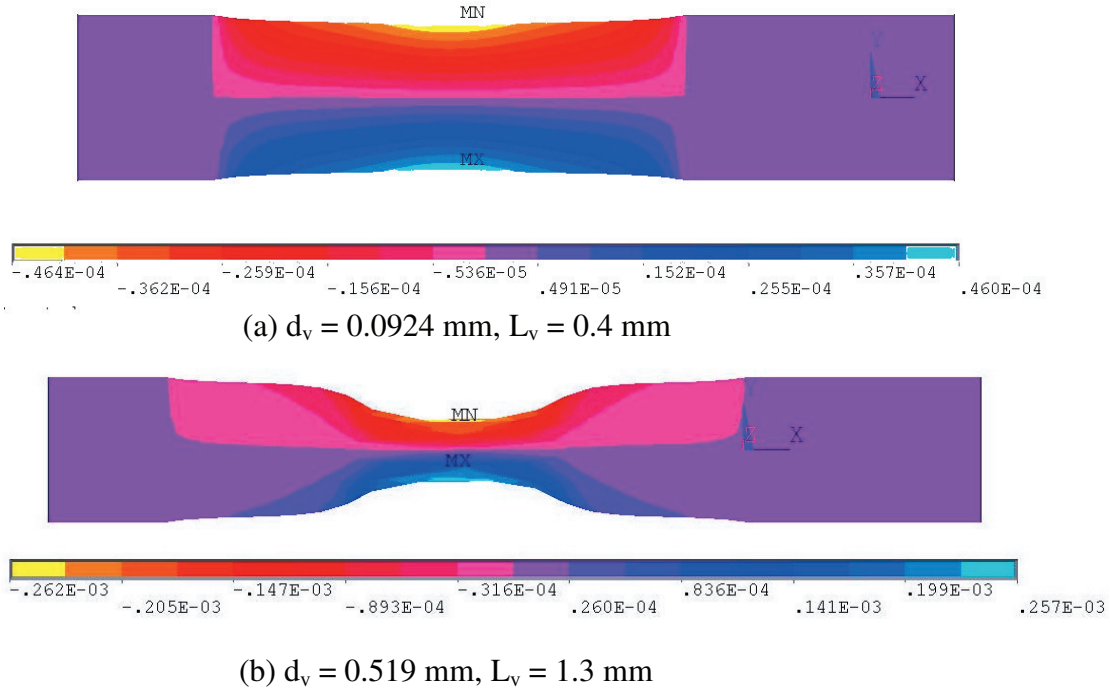


Figure 6.15 Sample results from finite element analysis

The computational finite element model shown in Figure 6.14 predicts the relationship between the variation in length and diameter. The model clearly elucidates that the rise in support cavity length initially causes a larger variation in diameter. However for high values of support cavity lengths, the change in diameter variation is much lower.

Figure 6.15 shows sample results from the finite element analysis that was performed. Figure 6.15 (a) shows the results for a support cavity length of 0.4 mm. These results show an onset of non-linear stress strain behavior in the deformation of the pin due to the forces applied by the second stage melt flow. These forces cause a variation in both diameter and length as illustrated in the figure. Figure 6.15 (b) on the other hand shows a clear tendency of *necking* in the pin for high values of support cavity length. This behavior clearly indicates extremely high values of strains in these regions. From the manufacturing perspective, this kind of behavior is clearly

unacceptable since it results in structurally weak mesoscale revolute joints. Hence it can be safely said that high values of support cavity length are undesirable.

However in order to ensure a smooth running revolute joint, some amount of plastic deformation resulting in diameter change is essential. This diameter change prevents joint jamming. A higher value of diameter change will ensure a smoother joint. Lower diameter changes on the other hand will ensure structural integrity of the joint. Hence the diameter variation is a design parameter that should be selected based on the requirements of the product.

In order to select the right support cavity length, the designer can make a decision on the appropriate amount of diameter variation based on his experience with the material being used. Subsequently, with the help of FE simulations, a relationship can be established between the designed diameter variation and the corresponding required support cavity length. The designer can then use this support cavity length to manufacture the in-mold assembled mesoscale revolute joint satisfying the design requirements.

Figure 6.16 shows a general rule that can be adopted in selecting the support cavity lengths for different pin diameters keeping the other material and geometric parameters same as that described earlier in this paper. This graph was generated based on the computational FE model described earlier in the section for the material and geometry described in this chapter.

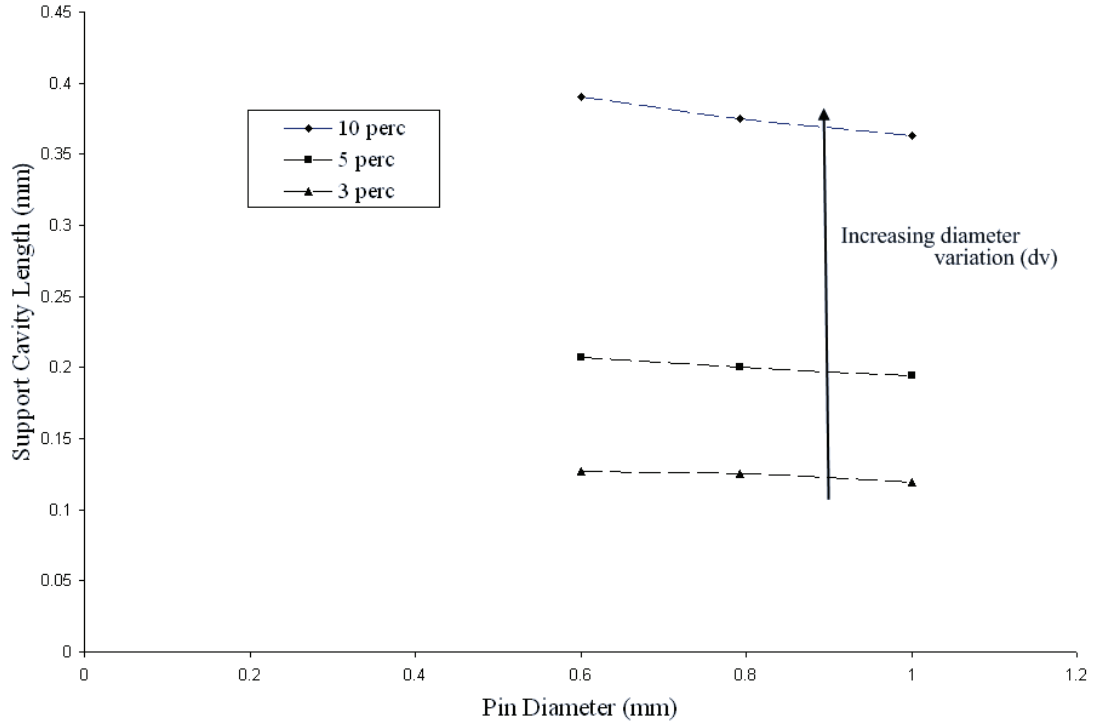


Figure 6.16 Designed support cavity lengths for desired value of diameter variation

Asymmetry in the pin diameter due to the initial elastic deformation during the filling phase causes the joint to be dysfunctional. In order to obtain a functional mesoscale revolute joint, it is also essential to maintain symmetry in the joint. This asymmetry is induced by the initial elastic deformation of the mesoscale pin during the filling phase. Hence along with controlling the plastic deformation of the pin on the premolded component during the first stage injection (as discussed in Chapter 4), it is also important to control the elastic deformation of the pin.

However asymmetry in the pin diameter can not be completely avoided. This is because a nonzero force is applied on the pin by the second stage melt flow. Hence elastic deformation cannot be completely eliminated. However the elastic deformation can be controlled in order to keep the asymmetry in the pin diameter within tolerance levels.

In this dissertation, methods have been described to choose a radial support length based on inhibition of plastic deformation using computational modeling. Subsequently a factor of safety is applied to this radial support length in the actual design of the mold for in-mold assembly. By choosing a high enough factor of safety, the elastic deformation of the pin is also inhibited. This ensures that asymmetry in the pin is within tolerance levels.

Further research is required to develop an understanding of this asymmetry by relating it to both the radial support length and the support cavity length. A higher radial support length ensures that elastic deformation is kept low. However this increases the mold tooling costs. On the other hand a low support cavity length ensures that the pin does not deform and therefore there is no asymmetry. However this may lead to joint jamming.

## **6.5 Summary**

This chapter demonstrates a novel method to control pin diameters in in-mold assembled mesoscale revolute joints. It also establishes the technical feasibility and supports the need to use a reversed molding sequence for manufacturing in-mold assembled revolute joints at the mesoscale.

The following new results are reported:

- 1) Change in diameter of the pin is related to the size of the pin on the premolded component. This result can be used to choose the appropriate in-mold assembly process by delineating between the mesoscale and the macroscale.
- 2) Results are reported for dependence of the final pin diameter on the support cavity length in mesoscale in-mold assemblies.

- 3) A mold design with varying support cavity lengths to control the final pin diameters obtained from in-mold assembled mesoscale revolute joints is described.
- 4) A computational model which describes the relationship between the pin diameter variation and the support cavity length is demonstrated. This predictive model can be used by the manufacturers as a tool for designing the appropriate assembly clearances in mesoscale in-mold assemblies. This model also presents designers with a tool to select the appropriate support cavity lengths for the desired joint properties.

This is the first attempt at studying the assembly clearances in mesoscale in-mold assemblies. Using these techniques mesoscale revolute joints with the required joint characteristics have been successfully molded.

## **7 Design and Development of In-mold Assembled Miniature Robot**

### ***7.1 Motivation***

The previous chapters have presented novel mold design strategies. They also present fundamental computational modeling methods which serve as a design tool to select the mold design and injection molding parameters for manufacturing in-mold assembled mesoscale revolute joints. Any joint which falls under the category of a mesoscale revolute joint as described in chapter 3, can be manufactured using the methods described previously. To demonstrate the generality of these methods this chapter will present a case study. The mold design and computational modeling methods will be used to select the appropriate mold design and processing parameters for manufacturing an in-mold assembled finger inspired robot.

### ***7.2 Challenges in Manufacturing Miniature Robots***

Miniature robots having high maneuverability in tight spaces find several applications in search, rescue and reconnaissance missions, biomedical applications, toy industry etc. Current methods to manufacture robots involve fabrication of individual parts using machining or rapid prototyping among other processes. Subsequently, these parts are assembled manually using small scale fasteners. However, owing to their overall dimensions, development of a cost effective strategy for manufacturing these robots remains a challenge. One of the most significant challenges is the assembly of the individual parts for manufacturing the robot. This is



because, owing to the individual part sizes, it is impossible for a skilled human operator to assemble the parts. Also fasteners are usually unavailable or are very expensive at the smaller scale. If all the abovementioned challenges are addressed, another significant challenge is that a multi part assembly for a miniature robot makes the individual part less rigid. Therefore the individual parts thereby the overall robot is more prone to failure.

To demonstrate the capabilities of the mesoscale in-mold assembly process, we picked a miniature robot, MINIR (Minimally Invasive Neurosurgical Intracranial Robot) which can potentially be used in neurosurgical applications [96]. Figure 7.1 shows the 6 degree of freedom robot which was designed and developed by Pappafotis et al. [96]. The robot needs to be capable of removing intracranial tumors and masses while operating through an extremely narrow corridor in the brain, thus producing minimal disturbance to normal brain tissue. This makes the robot suitable to aid surgeons in performing neurosurgery operations to remove brain tumors. The robot is actuated using shape memory alloys (SMA) which allows robust and accurate motion control which is imperative in such applications. Hence the design has to provide for the SMA wiring. After applying all the design constraints for the overall size and the SMA wiring capability, the joint dimensions had to be restricted to around 0.8 mm. Pappafotis et al. [96] have manufactured this robot using traditional machining and manual assembly methods. Their robot consists of six identical modules having one revolute joint. The six degrees of freedom are finally achieved by attaching these modules together. Each module consists of a five parts which are assembled manually. The robot weighs a total of 2.94 grams. Although the robot has

the capability for individual actuation of joints, the current version actuates all joints together. Hence significant redesign of the robot is required to realize its true potential. The next section will present an improvement to this design using in-mold assembly strategies.

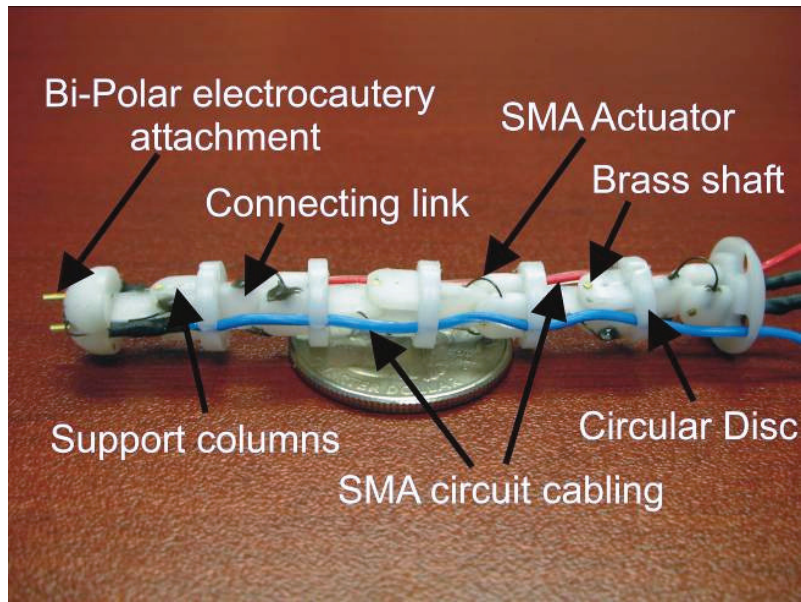


Figure 7.1 MINIR: A 6-DOF robot with the various components [96]

### ***7.3 Robot Redesign for In-Mold Assembly***

One of the most significant limitations of the manufacturing method for MINIR is that the assembly consists of 5 difficult to machine parts. Manual assembly of these miniature parts is also extremely challenging and prone to errors. This may significantly compromise the robustness of the device. Accounting for the application for which the robot is to be used, robustness is of foremost importance.

Considering the challenges presented above, in-mold assembly presents one of the most viable solutions for miniature robot fabrication. This is because the in-mold assembly process eliminates the need for any post production assembly. The nature of

the process ensures that the injection molded parts are manufactured and assembled simultaneously. In-mold assembly utilizes the injection molding process and does not involve any drastic design changes in the mold. The process is an efficient, high throughput process. Being a highly scalable process, the cost of producing each part can be reduced for high production volumes. Methods have been presented in this dissertation to scale down the in-mold assembly process to the mesoscale. Hence they find easy applications in miniature robotics.

Using in-mold assembly process for manufacturing the miniature robot described in the previous section facilitates significant reduction in part count of each module. This makes the device more robust and hence more suitable for the applications being considered. Also manual assembly is completely eliminated which eases the manufacturing process considerably. However designing the robot to be manufactured using mesoscale in-mold assembly methods is non trivial. The design process involves redesigning each module of the robot to satisfy molding constraints.

The objective of this case study was to apply the experimental and modeling methods described in this dissertation to fabricate the 6 degree of freedom robot suitable for neurosurgery. This involves redesigning the modules described by Pappafotis et al. [96] and adapting it to suit the in-mold assembly processes. The design should be such that moldability constraints such as part filling, part ejection constraints are met. Also the design should be such that weld-lines are placed in structurally less demanding positions of the joint. Hence there is a need for an integrated product and process design for manufacturing the robot. Bejgerowski et al. [97] discuss methods for designing a flapping wing drive mechanism while satisfying

moldability constraints. These methods have been extended to be used for designing the molds for manufacturing in-mold assembled modules of the robot.

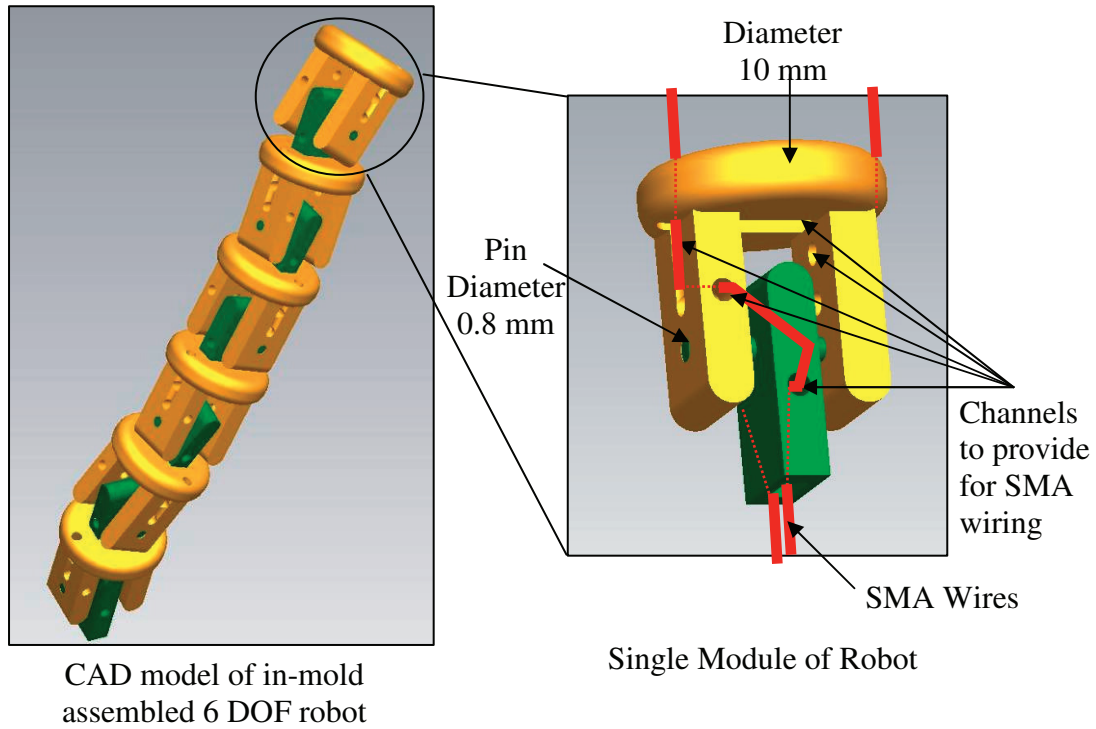


Figure 7.2 Design of Robot for In-mold Assembly

Figure 7.2 illustrates the CAD model of the 6 DOF robot that was designed for in-mold assembly. The robot consisted of 6 modules. The design provides for channels through which SMA wires can be drawn which will facilitate actuation of each module independently. The SMA wiring scheme is also illustrated in the figure.

## 7.4 Design of In-Mold Assembly Methods

This dissertation has described in-mold assembly methods specific to the mesoscale. Two different mold design strategies and computational modeling strategies for selecting design parameters for both strategies have also been described. However in order to successfully manufacture in-mold assembled designs, mold

design parameters specific to the design under consideration need to be selected. These include:

- 1) The molding sequence that should be used for in-mold assembly.
- 2) The mold filling strategy that would be most suitable to the design. In this dissertation we have described two different mold filling strategies:
  - a) Uni-directional filling for second stage polymer melt: This involves selection of appropriate radial supports. The modeling methods for selecting this parameter have been described in chapter 4.
  - b) Bi-directional filling for second stage polymer melt: This involves selecting the allowable temporal misalignment. The modeling methods for selecting this parameter have been described in chapter 5.
- 3) The support cavity length which will allow for appropriate clearance in the in-mold assembled mesoscale revolute joint. The modeling methods for selecting this parameter have been described in chapter 6.

This section will describe the methods used to apply the models described in the previous chapters to select the mold design parameters for manufacturing the in-mold assembled 6 DOF robot.

#### **7.4.1 Selecting the Molding Sequence**

The 6 DOF robot design illustrated in Figure 7.2 consists of a revolute joint in each module. This joint consists of a pin and a cavity of 0.8 mm diameter. Chapter 3 describes methods to select the molding sequence based on the joint dimensions. For joint dimensions which fall into the macroscale domain, a molding sequence involving the part consisting of the cavity being molded first is used. However when

the joint dimensions fall into the mesoscale the molding sequence involves the part with the pin being molded in the first stage. Distinction between the macroscale and mesoscale can be made based on the material combination to be used for manufacturing the joint.

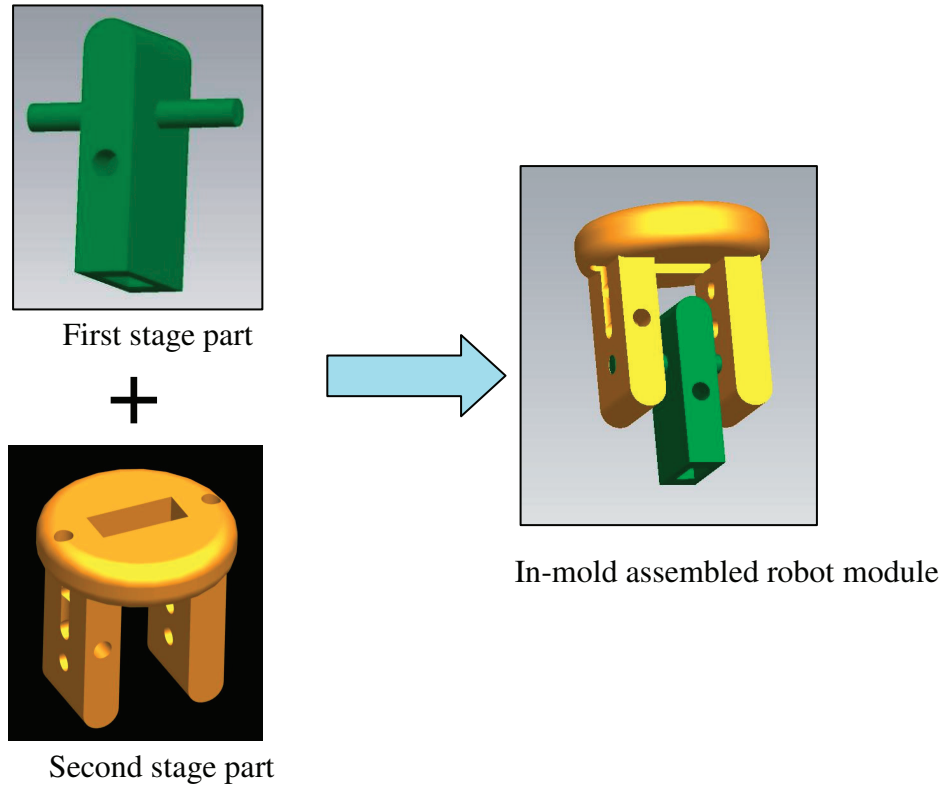


Figure 7.3 Molding sequence for in-mold assembly of 6 DOF robot

For fabricating the in-mold assembled 6 DOF robot, a material combination involving Hival ABS HG6 manufactured by Ashland Chemicals and Grillamid-L16 LM (Nylon 12) manufactured by EMS Grivory was used. For ABS, joint dimensions of less than 1 mm require mesoscale in-mold assembly methods. This has been described in Chapter 3. Hence the component with the pin was molded in the first stage with ABS. The molding sequence that was used is illustrated in Figure 7.3.

### **7.4.2 Selection of the Mold Filling Strategy**

This dissertation describes two different mold filling strategies for the second stage polymer melt. From the perspective of the mold design for in-mold assembly of the 6 DOF robot, it is important to pick the most appropriate mold filling strategy. Considering the number of cavities necessary in each module of the robot, a multi piece mold design for each module is mandatory. Each cavity in the part needs a separate side-action core. This significantly complicates the mold design for each module. This is because the side action cores need to be aligned appropriately in the mold cavity before injection. Considering the overall size of the part, designing the mold to accommodate all side action cores in the tight spaces is challenging. Also while providing for the cavities in the part; ensuring complete mold filling is a challenge. Hence the runner and gates have to be appropriately positioned to ensure that the cavity is filled completely.

Owing to the complexity of the mold design and presence of multiple side action cores to provide for the SMA wiring, bi-directional filling strategy for in-mold assembly was impossible. This is because it was impossible to position the gates for the second stage mold cavity while keeping the temporal misalignment within acceptable values and preventing weld-lines from forming at structurally demanding portions. Hence the mold design had to provide for radial supports to constrain the pins on the premolded component or the first stage part illustrated in Figure 7.3.

### **7.4.3 Selection of Design Parameters**

It was important to minimize mold manufacturing cost while ensuring that the premolded component does not deform plastically due to the second stage polymer

melt flow. Hence the optimal radial support length which would inhibit the plastic deformation had to be computed. To accomplish this, the modeling method to predict plastic deformation as a function of the radial support length was employed. This strategy has been defined in chapter 4.

In the first step, flow simulations for filling of the second stage mold cavity were conducted. These flow simulations reveal the force applied on the mesoscale premolded component by the second stage polymer melt flow. Since a uni-directional filling strategy for filling of the second stage mold cavity is adopted, the drag force builds up on the premolded component until the second stage polymer melt encounters a mold wall downstream of the premolded component.

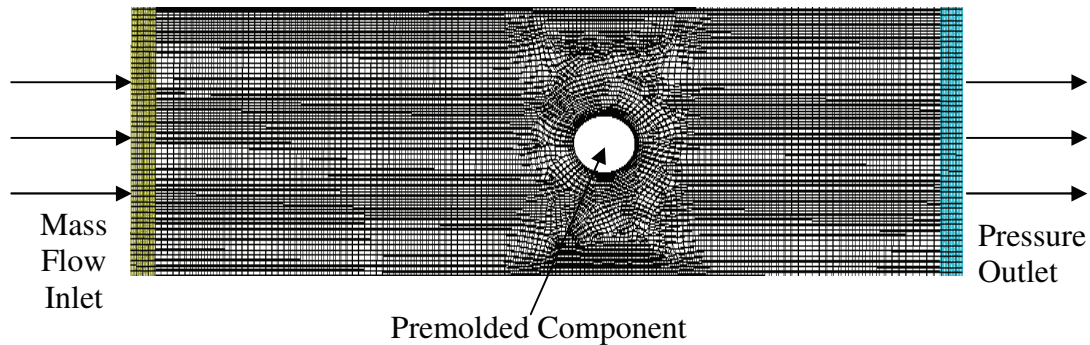


Figure 7.4 Mesh used for flow simulations for filling of second stage polymer melt

For modeling purposes, it was unnecessary to obtain a mesh of the entire second stage cavity. Hence only the portion of the second stage mold cavity which contained the mesoscale premolded component was modeled and meshed. This modeling and meshing was done using GAMBIT. Figure 7.4 shows the mesh that was used for the flow simulations. The mesh was then exported to FLUENT 6.3.26 to conduct the flow simulations.



The flow simulations computed the drag force on the premolded component as a function of the flow front progression. As described earlier, the drag force on the premolded component builds up until the flow encounters a mold wall. The maximum force was recorded at the instant the second stage polymer melt encountered the mold wall.

This maximum force was then used to conduct structural simulations in ANSYS 11.0. The premolded component was modeled and meshed to compute the effective plastic deformation due to the force applied by the second stage polymer melt as a function of the radial support length. This methodology is described in detail in section 4.3.2. Using these simulations the radial support length which resulted in premolded component deformations within the tolerance limit were predicted. Finally a radial support length was chosen for the mold design with an appropriate factor of safety.

Another important consideration for a revolute joint is the clearance between the pin and the cavity. This clearance is ensured by the compression and corresponding reduction in diameter of the mesoscale pin in the premolded component. This plastic deformation of the pin is controlled by selecting the right support cavity length. This is described in chapter 6. A low value of the support cavity length ensures low changes in the pin diameter. However this may induce jamming of the revolute joint. A high value of the support cavity length on the other hand results in high levels of plastic deformation of the pin. Hence an optimum value of the support cavity length needs to be designed. This length is selected based on the desired change in diameter

of the pin in the joint. This depends on the material selected for the premolded component.

#### 7.4.4 Mold Design

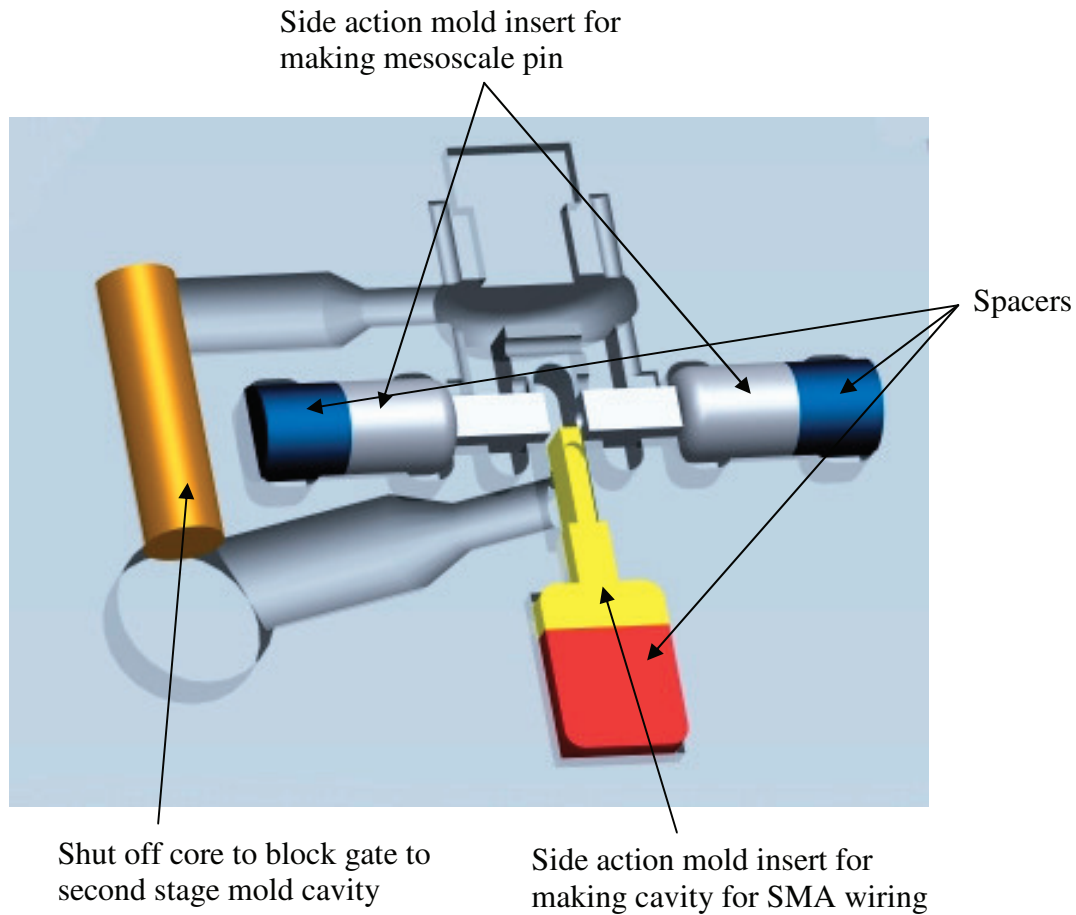


Figure 7.5 Mold assembly for first stage part

Once the design parameters were selected using the computational modeling methods, the final mold which was used for in-mold assembly of the robot module was designed. The mold assembly for molding the first stage part is illustrated in Figure 7.5. Three side action mold inserts (SAMI) were necessary for molding the first stage part or the premolded component. Two SAMIs were utilized to mold the

pin. The other SAMI was used to create a cavity which was necessary for SMA wiring of the robot module.

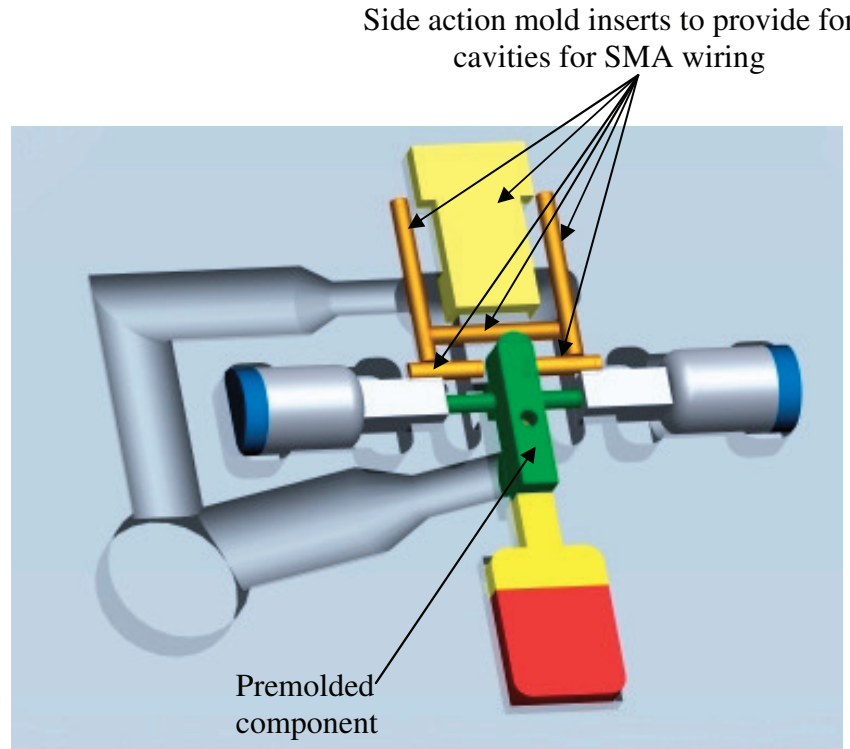


Figure 7.6 Mold assembly for second stage

A morphing cavity mold was designed for the in-mold assembly of the robot module. This required additional mold pieces to create shut off surfaces to block the second stage mold cavity during the first stage injection. Figure 7.5 illustrates the shut off core that was used.

Figure 7.6 illustrates the mold assembly that was used for the second stage injection. For the second stage mold, the two SAMIs that were used to make the pin in the premolded component were retracted so as to support the premolded component with the appropriate radial support length. This radial support length was chosen using the strategy described in the previous section. To provide for cavities for

SMA wiring, the second stage mold assembly also contained 6 other side action mold inserts as illustrated in the figure.

## 7.5 Results and Discussion

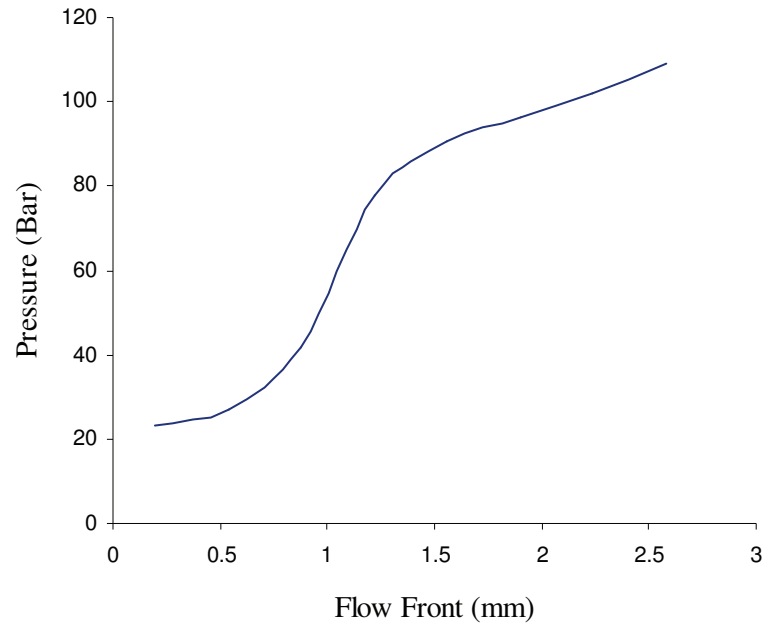


Figure 7.7 Force estimate on premolded component v/s Flow front progression

The robot modules were made using Hival ABS HG6 manufactured by Ashland Chemicals for the premolded component and Grillamid-L16 LM (Nylon 12) manufactured by EMS Grivory for the second stage part. Flow simulations were conducted in FLUENT 6.3.26 to compute the force applied by the second stage polymer melt on the premolded component. Flow properties of Nylon 12 which are described in Table 5.3 were used for the flow simulations. Results of the flow simulations can be seen in Figure 7.7. The second stage melt encounters a mold wall when the flow front progresses to 2 mm downstream of the pin. Hence flow

simulations beyond 2 mm are invalid from the in-mold assembly perspective. Figure 7.8 shows sample results of the FLUENT simulations.

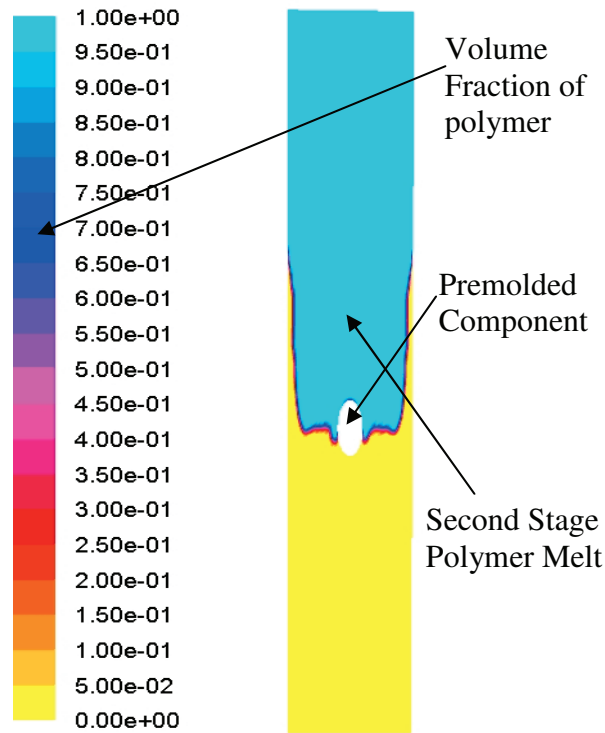


Figure 7.8 Sample flow simulations in FLUENT for flow front progression = 0.2 mm

The force estimate from the flow simulations were then used to conduct structural simulations on the premolded component. These simulations estimated the net plastic deformation of the premolded component due to the applied force. As can be seen in the Figure 7.7, the maximum force applied on the premolded component before the flow encounters a mold wall corresponds to a pressure of 110 bar. Structural simulations in ANSYS 11.0 were then used to compute the effective plastic deformation of the premolded component resulting from the force applied by the second stage polymer melt. The plastic deformation was computed for different radial support lengths so that the optimal radial support which inhibits plastic deformation could be selected. Figure 7.9 illustrates sample results of the plastic deformation of

the premolded component for two different radial support lengths. Figure 7.10 shows the relationship between the radial support length and the plastic deformation for the force applied.

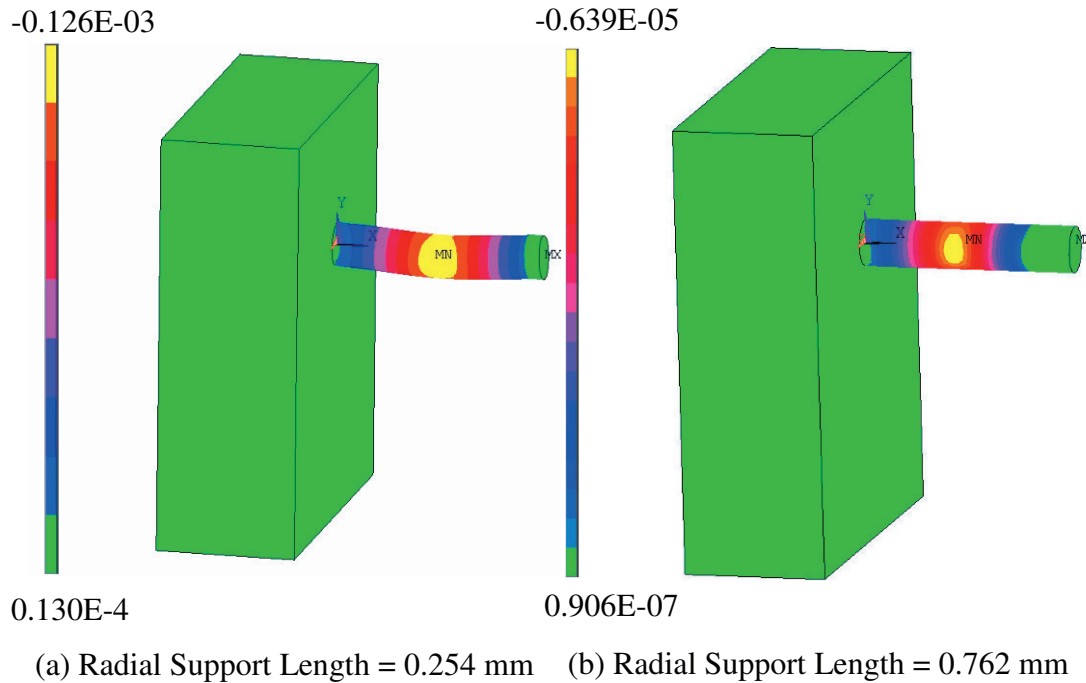


Figure 7.9 Sample ANSYS results for two different radial support lengths

While designing the mold for in-mold assembly of the 6 DOF robot module, the appropriate radial support were predicted by the simulation results. From the plot in Figure 7.10, it can be seen that the plastic deformation is within acceptable limits for radial support lengths greater than 0.75 mm. A factor of safety of 1.5 was used while designing the radial support length for the mold design. This ensured that the mesoscale pin in the premolded component does not undergo plastic deformation due to flow of the second stage polymer melt around it.

The last mold design parameter that had to be selected was the support cavity length which ensures that the mesoscale revolute joint does not jam during in-mold

assembly. As described in chapter 6, the support cavity length determines the variation in diameter of the pin during in-mold assembly. The support cavity length appropriate for the specific in-mold assembly mold design, depends on the material combination that is used. In this case, ABS is used as the material for the premolded component. For ABS a diameter variation of up to 10% due to plastic deformation is acceptable. This diameter variation keeps the effect of strain hardening due to plastic deformation of the pin within acceptable levels. A higher degree of strain hardening causes the material of the premolded component to be brittle. This affects the quality of the joint. Hence for manufacturing the module of the 6 DOF robot, a support cavity length of 0.4 mm was selected. This value is taken from Figure 6.14.

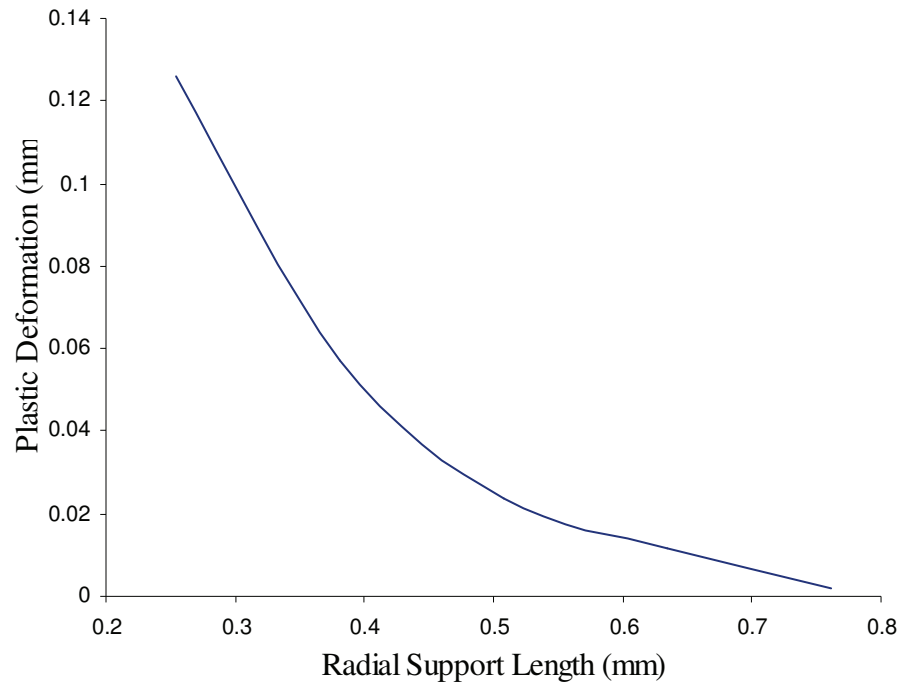


Figure 7.10 Plastic deformation of premolded component as a function of the radial support length

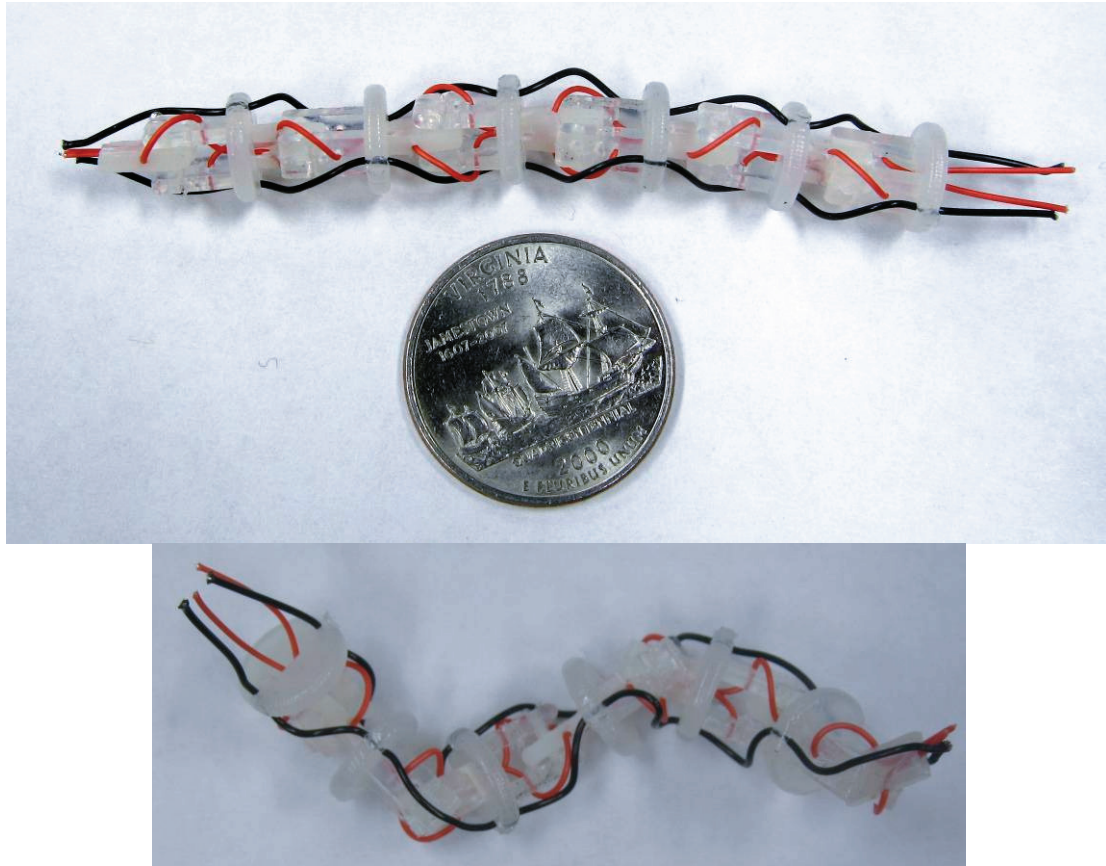


Figure 7.11 Two different orientations of prototype of 6 DOF robot manufactured using in-mold assembly

The mold design illustrated in Figure 7.5 and Figure 7.6 was then used to successfully manufacture a prototype of the in-mold assembled 6 DOF robot. 6 individual modules of the robot were fabricated using in-mold assembly. Each of these modules was wired using 24 gauge wires to demonstrate the capability of the design to be SMA wired. Finally the six modules were assembled together to obtain the in-mold assembled version of the 6 DOF robot. A prototype of this robot can be seen in Figure 7.11. This robot weighs 1.9 grams which is about 35% lighter than that reported by Pappafotis et al. [96].



It was envisioned to use the design methods that have been discussed in this chapter to fabricate an in-mold assembled hand robot. However one of the key features of the 6 DOF robot discussed in this chapter was the capability of out of plane motion of its links. Due to this out of plane motion of the links, this robot can not be used as a finger inspired robot. The CAD models of these two designs are illustrated in Figure 7.12. After careful inspection of the design for the 6 DOF robot, it was realized that a simple design change will allow in plane motion of the links of the 6 DOF robot. This design change, if incorporated can then be used to manufacture in-mold assembled fingers for a hand robot. This design change is illustrated in Figure 7.13.

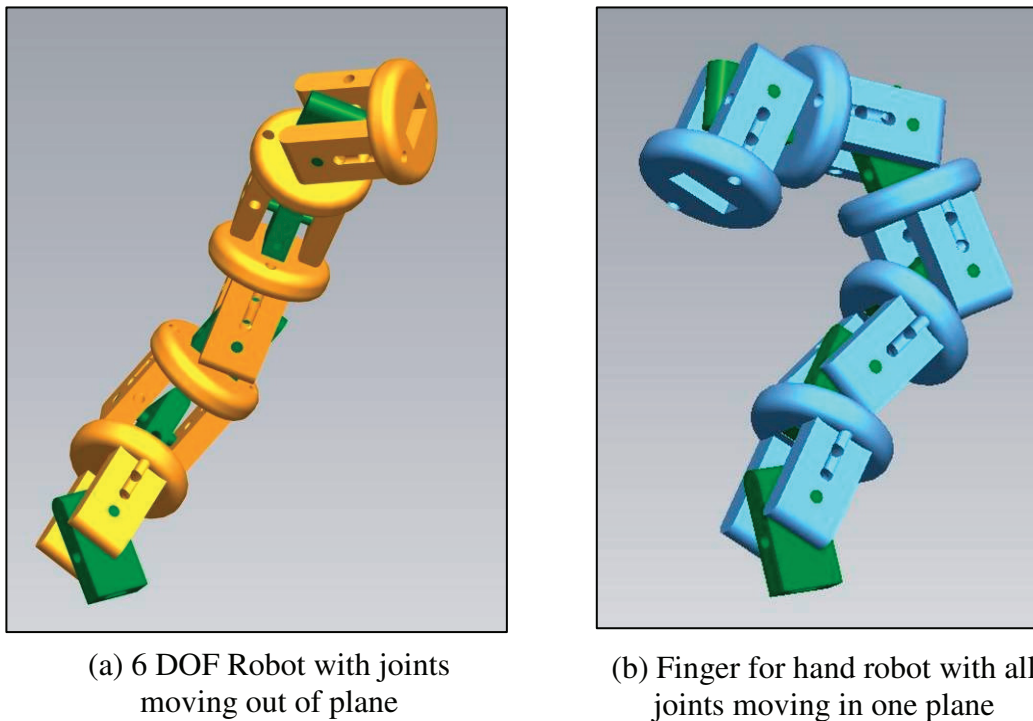


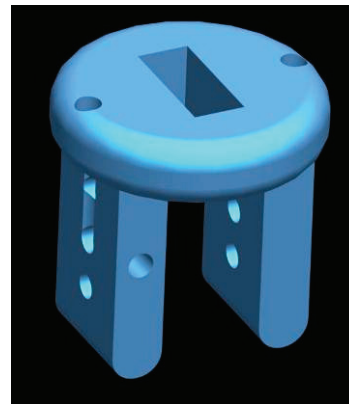
Figure 7.12 Distinction between 6 DOF robot and finger inspired robot

A separate mold was then designed to manufacture in-mold assembled modules for the hand robot. The design methods described in the previous sections were used to select the design parameters for this design. Using these methods a hand robot was

then fabricated. This is illustrated in Figure 7.14. This robot can potentially be actuated using SMA wires. It can be used as a robotic gripper for several applications.



Second Stage part for  
6 DOF robot



Second Stage part for  
Hand Robot

Figure 7.13 Design change for fabricating Hand Robot

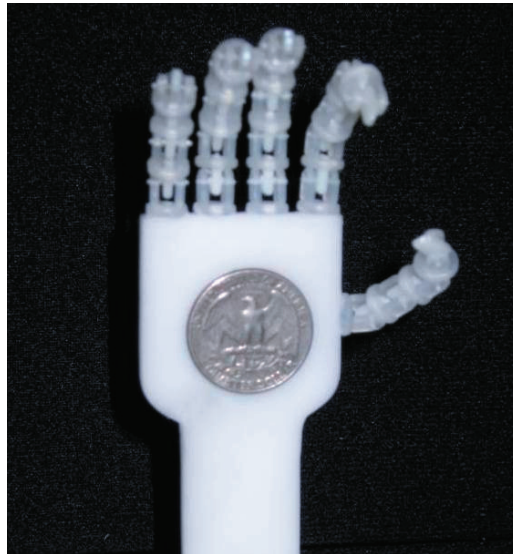


Figure 7.14 Hand robot consisting of 5 finger inspired robots

## 7.6 Summary

This chapter has described a case study of a 6 DOF robot which was manufactured using the in-mold assembly methods described in this dissertation. This robot was

inspired by the design developed by Pappafotis et al. [96]. Use of in-mold assembly methods resulted in successful fabrication of a robot compatible for SMA wiring. This robot consists of a lower overall part count due to use of in-mold assembly. This potentially results in higher durability of the robot. Due to lower overall part count the robot is also less susceptible to failure due to higher reliability. Elimination of fasteners results in significant reduction in overall weight of the robot. The robot fabricated using in-mold assembly methods was found to be 35% lighter than that manufactured by machining and assembly.

The results described in this section clearly demonstrate the power of the mold design and modeling methods that have been developed as part of this dissertation. The computational modeling methods were used efficiently to choose appropriate design parameters which could be used for in-mold assembly of the 6 DOF robot and the finger inspired robot.

## **8 Conclusions**

This chapter will present the intellectual contributions and the anticipated benefits to the industry resulting from the advances reported as part of this dissertation.

### ***8.1 Intellectual Contributions***

This dissertation is expected to yield various contributions to the body of work in in-mold assembly. The dissertation is expected to be the first of its kind to make inroads into development of an automated process for mesoscale in-mold assembly. The three most important and potentially useful contributions will be: (1) identification of defect modes unique to in-mold assembly at the mesoscale and development of methods to delineate the mesoscale and the macroscale from the in-mold assembly perspective, (2) development of a mold design which will allow constraining of premolded components to enable mesoscale in-mold assembly, (3) development of a process utilizing multiple gates placed at appropriate locations to fill the second stage mold cavity and (4) development of a predictive model to control clearances obtained in mesoscale in-mold assembled components.

#### **8.1.1 Identification of Defect Modes Specific to Mesoscale In-Mold Assembly**

As part of this effort, defect modes which are specific to in-mold assembly at the mesoscale have been identified. A detailed understanding of the physics behind the occurrence of these defects has also been developed. Computational modeling methods have been suggested to accurately estimate the size scales at which the

defects specific to the mesoscale are observed. Experimental methods have been developed to measure the forces developed inside the mold cavity. These forces are responsible for the deformation of mold pieces preexisting in the mold during injection molding. Computational modeling methods have also been developed to predict the force developed inside the mold cavity.

### **8.1.2 Development of Mold Design Solutions for Realizing In-Mold Assembly of Mesoscale Revolute Joints**

Two novel mold designs for realizing mesoscale in-mold assembled revolute joints were developed as part of this dissertation. The first design involves a unidirectional flow of the second stage polymer melt around the premolded component. The plastic deformation of the premolded component is controlled by use of radial supports to constrain it. In an alternate design, two gates are positioned at appropriate distances from the premolded component such that the force on the premolded component is controlled. Using this strategy the plastic deformation of the premolded component was controlled.

#### **8.1.2.1 Characterization of Plastic Deformation in Premolded Component during Mesoscale In-Mold Assembly**

As part of this effort, mold design templates have been developed to facilitate the in-mold assembly process at the mesoscale for polymer combinations having significantly different material properties viz. melting temperatures. This requires significant design changes to the molds used for manufacturing macroscale in-mold assembled revolute joints. A physics based computational model has been developed

to characterize and control the plastic deformation of the premolded component during the mesoscale in-mold assembly process. This model incorporates the dependence of the deformation on the following aspects of the injection molding process:

- 1) The material properties of the premolded component
- 2) The flow characteristics of the second stage polymer melt
- 3) The processing parameters used for injection molding of the second stage polymer
- 4) The mold design parameters such as those used to constrain the premolded component

The modeling approach that has been developed requires little or no further experimentation to choose design parameters which allow successful in-mold assembly at the mesoscale.

#### **8.1.2.2 Characterization of a Bi-directional Filling Process for**

##### **Mesoscale In-Mold Assembly**

Another significant contribution is in the area of using multi gated mold designs for mesoscale in-mold assembly. This strategy utilizes the advantages of bi-directional filling to facilitate mesoscale in-mold assembly. As part of this effort, mold design templates to manufacture in-mold assembled revolute joints have been developed. Computational modeling methods have been developed to solve a coupled physical problem using metamodels of the decouple solutions and applying them iteratively. This iterative modeling approach has been useful in creating knowledge to develop an

understanding of the sensitivity of the deformation of the premolded component due to the filling pattern of the bi-directional flow of the second stage part.

### **8.1.3 Characterization of Pin Diameter in In-Mold Assembled**

#### **Mesoscale Revolute Joints**

As part of this effort, an understanding of clearances in mesoscale in-mold assembled revolute joints has been developed. Revolute joints require a clearance fit between the core and the cavity for desirable operation. At the macroscale this clearance can be obtained and controlled by controlling the shrinkage of the molded components. However due to a reversed molding sequence at the mesoscale, shrinkage may result in joint jamming at the mesoscale. Methods have been described to overcome this jamming by providing for deformation of the pin such that the jamming does not occur. In order to maintain part quality and joint quality concurrently methods have been developed to control the deformation of the premolded component.

A predictive model has been developed to relate the pin deformation to mold design parameters. This predictive model can be used by the manufacturers as a tool for designing the appropriate assembly clearances in mesoscale in-mold assemblies. This model also presents designers with a tool to select the appropriate design parameters for the desired joint properties.

## **8.2 Anticipated Benefits**

The focus of this dissertation is on the development of methods to enable manufacturing of mesoscale revolute joints using in-mold assembly. Current

manufacturing processes for production of mesoscale assembled products are highly labor intensive and therefore expensive. Injection molding on the other hand is a high throughput process which is fully automated. Hence use of the methods developed as part of this work will enable a fully automated large scale production of mesoscale in-mold assembled components. This will therefore significantly reduce the labor costs for production of such components.

Another benefit of using in-mold assembly is the potential of reduced part costs. This is because injection molding uses polymer as the raw material. Polymers are usually cheaper than their metallic counterparts. They also require much lesser post processing when compared to metal ores. They are also significantly lighter than metallic parts. Because of this advantage, the parts manufactured using the in-mold assembly can potentially replace several metallic assemblies which are bulkier and costlier.

In-mold assembly results in elimination of screws and fasteners in revolute joints. This leads to a significant reduction in part count of the assembly. This leads to a much better product performance. At the mesoscale, this is not only beneficial in terms of reduction of part count, but also in creating new product possibilities. This is because screws and fasteners are usually unavailable at such a small scale. Hence use of in-mold assembly at the mesoscale has the potential to manufacture products which were previously impossible to manufacture using the conventional assembly methods.

### ***8.3 Future Directions***

This dissertation is one of the first works in the area of in-mold assembly at the mesoscale. It shows the feasibility of manufacturing in-mold assembled joints at the



mesoscale. However the advances reported as part of this work opens several new research directions. This section will discuss some of the impending issues that need to be addressed.

### **8.3.1 Development of Mold Design Templates to Manufacture**

#### **Other Classes of Mesoscale Articulating Joints**

This dissertation focuses primarily on manufacture of mesoscale revolute joints. Revolute joints present one of the most general classes of joints. Hence methods developed for revolute joints can be extended to be applied to several other classes of joints such as universal joint, prismatic joint etc. However several issues will arise during mesoscale in-mold assembly of other classes of joints. Hence direct extension of the methods developed for revolute joints will not be possible. Experiments need to be conducted to create mold design templates which can be used to manufacture other classes of mesoscale articulating joints such as prismatic joints, universal joints etc.

### **8.3.2 Experimental Methods for Real-time Force Measurement**

#### **inside the Mold**

This dissertation has for the first time reported a real-time in-mold measurement technique to measure the forces applied by a polymer melt on a mold piece during filling. An innovative experimental setup for this measurement is described in section 3.3. However the experiments conducted using this setup were for only one specific diameter of the mold piece. Hence this experiment only qualitatively verifies the trend of the computational model developed for the force experienced by a mold piece during injection molding. For several design scenarios which involve use of

mold inserts, there is a need for verifiable quantitative force prediction methods. For this, force measurement experiments need to be conducted using different diameters of the mold insert. Using these experiments, an empirical formulation of the force on the mold insert during injection molding can be developed. Such a model will be useful in selecting appropriate design parameters for mold inserts used during injection molding. To develop a general model for force prediction, it is necessary to repeat these experiments for at least two polymer melts. This model then needs to be verified for a different polymer.

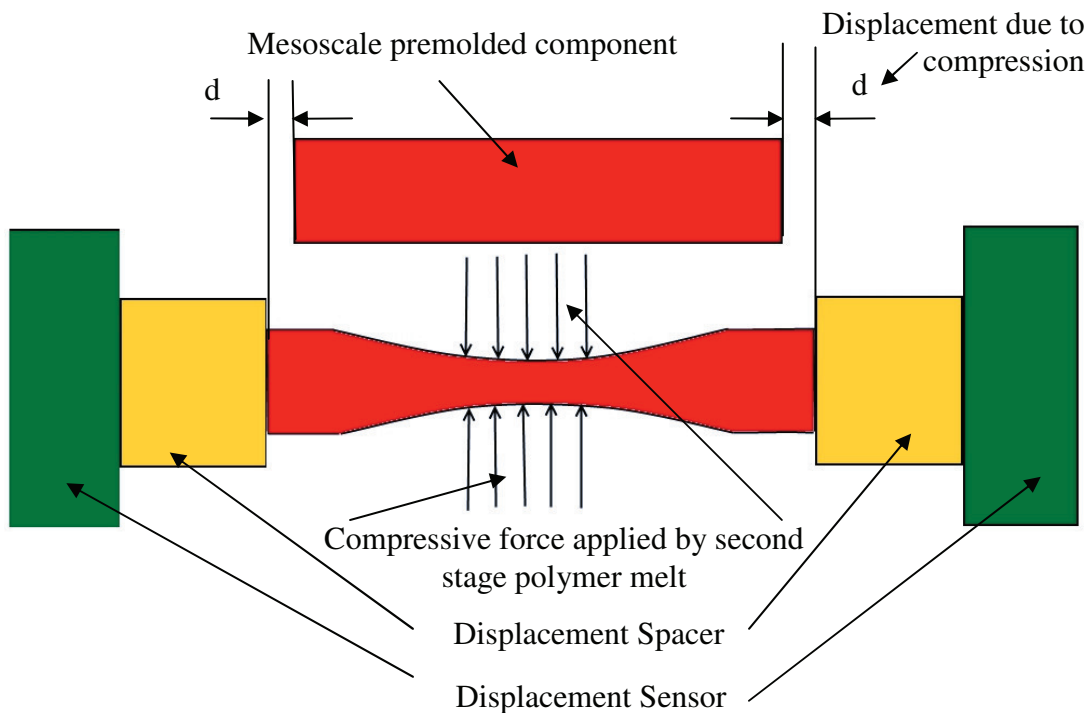


Figure 8.1: Measurement of displacement to estimate compressive force

Another important force that needs to be measured for accurate prediction of assembly clearances during in-mold assembly is the compressive force applied on the premolded component during in-mold assembly. This force can change the joint dimensions due to extrusion of the premolded component, and can be controlled by

part constraining features in the mold (Figure 6.2). However direct experimental measurement of these forces using non-intrusive techniques is impossible. This is because a device for force measurement needs to be embedded inside the polymer melt. The presence of such a device causes interruption in the melt flow which would result in intrusive measurements. Hence a non-intrusive measurement technique which can be used in conjunction with computational modeling can be developed for the measurement of this force. One such experimental setup is illustrated in Figure 8.1.

This setup can be used to measure the compressive force on the mold insert using indirect measurement. The elongation of the pin can be measured real-time during the injection molding process. Two different kinds of measurement techniques can be used to measure the same

- 1) Spring/cantilever based measurement of deformation
- 2) Resistive/Capacitive/Inductive displacement sensor based measurement of deformation

The changes in dimensions can then be related to the compressive force using the material properties in computational simulations of the extrusion process. The challenge in the first approach is to keep the reaction force of the measurement device considerably low so it does not interfere with the extension of the premolded component and affect accuracy.

### **8.3.3 Ejection of In-Mold Assembled Mesoscale Revolute Joints**

Another important issue which arises during in-mold assembly at the mesoscale is ejection. Due to the presence of multiple components with delicate features inside the

mold after in-mold assembly, traditional ejection methods involving ejector pins, tend to destroy the parts with miniature features. Currently, utmost care is required to eject in-mold assemblies from the mold using manual methods. However to make the in-mold assembly process at the mesoscale more cost effective, it is important to keep the overall cycle time low. This can be ensured only with the use of automatic ejection strategies.

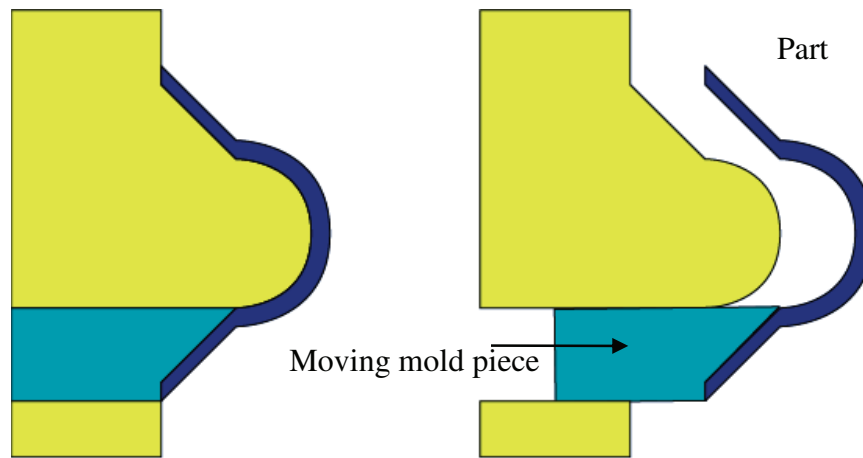


Figure 8.2: Surface based ejection system

A surface based ejection strategy would be most suitable for ejecting mesoscale in-mold assemblies from the mold. This strategy is illustrated in Figure 8.2. In this technique the core half of the mold is split into two or more pieces to create relative motion between the pieces to eject the part (see Figure 8.2). This technique will distribute the ejection force over a large portion of the surface area of the part. However for mesoscale in-mold assemblies, it is imperative to use these surface based techniques concurrently on all the different parts of the assembly so that the assembly is ejected together. To implement this, it is important to predict accurately

the force required for ejection of each part of the assembly. A closed loop control system needs to be built to control the ejection forces precisely.

#### **8.3.4 In-Mold Assembly at the Mesoscale Using Filled Polymers**

Recently developed fiber-filled polymer composite formulations exhibit significantly improved mechanical properties (e.g., greater Young modulus and tensile strength) and thermal conductivities. For example the carbon fiber filled Nylon 12 formulation available from PolyOne known as NJ-6000 TC has up to 2.6 times higher tensile strength, 20 times higher Young's modulus and 50 times higher thermal conductivity compared to unfilled Nylon 12. This fiber-filled polymer composite holds tremendous promise in making 3D articulating structures. However use of fiber-filled polymer composites poses several challenges during in-mold assembly. These include:

- 1) Injection molding of fiber-filled polymer composites require use of heated molds. During in-mold assembly, a premolded component is present in the mold during second stage injection. Hence use of a heated mold tends to pre-soften the premolded component much before it interacts with the second stage polymer melt. Hence a different strategy may be needed for in-mold assembly using a fiber-filled polymer composite
- 2) Fiber orientations of the molded fiber-filled polymers significantly affect its microstructure and physical properties. Hence in order to make mesoscale in-mold assemblies using filled polymer composites requires prediction of the fiber orientation accurately and thereby prediction of the mechanical and

thermal properties of the part. This is necessary to select the right mold design parameters which are necessary for achieving in-mold assembly.

- 3) This dissertation has described methods to compute the effective force applied on a mold insert by an unfilled polymer melt flow. The findings of this dissertation indicate that the effect of the drag force of the unfilled polymer melt flow significantly exceeds the effect of the impact force. However for fiber-filled polymer composites, this impact force can not be neglected. This is because the impact force is induced by a combination of the polymer melt flow and the micro-scale fiber filler particles. The superposition of these two force components is expected to be higher than the impact force in the case of unfilled polymer melt flows. Hence it is important to develop methods to measure this impact force and develop methods to predict them.

## References

1. H.Y. Wong, K.T. Fung, and F.R. Gao, 2008, "Development of a transducer for in-line and through cycle monitoring of key process and quality variables in injection molding," *Sensors and Actuators a-Physical*. **141**(2), pp. 712-722.
2. J.P. Beaumont, 2004, *Runner and Gating Design Handbook: Tools for Successful Injection Molding*. Hanser Gardner Publications
3. J.P. Beaumont, R. Nagel, and R. Sherman, 2002, *Successful Injection Molding: Process, Design, and Simulation*. 1st Edition ed. Hanser Gardner Publications.
4. J.Y.H. Fuh, Y.F. Zhang, A.Y.C. Nee, and M.W. Fu, *Computer Aided Injection Mold Design*. 2004, Marcel Dekker Inc. .
5. R.A. Malloy, 1994, *Part Design for Injection Molding*. Hanser Gardner Publications
6. G. Menges, W. Michaeli, and P. Mohren, 2001, *How to Make Injection Molds*. 3rd Edition ed. Hanser Gardner Publications.
7. M. Knights. *Micro Molds Make Micro Parts*. as seen on 4/6/2009.
8. A.K. Priyadarshi, S.K. Gupta, R. Gouker, F. Krebs, M. Shroeder, and S. Warth, 2007, "Manufacturing multi-material articulated plastic products using in-mold assembly," *International Journal of Advanced Manufacturing Technology*. **32**(3-4), pp. 350-365.
9. R. Brock, 2002, "It's a small world after all - A leaner approach to micro molding," *Plastics Engineering*. **58**(8), pp. 6-+.

10. M. Hecke and W.K. Schomburg, 2004, "Review on micro molding of thermoplastic polymers," *Journal of Micromechanics and Microengineering*. **14**(3), pp. R1-R14.
11. C. Goll, W. Bacher, B. Bustgens, D. Maas, R. Ruprecht, and W.K. Schomburg, 1997, "An electrostatically actuated polymer microvalve equipped with a movable membrane electrode," *Journal of Micromechanics and Microengineering*. **7**(3), pp. 224-226.
12. M. Nakao, M. Yoda, and T. Nagao, 2003, "Locally controlling heat flux for preventing micrometre-order deformation with injection molding of miniature products," *Cirp Annals-Manufacturing Technology*. **52**(1), pp. 451-454.
13. D.G. Yao and B. Kim, 2002, "Simulation of the filling process in micro channels for polymeric materials," *Journal of Micromechanics and Microengineering*. **12**(5), pp. 604-610.
14. J. Zhao, R.H. Mayes, G.E. Chen, H. Xie, and P.S. Chan, 2003, "Effects of process parameters on the micro molding process," *Polymer Engineering and Science*. **43**(9), pp. 1542-1554.
15. D.O. Kazmer, 2007, *Injection Mold Design Engineering*. Hanser Gardner Publications
16. A.G. Banerjee, X.J. Li, G. Fowler, and S.K. Gupta, 2007, "Incorporating manufacturability considerations during design of injection molded multi-material objects," *Research in Engineering Design*. **17**(4), pp. 207-231.
17. R.M. Gouker, S.K. Gupta, H.A. Bruck, and T. Holzschuh, 2006, "Manufacturing of multi-material compliant mechanisms using multi-material



- molding," *International Journal of Advanced Manufacturing Technology*. **30**(11-12), pp. 1049-1075.
18. L.M. Arzondo, N. Pino, J.M. Carella, J.M. Pastor, J.C. Merino, J. Poveda, and C. Alonso, 2004, "Sequential injection overmolding of an elastomeric ethylene-octene copolymer on a polypropylene homopolymer core," *Polymer Engineering and Science*. **44**(11), pp. 2110-2116.
  19. H.A. Bruck, G. Fowler, S.K. Gupta, and T. Valentine, 2004, "Using geometric complexity to enhance the interfacial strength of heterogeneous structures fabricated in a multi-stage, multi-piece molding process," *Experimental Mechanics*. **44**(3), pp. 261-271.
  20. C.C. Cheng, Y. Ono, and C.K. Jen, 2007, "Real-time diagnosis of co-injection molding using ultrasound," *Polymer Engineering and Science*. **47**(9), pp. 1491-1500.
  21. F. Ilinca, J.F. Hetu, and A. Derdouri, 2006, "Numerical investigation of the flow front behaviour in the co-injection moulding process," *International Journal for Numerical Methods in Fluids*. **50**(12), pp. 1445-1460.
  22. M. Kadota, M. Cakmak, and H. Hamada, 1999, "Structural hierarchy developed in co-injection molded polystyrene/polypropylene parts," *Polymer*. **40**(11), pp. 3119-3145.
  23. M. Kumar and S.K. Gupta, 2002, "Automated design of multi-stage molds for manufacturing multi-material objects," *Journal of Mechanical Design*. **124**(3), pp. 399-407.

24. C.T. Li and A.I. Isayev, 2003, "Interface development and encapsulation in simultaneous coinjection molding. I. Two-dimensional modeling and formulation," *Journal of Applied Polymer Science*. **88**(9), pp. 2300-2309.
25. X.J. Li and S.K. Gupta, 2004, "Geometric algorithms for automated design of rotary-platen multi-shot molds," *Computer-Aided Design*. **36**(12), pp. 1171-1187.
26. W. Michaeli, A. Rogalla, and C. Ziegmann, 2001, "Micro assembly injection molding of hybrid microsystems," *Journal of Polymer Engineering*. **21**(2-3), pp. 99-109.
27. S. Patcharaphun and G. Mennig, 2006, "Simulation and experimental investigations of material distribution in the sandwich injection molding process," *Polymer-Plastics Technology and Engineering*. **45**(6), pp. 759-768.
28. G. Schlatter, J.F. Agassant, A. Davidoff, and M. Vincent, 1999, "An unsteady multifluid flow model: Application to sandwich injection molding process," *Polymer Engineering and Science*. **39**(1), pp. 78-88.
29. R. Selden, 2000, "Co-injection molding: Effect of processing on material distribution and mechanical properties of a sandwich molded plate," *Polymer Engineering and Science*. **40**(5), pp. 1165-1176.
30. C.M. Vaz, P. van Doeveren, R.L. Reis, and A.M. Cunha, 2003, "Development and design of double-layer co-injection moulded soy protein based drug delivery devices," *Polymer*. **44**(19), pp. 5983-5992.
31. D. Watanabe, 2003, "The flow behavior of core material and breakthrough phenomenon in sandwich injection molding - Part I: Dependence on viscosity

- and injection speed of skin/core materials," *International Polymer Processing*. **18**(4), pp. 398-404.
32. D. Watanabe, 2003, "The flow behavior of core material and breakthrough phenomenon in sandwich injection molding - Part II: Influence of mold cavity thickness and core cylinder temperature," *International Polymer Processing*. **18**(4), pp. 405-411.
  33. W.C. Bushko and V.K. Stokes, 1996, "Solidification of thermoviscoelastic melts. Part 4. Effects of boundary conditions on shrinkage and residual stresses," *Polymer Engineering and Science*. **36**(5), pp. 658-75.
  34. D. Delaunay, P. Le Bot, R. Fulchiron, J.F. Luye, and G. Regnier, 2000, "Nature of contact between polymer and mold in injection molding. Part 2. Influence of mold deflection on pressure history and shrinkage," *Polymer Engineering and Science*. **40**(7), pp. 1692-1700.
  35. S. Fathi and A.H. Behraves, 2007, "Visualization of in-mold shrinkage in injection molding process," *Polymer Engineering and Science*. **47**(5), pp. 750-756.
  36. S. Han and K.K. Wang, 1997, "Shrinkage prediction for slowly crystallizing thermoplastic polymers in injection molding," *International Polymer Processing*. **12**(3), pp. 228-237.
  37. C.A. Hieber, 2002, "Modeling/simulating the injection molding of isotactic polypropylene," *Polymer Engineering and Science*. **42**(7), pp. 1387-1409.

38. K. Jansen and G. Titomanlio, 1996, "Effect of pressure history on shrinkage and residual stresses - Injection molding with constrained shrinkage," *POLYMER ENGINEERING AND SCIENCE*. **36** (15), pp. 2029-2040.
39. K.M.B. Jansen, R. Pantani, and G. Titomanlio, 1998, "As-molded shrinkage measurements on polystyrene injection molded products," *Polymer Engineering and Science*. **38**(2), pp. 254-264.
40. K.M.B. Jansen, D.J. Van Dijk, and M.H. Husselman, 1998, "Effect of processing conditions on shrinkage in injection molding," *Polymer Engineering and Science*. **38**(5), pp. 838-846.
41. J.G. Kovacs, 2006, "Construction of pre-deformed shapes for rapid tooling in injection molding," *Macromolecular Symposia*. **239**, pp. 259-265.
42. K. Kwon, A.I. Isayev, and K.H. Kim, 2005, "Toward a viscoelastic modeling of anisotropic shrinkage in injection molding of amorphous polymers," *Journal of Applied Polymer Science*. **98**(5), pp. 2300-2313.
43. K. Kwon, A.I. Isayev, and K.H. Kim, 2006, "Theoretical and experimental studies of anisotropic shrinkage in injection moldings of various polyesters," *Journal of Applied Polymer Science*. **102**(4), pp. 3526-3544.
44. K. Kwon, A.I. Isayev, K.H. Kim, and C. van Sweden, 2006, "Theoretical and experimental studies of anisotropic shrinkage in injection moldings of semicrystalline polymers," *Polymer Engineering and Science*. **46**(6), pp. 712-728.
45. S.J. Liao, D.Y. Chang, H.J. Chen, L.S. Tsou, J.R. Ho, H.T. Yau, W.H. Hsieh, J.T. Wang, and Y.C. Su, 2004, "Optimal process conditions of shrinkage and

- warping of thin-wall parts," *Polymer Engineering and Science*. **44**(5), pp. 917-928.
46. A.J. Pontes and A.S. Pouzada, 2004, "Ejection force in tubular injection moldings. Part I: Effect of processing conditions," *Polymer Engineering and Science*. **44**(5), pp. 891-897.
  47. L. Sridhar, B.M. Sedlak, and K.A. Narh, 2000, "Parametric study of heat transfer in injection molding - Effect of thermal contact resistance," *Journal of Manufacturing Science and Engineering-Transactions of the Asme*. **122**(4), pp. 698-705.
  48. G. Titomanlio and K.M.B. Jansen, 1996, "In-mold shrinkage and stress prediction in injection molding," *Polymer Engineering and Science*. **36**(15), pp. 2041-2049.
  49. X. Chen and F. Gao, 2003, "A study of packing profile on injection molded part quality," *Materials Science and Engineering a-Structural Materials Properties Microstructure and Processing*. **358**(1-2), pp. 205-213.
  50. C.K. Huang, S.W. Chen, and C.T. Yang, 2005, "Accuracy and mechanical properties of multiparts produced in one mold in microinjection molding," *Polymer Engineering and Science*. **45**(11), pp. 1471-1478.
  51. C.L. Thomas and A.J. Bur, 1999, "In-situ monitoring of product shrinkage during injection molding using an optical sensor," *Polymer Engineering and Science*. **39**(9), pp. 1619-1627.

52. F. Boitout, J.F. Agassant, and M. Vincent, 1995, "Elastic Calculation of Residual-Stress in Injection-Molding - Influence of Mold Deformation and Pressure in the Liquid," *International Polymer Processing*. **10**(3), pp. 237-242.
53. S.P. Brian Carpenter, Rebecca Hoffman, Blaine Lilly and Jose Castro, 2006, "Effect of Machine Compliance on Mold Deflection During Injection and Packing of Thermoplastic Parts," *POLYMER ENGINEERING AND SCIENCE*. pp. 844-852.
54. V. Leo and C. Cuvellez, 1996, "The effect of the packing parameters, gate geometry, and mold elasticity on the final dimensions of a molded part," *Polymer Engineering and Science*. **36**(15), pp. 1961-1971.
55. R. Pantani, V. Speranza, and G. Titomanlio, 2001, "Relevance of mold-induced thermal boundary conditions and cavity deformation in the simulation of injection molding," *Polymer Engineering and Science*. **41**(11), pp. 2022-2035.
56. C.H. Wu and Y.J. Huang, 2007, "The influence of cavity deformation on the shrinkage and warpage of an injection-molded part," *International Journal of Advanced Manufacturing Technology*. **32**(11-12), pp. 1144-1154.
57. B.D. De Besses, A. Magnin, and P. Jay, 2003, "Viscoplastic flow around a cylinder in an infinite medium," *Journal of Non-Newtonian Fluid Mechanics*. **115**(1), pp. 27-49.
58. E. Esirgemez, J.W. Newby, C. Nott, S.M. Olcmen, and V. Otugen, 2007, "Experimental study of a round jet impinging on a convex cylinder," *Measurement Science & Technology*. **18**(7), pp. 1800-1810.

59. A. Kumar and P.S. Ghoshdastidar, 2002, "Numerical simulation of polymer flow into a cylindrical cavity," *Journal of Fluids Engineering*. **124**(1), pp. 251-262.
60. E. Mitsoulis, 2004, "On creeping drag flow of a viscoplastic fluid past a circular cylinder: wall effects," *Chemical Engineering Science*. **59**(4), pp. 789-800.
61. C. Fetecau and F. Stan, 2007, "Computational prediction of defects during injection molding in a complex part," *Materiale Plastice*. **44**(3), pp. 180-184.
62. S.J. Liu, J.Y. Wu, J.H. Chang, and S.W. Hung, 2000, "An experimental matrix design to optimize the weldline strength in injection molded parts," *Polymer Engineering and Science*. **40**(5), pp. 1256-1262.
63. C. Lu, X.F. Yu, and S.Y. Guo, 2006, "The mechanism of ultrasonic improvement of weld line strength of injection molded polystyrene and polystyrene/polyethylene blend parts," *Journal of Polymer Science Part B-Polymer Physics*. **44**(10), pp. 1520-1530.
64. T. Nguyen-Chung, 2004, "Flow analysis of the weld line formation during injection mold filling of thermoplastics," *Rheologica Acta*. **43**(3), pp. 240-245.
65. R. Selden, 1997, "Effect of processing on weld line strength in five thermoplastics," *Polymer Engineering and Science*. **37**(1), pp. 205-218.
66. J. Tung, G.P. Simon, and G.H. Edward, 2005, "Weld lines in nylon 6 melt-blended nanocomposites," *Polymer Engineering and Science*. **45**(12), pp. 1606-1614.

67. C.H. Wu and W.J. Liang, 2005, "Effects of geometry and injection-molding parameters on weld-line strength," *Polymer Engineering and Science*. **45**(7), pp. 1021-1030.
68. K. Yamada, K. Tomari, U.S. Ishiaku, and H. Hamada, 2005, "Evaluation of mechanical properties of adjacent flow weldline," *Polymer Engineering and Science*. **45**(8), pp. 1180-1186.
69. N. Mekhilef, A. Aitkadi, and A. Ajji, 1995, "Weld Lines in Injection-Molded Immiscible Blends - Model Predictions and Experimental Results," *Polymer*. **36**(10), pp. 2033-2042.
70. J.K. Kim, J.H. Song, S.T. Chung, and T.H. Kwon, 1997, "Morphology and mechanical properties of injection molded articles with weld-lines," *Polymer Engineering and Science*. **37**(1), pp. 228-241.
71. E. Debondue, J.E. Fournier, M.F. Lacrampe, and P. Krawczak, 2004, "Weld-line sensitivity of injected amorphous polymers," *Journal of Applied Polymer Science*. **93**(2), pp. 644-650.
72. M. Boyanova, F.J.B. Calleja, and S. Fakirov, 2005, "Influence of processing conditions on the weld line in doubly injection-molded glassy polycarbonate and polystyrene: Microindentation hardness study," *Advances in Polymer Technology*. **24**(1), pp. 14-20.
73. C. Lu, X.F. Yu, and S.Y. Guo, 2005, "Ultrasonic improvement of weld line strength of injection-molded polystyrene and polystyrene/polyethylene blend parts," *Polymer Engineering and Science*. **45**(12), pp. 1666-1672.



74. K. Yamada, K. Tomari, U.S. Ishiaku, and H. Hamada, 2005, "Fracture toughness evaluation of adjacent flow weld line in polystyrene by the SENB method," *Polymer Engineering and Science*. **45**(8), pp. 1059-1066.
75. C.S. Chen, T.J. Chen, R.D. Chien, and S.C. Chen, 2007, "Investigation on the weldline strength of thin-wall injection molded ABS parts," *International Communications in Heat and Mass Transfer*. **34**(4), pp. 448-455.
76. S.G. Kim and N.P. Suh, 1986, "Performance Prediction of Weldline Structure in Amorphous Polymers," *Polymer Engineering and Science*. **26**(17), pp. 1200-1207.
77. W.F. Zoetelief, G.W.M. Peters, and H.E.H. Meijer, 1997, "Numerical simulation of the multi-component injection moulding process," *International Polymer Processing*. **12**(3), pp. 216-227.
78. D. Watanabe, U.S. Ishiaku, T. Nagaoka, K. Tomari, and H. Hamada, 2003, "Flow behavior of sandwich injection molding in sequential and simultaneous injection," *International Polymer Processing*. **18**(2), pp. 199-203.
79. D.A. Messaoud, B. Sanchagrin, and A. Derdouri, 2005, "Study on mechanical properties and material distribution of sandwich plaques molded by co-injection," *Polymer Composites*. **26**(3), pp. 265-275.
80. R.P. Bharti and R.P. Chhabra, 2007, "Two-dimensional steady Poiseuille flow of power-law fluids across a circular cylinder in a plane confined channel: Wall effects and drag coefficients," *Industrial & Engineering Chemistry Research*. **46**(11), pp. 3820-3840.

81. J.W.J. Cheng, T.C. Chao, L.H. Chang, and B.F. Huang, 2004, "A model-based virtual sensing approach for the injection molding process," *Polymer Engineering and Science*. **44**(9), pp. 1605-1614.
82. X. Chen, F.R. Gao, and G.H. Chen, 2004, "A soft-sensor development for melt-flow-length measurement during injection mold filling," *Materials Science and Engineering a-Structural Materials Properties Microstructure and Processing*. **384**(1-2), pp. 245-254.
83. H.W. Wu, S.D. Zhang, J.P. Qu, and H.H. Xu, 2007, "Measurement and analysis of cavity pressure and melt filling capacity during injection molding," *Polymer-Plastics Technology and Engineering*. **46**(2), pp. 123-127.
84. X. Chen, G.H. Chen, and F.R. Gao, 2004, "Capacitive transducer for in-mold monitoring of injection molding," *Polymer Engineering and Science*. **44**(8), pp. 1571-1578.
85. Y. Farouq, C. Nicolazo, A. Sarda, and R. Deterre, 2005, "Temperature measurements in the depth and at the surface of injected thermoplastic parts," *Measurement*. **38**(1), pp. 1-14.
86. Y.W. Lin and J.W.J. Cheng, 2008, "Model-based melt flow virtual sensors for filling process of injection molding," *Polymer Engineering and Science*. **48**(3), pp. 543-555.
87. FLUENT 6.2.36 documentation, F. Incorporated, Lebanon, NH
88. J. Happel and H. Brenner, 1973, *Low Reynolds number hydrodynamics*. 2nd Edition ed. Noordhoff International Publishing, Leyden, The Netherlands.
89. ANSYS 9.0 documentation, A. Inc., Canonsburg, PA

90. A. Ananthanarayanan, S.K. Gupta, and H.A. Bruck, 2009, "Characterization and Control of Plastic Deformation in Mesoscale Premolded Components to Realize In-mold Assembled Mesoscale Revolute Joints," *Polymer Engineering Science*. **49**(2), pp. 293-304.
91. R. Selden, 1997, "Effect of processing on weld-line strength in five thermoplastics," *Polymer Engineering and Science*. **37**(1), pp. 205-218.
92. A. Ananthanarayanan, W. Bejgerowski, D. Mueller, and S.K. Gupta. 2008, "Development of a multi-piece multi-gate mold for manufacturing a flapping wing drive-mechanism." *North American Manufacturing Research Conference*. Monterrey, Mexico.
93. A. Ananthanarayanan, S.K. Gupta, and H.A. Bruck. 2008, "Mechanical characterization of cold weld-lines and meld lines in mesoscopic revolute joints for bioinspired structures." *SEM Annual Conference and Exposition*. Orlando, Florida.
94. Ananthanarayanan A., Gupta S.K., and Bruck H.A., 2008, "Mechanical Characterization of Cold Weld-lines and Meld Lines in Mesoscopic Revolute Joints for Bioinspired Structures." *Society of Experimental Mechanics XI International Congress & Exposition on Experimental and Applied Mechanics*. Orlando, FL.
95. A. Ananthanarayanan, S.K. Gupta, H.A. Bruck, Z. Yu, and K.P. Rajurkar. 2007, "Development of In-Mold Assembly Process for Realizing Mesoscale Revolute Joints." *North American Manufacturing Research Conference*. Ann Arbor, MI.

96. N. Pappafotis, W. Bejgerowski, R. Gullapalli, J.M. Simard, S.K. Gupta, and J.P. Desai. 2008, "Towards design and fabrication of a miniature MRI-compatible robot for applications in neurosurgery." ASME 2008 International Design Engineering Technical Conferences & Computers and Information in Engineering Conference IDETC/CIE. New York, NY.
97. W. Bejgerowski, A. Ananthanarayanan, D. Mueller, and S.K. Gupta, 2009, "Integrated product and process design for a flapping wing drive-mechanism," Journal of Mechanical Design (accepted for publication).